Optically driven nanostructures with strong vibronic coupling

Henry E. J. Maguire

School of Physics and Astronomy
2019

A thesis submitted to the University of Manchester for the degree of Doctor of Philosophy
in the Faculty of Science and Engineering

Blank page

Contents

Word count: 28840

Abstract

Many developments in modern physics rely on the understanding of quantum systems that are strongly coupled to complex, structured environments. In particular, quantum emitters such as single molecules and quantum dots are of great interest in many applications in photonics, solar energy and nano-electronics. In many of these situations, the traditional tools of quantum optics break down, requiring a non-perturbative approach to system-environment coupling. Understanding strongly-coupled open quantum systems is still an active area of research, with many powerful numerical and analytical techniques being developed. In this thesis, we attempt to combine the approaches of strongly-coupled open quantum systems with the study of natural and artificial solar energy conversion. Light-harvesting systems are highly non-equilibrium in nature, since they interact with multiple environments at different temperatures - a regime which is difficult to treat with many cutting edge open systems techniques. Starting from the simplest possible model, that of a single transition in a molecule, we uncover some common inconsistencies that get made in the literature and develop further the notion of *environmental non-additivity*. We show that this effect, where the coupling of a quantum system to one environment affects how it couples to another environment, is a general property of many non-equilibrium models. We see that for sufficient phonon-coupling it can directly lead to population inversion in a two-level emitter under incoherent thermal driving.

After analysing the two-level case, we then expand the model to include two interacting emitters. This builds on the previous work in the literature on excitonic energy transfer, in order to more realistically evaluate the effectiveness of these systems within a quantum photocell context. Using non-perturbative open systems techniques, we demonstrate a striking diversion from the weak-coupling theory in the resultant dynamics and steady-states.

Finally, we derive a novel model for a molecular photocell, which allows us to explore the interplay between strongly-coupled vibrations, photon absorption and molecule-electrode coupling. This setting gives rise to an array of rich non-additive phenomena, which ultimately determines the photocell performance. We identify regimes where strong phonon-coupling enhances photocurrent.

Declaration

No portion of the work referred to in this thesis has been submitted in support of an application for another degree or qualification of this or any other university or other institute of learning.

Copyright statement

Blank page

Chapter 1

Introduction to Open Quantum Systems

1.1 Overview

The preparation and control of quantum systems is an area of great interest in physics and engineering. These systems are never truly isolated from their environment, which can often lead to the destruction of their coherence properties, causing a decay of quantum mechanical behaviour as both system and environment tend towards maximal disorder. Probing the properties of a quantum system often relies on observing how it relaxes back to equilibrium after it has been perturbed or excited by an external energy source. Additionally, a rich set of behaviour can occur when a dissipative system is continuously driven. As we will see, the strength and nature of the dissipation and driving can determine a wide variety of observable phenomena within even the simplest quantum systems, making system-environment interactions an important aspect to consider in developing new quantum technologies.

Much like in open-classical systems, such as classical thermodynamics, there is a temptation to model the interplay between a system and its environment in the limit of weak coupling. This assumes that the correlations between system and bath decay extremely quickly and any energy or information transferred from the system is irretrievably lost to the many degrees of freedom of the bath. This information is not accessible at later times and so the bath contains no *memory* of the past system states. In this limit it is not possible to model strong system-bath coupling, where correlations caused by the interactions can persist on timescales relevant to the system evolution itself. If these correlations exist, they can non-trivially alter the future evolution of a system. For many quantum systems, such as semiconductor quantum dots [1, 2], it is crucial to account for these memory effects in order to accurately predict the true dynamics.

The design principles of many modern solid-state quantum technologies rely on controlling quantum degrees of freedom that are under the influence of strongly-coupled electromagnetic fields, vibrations and phonon modes [3]. In many such instances, it becomes necessary

to move beyond the weak-coupling regime and develop formalism which allows for strong-coupling, capturing the non-equilibrium nature of the environment and the build up of system-environment correlations.

Open-quantum systems techniques have also been used extensively to study excitation behaviour during light-harvesting processes in natural photosynthetic organisms. Dynamical properties observed in time-resolved spectroscopy of such systems not only suggest inherently quantum evolution [4, 5, 6] which could be enabled by strong electron-vibrational interactions [7, 8, 9, 10], but also that the interplay between electronic coherence and strong phonon dissipation could play a key role in the highly efficient energy transfer [11, 12, 13, 14, 15, 16]. This indicates that weak-coupling treatments which neglect bath-memory effects may not capture the complete dynamics, since strongly-coupled low-frequency modes result in longer bath-correlation times and significant system-bath correlations. The charge-separation mechanism of photosynthesis is responsible for all life on Earth, so understanding it is not only fundamentally important, but it also has the potential to inspire the future design of nanoscopic photocells [17]. Again, the fabrication of such systems relies on the understanding of very far from equilibrium systems and excitation dynamics which are significantly influenced by complex, structured molecular environments.

Photovoltaic and photosynthetic systems can also be modelled as non-equilibrium quantum heat engines and their thermodynamic properties are currently of great interest [18, 19]. Many classical thermodynamic quantities and limits are yet to be understood in the quantum regime and strong system-bath coupling marks a fundamental departure from the classical theory. The non-equilibrium nature of these problems inherently relies on the existence of multiple environments, some of which are strongly-coupled to the system, which poses a difficult theoretical problem. In this thesis, I will develop methods for dealing with multiple baths, as well as study the interplay between electromagnetic and vibrational environments in simple molecular systems and photocells.

This chapter will lay the theoretical groundwork necessary for later chapters, that of open quantum systems formalism and the weak system-environment coupling regime. In Chapter 2 I will then move beyond weak-coupling and introduce two non-perturbative techniques that are used in later chapters. In Chapter 3, a simple toy model of a quantum emitter which has strongly-coupled vibrations, as well as a weakly-coupled optical environment is studied. I show that a full treatment of the interplay between vibrational and electromagnetic environments is required for physically consistent results - an important requirement that is often ignored in the literature. I show that this can lead to wildly different predictions, particularly in the case of thermal optical driving - conditions that are relevant for photovoltaic applications. In Chapter 4, I explore how strong vibrational coupling affects energy transfer between systems of coupled emitters, such as molecular dimers found in photosynthetic pigment-protein complexes. I show that the non-perturbative theory leads to profoundly different predictions compared to weak-coupling. In Chapter 5, I then introduce a novel model

of a toy molecular photocell, which requires the coupling of quantum emitters to electrodes and leads to a rich array of behaviour due to the interplay with strongly-coupled vibrations.

1.2 Mathematical preliminaries

Quantum mechanics was devised to explain the behaviour of systems which are isolated enough to justifiably be described as closed. The Schrödinger equation describes the reversible and unitary evolution of wave functions, but cannot deal with the uncertainty introduced by randomly fluctuating environments on its own. Therefore, in order to study open-quantum systems some formalism for dealing with statistics in quantum dynamics needs to be introduced. I will also review other useful analytical tools which shall be needed to derive the dynamical equations of these statistical ensembles, such as the interaction picture representation. Many further details can be found in [20, 21, 22].

1.2.1 Time evolution of density operators

In many applications, we do not know precisely which quantum state a system is in. In this case, *ensembles* of pure states need to be accounted for, which probabilistically describe the actual state of a quantum system in question. The probability of finding a quantum system in a particular state, or superposition of states, is therefore going to be a classical probability. This classical randomness might arise from a lack of information about the measuring apparatus or due to being coupled with an unobserved external system, such as a bath.

To describe these ensembles, or *mixed* states, *density operators* are used. In the density operator formalism, we can represent a pure state $|\psi(t)\rangle$ as a simple outer product,

$$\rho(t) = |\psi(t)\rangle\langle\psi(t)| \,. \tag{1.1}$$

In the case that $|\psi(t)\rangle$ is an N-dimensional vector, $|\psi(t)\rangle\langle\psi(t)|$ is now an $N \times N$ matrix. Now suppose that we have a system that is described by an ensemble of pure states $\{|\psi_n\rangle\}$, with corresponding probabilities $\{p_n\}$. We can construct a density matrix by a sum of the underlying states weighted by their probability

$$\rho(t) = \sum_n p_n \, |\psi_n(t)\rangle\langle\psi_n(t)| \,. \tag{1.2}$$

From this we can see immediately that density matrices are Hermitian, since $\{p_n\}$ are real numbers. For pure states, which can always be written as equation (1.1), we have effectively $p_n = p = 1$, so $\rho^2 = \rho$. Whereas, for mixed states the same is not true.

If a particular basis $\{|u_n\rangle\}$ is chosen, the density operator can be written as a matrix. In this form the diagonal elements of the matrix correspond to probabilities of the various basis

states being occupied and the off-diagonal elements to coherences between basis states,

$$\rho_{ij}(t) = \sum_n p_n \langle u_i|\psi_n(t)\rangle \langle \psi_n(t)|u_j\rangle = \langle u_i| \rho(t) |u_j\rangle . \tag{1.3}$$

We can write any operator as a spectral decomposition $A = \sum_m a_m |v_m\rangle\langle v_m|$, so the definition of an expectation value follows

$$\langle A(t)\rangle = \sum_{nm} p_n a_m |\langle \psi_n(t)|v_m\rangle|^2 = \mathrm{Tr}(\rho(t)A). \tag{1.4}$$

So, to find the expectation value of the ensemble, we find the expectation value of the operator for each (nth) item in the ensemble and then find the weighted sum over the classical probability distribution.

We summarise some general properties of density matrices:

- $\rho^\dagger = \rho$
- $\mathrm{Tr}\,\rho = 1$ or $\sum_n p_n = 1$
- For mixed states $\mathrm{Tr}\,\rho^2 < \mathrm{Tr}\,\rho = 1$
- For pure states $\mathrm{Tr}\,\rho^2 = \mathrm{Tr}\,\rho = 1$
- Expectation value of an operator A is given by $\langle A\rangle = \mathrm{Tr}(\rho A) = \mathrm{Tr}(A\rho)$

In order to study the dynamics of open-quantum systems, we must first have the formalism for time-dependent closed quantum systems in place. The state of a system $|\psi(t)\rangle$ as it evolves in time and space depends on the Hamiltonian $H(t)$, which is a description of the total energy of a system. In the non-relativistic case, this evolution is described by the Schrödinger equation

$$\frac{\partial |\psi(t)\rangle}{\partial t} = -iH(t) |\psi(t)\rangle , \tag{1.5}$$

which has the formal solution

$$|\psi(t)\rangle = U(t, t_0) |\psi(t_0)\rangle . \tag{1.6}$$

Note that we take $\hbar = 1$ throughout this thesis.

In the case that the governing Hamiltonian is time-dependent, the *unitary* operator $U(t, t_0)$ mapping the system from some initial time to future time t involves a time-ordered exponential,

$$U(t, t_0) = T_{\leftarrow} \exp\left[-i \int_{t_0}^{t} ds H(s)\right] \tag{1.7}$$

which are difficult to treat in practice. In the time-independent case, where $H(t) = H$, the unitary operator reduces to

$$U(t, t_0) = e^{-iH(t-t_0)}, \tag{1.8}$$

which is often far easier to compute. To make the solution of many problems more mathematically tractable, the time-dependence is removed from the system Hamiltonian by transforming to a moving reference-frame. This typically happens in sinusoidally-driven systems, which we will study in Chapter 3.

In order to describe the time-evolution of mixed states, we now need an equivalent to the Schrödinger equation but for density matrices rather than state vectors.

Using equation 1.6 we write

$$\rho(t) = \sum_n p_n U(t,t_0) \left|\psi_n(t_0)\right\rangle\!\left\langle\psi_n(t_0)\right| U^\dagger(t,t_0) = U(t,t_0)\rho(t_0)U^\dagger(t,t_0), \tag{1.9}$$

which can be differentiated with respect to time

$$\frac{\partial\rho(t)}{\partial t} = \frac{\partial U(t,t_0)}{\partial t}\rho(t_0)U^\dagger(t,t_0) + U(t,t_0)\rho(t_0)\frac{\partial U^\dagger(t,t_0)}{\partial t} \tag{1.10}$$

$$= -iHU(t,t_0)\rho(t_0)U^\dagger(t,t_0) + iU(t,t_0)\rho(t_0)U^\dagger(t,t_0)H \tag{1.11}$$

$$= -i[H,\rho(t)], \tag{1.12}$$

where we have used the derivative of equation (1.8) and its Hermitian conjugate to get the commutator form, although the same approach is valid for the time-ordered form in (1.7). This is known as the Liouville-Von Neumann equation, which is the equivalent to the Schrödinger equation but holds for any density operator.

1.2.2 The interaction picture

When dealing with interactions between different degrees of freedom of quantum systems, it becomes useful to transform to the interaction picture, or interaction representation. In the interaction picture, the time-dependence of a quantum system is incorporated into both the wave function *and* the operators. This is in contrast to the both the Schrödinger picture, where time-dependence is included only in the states and the Heisenberg picture where time-dependence is contained within in the operators acting on time-independent quantum states [20]. We initially write down the total system plus interaction Hamiltonian as

$$H = H_0 + H_I \tag{1.13}$$

where typically H_0 gives the free evolution of the system and the environment, which are usually exactly solvable in isolation. H_I is a more complicated interaction term which dynamically mixes the two subsystems.

In changing from the Schrödinger to the interaction representation, we perform a unitary transformation on the states and operators which moves the time-dependence due to H_0 to

the system operators

$$\tilde{A}(t) = e^{iH_0(t-t_0)} A e^{-iH_0(t-t_0)} = U_0^\dagger(t,t_0) A U_0(t,t_0), \tag{1.14}$$

from which it can be seen that the free Hamiltonian H_0 is left unchanged by such a transformation, since this means moving the time-dependence due to the operator onto itself.

As seen in 1.2.1, the expectation value of a Schrödinger picture operator A is given by

$$\langle A(t) \rangle = \mathrm{tr}\left(A\rho(t)\right) = \mathrm{tr}\left(AU(t,t_0)\rho(t_0)U^\dagger(t,t_0)\right). \tag{1.15}$$

The time-evolution operator can be decomposed

$$U(t,t_0) = U_0(t,t_0)U_I(t,t_0) \tag{1.16}$$

where $U_0(t,t_0) = e^{-iH_0(t-t_0)}$, which means (1.15) becomes

$$\langle A(t) \rangle = \mathrm{tr}\left(A\rho(t)\right) = \mathrm{tr}\left(AU_0(t,t_0)U_I(t,t_0)\rho(t_0)U_I^\dagger(t,t_0)U_0^\dagger(t,t_0)\right), \tag{1.17}$$

where we have used Eq. (1.14). Using the cyclic property of the trace, such that $\mathrm{tr}(ABC) = \mathrm{tr}(BCA) = \mathrm{tr}(CAB)$ we find

$$\langle A(t) \rangle = \mathrm{tr}\left(U_0^\dagger(t,t_0)AU_0(t,t_0)U_I(t,t_0)\rho(t_0)U_I^\dagger(t,t_0)\right) = \mathrm{tr}\left(\tilde{A}(t)\tilde{\rho}(t)\right), \tag{1.18}$$

where we have used equation 1.14 and

$$\tilde{\rho}(t) = U_I(t,t_0)\rho(t_0)U_I^\dagger(t,t_0) = U_0^\dagger(t,t_0)\rho(t)U_0(t,t_0), \tag{1.19}$$

where we have used (1.16). We then differentiate equation (1.19) with respect to time to get the time evolution:

$$\begin{aligned}
\frac{\partial\tilde{\rho}(t)}{\partial t} &= i\left[H_0, \tilde{\rho}(t)\right] + U_0^\dagger(t,t_0)\left(\frac{\partial\rho(t)}{\partial t}\right)U_0(t,t_0) \\
&= i\left[H_0, \tilde{\rho}(t)\right] - iU_0^\dagger(t,t_0)\left[H, \rho(t)\right]U_0(t,t_0) \\
&= i\left[H_0, \tilde{\rho}(t)\right] - i\left[H_0, \tilde{\rho}(t)\right] - iU_0^\dagger(t,t_0)\left[H_I, \rho(t)\right]U_0(t,t_0) \\
&= -i\left[\tilde{H}_I(t), \tilde{\rho}(t)\right].
\end{aligned} \tag{1.20}$$

The third line is reached by noticing that H_0 is left unchanged by the interaction picture transformation, since it is unitary. This is the Liouville-Von-Neumann equation for the interaction picture representation. Note that we have used a general start time t_0, but for the rest of the thesis we will assume $t_0 = 0$.

1.2.3 Composite systems and the reduced density operator

If a system and its environment are two separate, distinguishable entities, each with its own Hilbert space, we can represent the joint Hilbert space with a tensor product

$$\mathcal{H} = \mathcal{H}_S \otimes \mathcal{H}_E \tag{1.21}$$

where $\mathcal{H}_S$ is that of the system, with basis set $\{|\psi_i\rangle_S\}$ and $\mathcal{H}_E$ of the environment, with basis set $\{|\psi_j\rangle_E\}$. In this case the complete basis of the joint Hilbert space is $\{|\psi_i\rangle_S \otimes |\psi_j\rangle_E\}$. In the case of indistinguishable subsystems, which arise when dealing with fermionic environments, this tensor product structure does not necessarily exist and so further steps must be made - we will deal with these in Chapter 5.

For most of this thesis we will be dealing with bosonic baths, which are commonly modelled as infinite collections of harmonic oscillators. The combined Hilbert space of these oscillators is normally vast in comparison to the small system of interest, which may only have a few available states. In this case we will not be able to keep track of the entire environment, but it is possible to obtain expectation values for the subsystem of interest by defining system operators as

$$A = A_S \otimes \mathbb{1}_E \tag{1.22}$$

where $\mathbb{1}_E$ is the identity operator in the environment Hilbert space. Expectation values for the reduced density matrix $\rho_S(t)$ are then essentially marginal probability distributions over the total density matrix, where the bath degrees of freedom are averaged over

$$\langle A(t) \rangle = \mathrm{tr}_{S+E} \left(A_S \otimes \mathbb{1}_E \cdot \rho(t) \right) = \mathrm{tr}(A_S \rho_S(t)), \tag{1.23}$$

with the reduced density operator

$$\rho_S(t) = \mathrm{tr}_E(\rho(t)). \tag{1.24}$$

This will allow us to gain expectation values for the observables of interest A_S without having to keep track of the enormous environment Hilbert space. In many instances we will calculate expressions of the form

$$M_S = \mathrm{tr}_E \left(A_S \otimes B_E \rho_S(t) \otimes \rho_E(t) \right) = A_S \rho_S(t) \cdot \mathrm{tr} \left(B_E \otimes \rho_E(t) \right) \tag{1.25}$$

where the density operator can be factorised $\rho(t) = \rho_S(t) \otimes \rho_E(t)$, the environment state is time independent and operators are acting in both the system and environment Hilbert spaces. If the operators A_S and B_E commute, they can simply *pass through* the density matrix of the other Hilbert space and the *partial* trace can be taken directly over the environment where the tensor product has turned into a normal multiplication as the partial trace is a (potentially complex) scalar. This gives rise to the right-hand side of (1.25).

1.3 Dynamics of open quantum systems

I will now introduce a widely used method for modelling open quantum systems, specifically the evolution of the reduced density matrix $\rho_S(t)$. This will be done by deriving a quantum mechanical master equation for a system interacting with a large thermal bath, in the Born and Markov approximations. This is the standard approach that assumes weak-coupling between the two subsystems, an assumption that we will go beyond in this thesis. This section follows the references [21, 22] closely.

1.3.1 Born-Markov master equation

In this section, we derive an equation which describes the evolution of an open-quantum system whose influence from some large environment is described perturbatively in the coupling strength between the two. We first split up the total Hamiltonian of the system and environment

$$H = H_S + H_E + H_I, \tag{1.26}$$

where H_S and H_E are assumed to not share the same Hilbert-space and thus commute, H_I contains operators which are in both the system and environment Hilbert spaces. We now transform to the interaction picture, where the evolution due to the interaction Hamiltonian is treated perturbatively,

$$\tilde{H}_I(t) = e^{i(H_S+H_E)t} H_I e^{-i(H_S+H_B)t}. \tag{1.27}$$

The evolution of the total, *closed* system can be described by the Liouville-von Neumann equation in the interaction picture

$$\frac{\partial\tilde{\rho}(t)}{\partial t} = -i[\tilde{H}_I(t), \tilde{\rho}(t)], \tag{1.28}$$

which can be integrated directly to obtain the formal solution

$$\tilde{\rho}(t) = \rho(0) - i\int_0^t ds[\tilde{H}_I(s), \tilde{\rho}(s)]. \tag{1.29}$$

Equation (1.29) can be substituted back into (1.28) to obtain an exact dynamical equation in terms of second order products of H_I

$$\frac{\partial\tilde{\rho}(t)}{\partial t} = -i[\tilde{H}_I(t), \tilde{\rho}(0)] - \int_0^t ds[\tilde{H}_I(t), [\tilde{H}_I(s), \tilde{\rho}(s)]]. \tag{1.30}$$

We now perform a partial trace over the environmental degrees of freedom, to obtain a marginal distribution function - or reduced density matrix - for the system variables only,

$$\frac{\partial\tilde{\rho}(t)}{\partial t} = -i\,\mathrm{tr}_E[\tilde{H}_I(t),\tilde{\rho}(0)] - \int_0^t ds\,\mathrm{tr}_E[\tilde{H}_I(t),[\tilde{H}_I(s),\tilde{\rho}(s)]]. \tag{1.31}$$

We now set $\mathrm{tr}_E[\tilde{H}_I(t),\tilde{\rho}(0)] = 0$ since it is proportional to the identity and may instead be included in the system Hamiltonian without loss of generality, this gives

$$\frac{\partial\tilde{\rho}(t)}{\partial t} = -\int_0^t ds\,\mathrm{tr}_E[\tilde{H}_I(t),[\tilde{H}_I(s),\tilde{\rho}(s)]]. \tag{1.32}$$

We now make a few important assumptions:

- The system and bath density operators are initially in a product state $\rho(0) = \rho_S(0)\otimes\rho_B(0)$.

- The bath density operator is time-independent, so is unaffected by the influence of the system, $\rho_B \equiv \rho_B(0) = \rho_B(t)$, and does not have time-dependent statistical properties (stationary process). Due to the first approximation, this means also that the system and bath density operators are in a product state at all times $\rho(t) = \rho_S(t)\otimes\rho_B$ for $t \geq 0$.

The second assumption is known as the Born approximation and is heavily association with regimes of weak-coupling. This leaves

$$\frac{\partial\tilde{\rho}(t)}{\partial t} = -\int_0^t ds\,\mathrm{tr}_E[\tilde{H}_I(t),[\tilde{H}_I(s),\tilde{\rho}_S(s)\otimes\rho_B]], \tag{1.33}$$

which still involves an integral over time in $\tilde{\rho}_S(s)$, so its dynamics depend on its entire history, making the calculations potentially difficult to deal with. We now make the Markov approximation, in which we assume that any correlations in the environment decay on timescales much faster than the system evolution. This means that if the current state of the system affects the state of the environment, the effect equilibrates fast enough that it does not change the future system evolution, so the environment contains no memory of past system states. This is often physically relevant when the environment is a very large heat bath which is likely to tend back to equilibrium on very fast timescales.

Note that the Markov and Born approximations are closely related, but they can be made independently of one another, for example if the system and bath are sufficiently weakly-coupled so as to enforce a product state of the density operator, but correlations are not short-lived.

The Markov approximation allows us to put the integral into time-local form by replacing

$\tilde{\rho}_S(s) \to \tilde{\rho}_S(t)$ so that

$$\frac{\partial\tilde{\rho}(t)}{\partial t} = -\int_0^t ds\, \mathrm{tr}_E[\tilde{H}_I(t), [\tilde{H}_I(s), \tilde{\rho}_S(t)\otimes\rho_B]]. \tag{1.34}$$

In the Markov approximation, we also assume that the dynamics do not depend on any initial time $t = 0$, but only on the difference in time between s and t, this means we can make the substitution $s = t - \tau$ which gives

$$\frac{\partial\tilde{\rho}(t)}{\partial t} = -\int_0^t d\tau\, \mathrm{tr}_E[\tilde{H}_I(t), [\tilde{H}_I(t-\tau), \tilde{\rho}_S(t)\otimes\rho_B]]. \tag{1.35}$$

Since there is such a separation in timescales between system and environmental evolution, we can also extend the integral $t \to \infty$, so that all time-differences are included. This allows many of the subsequent integrals to be evaluated analytically and yields

$$\frac{\partial\tilde{\rho}(t)}{\partial t} = -\int_0^\infty d\tau\, \mathrm{tr}_E[\tilde{H}_I(t), [\tilde{H}_I(t-\tau), \tilde{\rho}_S(t)\otimes\rho_B]], \tag{1.36}$$

which is a Born-Markov master equation in the interaction picture.

In several models we encounter in this thesis, the interaction Hamiltonians take the product form

$$H_I = \sum_\alpha A_\alpha \otimes B_\alpha \tag{1.37}$$

which become

$$\tilde{H}_I(t) = \sum_\alpha e^{iH_s t_s} A_\alpha e^{-itH_s} \otimes e^{iH_B t_B} B_\alpha e^{-itH_B} = \sum_\alpha \tilde{A}_\alpha(t)\otimes\tilde{B}_\alpha(t), \tag{1.38}$$

in the interaction picture since the system and bath Hamiltonians are mutually commutative. Substituting this into the definition of a Born-Markov master equation yields

$$\begin{aligned}\frac{\partial\tilde{\rho}_S(t)}{\partial t} &= -i\tilde{\lambda}\left[\tilde{A}^2(t), \tilde{\rho}_S(0)\right] - \tilde{\lambda}^2\int_0^\infty d\tau\left[\tilde{A}^2(t), [\tilde{A}^2(t-\tau), \tilde{\rho}_S(t)]\right] - \\ -\sum_{\alpha\beta}\int_0^\infty d\tau\Big(&\left[\tilde{A}_\alpha(t), \tilde{A}_\beta(t-\tau)\tilde{\rho}_S(t)\right] C_{\alpha\beta}(\tau) + \left[\tilde{\rho}_S(t)\tilde{A}_\beta(t-\tau), \tilde{A}_\alpha(t)\right] C_{\beta\alpha}(-\tau)\Big)\end{aligned} \tag{1.39}$$

where we define the correlation functions

$$C_{\alpha\beta}(\tau) = \mathrm{tr}\left(B_\alpha(\tau)B_\beta\rho_B\right) \tag{1.40}$$

and we have assumed that $[H_B, \rho_E]$=0, which is true for a thermal state with respect to H_B, and have used the cyclic property of the trace. Finally, converting back to the Schrödinger

picture gives

$$\mathcal{L}[\rho_S(t)] = -i[H_S, \rho_S(t)] - \sum_{\alpha\beta} \int_0^\infty d\tau \Big(\Big[A_\alpha, \tilde{A}_\beta(-\tau)\rho_S(t)\Big] C_{\alpha\beta}(\tau) + \Big[\rho_S(t)\tilde{A}_\beta(-\tau), A_\alpha\Big] C_{\beta\alpha}(-\tau) \Big), \tag{1.41}$$

which is a Born-Markov master equation, valid in the limit of weak coupling between the system and environment. The formal solution of (1.41) is given by [22]

$$\rho_S(t) = e^{\mathcal{L}t}[\rho_S(0)], \tag{1.42}$$

1.3.2 The secular approximation

In some applications, the non-secular form of the Born-Markov master equation (1.41) does not give reliable physical results since the dynamical maps are not completely positive or necessarily trace-preserving [21]. For this reason, it is common to make a further secular approximation on (1.39) by discarding terms that have time-dependence in the interaction picture. To elucidate this time-dependence, we define

$$[H_S, A_\alpha(\omega)] = -\omega A_\alpha(\omega) \tag{1.43}$$

$$[H_S, A_\alpha^\dagger(\omega)] = \omega A_\alpha^\dagger(\omega) \tag{1.44}$$

where $\{\omega\}$ are the spectrum of fixed differences of eigenenergies of H_S. This means that $\tilde{A}_\alpha(t) = \sum_\omega e^{-i\omega t} A_\alpha(\omega)$ and $\tilde{A}_\alpha^\dagger(t) = \sum_\omega e^{i\omega t} A_\alpha^\dagger(\omega)$, enabling the interaction Hamiltonian to be written

$$\tilde{H}_I(t) = \sum_\omega e^{-i\omega t} A_\alpha(\omega) \otimes \tilde{B}_\alpha(t) = \sum_\omega e^{i\omega t} A_\alpha^\dagger(\omega) \otimes \tilde{B}_\alpha^\dagger(t) \tag{1.45}$$

where the second equality comes from the completeness of the eigenbasis. Inserting these forms of the interaction Hamiltonian into (1.36) and decomposing system operators into sums of operators with a spectrum of eigenenergy differences leads to the interaction picture equation

$$\begin{aligned} \mathcal{L}[\tilde{\rho}_S(t)] = -\sum_{\alpha,\beta} \sum_{\omega,\omega'} \int_0^\infty \Big(& d\tau e^{i\omega\tau} e^{i(\omega'-\omega)t} (\mathcal{C}_{\alpha\beta}(\tau)[A_\alpha^\dagger(\omega'), A_\beta(\omega)\rho_S(t)] \\ & + \mathcal{C}_{\beta\alpha}(-\tau)[\rho_S(t)A_\beta(\omega), A_\alpha^\dagger(\omega')]) \Big) + h.c. \end{aligned} \tag{1.46}$$

where we have defined correlation functions $\mathcal{C}_{\alpha,\beta}(\tau) = \left\langle \tilde{B}_\alpha^\dagger(\tau) B_\beta \right\rangle$ which take a different form to (1.40).

We now discard terms for which $\omega' \neq \omega$, which allows us to put the master equation into Lindblad form, which ensures that it is a completely positive trace preserving maps that gives physical evolution of the reduced density matrix. This is known as the *secular* approximation and is justified for most quantum optical systems along the same lines as

the rotating wave approximation, which occurs at the Hamiltonian level. After moving back into the Schrödinger picture, the secular approximation results in a dissipator which is in Lindblad form:

$$\mathcal{L}[\rho_S(t)] = -i[H_{LS}, \tilde{\rho}_S(t)] + \sum_{\omega} \sum_{\alpha,\beta} \Gamma_{\alpha\beta}(\omega) \Big(2A_\beta(\omega)\rho_S(t)A_\alpha^\dagger(\omega) - \{A_\alpha^\dagger(\omega)A_\beta(\omega), \rho_S(t)\} \Big) \tag{1.47}$$

with Lamb-shift Hamiltonian

$$H_{LS} = \sum_{\omega} \sum_{\alpha,\beta} -iS_{\alpha\beta}(\omega)[A_\alpha^\dagger(\omega)A_\beta(\omega), \rho_S(t)] \tag{1.48}$$

and decay rates and Lamb-shifts defined as $\Lambda_{\alpha\beta}(\omega) = \Gamma_{\alpha\beta}(\omega) + iS_{\alpha\beta}(\omega)$ given

$$\Lambda_{\alpha\beta}(\omega) = \int_0^\infty d\tau e^{i\omega\tau} \mathcal{C}_{\alpha\beta}(\tau). \tag{1.49}$$

1.4 Application: The spin-boson model

The aim of future work is to study complex molecular systems which naturally have many energetic degrees of freedom and excited states. Molecules often have highly structured vibrational characteristics and any bound excitations are likely to interact with these vibrations, or phonons, affecting their dynamics. Often the interaction between phonon environments and excitations are described in the limit that the two are weakly coupled. As we have seen in the previous section, in making a Born approximation we have restricted the dynamical equations of the reduced system to the case where there is no entanglement between the system and its environment, meaning that the bath does not evolve from its initial state. We have also used the likelihood of a separation of timescales between the system evolution and environment correlation times to justify ignoring any past states of the system. This means that the future state of the system at any time only depends on its current state and not on the reaction of the bath to any events in the past.

Here we will treat a canonical model, known as the Spin-Boson model, of a spin-1/2 system coupled to an infinite bath of harmonic oscillators. As we will see, the non-commutative relationship between the system and interaction Hamiltonians gives rise to a rich set of behaviour.

A system interacting with a bath of quantum harmonic oscillators, where interactions are mediated by a generic system operator s, can be described by the Hamiltonian [23]

$$H = H_S(t) + \frac{1}{2} \sum_k \left[p_k^2 + \omega_k^2 \left(x_k - \frac{f_k}{\omega_k^2} s \right)^2 \right], \tag{1.50}$$

where k counts over bosonic wavevectors and f_k is the coupling strength between the system

and environment which we have assumed to be real. Here we have written the harmonic oscillator degrees of freedom in *second-quantised* notation,

$$x_k = \frac{1}{\sqrt{2\omega_k}}(b_k^\dagger + b_k) \quad \text{and} \quad p_k = i\sqrt{\frac{\omega_k}{2}}(b_k^\dagger - b_k). \tag{1.51}$$

The Hamiltonian in this form is analogous to Hooke's law for classical oscillators, since the energy depends on the displacement of each oscillator away from its equilibrium position, this ensures that the spectrum of the Hamiltonian is properly bounded from below for all coupling strengths [24, 23]. Expanding out to make the system-bath interaction explicit gives

$$H = H_S(t) - s\sum_k f_k x_k + \frac{1}{2}\sum_k \frac{f_k^2}{\omega_k^2}s^2 + \frac{1}{2}\sum_k (p_k^2 + \omega_k^2 x_k^2). \tag{1.52}$$

Substituting the definitions of position and momentum operators, we identify a new scaled coupled strength $g_k = f_k/\sqrt{2\omega_k}$ to get the simple well-known form:

$$H = H_S(t) - s\sum_k g_k(b_k^\dagger + b_k) + \sum_k \frac{g_k^2}{\omega_k}s^2 + \sum_k \omega_k\left(b_k^\dagger b_k + \frac{1}{2}\right). \tag{1.53}$$

In order to get some insight into this Hamiltonian, we will now choose a time-independent system Hamiltonian. For a two-level system (TLS), we define the Hamiltonian,

$$H_S = \epsilon\sigma^\dagger\sigma + V\sigma_x \tag{1.54}$$

where ϵ quantifies the two-level system energy splitting and V the tunneling term and the TLS operators are defined as $\sigma^\dagger = |e\rangle\langle g|$, $\sigma = |g\rangle\langle e|$ and $\sigma_x = \sigma^\dagger + \sigma$.

For bosons with sufficiently low energy, such as acoustic phonons, the interactions with a quantum system often cannot mediate electronic transitions, i.e. do not couple to system populations, but instead couple to the phase. This is equivalent to having a diagonal dipole-transition matrix [1], so we can set $s = \sigma^\dagger\sigma$ which means the quadratic term causes an upward shift of the excited state energy. The interaction Hamiltonian can be then be written in the form

$$H_I = -\sigma^\dagger\sigma\sum_k g_k(b_k^\dagger + b_k) + \sum_k \frac{g_k^2}{\omega_k}\sigma^\dagger\sigma. \tag{1.55}$$

Choosing Hamiltonians (1.54) and (1.55) means that Eq. (1.53) is now the Spin-Boson model.

For an environment mode k with n excitations we denote the state $|n_k\rangle_E$, the creation and annihilation operators, $b_k^\dagger$ and b_k respectively, have the effect [20]

$$b_k^\dagger |n_k\rangle_E = \sqrt{n+1}\,|n_k+1\rangle_E \quad \text{and} \quad b_k|n_k\rangle_E = \sqrt{n}\,|n_k-1\rangle_E\,, \tag{1.56}$$

recalling the multi-mode commutation relations for the creation and annihilation operators

$\left[b_k, b_{k'}^\dagger\right] = \delta_{kk'}$.

The interaction between the two-level system and the harmonic environment is characterised completely by the spectral density

$$J_{SB}(\omega) = \sum_k |g_k|^2 \delta(\omega - \omega_k), \tag{1.57}$$

where $|g_k|^2$ is a measure of both the coupling-strength and environmental density of states of the kth mode.

Throughout this thesis, when considering the weak-coupling case, we shall assume that the environment is at thermal equilibrium, so described by the state

$$\rho_B = \frac{\exp(-\beta H_B)}{\mathrm{Tr}[\exp(-\beta H_B)]}, \tag{1.58}$$

where inverse temperature is defined $\beta = 1/k_B T$. In order to proceed with the calculation of a weak-coupling master equation as in section 1.3.1 we need to directly transform the interaction Hamiltonian of the system to the interaction picture. Depending on the commutativity of s and H_S, the unitary transformation can sometimes be expanded as a series of nested commutators and converges to something analytically manageable, such as in the case where the tunneling term V is taken to zero, known as the independent-boson model. In the spin-boson model this step becomes more complicated, so we write the interaction Hamiltonian H_I in terms of eigenstates of the system Hamiltonian H_S. The eigenstates of the single-excitation subspace are:

$$|\nu_\pm\rangle = \frac{1}{\sqrt{2\eta}} \left(\sqrt{\eta \pm \epsilon}\,|e\rangle \pm \sqrt{\eta \mp \epsilon}\,|g\rangle\right), \tag{1.59}$$

with corresponding energies

$$\lambda_\pm = \frac{1}{2}(\epsilon \pm \eta) \tag{1.60}$$

where $\omega_e = \omega_g + \epsilon$ and $\eta = \sqrt{\epsilon^2 + 4V^2}$. These states have been written so that V only appears within η. We can also express the original states in terms of the eigenstates $|\nu_\pm\rangle$:

$$\begin{aligned} |e\rangle &= \frac{1}{\sqrt{2\eta}} \left(\sqrt{\eta + \epsilon}\,|\nu_+\rangle + \sqrt{\eta - \epsilon}\,|\nu_-\rangle\right) \\ |g\rangle &= \frac{1}{\sqrt{2\eta}} \left(\sqrt{\eta - \epsilon}\,|\nu_+\rangle - \sqrt{\eta + \epsilon}\,|\nu_-\rangle\right), \end{aligned} \tag{1.61}$$

which allows us to write the system operator $\sigma^\dagger\sigma$ in the eigenstate basis

$$\sigma^\dagger\sigma = \frac{1}{2\eta}\left((\eta + \epsilon)\,|\nu_+\rangle\langle\nu_+| + (\eta - \epsilon)\,|\nu_-\rangle\langle\nu_-| + 2V(|\nu_+\rangle\langle\nu_-| + |\nu_-\rangle\langle\nu_+|)\right) \tag{1.62}$$

which is transformed trivially to the interaction picture

$$\tilde{\sigma}^\dagger\tilde{\sigma}(t) = \frac{1}{2\eta}\left((\eta+\epsilon)\left|\nu_+\right\rangle\!\left\langle\nu_+\right| + (\eta-\epsilon)\left|\nu_-\right\rangle\!\left\langle\nu_-\right| + 2V(\left|\nu_+\right\rangle\!\left\langle\nu_-\right| e^{i\eta t} + \left|\nu_-\right\rangle\!\left\langle\nu_+\right| e^{-i\eta t})\right). \quad (1.63)$$

Due to the form of the interaction, a secular approximation cannot be made, so we insert (1.63) into our definition of a Born-Markov master equation using the definitions

$$\tilde{A}(t) \equiv \tilde{\sigma}^\dagger\tilde{\sigma}(t) \quad \text{and} \quad \tilde{B}(t) \equiv \sum_k g_k(b_k^\dagger e^{i\omega_k t} + b_k e^{-i\omega_k t}), \quad (1.64)$$

since the shift term is also in the interaction Hamiltonian, this also appears as a term in the dissipator:

$$-i[\tilde{H}_{\text{shift}}(t), \tilde{\rho}_S(t)] \equiv -i\tilde{\lambda}\left[\tilde{A}^2(t), \tilde{\rho}_S(0)\right] - \tilde{\lambda}^2\int_0^\infty d\tau\left[\tilde{A}^2(t), [\tilde{A}^2(t-\tau), \tilde{\rho}_S(t)]\right] \quad (1.65)$$

where $\tilde{\lambda} = \sum_k g_k^2/\omega_k$. Since this does not converge for ohmic spectral densities, we use the fact that $-i[\tilde{H}_{\text{shift}}(t), \tilde{\rho}_S(t)] \approx -i\tilde{\lambda}\left[\tilde{\sigma}^\dagger\tilde{\sigma}(t), \tilde{\rho}_S(t)\right]$, where $\tilde{H}_{\text{shift}} \equiv \tilde{\lambda}\sigma^\dagger\sigma$, which comes from the second-order expansion of the interaction in the Liouville Von-Neumann equation. This yields the expression

$$\begin{aligned}\frac{\partial\tilde{\rho}_S(t)}{\partial t} = -i[H_S + H_{\text{shift}}, \tilde{\rho}_S(t)] - \int_0^\infty d\tau\Bigg(&\left[\tilde{\sigma}^\dagger\tilde{\sigma}, \tilde{\sigma}^\dagger\tilde{\sigma}(-\tau)\tilde{\rho}_S(t)\right] C(\tau) \\ &+ \left[\tilde{\rho}_S(t)\tilde{\sigma}^\dagger\tilde{\sigma}(-\tau), \tilde{\sigma}^\dagger\tilde{\sigma}\right] C(-\tau)\Bigg).\end{aligned} \quad (1.66)$$

Here, the double sum has disappeared since there is only one object being summed over in the decomposition, leading to the autocorrelation functions

$$\mathcal{C}(\tau) = \sum_{kk'}\text{Tr}\left[g_k g_{k'}\left(c_k^\dagger e^{i\omega_k\tau} + c_k e^{-i\omega_k\tau}\right)\left(c_{k'}^\dagger + c_{k'}\right)\rho_B\right]. \quad (1.67)$$

This expression can be simplified by calculating the operator-product expectation values over the thermal environment state ρ_B,

$$tr_E(c_k c_{k'}\rho_E) = 0 \quad (1.68)$$

$$tr_E(c_k^\dagger c_{k'}^\dagger\rho_E) = 0 \quad (1.69)$$

$$tr_E(c_k c_{k'}^\dagger\rho_E) = \delta_{kk'}(1 + N(\omega_{k'})) \quad (1.70)$$

$$tr_E(c_k^\dagger c_{k'}\rho_E) = \delta_{kk'}N(\omega_{k'}), \quad (1.71)$$

where $N(\omega_k)$ is the occupation number of the oscillator mode with wavevector k,

$$N(\omega_k) = \frac{1}{e^{\beta\omega_k} - 1}. \quad (1.72)$$

This allows us to simplify the autocorrelation function

$$C(\tau) = \sum_k g_k^2 \left(N(\omega_k) e^{i\omega_k \tau} + (1 + N(\omega_k)) e^{-i\omega_k \tau} \right) \tag{1.73}$$

$$= \sum_k g_k^2 \left(\coth\left(\frac{\beta\omega_k}{2}\right) \cos(\omega_k \tau) - i \sin(\omega_k \tau) \right). \tag{1.74}$$

We can now move to the continuum limit by turning the sum over wavevectors to an integral over frequency, utilising the spectral density $J(\omega) = \sum_k g_k^2 \delta(\omega - \omega_k)$

$$C(\tau) = \int_0^\infty d\omega J(\omega) \left(\coth\left(\frac{\beta\omega}{2}\right) \cos(\omega\tau) - i \sin(\omega\tau) \right). \tag{1.75}$$

With the master equation in the form 1.66, we can take the integrals into a single operator to yield the form

$$\frac{\partial \rho_S(t)}{\partial t} = -i[H_S, \rho(t)] - [\sigma_z, Z\rho_S(t)] - [\rho_S(t) Z^\dagger, \sigma_z], \tag{1.76}$$

where we have defined the operator

$$Z = \frac{1}{\eta} \left(\epsilon(|\psi_+\rangle\langle\psi_+| - |\psi_-\rangle\langle\psi_-|)\Lambda(0) + V(|\psi_+\rangle\langle\psi_-| \, \Lambda(\eta) + |\psi_-\rangle\langle\psi_+| \, \Lambda(-\eta)) \right). \tag{1.77}$$

The complex factors $\Lambda(\nu)$ are given by

$$\Lambda(\nu) \equiv \int_0^\infty e^{i\nu\tau} C(\tau) d\tau = \int_0^\infty e^{i\nu\tau} d\tau \int_0^\infty d\omega J(\omega) \left(\coth\left(\frac{\beta\omega}{2}\right) \cos(\omega\tau) - i \sin(\omega\tau) \right), \tag{1.78}$$

with real and imaginary parts corresponding to decay rates and energy level shifts, respectively. These can be evaluated using the Sokhotski integral identity

$$\int_0^\infty f(\omega) d\omega \int_0^\infty d\tau e^{\pm(\omega-\eta)\tau} = \pi \int_0^\infty f(\omega)\delta(\omega - \eta) d\omega \pm i\mathcal{P} \left[\int_0^\infty \frac{f(\omega)}{\omega - \eta} d\omega \right], \tag{1.79}$$

where $\mathcal{P}$ denotes taking the Cauchy principle value of the divergent integral. The Cauchy principle value can be calculated by integrating up to some small ϵ from the pole of the integrand from both sides and taking the limit as $\epsilon \to 0$,

$$\mathcal{P} \left[\int_0^\infty \frac{f(\omega)}{\omega - \eta} d\omega \right] = \lim_{\epsilon \to 0} \left(\int_0^{\eta - \epsilon} \frac{f(\omega)}{\omega - \eta} + \int_{\eta + \epsilon}^\infty \frac{f(\omega)}{\omega - \eta} \right). \tag{1.80}$$

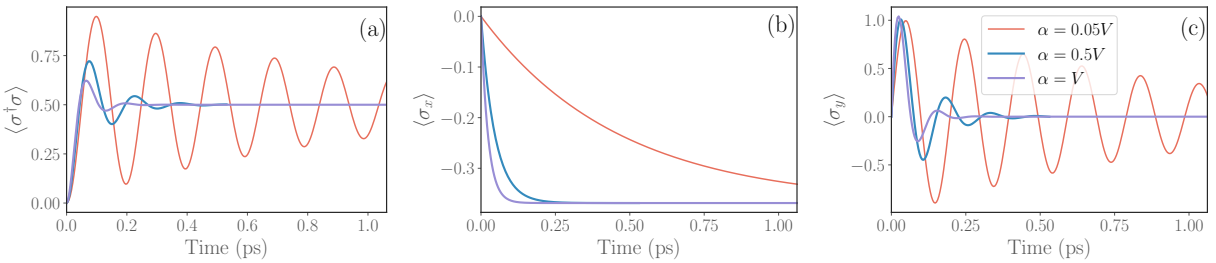

Figure 1.1: Dynamics of **(a)**: excited state population, **(b)**: $\langle\sigma_x\rangle$ and **(c)**: $\langle\sigma_y\rangle$ for the spin-boson model in the weak-coupling approximation at different phonon coupling strengths α. Parameters are $\epsilon = 0$, $V = 10\text{meV}$, $\Gamma = 30\text{meV}$, $\omega_0 = 20\text{meV}$, $T = 300\text{K}$.

Resolving the delta functions yields the expressions for rates,

$$\Lambda(\nu) = \begin{cases} \frac{\pi}{2} J(\nu)\left(\coth\left(\frac{\beta\nu}{2}\right) - 1\right) + i\mathcal{P}\left[\int_0^\infty J(\omega)\left(\frac{\coth\left(\frac{\beta\omega}{2}\right)-1}{\omega-\nu} - \frac{\coth\left(\frac{\beta\omega}{2}\right)+1}{\omega+\nu}\right)d\omega\right] & \text{if } \nu > 0, \\ \frac{\pi}{2}\lim\limits_{\nu\to 0}\left(J(\nu)\coth\left(\frac{\beta\nu}{2}\right)\right) - i\mathcal{P}\left[\int_0^\infty \frac{J(\omega)}{\omega} d\omega\right] & \text{if } \nu = 0, \\ \frac{\pi}{2} J(|\nu|)\left(\coth\left(\frac{\beta|\nu|}{2}\right) + 1\right) + i\mathcal{P}\left[\int_0^\infty J(\omega)\left(\frac{\coth\left(\frac{\beta\omega}{2}\right)-1}{\omega+|\nu|} - \frac{\coth\left(\frac{\beta\omega}{2}\right)+1}{\omega-|\nu|}\right)d\omega\right] & \text{if } \nu < 0, \end{cases} \tag{1.81}$$

To solve for the dynamics we choose a Drude-Lorentz spectral density

$$J(\omega) = \frac{\alpha\Gamma\omega_0^2\omega}{(\omega^2 - \omega_0^2)^2 + \Gamma^2\omega^2}, \tag{1.82}$$

which has approximately linear behaviour at low frequencies $\omega \ll \omega_c$ but tends to zero as $\omega \to \infty$. The Drude-Lorentz spectral density is often used to approximate the spectral density of electron-phonon interactions in molecular systems. The rate operators Z and principal value integrals are all calculated numerically to solve the dynamical equations.

1.4.1 Dynamics of the spin-boson model

In figure 1.1 (a)-(c), the dynamics of (1.66) from weak to intermediate coupling are shown. It can be seen in that the Rabi oscillations in the TLS population are dampened by the system-environment interaction. Coherences are also strongly affected, illustrated by $\langle\sigma_x\rangle$ and $\langle\sigma_y\rangle$. The environmental coupling causes transitions between the TLS eigenstates, eventually leading to a thermal equilibrium with respect to H_S. Larger system-environment couplings mean this steady-state is reached more quickly, which is reflected in the large increases in magnitude of $\langle\sigma_y\rangle$.

In figures 1.2 (a)-(c), the same expectation values are calculated as in 1.1 but for different values of vibrational peak position, ω_0. When $\omega_0 = V$, the vibrations are off resonance with the energy gap η, which means that the effective coupling is weaker, causing the decay rate to be smaller.

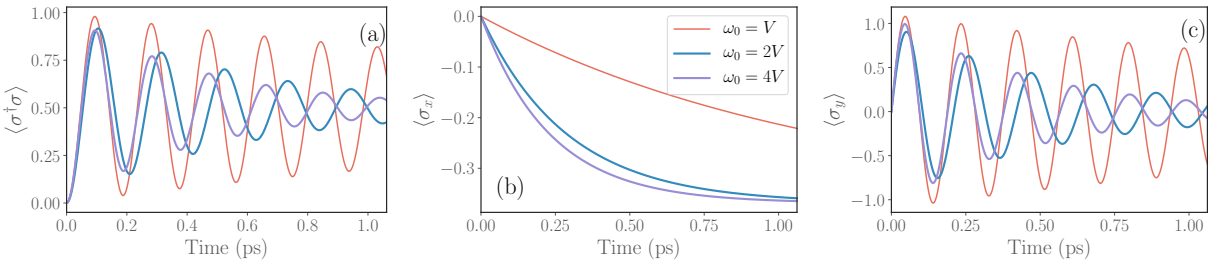

Figure 1.2: Dynamics of **(a)**: excited state population, **(b)**: $\langle\sigma_x\rangle$ and **(c)**: $\langle\sigma_y\rangle$ for the spin-boson model in the weak-coupling approximation at different vibrational frequencies ω_0. Other parameters are $\epsilon = 0$, $V = 10\text{meV}$, $\Gamma = 30\text{meV}$, $T = 300\text{K}$.

1.5 Summary

In this chapter I have introduced the basic building blocks of the theory of open quantum systems and derived a generic Born-Markov master equation. I then applied this theory to a canonical model, the spin-boson model, and investigated how bath properties change its behaviour. Now I will investigate the short-comings of the weak-coupling approach and propose some methods for going beyond it.

Chapter 2

Beyond the weak-coupling approximation

2.1 Introduction

In many applications, it becomes necessary to model the coupling between a system and its environment beyond the second-order perturbation in coupling-strength seen in the previous chapter. Additionally, the Born and Markov approximations mean that correlations cannot build up between the two subsystems as they interact with one another. The existence of these correlations can lead to many qualitative changes to the short-time and steady-state behaviour of the reduced system [25].

Here I will outline two techniques for going beyond the weak-coupling approximation, namely the polaron transformation [26, 27, 1] and the collective coordinate (CC) mapping [28, 29, 25, 23]. I do not present any original results in this chapter, only redeveloping previous work for the context of this thesis.

Both of the polaron and CC approaches apply unitary transformations to the original Hamiltonian to essentially extend the boundary of what the system of interest is, to include important elements of the bath. By including salient environmental features within the system description, the strong interactions can be dealt with non-perturbatively and anything that remains can be expanded to second order as we have seen in the previous section. As we will see, this can come at a cost, either by enlarging the basis considerably, as in the CC approach, or by shifting the perturbation expansion onto other important interactions, as with the polaron approach.

Currently, the polaron and CC theories also have limitations, which encourage their use in slightly different parameter regimes. As we will see, the regions of validity are determined by the low-frequency character of the bath modes. Apart from introducing the reader to these important tools, the central focus of this chapter is to evaluate which approach is most suitable for studying molecular systems. The validity restrictions of each theory ultimately determine the choice of approach taken throughout this thesis.

It should also be noted that there are several other advanced non-perturbative open quantum systems techniques, these include path-integral methods [30, 31, 32], many-body wave functions with tensor networks [33] and multi-configuration time-dependent Hartree-Fock [34]. Notably, the hierarchical equations of motion (HEOM) approach [35] is valid in similar regimes to the CC methods and is widely used in chemical physics applications [36, 37]. All of these powerful techniques also have their limitations, particularly in the case of say path-integral and HEOM methods when it comes to dealing with so called *non-additive effects* where systems are coupled to multiple independent environments [38]. We will see in the next chapters how the CC model can be used to account for non-additivity in a simple and elegant way. The simplicity of CC and polaron approaches also allows us to gain deep physical insight into fundamental problems in open quantum systems.

Formally exact methods also exist, such as Zwanzig-Nakajima projection operator techniques [39], but these often give equations that are intractable without perturbative expansions in coupling strength [21]. Due to their complicated dynamical maps, these techniques also do not lend themselves to treating systems coupled to multiple baths, which form the focus of this thesis.

2.2 Polaron transformation

In situations where some quantum system of interest interacts with a harmonic bath, the true state of the bath will be dependent on the exact state of the system. As a simple example, we take exciton formation in a semiconductor lattice. When the electron is in its ground state, the surrounding bulk will approach a particular equilibrium configuration. Upon excitation, say by the absorption of a photon, the electron moves to a new orbital with a totally different charge configuration, causing the surrounding lattice to distort. Depending on the coupling between charge carriers and lattice conformation, these displacements can be considerable enough that it makes sense for the entire exciton-plus-distortion cloud to be thought of as a separate quasi-particle, called a *polaron* [27, 1].

By incorporating the lattice displacements due to the electronic excited state into the Hamiltonian, one can derive equations of motion for the electronic degrees of freedom which are far more widely applicable than those obtained from perturbation theory in the original frame. In some simple models, such as the independent boson model, which will be visited later, a polaron transformation alone can be enough to obtain an exact solution for the dynamics of both the system and the bath.

Given a Hamiltonian of the form $H = H_S + H_I + H_B$, a transformation which only mixes the subsystems together and performs coordinate displacements must be unitary $H' = UHU^\dagger$ where $U = e^S$ and S is a Hermitian operator [26]. Specifically, most Hamiltonians I treat

will be some variant of

$$H = H_S + A\sum_k g_k(b_k^\dagger + b_k) + \sum_k \omega_k b_k^\dagger b_k + A^2 \sum_k \frac{g_k^2}{\omega_k} \tag{2.1}$$

which permits a choice for S of the form $S = A(\sum_k \frac{g_k}{\omega_k}(b_k^\dagger - b_k))$. For a general H_S and A, the transformation gives rise to the partition $H' = H'_S + H'_I + H'_B$:

$$H'_S = e^S H_S e^{-S} + A^2 \sum_k \frac{g_k^2}{\omega_k} \tag{2.2}$$

$$H'_B = \sum_k \omega_k b_k^\dagger b_k - A\sum_k g_k(b_k^\dagger + b_k) + A^2 \sum_k \frac{g_k^2}{\omega_k} \tag{2.3}$$

$$H'_I = A\sum_k g_k(b_k^\dagger + b_k) - 2A\sum_k \frac{g_k^2}{\omega_k}, \tag{2.4}$$

which allows us to see exactly how the linear coupling term $A\sum_k g_k(b_k^\dagger + b_k)$ is removed by the transformation. If H_S commutes with A, as in the independent boson model, then $e^S H_S e^{-S} = H_S$ and this transformation displaces the Hamiltonian to a representation which completely removes any interaction term and just renormalises the system and bath energy scales. In this decoupled representation an exact solution of system and bath dynamics can be found.

Where $[A, H_I] \neq 0$, e.g. in the Spin-Boson model, then further interaction terms arise and various approximations are usually made to obtain closed solutions.

2.3 Collective-coordinate formalism

Here I will give an overview of another non-perturbative technique which is typically valid in complementary parameter regimes to the polaron formalism, known as the Collective Coordinate mapping. They are complementary because they are each valid for different subclasses of environmental spectral densities.

The underlying idea of the Collective Coordinate mapping [28, 29, 25] is that we can perform a normal mode transformation on the original closed system Hamiltonian 2.1 to gain a completely equivalent model but in slightly different form. Essentially, the most important effects of the entire bath are summarised in a single bath coordinate, known as the collective coordinate (CC). The mapping is such that the system only interacts with this CC, which in turn couples to a bath of residual modes. The idea is that this CC-residual bath coupling should be weak enough to perform perturbation theory on, as in the previous chapter, giving rise to time-local, Born-Markov master equations which describe the time-evolution of the entire system-plus-CC. This means that the original system Hamiltonian is *augmented* to explicitly include a bosonic or fermionic mode, of the same type as the original bath, thus enlarging the dimension of the reduced system.

We restate the generic Hamiltonian (1.52) in Hooke's law form for convenience

$$H = H_S(t) - s\sum_k \tilde{g}_k x_k + \frac{1}{2}\sum_k \frac{\tilde{g}_k^2}{\omega_k^2}s^2 + \frac{1}{2}\sum_k (p_k^2 + \omega_k^2 x_k^2), \tag{2.5}$$

and define the spectral density for the system-bath interaction as $J_0(\omega) = \sum_k g_k^2\delta(\omega - \omega_k)$ where we scale the coupling strength for convenience $g_k = \tilde{g}_k/\sqrt{2\omega_k}$. We now define the normal mode transformation [25, 23]:

$$\vec{X} = \Lambda\vec{x} \quad \text{and} \quad \vec{P} = \Lambda\vec{p} \tag{2.6}$$

such that the operators for the new set of oscillators are given by $M_j = \sum_k \Lambda_{jk} m_k$, where $\Lambda^T = \Lambda^{-1}$. The collective coordinate is defined by

$$\sum_k \tilde{g}_k x_k = \lambda_0 X_1, \tag{2.7}$$

where λ_0 is the system-CC coupling strength. The residual bath oscillator frequencies, Ω_m for $m > 1$, are related to the original frequencies by the orthogonality condition $\Lambda\Lambda^T = \mathbb{1}$ which gives

$$\sum_k \omega_k^2 \Lambda_{mk}\Lambda_{nk} = \sum_k \omega_k^2 \Lambda_{mk}\Lambda_{kn}^T = \delta_{m,n}\Omega_m^2. \tag{2.8}$$

Focusing on the final term in (2.5), we get

$$\frac{1}{2}\sum_k (p_k^2 + \omega_k^2 x_k^2) = \frac{1}{2}\sum_k \sum_{m,n} (\Lambda_{mk}\Lambda_{nk}P_m P_n + \omega_k^2 \Lambda_{mk}\Lambda_{nk}X_m X_n) \tag{2.9}$$

which allows us to identify

$$\tilde{h}_n \equiv \omega_k^2 \Lambda_{1k}\Lambda_{nk} \quad \text{for } m = 1 \tag{2.10}$$

$$\tilde{h}_m \equiv \omega_k^2 \Lambda_{mk}\Lambda_{1k} \quad \text{for } n = 1 \tag{2.11}$$

so an interaction term $X_1 \sum_k \tilde{h}_k X_k$ can be extracted. We also notice that $\Lambda_{1k} = \lambda_0^{-1} h_k$, which comes from (2.7). Further, we can see that $[X_1, P_1] = i\sum_{k,k'} \frac{\tilde{h}_k}{\lambda_0}\Lambda_{1k}[x_k, p_{k'}]$, which means that $\sum_k \tilde{h}_k \Lambda_{1k} = \lambda_0$ and so $\lambda_0^2 = \sum_k \tilde{h}_k$ must be true to preserve commutation relations for the CC since $[x_k, p_{k'}] = i\delta_{k,k'}$ for any harmonic oscillator. Finally, by also defining $\Omega_1^2 = \sum_k \omega_k^2 \Lambda_{1k}$, the full mapped Hamiltonian then becomes

$$H = H_S(t) - \lambda_0 s X_1 + \frac{1}{2}\sum_k \frac{\tilde{g}_k^2}{\omega_k^2}s^2 + \frac{1}{2}(P_1^2 + \Omega_1^2 X_1^2) + X_1\sum_{k>1}\tilde{h}_k X_k + \frac{1}{2}\sum_{k>1}(P_k^2 + \Omega_k^2 X_k^2). \tag{2.12}$$

We can also define the CC-residual bath spectral density as $J_1(\omega) = \sum_k h_k^2\delta(\omega - \omega_k)$, where the CC-residual bath coupling strength has been scaled as $h_k = \tilde{h}_k/\sqrt{2\omega_k}$. This mapped

Hamiltonian looks formidable, given that we do not know from the outset what Λ is. However, for the mapping to be exact, the dynamics of the system of interest in the original and mapped cases must be the same. Thus by calculating the equations of motion for the system of interest in each case, we can relate the two models and calculate dynamics from knowledge of the original spectral density only. The original spectral density does not specify any information about the system of interest itself, only its interaction with the environment, so we can replace the system with a classical coordinate with position q and momentum p,

$$H_q = \frac{P_q^2}{2} + U(q) - q\sum_k \tilde{g}_k x_k + q^2 \frac{1}{2}\sum_k \frac{\tilde{g}_k^2}{\omega_k^2} + \frac{1}{2}\sum_k (p_k^2 + \omega_k^2 x_k^2), \tag{2.13}$$

where we also write the oscillator degrees of freedom in the position-representation,

$$x_k = \frac{1}{\sqrt{2\omega_k}}(b_k^\dagger + b_k) \quad \text{and} \quad p_k = i\sqrt{\frac{\omega_k}{2}}(b_k^\dagger - b_k) \tag{2.14}$$

and we have drop the time arguments from the system Hamiltonian. From this, the equations of motion are calculated using Hamilton's equations $\dot{q} = \frac{\partial H}{\partial p}$, $\dot{p} = \ddot{q} = -\frac{\partial H}{\partial q}$ yielding,

$$\ddot{q}(t) = -U'(q) - \sum_k \tilde{g}_k x_k(t) - q(t)\sum_k \frac{\tilde{g}_k^2}{2\omega_k^2}, \tag{2.15}$$

$$\ddot{x}_k(t) = -\tilde{g}_k q(t) - \omega_k^2 x_k(t), \tag{2.16}$$

where $U'(q) = \frac{dU(q)}{dq}$. The bath variables $x_k(t)$ and $p_k(t)$ are then eliminated by making use of the Fourier transform $f(z) = \int_{-\infty}^{\infty} f(t)e^{-izt}dt$. This is done by substituting the definition of the inverse Fourier transform into the equation above and rearranging. This leads to an equation of the form $K(z)q(z) = -U'$, where the Fourier space operator is defined as:

$$K(z) = -z^2\left(1 + \sum_k \frac{\tilde{g}_k^2}{\omega_k^2(\omega_k^2 - z^2)}\right) = -z^2\left(1 + \int_0^\infty \mathrm{d}\omega\, \frac{J_0(\omega)}{\omega(\omega^2 - z^2)}\right). \tag{2.17}$$

In getting to the integral in the last equality, we have moved to the continuum limit in the number of boson modes. The integration over frequency is now performed for the most general spectral density that could be found, the details of which are contained in Appendix 1. In summary, we assume that a general spectral density can be written in the form

$$J_0(\omega) = \frac{\omega f(\omega)}{\prod_k^N (\omega - ia_k)(\omega + ia_k)}, \tag{2.18}$$

where any poles are written explicitly in the denominator and must be imaginary ($a_k \in \mathcal{R}$) to avoid non-physicality, specifically appearing in conjugate pairs to ensure $J_0(\omega)$ is real. It should be noted that the spectral density is decomposed in a similar manner to 2.18 within the hierarchical equations of motion (HEOM) formalism [35, 40]. The function $h(\omega)$ is

arbitrary but well behaved (say some polynomial), real-valued and has no poles. To simplify the calculation we treat the case where there are only two poles but as long as they are all imaginary the actual number of poles does not matter. We can then write (2.17) as

$$K(z) = -z^2\left(1 + i\pi\left(\frac{J_0(z)}{z^2}\right) - \frac{\pi f(ia_1)}{(a_1^2 - a_2^2)(a_2^2 + z^2)(a_1)} - \frac{\pi f(ia_2)}{(a_1^2 - a_2^2)(a_1^2 + z^2)(a_2)}\right). \quad (2.19)$$

Since the z^2 cancels out on the imaginary term ($f(\omega)$ is real-valued), the spectral density can be retrieved from the Fourier-space operator by writing $z = \omega - i\epsilon$ and taking ϵ to zero from the positive direction (so it lies in the contour) and discarding the real part,

$$J_0(\omega) = \frac{1}{\pi}\lim_{\epsilon\to 0^+}\mathrm{Im}\left[K(\omega - i\epsilon)\right]. \quad (2.20)$$

Now we have the form of the spectral density in terms of the Fourier space operator which governs the dynamical evolution of the classical coordinate. The equations of motion of the classical coordinate should be the same before and after the mapping, since it is exact. We now do the same procedure to write $K(z)$ in terms of the CC spectral density, to equate the original spectral density with the CC spectral density. Firstly, we swap the system for a continuous coordinate in CC Hamiltonian

$$H = \frac{P_q^2}{2} + U(q) - \lambda_0 q X_1 + q^2\frac{1}{2}\sum_k \frac{\tilde{g}_k^2}{\omega_k^2} + \frac{1}{2}(P_1^2 + \Omega_1^2 X_1^2) + X_1\sum_{k>1}\tilde{h}_k X_k + \frac{1}{2}\sum_{k>1}(P_k^2 + \Omega_k^2 X_k^2). \quad (2.21)$$

This Hamiltonian enables the equations of motion to be calculated

$$\ddot{q}(t) + \lambda_0 + \frac{\lambda_0^2}{\Omega^2}q = -U'(q) \quad (2.22)$$

$$\ddot{\hat{x}} + \left(\Omega^2 + \sum_k \frac{\tilde{h}_k^2}{\omega_k^2}\right)\hat{x} + \lambda_0 q + \sum_k \tilde{h}_k \hat{X}_k = 0 \quad (2.23)$$

$$\ddot{\hat{X}}_\alpha(t) + \tilde{h}_\alpha \hat{x} + \omega_\alpha^2 \hat{X}_\alpha. \quad (2.24)$$

As for the Hamiltonian in the original frame, we transform to the Fourier space operator to eliminate the CC and residual environment degrees of freedom:

$$K(z) = -z^2 + \frac{\lambda_0^2}{\Omega^2}\frac{\mathcal{L}(z)}{\Omega^2 + \mathcal{L}(z)}. \quad (2.25)$$

By moving to the continuum limit and using the definition of the CC-residual bath spectral density

$$\mathcal{L}(z) = -z^2\left(1 + \sum_k \frac{\tilde{h}_k^2}{\omega_k^2(\omega_k^2 - z^2)}\right) = -z^2\left(1 + 4\Omega\int_0^\infty \mathrm{d}\omega\, \frac{J_1(\omega)}{\omega(\omega^2 - z^2)}\right). \quad (2.26)$$

We can now relate $J_0(\omega)$ and $J_1(\omega)$ by equating (2.19) and (2.25) and taking the limit as in (2.20).

In order to go any further, we could use the method given by Martinazzo *et al* [41] to map from the original spectral density $J_0(\omega)$ to the new spectral density $J_1(\omega)$, however, there is a perfectly adequate mapping in the reverse direction $J_1(\omega) \rightarrow J_0(\omega)$ [25], for the case of Drude-Lorentz spectral densities as first described by Garg *et al* [28]. Since the Drude-Lorentz family of spectral densities is general enough for the applications within this thesis, this example is shown in the next section.

2.3.1 Example: Drude-Lorentz spectral density

With the aim of finding the associated Spin-Boson $J_0(\omega)$, we start with an Ohmic spectral density for the CC-residual bath,

$$J_1(\omega) = \gamma\omega \exp(-\omega/\Lambda). \tag{2.27}$$

In the limit that $\Lambda \rightarrow \infty$, following the same contour integration procedure as in the unmapped case and noticing that $J_1(\omega)$ has no poles yields

$$\mathcal{L}(z) = -z^2 + 2i\pi\Omega\gamma z. \tag{2.28}$$

Substituting this into (2.25) and then into the mapping (2.20) gives

$$J_0(\omega) = \frac{1}{\pi} \lim_{\epsilon \rightarrow 0^+} \mathrm{Im}[K(\omega - i\epsilon)] = \frac{1}{\pi} \frac{2\pi\Omega^2\gamma\lambda_0^2\omega}{(\Omega^2 - \omega^2)^2 + (2\pi\Omega\gamma)^2\omega^2}, \tag{2.29}$$

which is in the form of an under-damped Drude-Lorentz spectral density which we restate for convenience

$$J(\omega) = \frac{\alpha\Gamma\omega_0^2\omega}{(\omega^2 - \omega_0^2)^2 + \Gamma^2\omega^2}. \tag{2.30}$$

Setting $\Gamma = 2\pi\gamma\lambda_0^2$ and $\omega_0 = \Omega$ makes the mapping exact. However, this is in terms of λ_0 and γ which are as yet unspecified. By comparing the different derivatives of the equations of motion in the two cases, it can be shown that the following relations hold

$$\frac{\lambda_0^2}{\Omega} = \int_0^\infty \frac{J_0(\omega)}{\omega} d\omega \quad \text{and} \quad \lambda_0^2\Omega = \int_0^\infty \omega J_0(\omega) d\omega. \tag{2.31}$$

This gives $\gamma = \Gamma/2\pi\Omega$ and $\lambda_0^2 = \pi\alpha\Omega/2$.

The overdamped case can be found by defining

$$\omega_c = \frac{\Omega}{2\pi\gamma} \quad \text{and} \quad \alpha = \frac{2\lambda_0^2}{\pi\Omega} \tag{2.32}$$

which can be used to recast the spectral density (2.29) in the form

$$J(\omega) = \frac{1}{\pi} \frac{\alpha \omega_c \omega}{\omega_c^2 - \frac{2\omega^2 \omega_c^2}{\Omega^2} + \frac{\omega^4 \omega_c^2}{\Omega^4} + \omega^2}. \tag{2.33}$$

In the limit where $\Omega \gg \omega_c$ then this spectral density reduces to

$$J(\omega) = \frac{\alpha \omega_c \omega}{\omega^2 + \omega_c^2}, \tag{2.34}$$

where we have retrieved the overdamped Drude-Lorentz spectral density. Thus a CC spectral density in the form of (2.27) can be used to recover a spin-boson model with a Drude-Lorentz spectral density in both underdamped and overdamped regimes.

2.3.2 The collective-coordinate master equation

Now we have performed the mapping, we can derive a Born-Markov master equation for the interaction between the system and the residual bath. Inputting the definitions for the position and momentum operators for the collective coordinate

$$\hat{x} = \sqrt{\frac{1}{2\Omega}}(a^\dagger + a) \quad \text{and} \quad \hat{p} = i\sqrt{\frac{\Omega}{2}}(a^\dagger - a) \tag{2.35}$$

and the residual bath coordinates

$$\hat{X}_k = \sqrt{\frac{1}{2\nu_k}}(c_k^\dagger + c_k) \quad \text{and} \quad \hat{P}_k = i\sqrt{\frac{\nu_k}{2}}(c_k^\dagger - c_k) \tag{2.36}$$

into the mapped Hamiltonian (2.12) gives

$$\begin{aligned} H = H_S + s^2 \sum_k \frac{g_k^2}{\omega_k} - \lambda_0 s(a^\dagger + a) + \Omega a^\dagger a \\ + (a^\dagger + a)\sum_k h_k(c_k^\dagger + c_k) + \sum_k \omega_k c_k^\dagger c_k + (a^\dagger + a)^2 \sum_k \frac{h_k^2}{\omega_k}. \end{aligned} \tag{2.37}$$

Note that we have expressed this in terms of g_k and h_k instead of the scaled couplings $\tilde{g}_k$ and $\tilde{h}_k$. We now partition the Hamiltonian (2.37) into the form $H = H_0 + H_B + H_I$ where

$$H_0 = H_S + s^2 \sum_k \frac{g_k^2}{\omega_k} - \lambda_0 s(a^\dagger + a) + \Omega a^\dagger a \tag{2.38}$$

$$H_B = \sum_k \omega_k c_k^\dagger c_k \tag{2.39}$$

$$H_I = (a^\dagger + a)\sum_k h_k(c_k^\dagger + c_k) + (a^\dagger + a)^2 \sum_k \frac{h_k^2}{\omega_k} \tag{2.40}$$

where we have kept the quadratic counter term inside the interaction Hamiltonian.

We will now derive a master equation for the reduced density matrix of the two-level system and reaction-coordinate, where the CC is weakly-coupled to the residual environment. In the same way as previous sections, we transform to the interaction picture and decompose the Hamiltonian this time using

$$\tilde{H}_I(t) = \tilde{A}(t) \otimes \tilde{B}(t) + \tilde{\lambda}\tilde{A}^2(t) \tag{2.41}$$

where $\tilde{A}(t) = e^{iH_0 t}(a^\dagger + a)e^{-iH_0 t}$, $\tilde{B}(t) = \sum_k g_k(c_k^\dagger e^{i\omega_k t} + c_k e^{-i\omega_k t})$ and $\tilde{\lambda} = \sum_k \frac{h_k^2}{\omega_k}$. Using the Born-Markov master equation (1.36) this gives

$$\frac{\partial\tilde{\rho}_S(t)}{\partial t} = -i\,\mathrm{tr}_B\left[\tilde{H}_I(t), \tilde{\rho}_S(t)\otimes\rho_B\right] - \int_0^\infty d\tau\,\mathrm{tr}_B\left[\tilde{H}_I(t), \left[\tilde{H}_I(t-\tau), \tilde{\rho}_S(t)\right]\right] \tag{2.42}$$

$$\begin{aligned} &= -i\tilde{\lambda}\left[\tilde{A}^2(t), \rho(0)\right] - \tilde{\lambda}^2\int_0^\infty d\tau\left[\tilde{A}^2(t), [\tilde{A}^2(t-\tau), \tilde{\rho}_S(t)]\right] \\ &\quad - \int_0^\infty d\tau(\tilde{A}(t)\tilde{A}(t-\tau)\tilde{\rho}_S(t)\left\langle\tilde{B}(\tau)B\right\rangle_B - \tilde{A}(t)\tilde{\rho}_S(t)\tilde{A}(t-\tau)\left\langle\tilde{B}(-\tau)B\right\rangle_B \\ &\quad - \tilde{A}(t-\tau)\tilde{\rho}_S(t)\tilde{A}(t)\left\langle\tilde{B}(\tau)B\right\rangle_B + \tilde{\rho}_S(t)\tilde{A}(t-\tau)\tilde{A}(t)\left\langle\tilde{B}(-\tau)B\right\rangle_B). \end{aligned} \tag{2.43}$$

In this final equality, there are the bath correlation functions $\langle B(\pm\tau)B\rangle_B$ which are complex valued. It becomes useful to split the correlation functions into real an imaginary parts by defining rates such that $\langle B(\pm\tau)B\rangle_B \equiv \Gamma^+ \pm \Gamma^-$

$$\Gamma^\pm = \mathrm{tr}\left((B(\tau)B \pm B(-\tau)B)\rho_B\right)/2, \tag{2.44}$$

whereby Γ^+ is real and Γ^- is imaginary. If we assume a thermal bath, as in (1.58), then we can follow methods outlined in previous sections by moving into the continuum limit

$$\Gamma^+(\tau) = \int_0^\infty d\omega J_1(\omega)\coth\left(\frac{\beta\omega}{2}\right)\cos(\omega\tau) \quad \text{and} \quad \Gamma^-(\tau) = i\int_0^\infty d\omega J_1(\omega)\sin(\omega\tau). \tag{2.45}$$

This allows us to write the Equation (2.43) in the form

$$\begin{aligned} \frac{\partial\tilde{\rho}_S(t)}{\partial t} &= -i\tilde{\lambda}\left[\tilde{A}^2(t), \rho_S(0)\right] - \tilde{\lambda}^2\int_0^\infty d\tau\left[\tilde{A}^2(t), [\tilde{A}^2(t-\tau), \tilde{\rho}_S(t)]\right] \\ &\quad - \int_0^\infty d\tau\left(\left[\tilde{A}(t), \left[\tilde{A}(t-\tau), \tilde{\rho}_S(\tau)\right]\right]\Gamma^+(\tau) + \left[\tilde{A}(t), \{\tilde{A}(t-\tau), \tilde{\rho}_S(\tau)\}\right]\Gamma^-(\tau)\right). \end{aligned} \tag{2.46}$$

We now notice that the first two terms (involving $\tilde{A}^2(t)$) are reminiscent of a second order expansion of the Von-Neumann equation, e.g. Eq. (1.31),

$$-i\tilde{\lambda}\left[\tilde{A}^2(t), \tilde{\rho}_S(0)\right] - \tilde{\lambda}^2\int_0^\infty d\tau\left[\tilde{A}^2(t), [\tilde{A}^2(t-\tau), \tilde{\rho}_S(t)]\right] = -i\tilde{\lambda}\left[\tilde{A}^2(t), \tilde{\rho}_S(t)\right] \tag{2.47}$$

as seen in section 1.3.1, this means that the quadratic terms have induced a unitary, Hamiltonian-like contribution the open-system evolution. We also complete the Markov-approximation by extending the time integral to infinity, the evolution Equation (2.43) now becomes

$$\begin{aligned}\frac{\partial\tilde{\rho}_S(t)}{\partial t} &= -i\tilde{\lambda}\left[\tilde{A}^2(t),\tilde{\rho}_S(t)\right] \\ &\quad -\int_0^\infty\int_0^\infty d\omega d\tau\left[\tilde{A}(t),\left[\tilde{A}(t-\tau),\tilde{\rho}_S(t)\right]\right]J_1(\omega)\coth\left(\frac{\beta\omega}{2}\right)\cos(\omega\tau) \\ &\quad -\int_0^\infty\int_0^\infty d\omega d\tau\left[\tilde{A}(t),\{\tilde{A}(t-\tau),\tilde{\rho}_S(t)\}\right]J_1(\omega)\sin(\omega\tau).\end{aligned} \tag{2.48}$$

The spectral density $J_1(\omega)=\gamma\omega\exp\left(-\frac{\omega}{\Lambda}\right)$ where Λ is the CC cutoff frequency in the limit $\Lambda\to\infty$, is unbounded, which means that some of the frequency integrals appear divergent, though we can cancel some out by integrating the last term in equation 2.48 by parts using

$$\int_0^\infty d\tau\sin(\omega\tau)\tilde{A}(t-\tau)=\left[-\frac{\tilde{A}(t-\tau)}{\omega}\cos(\omega\tau)\right]_0^\infty+\int_0^\infty d\tau\frac{\cos(\omega\tau)}{\omega}\frac{\partial\tilde{A}(t-\tau)}{\partial\tau} \tag{2.49}$$

$$=-\mathcal{P}\left(\frac{\tilde{A}(t)}{\omega}\right)+\int_0^\infty d\tau\frac{\cos(\omega\tau)}{\omega}\frac{\partial\tilde{A}(t-\tau)}{\partial\tau}. \tag{2.50}$$

The principal value part of the integral cancels with the first term of (2.48) since $\tilde{\lambda}=\sum_k\frac{h_k^2}{\omega_k}$ and the original definition $J_1(\omega)=\sum_k h_k^2\delta(\omega-\omega_k)$, which gives

$$i\int_0^\infty d\omega\frac{J_1(\omega)}{\omega}\left[\tilde{A}(t),\{\tilde{A}(t),\tilde{\rho}(t)\}\right]=i\int_0^\infty\sum_k g_k^2\delta(\omega-\omega_k)\frac{1}{\omega}d\omega\left[\tilde{A}^2(t),\tilde{\rho}(t)\right] \tag{2.51}$$

$$=i\sum_k\frac{g_k^2}{\omega_k}\left[\tilde{A}^2(t),\tilde{\rho}(t)\right]=i\tilde{\lambda}\left[\tilde{A}^2(t),\tilde{\rho}(t)\right]. \tag{2.52}$$

Now we tranform into the Schrödinger representation and use the Heisenberg equations of motion $\frac{\partial\tilde{A}(t-\tau)}{\partial\tau}=i\left[H_0,\tilde{A}(t-\tau)\right]+\frac{\partial\tilde{A}}{\partial\tau}$:

$$\begin{aligned}\frac{\partial\rho(t)}{\partial t} &= -i\left[H_0,\rho(t)\right] \\ &\quad -\int_0^\infty\int_0^\infty d\omega d\tau\left[A,\left[A\tilde{A}(-\tau),\rho(t)\right]\right]J_1(\omega)\coth\left(\frac{\beta\omega}{2}\right)\cos(\omega\tau) \\ &\quad -\int_0^\infty\int_0^\infty d\omega d\tau\left[A,\left\{\left[\tilde{A}(-\tau),H_0\right],\rho(t)\right\}\right]J_1(\omega)\frac{\cos(\omega\tau)}{\omega}.\end{aligned} \tag{2.53}$$

At this point we can include the integrals over τ and ω in the definitions of two new operators

$$\chi \equiv \int_0^\infty \int_0^\infty d\omega d\tau J_1(\omega) \coth\left(\frac{\beta\omega}{2}\right) \cos(\omega\tau)\tilde{A}(-\tau) \tag{2.54}$$

$$\Xi \equiv \int_0^\infty \int_0^\infty d\omega d\tau J_1(\omega) \frac{\cos(\omega\tau)}{\omega} \left[H_0, \tilde{A}(-\tau)\right]. \tag{2.55}$$

With these expressions, the Liouvillian has essentially been derived, but in practice these operators are difficult to calculate analytically due to being in the interaction picture with respect to the augmented system Hamiltonian, which seldom commutes with the interaction Hamiltonian. To proceed, the operators (2.54)-(2.55) can be written in the augmented system eigenbasis:

$$A = \sum_{ij} \langle\phi_i| A |\phi_j\rangle |\phi_i\rangle\langle\phi_j| \tag{2.56}$$

where $H_0 |\phi_n\rangle = \phi_n |\phi_n\rangle$. The time-dependence on the operators $\tilde{A}(-\tau)$ is found via (1.14), the system operators become

$$\tilde{A}(t) = \sum_{ij} \langle\phi_i| A |\phi_j\rangle e^{i(\phi_i - \phi_j)t} |\phi_i\rangle\langle\phi_j|. \tag{2.57}$$

Substituting this into (2.54)-(2.55) and integrating using (1.79) yields

$$\chi \approx \sum_{ij} J_1(\xi_{ij}) \coth\left(\frac{\beta\xi_{ij}}{2}\right) \langle\phi_i| A |\phi_j\rangle |\phi_i\rangle\langle\phi_j| \tag{2.58}$$

$$\Xi \approx \sum_{ij} J_1(\xi_{ij}) \langle\phi_i| A |\phi_j\rangle |\phi_i\rangle\langle\phi_j| \tag{2.59}$$

where $\xi_{ij} = (\phi_i - \phi_j)$ and the imaginary Lamb-shift terms have been neglected, justified in [25] by numerical benchmarking.

This form of the operators lends itself to numerical construction, by truncating the space of the collective-coordinate to some appropriate excitation number and then numerically diagonalising the augmented system Hamiltonian H_0. Finally, we can write the CCME as

$$\frac{\partial\rho(t)}{\partial t} = -i\left[H_0, \rho(t)\right] + \left[A, \rho(t)Z\right] + \left[Z^\dagger\rho(t), A\right] \tag{2.60}$$

where (2.59)-(2.59) have now been simplified by the definition $Z \equiv \chi + \Xi$, which gives:

$$Z = \sum_{ij} J_1(\xi_{ij}) \left(\coth\left(\frac{\beta\xi_{ij}}{2}\right) + 1\right) \langle\phi_i| A |\phi_j\rangle |\phi_i\rangle\langle\phi_j|. \tag{2.61}$$

2.4 An exactly solvable model: the independent boson model

Here the canonical independent boson model (IBM) is treated, since it can be exactly diagonalised by using the polaron transformation [42, 21]. This will allow us to test the regimes of applicability of the CC method. The IBM corresponds to a choice of $H_S = \epsilon \left|X\right\rangle\!\left\langle X\right|$ and $A = \left|X\right\rangle\!\left\langle X\right|$ in (2.1), which means that $[H_S, A] = 0$.

2.4.1 Exact Solution

After accounting for the renormalisation term $\sum_k g_k^2/\omega_k$, the Hamiltonian becomes

$$H = \epsilon' \left|X\right\rangle\!\left\langle X\right| + \sum_k \omega_k b_k^\dagger b_k + \left|X\right\rangle\!\left\langle X\right| \sum_k g_k (b_k^\dagger + b_k) \tag{2.62}$$

where $\epsilon' = \epsilon + \sum_k \frac{g_k^2}{\omega_k}$. We then perform a unitary, polaron transformation $H' = e^S H e^{-S}$ where $S = \left|X\right\rangle\!\left\langle X\right| \sum_k \frac{g_k}{\omega_k}(b_k^\dagger - b_k)$. This yields transformed bath and interaction Hamiltonians

$$H'_S = \epsilon' \left|X\right\rangle\!\left\langle X\right| \tag{2.63}$$

$$H'_B = \sum_k \omega_k b_k^\dagger b_k - \left|X\right\rangle\!\left\langle X\right| \sum_k g_k (b_k^\dagger + b_k) + \left|X\right\rangle\!\left\langle X\right| \sum_k \frac{g_k^2}{\omega_k} \tag{2.64}$$

$$H'_I = \left|X\right\rangle\!\left\langle X\right| \sum_k g_k (b_k^\dagger + b_k) - 2 \left|X\right\rangle\!\left\langle X\right| \sum_k \frac{g_k^2}{\omega_k} \tag{2.65}$$

$$\tag{2.66}$$

which together form the polaron-frame Hamiltonian

$$H' = \epsilon \left|X\right\rangle\!\left\langle X\right| + \sum_k \omega_k b_k^\dagger b_k \tag{2.67}$$

whereby the system and bath are now decoupled but the initial system energy renormalisation has been exactly cancelled out due to the *polaron shift*, which is induced by the coupling. The time-evolution operator in the polaron frame is thus

$$U'(t) = e^{-i\epsilon \left|X\right\rangle\!\left\langle X\right| t} e^{-i \sum_k \omega_k b_k^\dagger b_k t}. \tag{2.68}$$

We will now show that in the original frame the environmental modes undergo a shift dependent on whether the system is in the ground or excited state. We partition the full original Hamiltonian as

$$H_0 = \epsilon' \left|X\right\rangle\!\left\langle X\right| + \sum \omega_k b_k^\dagger b_k \quad \text{and} \quad H_I = \left|X\right\rangle\!\left\langle X\right| \sum g_k (b_k^\dagger + b_k) \tag{2.69}$$

in order to write

$$\tilde{U}(t) \equiv e^{iH_0 t}U(t) = e^{iH_0 t}e^{-S}U'(t)e^{S} \tag{2.70}$$

$$= e^{iH_0 t}e^{-S}e^{-iH_0 t}e^{iH_0 t}U'(t)e^{S} \tag{2.71}$$

where we have used the reverse of the unitary polaron transformation $U(t) = e^{-S}U'(t)e^{S}$ and resolved the identity operator for the final equality. From this we identify

$$e^{iH_0 t}e^{-S}e^{-iH_0 t} = \exp\left(-|X\rangle\langle X|\sum \frac{g_k}{\omega_k}(e^{i\omega_k t}b_k^\dagger - e^{-i\omega_k t}b_k)\right) \tag{2.72}$$

and

$$e^{iH_0 t}U'(t) = e^{i\sum_k \frac{g_k^2}{\omega_k}|X\rangle\langle X|t}. \tag{2.73}$$

By using the theorem $e^{A+B} = e^A e^B e^{-[A,B]/2}$, after some algebra we reach

$$\tilde{U}(t) = e^{-i\Phi(t)}e^{|X\rangle\langle X|\sum(\alpha_k(t)b_k^\dagger - \alpha_k^*(t)b_k)} \tag{2.74}$$

where $\Phi(t) = \sum \frac{g_k^2}{\omega_k^2}\sin\omega_k t - \frac{g_k^2}{\omega_k}t$ and $\alpha_k = (1 - e^{i\omega_k t})\frac{g_k}{\omega_k}$. By performing a series expansion of the second exponent in (2.74) and inspecting the first few terms we can identify a convenient form of the time evolution operator (2.74) that is still exact:

$$\tilde{U}(t) = e^{-i\Phi(t)}\left(|0\rangle\langle 0| + |X\rangle\langle X|\prod_k D\left(\alpha_k(t)\right)\right) \tag{2.75}$$

where we have introduced the displacement operator $D(\alpha_k(t)) = \exp\Big(\alpha_k(t)b_k^\dagger - \alpha_k(t)b_k\Big)$. We assume that system and bath are initially in a product state $\rho(0) = \rho_S(0)\otimes\rho_B(0)$ and that the bath starts in thermal equilibrium at temperature T_R

$$\rho_B(0) = \exp\left(-\sum_k \omega_k b_k^\dagger b_k/k_{\mathrm{B}}T_R\right)/\operatorname{tr}\left[\exp\left(-\sum_k \omega_k b_k^\dagger b_k/k_{\mathrm{B}}T_R\right)\right]. \tag{2.76}$$

Since the interaction term in Eq. (2.62) commutes with the system Hamiltonian, within the independent boson model the phonon bath causes no transitions between system eigenstates and thus the system populations are static. Transforming back to the Schrödinger picture we have

$$\tilde{\rho}_{00}(t) = \rho_{00}(0)\,|0\rangle\langle 0| \quad \tilde{\rho}_{11}(t) = \rho_{11}(0)\,|X\rangle\langle X| \tag{2.77}$$

which we verify by using

$$\tilde{\rho}_{ij}(t) = \langle i|\operatorname{Tr}_B\left[\tilde{U}(t)\rho(0)\tilde{U}^\dagger(t)\right]|j\rangle\,. \tag{2.78}$$

The system coherences do evolve, and are governed by

$$\rho_{10}(t) = \rho_{10}(0)\,\mathrm{Tr}_B\left(\prod_k D(\alpha_k(t))\rho_B\right) = \rho_{10}(0)e^{-\Gamma(t)}e^{-i\epsilon t} \tag{2.79}$$

$$\rho_{01}(t) = \rho_{01}(0)\,\mathrm{Tr}_B\left(\rho_B\prod_k D^\dagger(\alpha_k(t))\right) = \rho_{01}(0)e^{-\Gamma^*(t)}e^{i\epsilon t} \tag{2.80}$$

where we have defined the decoherence function

$$\Gamma(t) = \ln\left(\mathrm{Tr}_B\left(\prod_k D(\alpha_k(t))\rho_B\right)\right) = \sum_k \ln\left(\left\langle D(\alpha_k(t))\right\rangle_B\right), \tag{2.81}$$

with the expectation value over the bath $\langle\mathcal{O}\rangle_B = \mathrm{tr}_B(\mathcal{O}\rho_B)$. This allows us to identify the Wigner characteristic function for bath mode k,

$$\left\langle D(\alpha_k(t))\right\rangle_B = \exp\left(-\frac{1}{2}|\alpha_k|^2\left\langle\{b_k, b_k^\dagger\}\right\rangle_B\right) \tag{2.82}$$

so the decoherence function becomes

$$\Gamma(t) = \sum_k -\frac{1}{2}|\alpha_k|^2\left\langle\{b_k, b_k^\dagger\}\right\rangle_B = -\sum_k(1-\cos(\omega_k t))\frac{|g_k|^2}{\omega_k^2}\coth\left(\frac{\omega_k}{2k_BT_R}\right) \tag{2.83}$$

where the second equality comes from the definition of $\alpha_k(t)$ after equation (2.74) and a fair amount of algebra. We can then use the spectral density we have already defined, $J_0(\omega) = \sum_k |g_k|^2\delta(\omega-\omega_k)$, to get

$$\Gamma(t) = -\int_0^\infty d\omega\frac{J(\omega)}{\omega^2}\coth\left(\frac{\omega}{2k_BT_R}\right)(1-\cos(\omega t)). \tag{2.84}$$

The full time evolution for the coherences is thus

$$\rho_{01}(t) = \rho_{01}(0)e^{-i\epsilon t}e^{-\Gamma(t)} \quad \text{and} \quad \rho_{10}(t) = (\rho_{01}(t))^*. \tag{2.85}$$

2.4.2 Weak-coupling approach

This calculation is very similar to the weak-coupling spin-boson model seen in the previous chapter, but it is greatly simplified by the fact $[H_S, A] = 0$. From the Born-Markov master equation in the Schrödinger picture (1.41), we input the appropriate system operator to get a master equation:

$$\frac{\partial\rho(t)}{\partial t} = \mathcal{L}(\rho_S(t)) = -i[\tilde{\epsilon}, \rho_S(t)] + \Gamma(0)\Big(2\,|X\rangle\langle X|\,\rho_S(t)\,|X\rangle\langle X| - \{|X\rangle\langle X|\,, \rho_S(t)\}\Big) \tag{2.86}$$

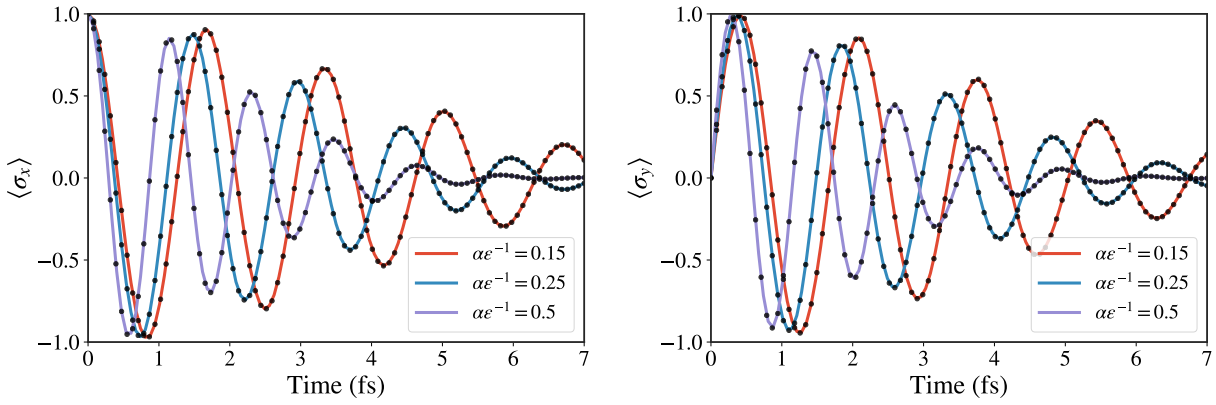

Figure 2.1: Two-level system coherence dynamics ($\langle\sigma_x\rangle = \rho_{eg}(t)+\rho_{ge}(t)$ and $\langle\sigma_y\rangle = i(\rho_{eg}(t)-\rho_{ge}(t))$) as a function of time for the independent boson model in the strong-coupling regime: exact solution (dots), collective coordinate master equation (solid curves) and Born-Markov master equation (dotted curves).

where $\tilde{\epsilon} = \epsilon' - S(0)$ and decay rates and Lamb-shifts defined as $\Lambda(0) = \Gamma(0) - iS(0)$ given

$$\Lambda(0) = \frac{\pi}{2}\lim_{\nu\to 0}\left(J(\nu)\coth\left(\frac{\beta\nu}{2}\right)\right) - i\mathcal{P}\left[\int_0^\infty \frac{J(\omega)}{\omega}d\omega\right]. \tag{2.87}$$

For a Drude-Lorentz spectral density, the decay rate can be evaluated analytically $\Gamma(0) = \pi\alpha\Gamma/(2\beta\omega_0^2)$, but the shift $S(0)$ principal value integral will be calculated numerically.

2.4.3 Comparison to collective coordinate approach

The dynamics of the exact solutions can be compared to the collective coordinate master equation and the weak-coupling approach. The initial condition for the two-level system is taken to be $\rho_{\rm S}(0) = \frac{1}{2}(|e\rangle + |g\rangle)(\langle e| + \langle g|)$. For the exact solution, the environment is initialised in the thermal state $\rho_{\rm B}(0)$ of Eq. (2.76), as stated before, while for the collective coordinate master equation the CC is initialised in the thermal state $\rho_{th} = \exp\left(-\Omega b^\dagger b/k_{\rm B}T_{\rm R}\right)/\operatorname{tr}\left[\exp\left(-\Omega b^\dagger b/k_{\rm B}T_{\rm R}\right)\right]$ with the residual environment held in thermal equilibrium at temperature T_R throughout the dynamics. In Fig. 2.1 above we compare the two approaches and find that the collective coordinate master equation matches the exact solution well into the strong phonon-coupling regime.

2.5 The spin-boson model revisited

In the previous section we saw that the collective coordinate master equation performed well at simulating non-perturbative open-quantum systems in the case where the system Hamiltonian and system coupling operator are mutually commutative. We will now revisit

the spin-boson model, as seen in Section 1.4, where

$$H = \epsilon'\sigma^\dagger\sigma + V(\sigma^\dagger + \sigma) + \sum_k \omega_k b_k^\dagger b_k + |X\rangle\langle X| \sum_k g_k(b_k^\dagger + b_k), \tag{2.88}$$

where $\epsilon' = \epsilon + \sum_k g_k^2/\omega_k$. In the weak-coupling case, the fact that the tunnelling term does not commute with the interaction Hamiltonian was circumvented by moving to the eigenbasis of the system Hamiltonian before transforming to the interaction picture. At strong-coupling, the eigenbasis of the system Hamiltonian may be a sub-optimal basis, incapable of expressing non-trivial contributions due to the environmental degrees of freedom. As we have seen, the collective coordinate formalism deals with this by expanding the Hilbert space of the system and transforming to the new *supersystem* basis. The polaron approach attempts to move to a representation where the displacements due to the system-bath interaction have already been accounted for, which we will now show becomes very limited in two key regimes of interest: finite intrasystem tunnellings and low-frequency environmental spectral densities.

Since the spin-boson model is not exactly solvable, we will benchmark the collective coordinate and polaron approaches against a numerically exact approach known as Hierarchical Equations of Motion (HEOM).

2.5.1 Polaron approach for the ohmic spin-boson model

After a polaron transformation, the Hamiltonian (2.88) becomes

$$H' = \epsilon\sigma^\dagger\sigma + V(\sigma^\dagger B_+ + \sigma B_-) + \sum_k \omega_k b_k^\dagger b_k \tag{2.89}$$

where $B_\pm = \prod_k D_k(\pm g_k)$ are the mode-dependent displacements due to the phonon-coupling, which now augment the tunnelling term. Before we expand this term in order to derive a master equation, we notice that the term proportional to V has a non-zero expectation value with respect to a thermal environment state $\mathrm{Tr}_B\{(\sigma^\dagger B_+ + \sigma B_-)\rho_E\} = \langle B\rangle\,\sigma_x$, which is a requirement for deriving Born-Markov master equations in the usual way [21]. We then subtract $\langle B\rangle\,\sigma_x$ from the interaction and add it to the system Hamiltonian, so the perturbative expansions represent fluctuations around the thermal average. The final partition is therefore $H_P = H_{SP} + H_{IP} + H_E$, where

$$H_{SP} = \epsilon\sigma^\dagger\sigma + \langle B\rangle\,\sigma_x \quad \text{and} \quad H_{IP} = V(\sigma_x B_x + \sigma_y B_y) \tag{2.90}$$

where we have defined

$$\begin{aligned} B_x &= \frac{1}{2}(B_- + B_+ - 2\langle B\rangle) \\ B_y &= \frac{1}{2i}(B_- - B_+). \end{aligned} \tag{2.91}$$

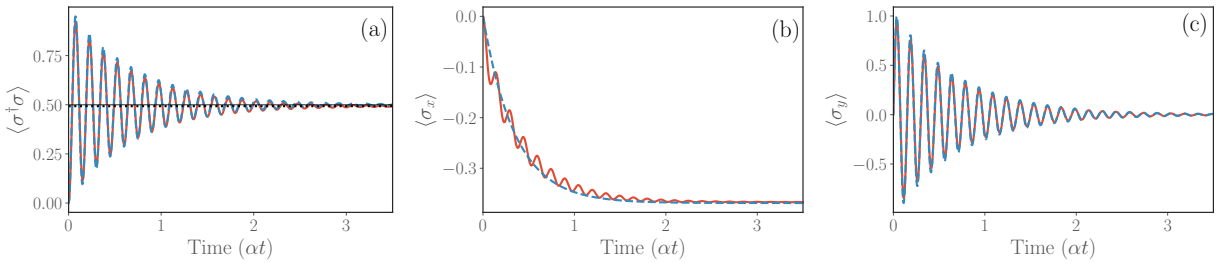

Figure 2.2: **(a)**: Dynamics of TLS population, **(b)**: $\langle\sigma_x\rangle$ and **(c)**: $\langle\sigma_y\rangle$ for the spin-boson model. Dashed lines correspond to the weak-coupling approach described in the previous chapter, solid red lines are from the CCME approach. Parameters are $\alpha = 0.5$meV, $\epsilon = 0$, $V = 10$meV, $\Gamma = 30$meV, $\omega_0 = 20$meV, $T = 300$K.

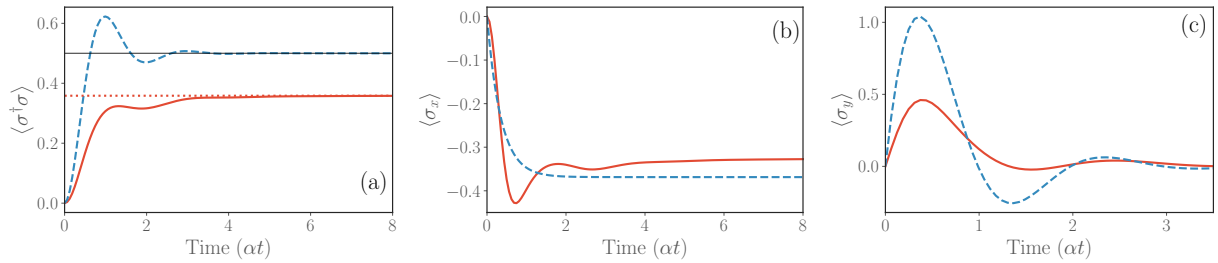

Figure 2.3: **(a)**: Dynamics of TLS population, **(b)**: $\langle\sigma_x\rangle$ and **(c)**: $\langle\sigma_y\rangle$ for the spin-boson model. Dashed lines correspond to the weak-coupling approach described in the previous chapter, solid red lines are from the CCME approach. Parameters are $\alpha = 10$meV, $\epsilon = 0$, $V = 10$meV, $\Gamma = 30$meV, $\omega_0 = 20$meV, $T = 300$K.

Following the approach of [27], $\langle B\rangle$ can be expressed in terms of the spectral density:

$$\langle B\rangle = \exp\left(-\frac{1}{2}\int_0^\infty d\omega \frac{J(\omega)}{\omega^2}\coth\frac{\beta\omega}{2}\right). \tag{2.92}$$

By series expansion of the coth $\frac{\beta\omega}{2}$ we can see that the integral only converges for spectral densities with at least cubic low-frequency dependence. This means that the Drude-Lorentz phonon spectral-densities which are considered throughout this thesis cannot be modelled properly using the polaron approach, since they have linear low-frequency dependence. This further motivates the use of the CCME for studying dynamics in molecular systems.

2.5.2 Comparison of CC and weak-coupling approaches

In figures 2.2 (a)-(c) the dynamics of $\langle\sigma^\dagger\sigma\rangle$, $\langle\sigma_x\rangle$ and $\langle\sigma_y\rangle$ are shown for the weak-coupling (dashed blue) and the CC (solid red) approaches in the weak-coupling regime, where $\alpha = 0.5$meV, $\epsilon = 0$, $V = 10$meV and $T = 300$K. We can see that the weak-coupling theory approximates $\langle\sigma^\dagger\sigma\rangle$ and $\langle\sigma_y\rangle$ well in this regime, however it does not replicate coherent oscillations that are observed in the dynamics of $\langle\sigma_x\rangle$ due to the CCME.

For a lower frequency bath where $\omega_0 = 10$meV, the weak-coupling approach predicts much smaller damping rates of the population oscillations, as seen in figure 2.4 (a). This

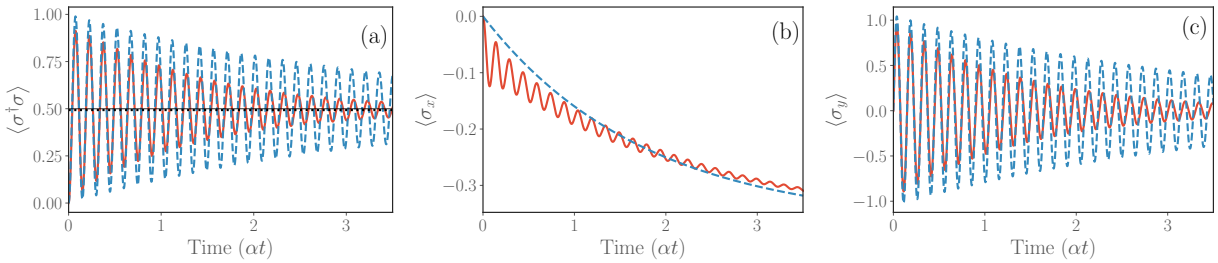

Figure 2.4: **(a)**: Dynamics of TLS population, **(b)**: $\langle \sigma_x \rangle$ and **(c)**: $\langle \sigma_y \rangle$ for the spin-boson model for $\alpha = 0.05V$ and $\omega_0 = 10\text{meV}$. Dashed lines correspond to the weak-coupling approach described in the previous chapter, solid red lines are from the CCME approach. Remaining parameters are the same as figure 2.2. We can see that the lower frequency environment has caused the weak-coupling theory to perform worse than when $\omega_0 = 20\text{meV}$ in figure 2.2.

spectral density is more sharply peaked at a lower frequency, which is a regime that can cause Redfield to break down, even at this weak coupling strength of $\alpha = 0.05V = 0.5\text{meV}$.

In figures 2.3 (a)-(c), the same dynamics are shown but this time in a strong-intermediate coupling regime, where $\alpha = V = 10\text{meV}$. We can see here that the dynamics and the steady-states of the weak-coupling theory are now significantly different to those predicted by the CCME theory.

2.6 Summary

Due to a requirement to go beyond the weak-coupling theory derived in the previous chapter, I presented two possible methods, namely the polaron and collective coordinate approaches. I have highlighted an inability of polaron theory to properly account for ohmic spectral densities, such as the Drude-Lorentz form - used ubiquitously to model molecular phonon environments - which supports the choice of the collective coordinate mapping as an appropriate non-perturbative technique to use in the following chapters. I derived the CC mapping and master equation, which was then benchmarked against the exact solution of the independent boson model. I then used the CCME to explore the spin-boson model in the intermediate and strong-coupling regimes. It was seen that the weak-coupling theory is not capable of reproducing the complexity of the CC model, particularly for peaked, low-frequency baths.

Chapter 3

Environmental non-additivity in quantum emitters

3.1 Introduction

The focus of this thesis is on the interplay between vibrational and optical interactions in quantum systems. In the previous chapter, I reviewed some non-peturbative open quantum systems techniques which are suited towards modelling exciton-phonon interaction processes, however so far optical interactions have not been treated at all. In order to be optically excited or de-excited, a dipole must interact with an electromagnetic field and absorb or emit quanta of energy. In the absence of vibrational modes, quantum emitters such as bare two-level atoms have Lorentzian emission lineshapes, with linewidths corresponding to the lifetime of the excited electronic states [43]

For many modern information processing applications, it becomes useful to embed quantum emitters into solid state devices [3], which means that the phonon modes of the host can interact with the electronic states of the emitter. For example, in quantum dots excited electrons interact with an effectively positively-charged host material, which has some bulk phonon modes or lattice distortions which change the local electromagnetic field around charge-carriers [27, 1]. Similarly, in photosynthetic systems, networks of light-sensitive molecules are embedded into large sheets of interconnected proteins, which constitute a low-frequency environment of delocalised phonons to the excited electronic states [44, 45, 46]. In both of these examples, the phonons interact in intermediate-strong coupling regimes where traditional weak-coupling approaches do not necessarily apply. These scenarios also require that the quantum system of interest interacts with both a vibrational/phonon environment and an ambient electromagnetic field, so I will now lay the foundations for how to do this in a consistent way.

I will begin this chapter by introducing Hamiltonians that will be used often throughout this thesis, that of a two-level dipole coupled to both the vibrational modes of a host lattice and also an external electromagnetic bath. Effectively, the model is the independent boson

model with the addition of optical fields, but I will term this the *monomer* Hamiltonian, since it is analogous to a two-level electronic transition in a single small molecule.

Applying a CC mapping to the phonon bath allows us to incorporate its influence on the electronic dynamics non-perturbatively, and in particular to capture the resulting dynamical generation of electron-vibrational correlations [28, 47, 25, 16].

Using this non-perturbative theory, I will investigate the phenomena of *environmental non-additivity*. This occurs when two or more environments interact with the same quantum system and where it is not valid to calculate their impact on the system in isolation and instead their collective effects must be accounted for to accurately describe the system. It is demonstrated that non-additivity is essential for modelling quantum emitters in the presence of vibrations, since enforcing an additive approximation essentially disregards the Franck-Condon principle and leads to inconsistencies in electronic transition rates. I show that the non-additive theory can lead to population inversion when the two-level emitter interacts with high temperature thermal electromagnetic fields.

The population inversion observed in the two-level emitter only occurs for *super-ohmic* spectral densities of the electromagnetic field, where the frequency dependence is greater than linear. I present a minimal analytical model that fully explains the remarkably different qualitative behaviour between the ohmic and super-ohmic cases, which also sheds light more generally on the nature of non-additivity.

A model of coherent excitation is then derived, where the monomer system is excited with a continuous-wave laser, rather than thermal electromagnetic fields. As well as calculating steady-state emission spectra of the monomer to better understand the dynamics, I also investigate the phenomenon of population inversion in vibronic systems under off-resonant coherent driving.

3.2 Exciton-phonon interaction

Here we introduce the form of exciton-phonon Hamiltonian that will be used in the following chapters. This is the same form that is used across the literature of open-quantum systems and within quantum optics, chemical physics and quantum biology. Starting from a generic form of system-bath coupling as in (1.50)-(1.55), I choose the system operator $s = \sigma^\dagger\sigma$ as in the case of the spin-boson model, which gives:

$$H^{\mathrm{PH}} = \sum_k \frac{g_k^2}{\nu_k}\sigma^\dagger\sigma - \sigma^\dagger\sigma \sum_k g_k(b_k^\dagger + b_k) + \sum_k \nu_k \left(b_k^\dagger b_k + \frac{1}{2}\right). \tag{3.1}$$

Here H^{PH} just denotes all of the contributions of the Hamiltonian, $H = H_S + H^{\mathrm{PH}} + H^{\mathrm{EM}}$, due to the phonon interaction. As we have already seen, for a Hamiltonian of spin-boson model form, $H_S = \epsilon\sigma^\dagger\sigma + \Omega\sigma_x$, the first term in (3.1) gives rise to a shift of the TLS energy. The second term is the system-phonon interaction, which in the absence of coherent

coupling $V \to 0$, commutes with the system Hamiltonian and thus does not cause transitions between the TLS states. This is justified phenomenologically by the fact that emission energies of the systems of interest to this thesis are on the order of a few electronvolts, with phonon/vibrational energies rarely exceeding 100meV. These low-frequency vibrational environments are unable to cause population transfer on their own.

As we have seen in the previous section, when $|V| > 0$, the system part of the Hamiltonian no longer commutes with the interaction part, so the environment can lead to direct transitions between the Hamiltonian eigenstates. In chemical physics, these are often known as *non-adiabatic* transitions [48], since the system exchanges energy with the phonon environment in order for the populations to equilibrate.

The final term is the self-energy of the oscillators in the phonon bath. We will omit the zero-point energy of $\sum_k \nu_k/2$, since this is proportional to the identity operator and does not influence the qualitative behaviour of the dynamics. It is useful to formally define a spectral density for the system-vibrational interaction, $J(\nu) = \sum_k |g_k|^2 \delta(\nu - \nu_k)$, which as discussed is a measure of the environmental density of states weighted by the system-environment coupling strength for a mode frequency.

Throughout this thesis a Drude-Lorentz spectral density is used:

$$J(\nu) = \alpha \nu_0^2 \gamma \nu / \left[(\nu^2 - \nu_0^2)^2 + \gamma^2 \nu^2 \right] \tag{3.2}$$

which is phenomenologically motivated as it is used to model both localised, intra-molecular vibrations as well as delocalised inter-molecular vibrational environments, by using small and large γ, respectively [48]. The latter case are often called *phonons*, since they arise from bulk mechanical effects in the host crystal [1] or protein substrate [45] that an emitter is embedded in. These can be derived in much the same way as the approach known to solid-state physics [1, 3].

3.3 Exciton-photon interactions

Here I sketch the derivation of the form of light-matter interaction Hamiltonian that is used throughout this thesis. The magnetic and electric field can be written as [49]

$$B = \boldsymbol{\nabla} \times \mathbf{A} \tag{3.3}$$

$$E = -\boldsymbol{\nabla}\Phi - \frac{\partial \mathbf{A}}{\partial t} \tag{3.4}$$

In the Coulomb gauge, where $\boldsymbol{\nabla} \cdot A = 0$, the scalar potential is $\Phi(\mathbf{r}, t) \propto \int d\mathbf{r}' \rho(\mathbf{r}', t)/|r' - r|$. It is assumed that the EM fields are in free space and there are no free charges, which means

that $\Phi = 0$:

$$E = -\frac{\partial \mathbf{A}}{\partial t}. \tag{3.5}$$

Since the magnetic fields are $1/c$ smaller than electric fields, they are neglected. The vector potential can be expressed as a superposition of plane waves

$$\mathbf{A}(\mathbf{r}, t) = \sum_{\mathbf{k}\lambda} \mathbf{e}_{ks} \left[A_{\mathbf{k}\lambda}(t) e^{i\mathbf{k}\cdot\mathbf{r}} + A^*_{\mathbf{k}\lambda}(t) e^{-i\mathbf{k}\cdot\mathbf{r}} \right] \tag{3.6}$$

where $A_{\mathbf{k}\lambda}(t)$ are complex field amplitudes, which have wave-vector $\mathbf{k}$ and polarisation λ and obey

$$\frac{\mathrm{d}A_{\mathbf{k}\lambda}(t)}{\mathrm{d}t} + \omega_k^2 A_{\mathbf{k}\lambda}(t) = 0, \tag{3.7}$$

which has the solution $A_{\mathbf{k}\lambda}(t) = A_{\mathbf{k}\lambda} e^{-i\omega_k t}$ where $A_{\mathbf{k}\lambda} = A_{\mathbf{k}\lambda}(0)$ and I have defined $\omega_k = c|\mathbf{k}|$. Differentiating this as in Eq. 3.5, gives the electric field in the form:

$$\mathbf{E}(\mathbf{r}, t) = i \sum_{\mathbf{k}\lambda} \omega_k \mathbf{e}_{ks} \left[A_{\mathbf{k}\lambda} e^{i(\mathbf{k}\cdot\mathbf{r} - \omega_k t)} - A^*_{\mathbf{k}\lambda} e^{-i(\mathbf{k}\cdot\mathbf{r} - \omega_k t)} \right]. \tag{3.8}$$

In quantising the electric field, it is assumed that the field is contained within a cavity of volume V, which gives rise to the Heisenberg picture operator [49]:

$$\hat{A}_{\mathbf{k}}(t) = \left(\frac{\hbar}{2\omega_k \epsilon_0 V} \right)^{\frac{1}{2}} \hat{a}_{\mathbf{k}}(t), \tag{3.9}$$

where $a_{\mathbf{k}}(t)$ are annihilation operators of the bosonic field. Using these definitions we can rewrite the electric field as

$$\hat{\mathbf{E}}(\mathbf{r}, t) = i \sum_{\mathbf{k}\lambda} \left(\frac{\hbar\omega_k}{2\epsilon_0 V} \right)^{\frac{1}{2}} \mathbf{e}_{ks} \left[\hat{a}_{\mathbf{k}}(0) e^{i(\mathbf{k}\cdot\mathbf{r} - \omega_k t)} - \hat{a}^\dagger_{\mathbf{k}}(0) e^{-i(\mathbf{k}\cdot\mathbf{r} - \omega_k t)} \right]. \tag{3.10}$$

In the case where the matter-system of interest is much smaller than important mode wavelengths, then $\lambda/2\pi = |\mathbf{k}|^{-1} \gg |\mathbf{r}_{\text{emitter}}|$, so $\mathbf{k}\cdot\mathbf{r} \ll 1$ and the variation of the electromagnetic field over the extent of the system can be neglected. In this thesis, I mostly consider small molecular systems which emit primarily in the visible and near-infrared part of the spectrum. For example Dibenzothiophene has a zero-phonon line at 785nm [50] but is only made up of three aromatic rings, so has length on the order of only one nanometre. Making this approximation gives:

$$\hat{\mathbf{E}}(\mathbf{r}, t) \approx \hat{\mathbf{E}}(t) = i \sum_{\mathbf{k}\lambda} \left(\frac{\hbar\omega_k}{2\epsilon_0 V} \right)^{\frac{1}{2}} \mathbf{e}_{ks} \left[\hat{a}_{\mathbf{k}}(0) e^{-i\omega_k t} - \hat{a}^\dagger_{\mathbf{k}}(0) e^{i\omega_k t} \right]. \tag{3.11}$$

Moving to the Schrödinger picture we have

$$\hat{\mathbf{E}} = i\sum_{\mathbf{k}\lambda}\left(\frac{\hbar\omega_k}{2\epsilon_0 V}\right)^{\frac{1}{2}}\mathbf{e}_{ks}\left(\hat{a}_{\mathbf{k}\lambda} - \hat{a}^\dagger_{\mathbf{k}\lambda}\right). \tag{3.12}$$

In the multipolar gauge [51] and the dipole approximation, the dipole-field interaction can be written [49, 52]

$$H_I^{\mathrm{EM}} = -\hat{\mathbf{d}}\cdot\hat{\mathbf{E}}. \tag{3.13}$$

If we write $\hat{\mathbf{d}} = \sum_{jk}\langle j|\,\hat{\mathbf{d}}\,|k\rangle\,|j\rangle\langle k|$ where we use the TLS basis $j,k\in\{g,e\}$ and $\langle e|\,\hat{\mathbf{d}}\,|g\rangle = \mathbf{d}$, then we get

$$H_I^{\mathrm{EM}} = -(|g\rangle\langle e| + |e\rangle\langle g|)\sum_{\mathbf{k}\lambda}\left(f_{\mathbf{k}\lambda}\hat{a}_{\mathbf{k}\lambda} + f^*_{\mathbf{k}\lambda}\hat{a}^\dagger_{\mathbf{k}\lambda}\right), \tag{3.14}$$

where $f_{\mathbf{k}\lambda} = i\left(\frac{\hbar\omega_k}{2\epsilon_0 V}\right)^{\frac{1}{2}}(\mathbf{d}\cdot\mathbf{e}_{\mathbf{k}\lambda})$.

It becomes useful to define a spectral density, such that $\mathcal{J}(\omega) = \sum_{\mathbf{k}\lambda}|f_{\mathbf{k}\lambda}|^2\delta(\omega-\omega_k)$, which gives

$$\mathcal{J}_M(\omega) = \sum_{\mathbf{k}\lambda}\frac{\hbar\omega_k}{2\epsilon_0 V}|\mathbf{d}\cdot\mathbf{e}_{\mathbf{k}\lambda}|^2\delta(\omega-\omega_k). \tag{3.15}$$

Following [22], I choose a coordinate system such that $|\mathbf{d}\cdot\mathbf{e}_{\mathbf{k}\lambda}|^2 = |\mathbf{d}|^2(1-\left|\vec{\mathbf{d}}\cdot\vec{\mathbf{k}}\right|) = |\mathbf{d}|^2(1-\cos^2\theta)$, where θ is the angle between the unit vectors $\vec{\mathbf{d}}$ and $\vec{\mathbf{k}}$. We now move to the continuum limit using $\sum_{k\lambda}\to L^3/(8\pi^3c^3)\int_0^\infty \mathrm{d}\omega_k\,\omega_k^2\int_0^\pi \mathrm{d}\theta\sin\theta\int_0^{2\pi}\mathrm{d}\phi$, which after integration by substitution gives

$$\mathcal{J}_M(\omega) = \frac{|\mathbf{d}|^2}{6\pi^2\epsilon_0}\omega^3. \tag{3.16}$$

For a TLS with energy splitting ϵ, optical spectral densities will be given in terms of a bare electronic decay rate $\Gamma_0 \equiv 2\pi\mathcal{J}(\epsilon)$, so

$$\mathcal{J}_M(\omega) = \frac{\Gamma_0}{2\pi\epsilon^3}\omega^3. \tag{3.17}$$

Alternatively, in the Coulomb gauge [51] we have

$$H_I^{\mathrm{EM}} = \hat{\mathbf{p}}\cdot\hat{\mathbf{A}} = -\sigma_y\sum_{\mathbf{k}} f_{\mathbf{k}\lambda}\left(\hat{a}_{\mathbf{k}\lambda} + \hat{a}^\dagger_{\mathbf{k}\lambda}\right), \tag{3.18}$$

where now $f_{\mathbf{k}\lambda} = i\left(\frac{\hbar\omega_0}{2\epsilon_0 V}\right)^{\frac{1}{2}}(\mathbf{d}\cdot\mathbf{e}_{\mathbf{k}\lambda})\left(\frac{\omega_0}{\omega_k}\right)^{1/2}$. Using the same analysis as above, a spectral density with a different frequency dependence is obtained

$$\mathcal{J}_C(\omega) = \frac{\Gamma_0}{2\pi\epsilon}\omega. \tag{3.19}$$

We can also see that $\mathcal{J}_M(\epsilon) = \mathcal{J}_C(\epsilon)$, so both theories give the same predictions for the decay

rate of the TLS.

3.3.1 Rotating-wave approximation

If the system Hamiltonian is considered to be $H_S = \epsilon |e\rangle\langle e|$, and transform (3.14) to the interaction picture with $\tilde{H}_I^{\mathrm{EM}}(t) = e^{iH_0 t} H_I^{\mathrm{EM}} e^{-iH_0 t}$ where $H_0 = H_S + H_B$, then we get:

$$\begin{aligned}\tilde{H}_I^{\mathrm{EM}}(t) &= -(\sigma e^{-i\epsilon t} + \sigma^\dagger e^{i\epsilon t}) \sum_{\mathbf{k}\lambda} \left(f_{\mathbf{k}\lambda} \hat{a}_{\mathbf{k}\lambda} e^{-i\omega_k t} + f^*_{\mathbf{k}\lambda} \hat{a}^\dagger_{\mathbf{k}\lambda} e^{i\omega_k t} \right) \\ &= -\sum_{\mathbf{k}\lambda} \left(f_{\mathbf{k}\lambda} \sigma \hat{a}_{\mathbf{k}\lambda} e^{-i(\epsilon+\omega_k)t} + f^*_{\mathbf{k}\lambda} \sigma \hat{a}^\dagger_{\mathbf{k}\lambda} e^{-i(\epsilon-\omega_k)t} + f^*_{\mathbf{k}\lambda} \sigma^\dagger \hat{a}^\dagger_{\mathbf{k}\lambda} e^{i(\epsilon+\omega_k)t} + f_{\mathbf{k}\lambda} \sigma^\dagger \hat{a}_{\mathbf{k}\lambda} e^{i(\epsilon-\omega_k)t} \right).\end{aligned} \tag{3.20}$$

Light-matter interactions will be dominant around resonance, where $\omega_k \approx \epsilon$, so the time evolution of the first and third terms ($\propto e^{\pm i(\epsilon+\omega_k)t}$) will be much faster that the time-evolution of the second and last terms ($\propto e^{\pm i(\epsilon-\omega_k)t}$), with the latter terms being almost stationary with respect to system evolution. This means that on time-scales relevant to system evolution, the fast-oscillating terms are likely to average out to zero and therefore be unimportant to the overall evolution of the system. On top of this, we can see that the fast-oscillating terms correspond to processes which do not conserve particle number: $\sigma \hat{a}_{\mathbf{k}\lambda}$ and $\sigma^\dagger \hat{a}^\dagger_{\mathbf{k}\lambda}$. It is often argued that these virtual processes are only likely to be significant at very large coupling strengths, on the order of system energies and so they are omitted to make the Hamiltonian exactly solvable, as in the Jaynes-Cummings model. This, known as the rotating-wave approximation (RWA), gives the light-matter interaction Hamiltonian in RWA form after moving back to the Schrodinger picture:

$$H_I^{\mathrm{EM}} \approx -\sum_{\mathbf{k}\lambda} \left(f_{\mathbf{k}\lambda} \sigma^\dagger \hat{a}_{\mathbf{k}\lambda} + f^*_{\mathbf{k}\lambda} \sigma \hat{a}^\dagger_{\mathbf{k}\lambda} \right). \tag{3.21}$$

Now I will move on to investigating the interplay between vibrational and electromagnetic degrees of freedom in the monomer system.

3.4 The Franck-Condon principle

The Franck-Condon (FC) principle [48, 52] is an invaluable tool in the study of solid-state and molecular emitters. The principle states that, due to the disparity in mass between electrons and nuclei, after absorption of a photon changes in electron configuration occur instantly on time-scales of nuclear motion. This means that electronic transitions of an emitter occur without changes to the position of its nuclei or those of its environment. As a result, transition rates become dependent on the overlap between vibrational configurations in the initial and final states, which are generally displaced from one another [see Fig. 3.1(a)]. This displacement comes from the instantaneous, vertical transition to a different electronic

manifold, such that the nuclear degrees of freedom are out of equilibrium.

The differing overlap between two displaced vibrational states in different electronic manifolds determines the intensity of that *vibronic* transition line in emission and absorption spectra. Larger displacements lead to an increase in absorption frequencies, as higher-lying vibrational states have an increased overlap. This also causes energy to be dissipated into the nuclear environment as the excited vibrational modes in the electronically excited state relax to their equilibrium configuration. This is observed as an energy difference between the absorption and emission profiles.

It is possible to calculate the optical response for such a system, where the system-vibrational interactions are accounted for non-perturbatively [43], with the optical interaction in the linear regime. These treatments are illuminating, however they do not generalise well to studying the full system dynamics or to cases where there is incoherent driving by thermal photons. As we will see, these are two important situations where environmental non-additivity manifests itself.

Finally, it is also worth noting that figure 3.1(a) shows a distinctly symmetrical system, where the potential energy surfaces of the excited and ground states have the same curvature. However, in many real systems, a change in electronic configuration can also be accompanied by a change in shape of the potential, leading to asymmetries in the emission and absorption profiles [48]. In the following, we will only treat the symmetrical case, but extensions to the formalism may be of interest to future work.

3.5 Environmental non-additivity in the monomer

The Franck-Condon picture provides an intuitive starting point for studying the complex interactions between the electronic and vibrational degrees of freedom of an emitter and its environment, for example through rate equations derived from Fermi's Golden Rule [48, 52].

Faithfully representing the full non-equilibrium dynamics of such systems requires moving beyond rate equations and instead employing an explicitly time-dependent approach. This should be non-perturbative in the electron-vibrational coupling and thus capable of capturing the dynamical influence of vibrational displacement on the electronic states. Examples include polaron [53, 1] and collective coordinate [25, 16, 28, 29, 54] master equations, hierarchical equations of motion [35, 55, 56], path integrals [57, 58, 59], and tensor network methods [60, 61, 30]. Nevertheless, it is interactions with the electromagnetic environment that ultimately give rise to the observed electronic (e.g. optical) transitions. Our focus in this chapter is thus on the important question of how to incorporate electromagnetic interactions into the dynamical formalism, such that they respect the non-perturbative nature of the vibrational coupling.

Given that interactions with the electromagnetic field in free space are weak, it is often assumed that the Markovian dynamics they generate can be added to the equations of motion

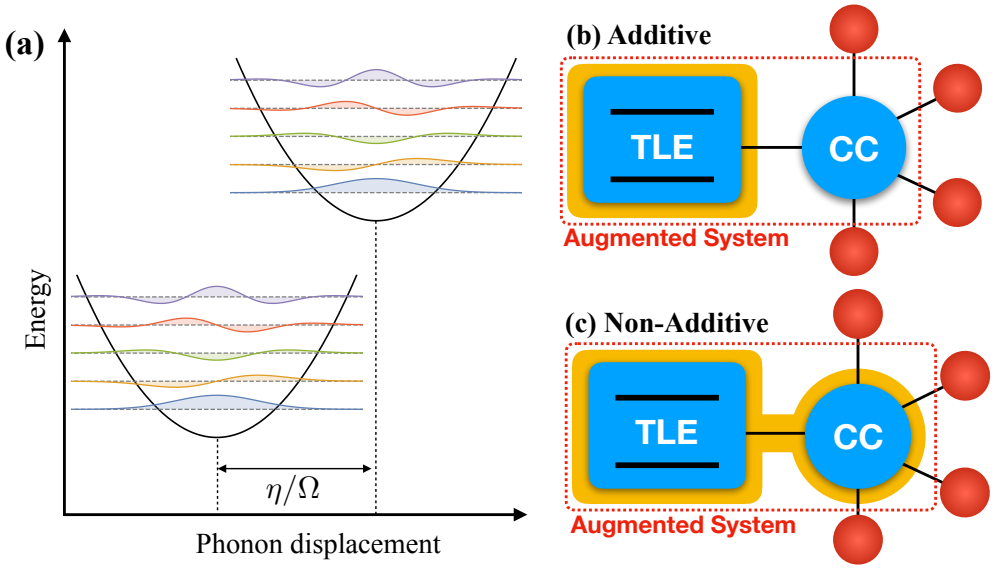

Figure 3.1: **(a)** Illustration of the vibronic energy structure commonly associated to the Franck-Condon principle. Vibrational coupling leads to the formation of manifolds corresponding to the ground and excited electronic configurations, with transition probabilities proportional to the overlap of the displaced and undisplaced vibrational states. **(b), (c)** Schematics of the collective coordinate (CC) mapping. In the additive case **(b)** the electromagnetic field (shaded) is sensitive only to the two-level emitter (TLE), whereas in the non-additive case **(c)** it is sensitive to the full augmented system (TLE+CC).

unmodified due to the presence of vibrations [62, 63, 64, 65, 66, 67, 68, 69, 70, 71, 72, 73, 74, 75, 76, 77]. Though justifiable in certain circumstances [78, 79, 67, 80, 81], additivity is in general a stringent requirement [80, 81, 82, 83, 84] that can break down even if all environments are weakly coupled to the system [82]. In fact, we shall show below that the dynamics obtained in this manner can exhibit fundamental flaws, such as disregarding the FC principle. In certain cases, both the vibrational and electromagnetic environments may be treated non-perturbatively [85, 86], but this comes at an inevitable cost in terms of computational effort and complexity within the formalism.

Here we seek to retain both the simplicity of the Markovian description of the electromagnetic interactions and a non-perturbative treatment of the electron-vibrational coupling, but without the undesirable additivity restriction. This is made possible through a collective coordinate transformation [28, 47, 25, 54] which, as we have seen in the previous chapter, incorporates non-perturbative effects of the vibrational environment into an enlarged (augmented) system [see Fig. 3.1(b),(c)]. This in turn enables a Markovian master equation to be derived in the eigenbasis of the augmented system space, rather than that of the original bare emitter, by tracing out the electromagnetic environment and residual vibrational modes [54]. On doing so we find that electromagnetic transitions become sensitive to the non-perturbative vibrational dynamics captured by the CC mapping, and our procedure thus retains the non-additive effects crucial to obtaining quantum dynamics that are consistent with the FC principle [Fig. 3.1(c)]. If instead we enforce additivity [Fig. 3.1(b)], the result-

ing electronic decay dynamics becomes independent of the electron-vibrational coupling. We show that capturing non-additivity is also vital for accurately representing the stationary non-equilibrium behaviour within our model. Specifically, under incoherent electromagnetic excitation the non-additive interplay between the electromagnetic field and vibrations directly enables electronic population inversion for situations impossible within the additive approach.

Before examining non-equilibrium dynamics explicitly, we can illustrate the shortcomings of an additive approximation through arguments based on a simple Fermi Golden Rule calculation. We consider a two-level molecular emitter (a monomer) with electronic excited state $|e\rangle$ and ground state $|g\rangle$, separated by an energy ϵ ($\hbar = 1$ throughout). Coupling to the electromagnetic field induces transitions between the electronic states, which are also assumed to couple with strength η to a single (harmonic) vibrational mode of frequency Ω, leading to the formation of a displaced manifold associated to the excited electronic configuration. This is the situation depicted qualitatively in Fig. 3.1(a), though our considerations here and throughout the rest of the paper also apply in the case of continuum phonon environments, where the discrete mode would be identified as the CC post mapping (see below). As we have seen in the previous chapter and as shown in [25], the CC approach can reproduce numerically exact dynamics of the spin-boson model for overdamped Drude-Lorentz bosonic environments, far from the single-mode regime.

We assume for the purpose of calculating the rate that shortly after excitation the system has relaxed to thermal equilibrium in the excited state manifold, $\rho_{\mathrm{eq}} = \sum_m p_m \, |e, \tilde{m}\rangle\langle e, \tilde{m}|$, where $p_m = e^{-m\Omega/k_{\mathrm{B}}T} / \sum_n e^{-n\Omega/k_{\mathrm{B}}T}$ with temperature T, and the displaced vibrational basis is denoted $|\tilde{m}\rangle = D(\eta/\Omega)\,|m\rangle$ for vibrational Fock state $|m\rangle$ and displacement operator $D(\alpha)$. From Fermi's Golden Rule the electronic excited to ground state decay rate is then [48]

$$\Gamma_{e\to g} = \sum_{n,m} p_n \mathcal{J}(\Delta\omega_{\tilde{m},n}) \, |\langle \tilde{m}|n\rangle|^2 \, . \tag{3.22}$$

There are two principal components to this expression. One is the overlap between vibrational configurations, $|\langle \tilde{m}|\, n\rangle|^2$, which is known as the FC factor. The other is the electromagnetic spectral density $\mathcal{J}(\omega)$. This describes the system-field coupling strength weighted by the electromagnetic density of states, and should be sampled at all energy differences between relevant states in the excited and ground manifolds, $\Delta\omega_{\tilde{m},n}$. In the additive approximation, however, the electromagnetic field coupling is treated in isolation from the vibrational interactions, and the electromagnetic spectral density is then incorrectly sampled only at the single frequency ϵ corresponding to the bare electronic ground and excited state splitting. The expression for the emission rate then reduces to $\Gamma_{e\to g} \approx \mathcal{J}_0 \sum_n \left|\langle \tilde{0}|\, n\rangle\right|^2 = \mathcal{J}_0$, where $\mathcal{J}_0 = \mathcal{J}(\epsilon)$ and we have used $\sum_n |n\rangle\langle n| = \mathbb{1}$. Thus, in the additive case the FC factor vanishes, and the transition rate loses its dependence on the electron-vibrational coupling. Note that this reasoning can be used to show that the flat spectral density approximation

commonly used in quantum optics theory [87] also fails in regimes of strong coupling to vibrational modes.

We now develop a microscopic description in order to establish the extent to which non-additivity can influence the quantum dynamics of electron-vibrational models beyond the heuristic arguments outlined above. Our Hamiltonian is written as $H = H_{\rm S} + H_{\rm I} + H_{\rm B}$, with system Hamiltonian $H_{\rm S} = \epsilon\,|e\rangle\langle e|$. The electronic configuration of the emitter molecule is directly influenced by both vibrational and electromagnetic environments, such that $H_{\rm I} = H_{\rm I}^{\rm PH} + H_{\rm I}^{\rm EM}$. Within the harmonic approximation the electron-vibrational coupling is written

$$H_{\rm I}^{\rm PH} = |e\rangle\langle e| \otimes \sum_k g_k(b_k^\dagger + b_k) + |e\rangle\langle e| \sum_k \frac{g_k^2}{\nu_k}, \tag{3.23}$$

where b_k is the annihilation operator for the $k^{\rm th}$ phonon mode and the second term shifts the excited state due to the reorganisation energy associated to vibrational displacement. The coupling to the phonon environment is characterised by its spectral density, for which we take the common form $J(\nu) = \sum_k |g_k|^2\delta(\nu - \nu_k) = \alpha\nu_0^2\gamma\nu/\left[(\nu^2 - \nu_0^2)^2 + \gamma^2\nu^2\right]$. Here α and ν_0 define the coupling strength and peak position, respectively, and γ controls whether $J(\nu)$ is narrow (underdamped) or broad (overdamped) [88, 16]. In addition to the phonon environment, we also have an explicit coupling to the electromagnetic field, given by $H_{\rm I}^{\rm EM} = -\mathbf{d}\cdot\mathbf{E}$ in the dipole approximation, where $\mathbf{d}$ is the emitter dipole operator and $\mathbf{E}$ is the electric field operator [89, 21, 90]. Ignoring polarisation degrees of freedom and working in the rotating wave approximation, this then takes the form

$$H_{\rm I}^{\rm EM} = \sum_l (f_l\hat{\sigma}^\dagger a_l + f_l^*\hat{\sigma}a_l^\dagger), \tag{3.24}$$

where $\hat{\sigma} = |g\rangle\langle e|$ and a_l is the annihilation operator for the $l^{\rm th}$ mode of the electromagnetic field. The spectral density for the light-matter coupling is defined as $\mathcal{J}(\omega) = \sum_l |f_l|^2\delta(\omega - \omega_l) = (2\pi\epsilon^3)^{-1}\Gamma_0\omega^3$ [89, 21, 90], where Γ_0 is the spontaneous emission rate for the two-level emitter in the absence of phonons. Finally, $H_{\rm B} = H_{\rm B}^{\rm EM} + H_{\rm B}^{\rm PH} = \sum_l \omega_l a_l^\dagger a_l + \sum_k \nu_k b_k^\dagger b_k$ is the sum of the internal Hamiltonians for the electromagnetic and vibrational environments.

After performing a CC mapping on the electron-phonon interaction as seen in the previous chapter, our Hamiltonian maps as $H = H_{\rm S} + H_{\rm I} + H_{\rm B} \to H_{\rm S}' + H_{\rm I}^{\rm R} + H_{\rm I}^{\rm EM} + H_{\rm B}^{\rm R} + H_{\rm B}^{\rm EM}$, which leaves the light-matter coupling unchanged. Here, we have introduced the transformed Hamiltonians

$$H_{\rm S}' = H_{\rm S} + \eta\,|e\rangle\langle e|\,(b^\dagger + b + \pi\alpha/2\eta) + \Omega b^\dagger b, \tag{3.25}$$

$$H_{\rm I}^{\rm R} = (b^\dagger + b)\sum_m h_m(c_m^\dagger + c_m) + (b^\dagger + b)^2\sum_m \frac{h_m^2}{\tilde{\nu}_m}, \tag{3.26}$$

$$H_{\rm B}^{\rm R} = \sum_m \tilde{\nu}_m c_m^\dagger c_m, \tag{3.27}$$

where $b+b^\dagger = \sum_k g_k(b_k^\dagger + b_k)/\eta$ defines creation and annihilation operators for the CC, c_m is the annihilation operator for the m^{th} mode of the residual environment to which it couples, and we have expressed the reorganisation energy as $\sum_k g_k^2/\nu_k = \int_0^\infty d\nu J(\nu)/\nu = \pi\alpha/2$. The CC parameters can be written in terms of the quantities defining the vibrational spectral density: $\eta^2 = \pi\alpha\nu_0/2$ and $\Omega = \nu_0$ [16]. As shown in Section 2.3.1, the coupling between the augmented emitter-CC system and the residual phonon environment is described by an Ohmic spectral density $J_{\text{R}}(\nu) = \sum_m |h_m|^2\delta(\nu - \tilde{\nu}_m) = \gamma\nu/2\pi\nu_0$ [16], which ensures that the vibrational environment still acts as a continuum of modes after the mapping. As in the single mode case discussed earlier, the coupling to the CC leads to the formation of two vibronic manifolds associated to the ground and excited electronic configurations. The coupling to the residual environment induces transitions *within* each vibronic manifold. This leads both to broadening and to dynamical relaxation of the phonon environment, which typically occurs on a sub-picosecond timescale.

From the mapped Hamiltonian we can follow the same procedure as in Section 2.3.2 and derive a second-order Born-Markov master equation by tracing over the residual environment and the electromagnetic field [21], both of which are assumed to remain in thermal equilibrium at temperatures T_{R} and T_{EM}, respectively: $\rho_i = e^{-H_{\text{B}}^i/k_{\text{B}}T_i}/\text{tr}[e^{-H_{\text{B}}^i/k_{\text{B}}T_i}]$, for $i = \text{R}, \text{EM}$. The resulting master equation can be written $\partial_t\rho(t) = \mathcal{L}[\rho(t)]$ with Liouvillian:

$$\mathcal{L}[\rho(t)] = -i\left[H'_{\text{S}}, \rho(t)\right] + \mathcal{K}_{\text{R}}[\rho(t)] + \mathcal{K}_{\text{EM}}[\rho(t)], \tag{3.28}$$

where $\rho(t)$ is the reduced state of the augmented emitter-CC system. Here, $\mathcal{K}_{\text{R}}$ is a super-operator representing the action of the residual phonon environment [16]:

$$\mathcal{K}_{\text{R}}[\rho(t)] = [S, \rho(t)\zeta] + \left[\zeta^\dagger\rho(t), S\right], \tag{3.29}$$

with $S = b^\dagger + b$ and

$$\zeta = \frac{\pi}{2}\sum_{jk} J_{\text{R}}(\lambda_{jk})\left[\coth\left(\frac{\lambda_{jk}}{2k_{\text{B}}T_{\text{R}}}\right) + 1\right] S_{jk}\left|\psi_j\right\rangle\!\left\langle\psi_k\right|, \tag{3.30}$$

where the eigenbasis of the augmented system is defined through $H'_{\text{S}}\left|\psi_j\right\rangle = \psi_j\left|\psi_j\right\rangle$, giving $\lambda_{jk} = \psi_j - \psi_k$ and $S_{jk} = \left\langle\psi_j\right| S\left|\psi_k\right\rangle$. We solve for the eigenvalues ψ_j and eigenstates $\left|\psi_j\right\rangle$ numerically, taking the basis $\{\left|g\right\rangle, \left|e\right\rangle\}$ for the TLE and a Fock (number) state basis for the CC.

The effects of the electromagnetic field interaction are contained within $\mathcal{K}_{\text{EM}}$. Importantly, the augmented emitter-CC system Hamiltonian, H'_{S}, is treated (numerically) exactly within the formalism. This is crucial in capturing non-additive effects of the electromagnetic and vibrational environments, as it means that when we move the electromagnetic interaction Hamiltonian [Eq. (3.24)] into the interaction picture, we do so with respect to the full augmented system Hamiltonian H'_{S} [Eq. (3.73)]. The mapping thus ensures that the elec-

tromagnetic environment is sensitive to the underlying eigenstructure of both the electronic and vibrational states.

3.5.1 Non-additive and additive quantum optical master equations

In this section we outline further details of the master equations used in the main text. We begin by considering the non-additive case, whereby, after the collective-coordinate (CC) mapping, our interaction Hamiltonian is given by the sum of residual phonon bath and electromagnetic field coupling terms, $H_{\rm I} = S \otimes B + S^2 \sum_m h_m^2/\tilde{\nu}_m + \sum_\alpha A_\alpha \otimes E_\alpha$. Here, $S = b^\dagger + b$ and $B = \sum_m h_m(c_m^\dagger + c_m)$ describe the CC-residual bath interaction, while $A_1 = \hat{\sigma}^\dagger$, $A_2 = \hat{\sigma}$, $E_1 = \sum_l f_l a_l$ and $E_2 = \sum_l f_l^* a_l^\dagger$ define the coupling of the two-level emitter (TLE) to the electromagnetic field. We now move into the interaction picture with respect to the augmented system Hamiltonian describing the coupled TLE and CC, $H'_{\rm S} = H_{\rm S} + \eta\,|e\rangle\langle e|\,(b^\dagger + b + \pi\alpha/2\eta) + \Omega b^\dagger b$, plus the residual and electromagnetic bath Hamiltonians $H_{\rm B}^{\rm R} = \sum_m \tilde{\nu}_m c_m^\dagger c_m$ and $H_{\rm B}^{\rm EM} = \sum_l \omega_l a_l^\dagger a_l$, respectively. This gives

$$\tilde{H}_{\rm I}(t) = \tilde{S}(t) \otimes \tilde{B}(t) + \tilde{S}(t)^2 \sum_m \frac{h_m^2}{\tilde{\nu}_m} + \sum_\alpha \tilde{A}_\alpha(t) \otimes \tilde{E}_\alpha(t), \tag{3.31}$$

where $\tilde{S}(t) = e^{iH'_{\rm S}t} S e^{-iH'_{\rm S}t}$, $\tilde{A}_\alpha(t) = e^{iH'_{\rm S}t} A_\alpha e^{-iH'_{\rm S}t}$, $\tilde{B}(t) = \sum_m h_m(c_m^\dagger e^{i\tilde{\nu}_m t} + c_m e^{-i\tilde{\nu}_m t})$, $E_1 = \sum_l f_l a_l e^{-i\omega_l t}$ and $E_2 = \sum_l f_l^* a_l^\dagger e^{i\omega_l t}$. Within the interaction picture, we then follow the standard procedure to derive a Redfield master equation, tracing out the residual and electromagnetic environments within the Born-Markov approximations [21]. Moving back into the Schrödinger picture, the resulting master equation may be written in the general form

$$\partial_t \rho(t) = \mathcal{L}[\rho(t)] = -i\,[H'_{\rm S}, \rho(t)] + \mathcal{K}_{\rm R}[\rho(t)] + \mathcal{K}_{\rm EM}[\rho(t)], \tag{3.32}$$

where $\rho(t)$ is the reduced density operator of the augmented system, from which either the TLE or CC dynamics may be obtained by tracing out the relevant degrees of freedom. The superoperators $\mathcal{K}_{\rm R}$ and $\mathcal{K}_{\rm EM}$ encode, respectively, the influence of the residual bath and the electromagnetic field interactions on the augmented system dynamics. Note that due to the Born-Markov approximations there are no mixed terms between the residual phonon bath and the electromagnetic field in the master equation above. Nevertheless, our master equation is still non-additive with respect to the *original* phonon environment and the electromagnetic field due to the CC mapping, which incorporates non-perturbative vibrational effects into the enlarged augmented system Hamiltonian $H'_{\rm S}$ used to move into the interaction picture. This results in an electromagnetic superoperator that has explicit dependence on the form and strength of the system-vibrational coupling, as we shall see below. Next, we consider the superoperator for the electromagnetic field, which can be

written

$$\begin{aligned}\mathcal{K}_{\mathrm{EM}}[\rho(t)] = &-\int_0^\infty d\tau \left(\left[\sigma^\dagger, \tilde{\sigma}(-\tau)\rho(t)\right] C_{12}(\tau) + \left[\rho(t)\tilde{\sigma}(-\tau), \sigma^\dagger\right] C_{21}(-\tau)\right) \\ &-\int_0^\infty d\tau \left(\left[\sigma, \tilde{\sigma}^\dagger(-\tau)\rho(t)\right] C_{21}(\tau) + \left[\rho(t)\tilde{\sigma}^\dagger(-\tau), \sigma\right] C_{12}(-\tau)\right).\end{aligned} \tag{3.33}$$

Here, the bath correlation functions are defined as $C_{\alpha\alpha'}(\tau) = \langle E_\alpha(\tau) E_{\alpha'}\rangle$ with the expectation value taken with respect to a thermal state at temperature T_{EM}. This gives

$$C_{12}(\tau) = \int_0^\infty d\tau \mathcal{J}(\omega)(n(\omega)+1)e^{-i\omega\tau} \quad \text{and} \quad C_{21}(\tau) = \int_0^\infty d\tau \mathcal{J}(\omega) n(\omega) e^{i\omega\tau}, \tag{3.34}$$

where we have defined the electromagnetic field spectral density $\mathcal{J}(\omega) = \sum_l |f_l|^2 \delta(\omega - \omega_l)$ and the field occupation number $n(\omega) = (\exp\{\omega/k_{\mathrm{B}}T_{\mathrm{EM}}\} - 1)^{-1}$.

For the non-additive treatment of the electromagnetic field interactions we again decompose the system operators into the eigenbasis of the augmented TLE-CC Hamiltonian such that $\sigma(t) = \sum_{jk} \sigma_{jk} e^{i\lambda_{jk}t} |\psi_j\rangle\langle\psi_k|$, where $\sigma_{jk} = \langle\psi_j| \sigma |\psi_k\rangle$. Inserting this decomposition into Eq. (3.33) and exchanging the order of the time and frequency integrals, we perform the integral over τ using the Sokhotski-Plemelj theorem as before, $\int_0^\infty d\tau e^{\pm i\epsilon\tau} = \pi\delta(\epsilon) \pm iP(1/\epsilon)$, where P stands for the Cauchy principal value. Again, after some algebra and neglecting small imaginary terms, we find

$$\mathcal{K}_{\mathrm{EM}}[\rho(t)] = -\left[\sigma^\dagger, \chi_1\rho(t)\right] - \left[\sigma, \chi_2\rho(t)\right] + \mathrm{h.\,c.}, \tag{3.35}$$

with rate operators

$$\chi_1 = \sum_{jk} \sigma_{jk}\Gamma_\downarrow(\lambda_{jk}) |\psi_j\rangle\langle\psi_k|, \tag{3.36}$$

$$\chi_2 = \sum_{jk} \sigma^*_{jk}\Gamma_\uparrow(\lambda_{jk}) |\psi_k\rangle\langle\psi_j|, \tag{3.37}$$

where

$$\Gamma_\downarrow(\lambda) = \begin{cases} \pi\mathcal{J}(|\lambda|)(n(|\lambda|)+1), & \text{if} \quad \lambda < 0 \\ \lim\limits_{x\to 0} \pi\mathcal{J}(x)(n(x)+1), & \text{if} \quad \lambda = 0 \\ 0, & \text{if} \quad \lambda > 0 \end{cases} \tag{3.38}$$

and

$$\Gamma_\uparrow(\lambda) = \begin{cases} \pi\mathcal{J}(|\lambda|)n(|\lambda|), & \text{if} \quad \lambda < 0 \\ \lim\limits_{x\to 0} \pi\mathcal{J}(x)n(x), & \text{if} \quad \lambda = 0 \\ 0, & \text{if} \quad \lambda > 0. \end{cases} \tag{3.39}$$

For the form of super-ohmic spectral density we have assumed, the $\lambda = 0$ case above goes to zero. In fact, for a general polynomial spectral density of the form $\mathcal{J}_s(\omega) = (2\pi\varepsilon^s)^{-1}\Gamma_0\omega^s$:

$$\lim_{x\to 0}\pi\mathcal{J}_s(x)n(x) = \lim_{x\to 0}\pi\mathcal{J}_s(x)(n(x)+1) = \begin{cases} 0 & \text{for} \quad s > 1 \\ \frac{\Gamma_0}{2\epsilon\beta_{EM}} & \text{for} \quad s = 1 \\ +\infty & \text{for} \quad s < 1. \end{cases} \tag{3.40}$$

This will become useful for section 3.5.4.

From the expressions (3.35)-(3.39), it is evident that the interaction between the system and the electromagnetic field is dependent on the eigenstructure of the augmented system, and thus on the emitter-vibrational coupling through the identification of the CC, and its coupling to the electronic system. We therefore refer to this theory as being *non-additive*.

Additive

Within the additive master equation the description of the residual phonon bath is unchanged, as $\mathcal{K}_{\mathrm{R}}[\rho(t)]$ has no dependence on the electromagnetic field coupling. However, the electromagnetic field superoperator $\mathcal{K}_{\mathrm{EM}}[\rho(t)]$ is altered significantly, as it is no longer sensitive to the (non-perturbative) vibrational coupling.

Specifically, to get $\mathcal{K}_{\mathrm{EM}}[\rho(t)]$ in the additive case, one should completely ignore the presence of vibrations when moving the relevant system operators σ and $\sigma^\dagger$ into the interaction picture. This results in $\tilde{\sigma}(t) = e^{iH_{\mathrm{S}}t}\sigma e^{-iH_{\mathrm{S}}t} = \sigma e^{-i\epsilon t}$ and $\tilde{\sigma}^\dagger(t) = e^{iH_{\mathrm{S}}t}\sigma^\dagger e^{-iH_{\mathrm{S}}t} = \sigma^\dagger e^{i\epsilon\tau}$, where $H_{\mathrm{S}} = \epsilon\left|e\right\rangle\left\langle e\right|$. The impact is a simplification of the rate operators to

$$\chi_1^{add.} = \Gamma_\downarrow(\epsilon)\sigma, \tag{3.41}$$

and

$$\chi_2^{add.} = \Gamma_\uparrow(\epsilon)\sigma^\dagger, \tag{3.42}$$

which when inserted into Eq. (3.35) results in the standard Lindblad form common in quantum optics theory:

$$\mathcal{K}_{\mathrm{EM}}[\rho(t)] = \frac{\Gamma_0}{2}(n(\epsilon)+1)\mathcal{L}_\sigma[\rho(t)] + \frac{\Gamma_0}{2}n(\epsilon)\mathcal{L}_{\sigma^\dagger}[\rho(t)], \tag{3.43}$$

with $\mathcal{L}_O[\rho] = 2O\rho O^\dagger - \{O^\dagger O, \rho\}$. It is thus clear that within the additive approximation the electromagnetic field superoperator loses its explicit dependence on the vibrational environment. For vanishing electromagnetic interactions ($\Gamma_0 \to 0$), the additive and non-additive theories become equivalent and the problem reduces to the independent boson model, for which we have already derived an exact solution and verified the CC model against within the appropriate parameter regimes in Figure 2.1.

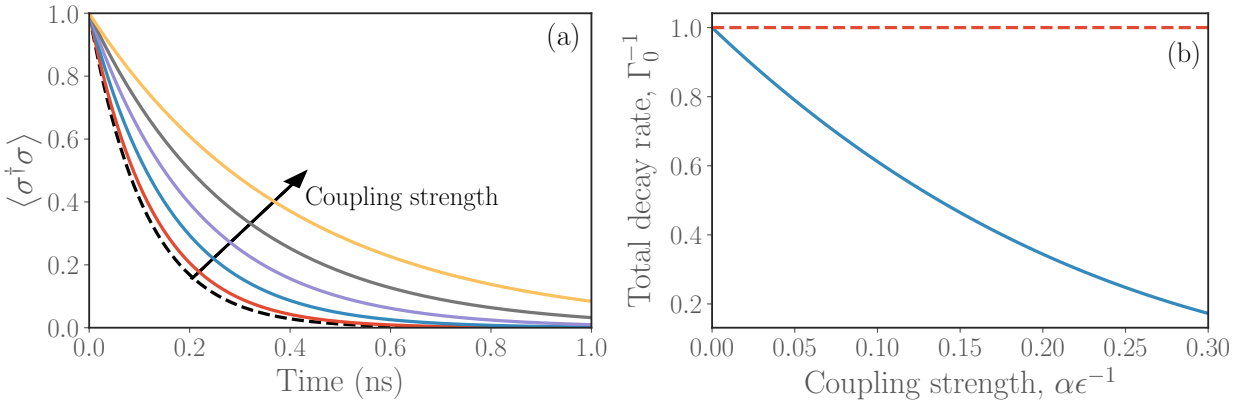

Figure 3.2: **(a)** Emitter population dynamics from the additive (dots) and non-additive (solid) theories for increasing vibrational coupling strength $\epsilon^{-1}\alpha = 0.025$, 0.05, 0.1, 0.15, 0.2, and 0.25. The non-additive theory shows a steady reduction of the decay rate for increasing coupling, whereas within the additive theory the rate remains constant (i.e. all dotted curves lie on top of each other). **(b)** Excited to ground state emission rate against vibrational coupling strength from the additive (dashed) and non-additive (solid) theories in units of the bare decay rate Γ_0. Parameters: $\epsilon = 2$ eV, $\nu_0 = 50$ meV, $\gamma = 10$ meV, $\Gamma_0^{-1} = 100$ ps, and $T_{\mathrm{R}} = T_{\mathrm{EM}} = 300$ K.

3.5.2 Non-additive effects on spontaneous emission

We are now in a position to investigate the impact of non-additive effects on the dynamics of our model system. We begin by considering the decay of an emitter initialised in its excited state with the collective coordinate in a thermal state set by the residual bath temperature T_{R}: $\rho(0) = |e\rangle\langle e| \otimes \rho_{th}$, where $\rho_{th} = \exp\left(-\Omega b^\dagger b/k_{\mathrm{B}}T_{\mathrm{R}}\right)/\operatorname{tr}\left[\exp\left(-\Omega b^\dagger b/k_{\mathrm{B}}T_{\mathrm{R}}\right)\right]$. This approximates a canonical thermal state of the original vibrational Hamiltonian in the unmapped representation at the same temperature, and is thus consistent with rapid (vertical) excitation of the system whereby the electronic state changes suddenly but the vibrational states remain unchanged. The vibrational environment will subsequently relax towards the displaced thermal state associated to the excited state manifold, captured dynamically within our approach. For concreteness, we consider an emitter splitting within the visible range and a vibrational spectral density peaked around a typical value for modes of certain dye molecules [50, 91], polymers [92], and photosynthetic complexes [93, 94].

Fig. 3.2(a) shows the emitter excited state population dynamics predicted by the additive (dotted) and non-additive (solid) theories for increasing electron-phonon coupling at ambient temperature. Both theories give rise to exponential decay, with the rate in the additive theory remaining constant across all electron-phonon coupling strengths. The non-additive theory, in contrast, displays a monotonic decrease in the decay rate with increasing phonon coupling. This can be seen explicitly in Fig. 3.2(b), where we extract the decay rates directly from the master equation. Specifically, the excited to ground state transition rate can be written as

$$\Gamma_{e\to g} = \sum_n \langle g, n|\, \mathcal{L}[\rho_X(0)]\, |g, n\rangle\,, \tag{3.44}$$

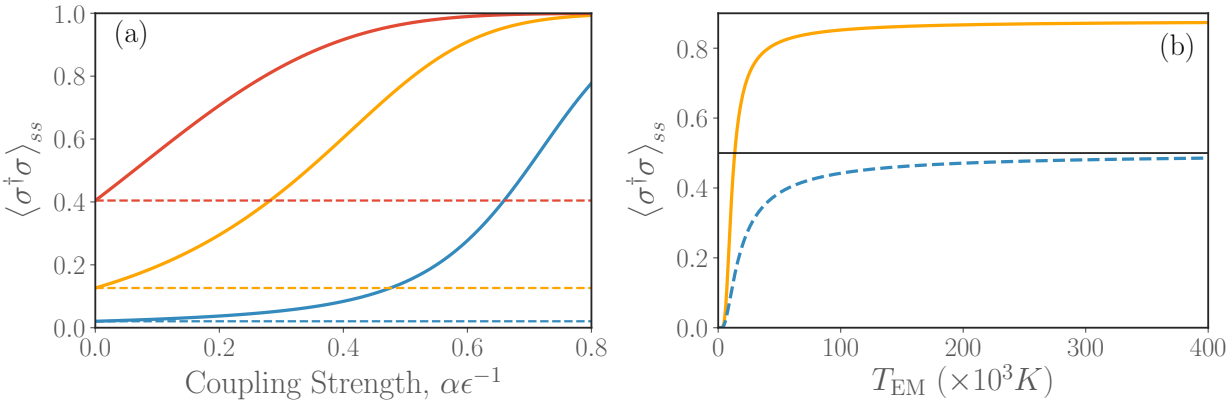

Figure 3.3: (a) Steady-state emitter population as a function of the electron-phonon coupling strength for the additive (dashed) and non-additive (solid) theories. The electromagnetic field temperatures are $T_{\mathrm{EM}} = 6000$ K (blue, lower), 12000 K (orange, middle), and 60000 K (red, upper). (b) Steady-state emitter population with varying temperature for $\alpha = 0.3\epsilon$ from the additive (dashed) and non-additive (solid) theories. In the additive theory the stationary population asymptotically approaches 0.5 (grey line) and never displays an inversion, in contrast to the non-additive treatment. Other parameters are as in Fig. 3.2.

with the Liouvillian taken to be additive or non-additive depending on which case is under investigation. Here we must modify the initial state to account for the aforementioned rapid residual bath induced relaxation of the CC to a displaced thermal state prior to emission: $\rho_X(0) = |e\rangle\langle e| \otimes e^{-X}\rho_{th}e^{X}$, where $X = \Omega^{-1}\eta(b^\dagger - b)$. As expected, the rate from the additive theory displays no variation with phonon coupling strength, in line with the simple Golden Rule calculation discussed previously but at odds with the FC principle. This again highlights deficiencies with the phenomenological additive treatment of the electromagnetic field. Conversely, the non-additive theory shows a steady reduction of the emission rate as a function of phonon coupling, consistent with FC physics. As the displacement between the ground and excited state manifolds increases linearly with the electron-phonon coupling strength, this reduces the overlap between the vibrational states and thus suppresses electromagnetic transitions.

3.5.3 Incoherent excitation

It is important to stress that discrepancies between the additive and non-additive treatments in our model extend further than spontaneous emission processes. For example, we now consider situations in which the emitter is driven incoherently via thermal occupation of the electromagnetic environment at increased temperature T_{EM}, which constitutes an important building block of widely used models for natural and artificial solar energy conversion. See also Chapters 4 and 5 for more on this topic. Fig. 3.3(a) shows the steady state population of the electronic excited state as a function of electron-phonon coupling strength, where the additive treatment once again displays no variation, simply matching the equilibrium distribution expected in the absence of vibrations. The non-additive treatment, on the

other hand, shows a monotonic increase in the steady state population of the excited state manifold. Most strikingly, at large coupling strengths there emerges a steady state population inversion. In the absence of phonons, such an inversion would be impossible, with emission and absorption processes balancing each other in equilibrium. This remains true in the presence of phonons when the electromagnetic field is treated additively, as highlighted in Fig. 3.3(b). Here, the additive theory approaches, but never exceeds, a maximum steady state population $\langle\hat{\sigma}^\dagger\hat{\sigma}\rangle = 0.5$ in the limit of very large temperatures. Since the phonons do not have any effect on the populations in the additive theory, the steady states are effectively at equilibrium. In contrast, within the non-additive theory, cooperative effects between the electromagnetic and vibrational environments lead to non-equilibrium stationary states that display substantial levels of population inversion. That such effects should be possible, even for continuum environments, is made clear from the CC mapping. Within the non-additive theory the electromagnetic field has access to the full vibrational structure of the emitter, providing the necessary states to drive a population inversion. This points to a crucial difference between non-additive and additive treatments, where disregarding the eigenstructure of the combined electronic and vibrational system misses key aspects of the non-equilibrium physics.

3.5.4 Requirements for population-inversion

As outlined above, using an optical spectral density

$$\mathcal{J}(\omega) = (2\pi\varepsilon^s)^{-1}\Gamma_0\omega^s \tag{3.45}$$

where $s = 3$ can lead to population inversion in the steady-state when the system is subject to high temperature incoherent driving. In this section, we show that non-additive population enhancement, and inversion, as shown in the previous section is restricted to a subset of s, namely $s > s_{min}$ where s_{min} is a real number greater than 1, for which we find an analytic value.

Equivalence of incoherent driving to 4-level laser model

We will now gain some more intuition about the behaviour observed in the previous section, by investigating the low phonon-temperature regime $k_BT \ll \hbar\Omega$, where a simple analytical model of the populations can be attained. Although the phonon-temperatures in the previous section are not particularly low, the insight we can gain from this analysis is be able to qualitatively explain higher temperature behaviour too.

For low phonon-temperatures $k_BT \ll \hbar\Omega$, the populations of the above model can be represented by a 4-level laser model, as depicted in Figure (3.4) (b). This means that ρ_{11} is the population of the state $|g,0\rangle \equiv |g\rangle \otimes |0\rangle$, where numbers indicate the excitation number of the CC, ρ_{33} of the state $\left|e,\tilde{0}\right\rangle$ and ρ_{ii} for $i \in \{2,4\}$ are the populations of non-equilibrated

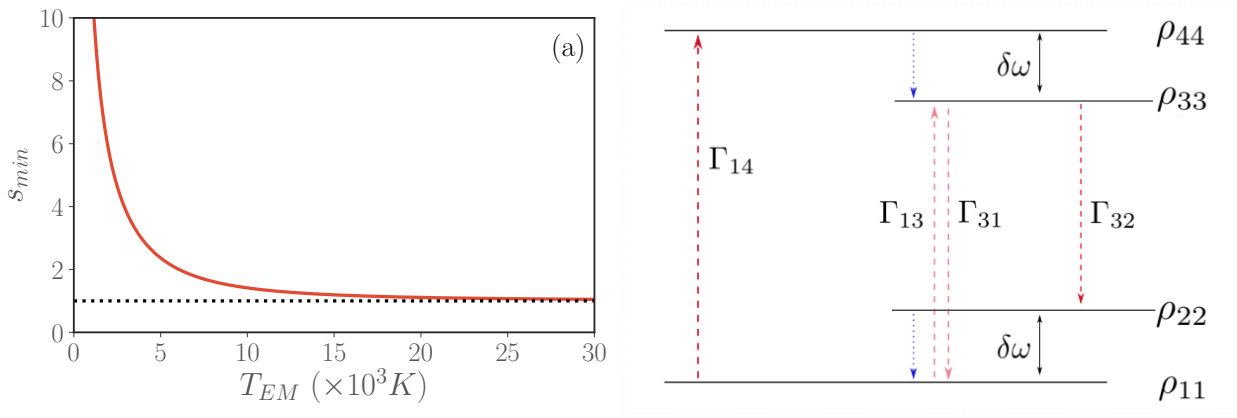

Figure 3.4: **(a)** : Threshold spectral density frequency-dependence, s_{min} as a function of electromagnetic temperature T_{EM} for $\epsilon = 2$eV. **(b)**: Diagram for the four-level laser model. Only important transitions have been included.

vibrationally excited states which are populated vertically by emission and absorption of a photon. As in the previous section, shifted bosonic states are denoted by $|\tilde{m}\rangle = D(\eta/\Omega)\,|m\rangle$. The ω_{34} and ω_{12} are effective energies that lie some $\delta\omega$ above the vibrational ground state in their respective manifolds, which is determined by the Franck-Condon overlap factors as described in the previous section. For this analysis, neither the exact value of $\delta\omega$ nor the form of the states corresponding to ρ_{44} and ρ_{22} are important. All we need to know is that $\delta\omega$ is some function of phonon-coupling strength α, which follows from the FC principle and the form of the displacements $\eta/\Omega = \sqrt{\pi\alpha/2\Omega}$.

The red and blue arrows in Figure (3.4) (b) represent photon and phonon-mediated processes, respectively and since phonon populations relax on sub-picosecond timescales and the electronic populations decay on nanosecond scale, we can assume that $\Gamma_{43} \approx \Gamma_{21} \gg \Gamma_{32}$. From the low-temperature assumption can also approximate that there is little thermal excitation to vibrationally excited states: $\Gamma_{21}/\Gamma_{12} \approx \Gamma_{34}/\Gamma_{43} \to 0$ and thus keeping only the dominant transitions we get the system of equations:

$$\begin{aligned}
\dot{\rho}_{11}(t) &= -(\Gamma_{14} + \Gamma_{13})\rho_{11} + \Gamma_{21}\rho_{22} + \Gamma_{31}\rho_{33} \\
\dot{\rho}_{22}(t) &= -\Gamma_{21}\rho_{22} + \Gamma_{32}\rho_{33} \\
\dot{\rho}_{33}(t) &= -(\Gamma_{32} + \Gamma_{31})\rho_{33} + \Gamma_{13}\rho_{11} + \Gamma_{43}\rho_{44} \\
\dot{\rho}_{44}(t) &= -\Gamma_{43}\rho_{44} + \Gamma_{14}\rho_{11}.
\end{aligned} \tag{3.46}$$

When setting the left-hand side to zero and solving for the steady state populations in terms

of ρ_{33}, these yield

$$\begin{aligned}\rho_{11} &= \frac{\Gamma_{32}+\Gamma_{31}}{\Gamma_{14}+\Gamma_{13}}\rho_{33}\\ \rho_{22} &= \frac{\Gamma_{32}}{\Gamma_{21}}\rho_{33}\\ \rho_{44} &= \frac{\Gamma_{14}}{\Gamma_{43}}\rho_{11}\end{aligned} \tag{3.47}$$

which give the population inversion ratio

$$P \equiv \frac{\rho_{44}+\rho_{33}}{\rho_{11}+\rho_{22}} = \frac{\Gamma_{14}+\Gamma_{13}}{\Gamma_{32}+\Gamma_{31}}. \tag{3.48}$$

Due to a separation of timescales, the non-radiative process do not factor into these rates and so we are left only with

$$\begin{aligned}\Gamma_{13} &= \frac{\Gamma_0}{2\pi}n(\omega_{13})\epsilon^{-s}\omega_{13}^s \propto n(\epsilon)\\ \Gamma_{14} &= \frac{\Gamma_0}{2\pi}n(\omega_{14})\epsilon^{-s}\omega_{14}^s \propto n(\epsilon+\delta\omega)\left(1+\frac{\delta\omega}{\epsilon}\right)^s\\ \Gamma_{32} &= \frac{\Gamma_0}{2\pi}(n(\omega_{23})+1)\epsilon^{-s}\omega_{23}^s \propto (n(\epsilon-\delta\omega)+1)\left(1-\frac{\delta\omega}{\epsilon}\right)^s\\ \Gamma_{31} &= \frac{\Gamma_0}{2\pi}(n(\omega_{13})+1)\epsilon^{-s}\omega_{13}^s \propto n(\epsilon)+1.\end{aligned} \tag{3.49}$$

Here we have introduced the energy definitions which are perturbed by $\delta\omega$, as defined via Figure 3.4 (b). We have also identified that $\omega_{13} = \epsilon$. The common factor of ϵ^{-s} comes from the denominator of the spectral density (3.45). As expected, if the driving field was on resonance only with ω_{14}, then $\Gamma_{13} \to 0$ and this would reduce to the normal model of a four-level laser. We will see this in more detail in the next section. Plugging in the rate expressions (3.49) and cancelling pre-factors yields

$$P = \frac{n(\epsilon+\delta\omega)\left(1+\frac{\delta\omega}{\epsilon}\right)^s + n(\epsilon)}{(n(\epsilon-\delta\omega)+1)\left(1-\frac{\delta\omega}{\epsilon}\right)^s + n(\epsilon)+1}. \tag{3.50}$$

As we have seen in the previous chapter, one hallmark of non-additivity is a positive dependence of population on phonon coupling strength. Due to the nature of displacements between manifolds, $P(\delta\omega)$ is a monotonically increasing function. This means that $dP/d\delta\omega > 0$ holds for all values of $\delta\omega$. We posit then that $dP/d\delta\omega > 0$ is a precondition for population inversion ($P > 1$) to occur under incoherent thermal driving. It follows then that a choice of s which causes $P(\delta\omega)$ to be increasing for small $\delta\omega$, will lead to non-additive population inversion at large $\delta\omega$. We assume that there is some threshold value of $s = s_{min}$, such that $dP/d\delta\omega = 0$.

For small phonon-couplings, the displacement between manifolds is small, so $\delta\omega \ll \epsilon$ and

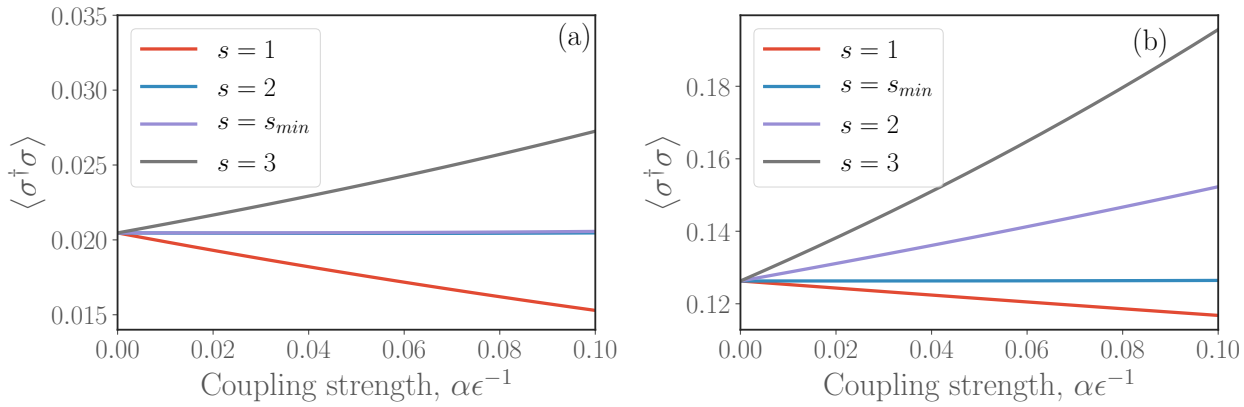

Figure 3.5: **(a)** : Steady-state population of TLS excited state as a function of phonon-coupling for $T_{EM} = 6000$K, where $s_{min} = 2.017$ and **(b)** where $T_{EM} = 12000$K and $s_{min} = 1.294$. Negative gradient of population for $s < s_{min}$, meaning that the phonons are suppressing the population of the electronically excited manifold.

we can expand P to first order in $\frac{\delta\omega}{\epsilon}$:

$$P = e^{-\epsilon/k_B T_{EM}} + e^{-\epsilon/k_B T_{EM}} \left(s - \frac{\epsilon}{2k_B T_{EM}} \right) \coth\left(\frac{\epsilon}{2k_B T_{EM}} \right) \frac{\delta\omega}{\epsilon} + \mathcal{O}((\frac{\delta\omega}{\epsilon})^2), \tag{3.51}$$

we then take the derivative and then set $dP/d\delta\omega = 0$ to get

$$s_{min} = \frac{\epsilon}{2k_B T_{EM}} \coth\left(\frac{\epsilon}{2k_B T_{EM}} \right). \tag{3.52}$$

In figure 3.4 (a) we plot $s_{min}(T_{EM})$ for $\epsilon = 2$eV, where we can see that s_{min} diverges as temperature decreases and converges to $s_{min} \to 1$ for large temperatures. This shows that the spectral density must always be ohmic and the temperature must be sufficient enough for population enhancement to occur.

We can also take the first order expansion of P in Eq. (3.51) and set $P > 1$ to see what the conditions are on $\delta\omega$ for population inversion, which gives:

$$\delta\omega > \frac{\epsilon(e^{\epsilon/k_B T_{EM}} - 1)}{s - s_{min}}. \tag{3.53}$$

This expression gives some intuition: if $s = s_{min}$ then $\delta\omega$ diverges since P has zero gradient, this means that phonon-coupling would have to be infinitely large for population enhancement to occur. If $s < s_{min}$ then the denominator is negative which means that, due to the positive numerator, population inversion is not possible since this would require states $|2\rangle$ and $|4\rangle$ to lie lower than $|1\rangle$ and $|3\rangle$, respectively. In effect this just means that the vibrationally excited and unexcited levels on each manifold will swap and the laser model in equation (3.46) breaks down.

In Figure 3.5, the full Collective Coordinate master equation is solved using $s = \{1, 2, 3, s_{min}\}$ for the optical spectral density at (a) $T_{EM} = 6000$K and (b) $T_{EM} = 12000$K.

We can see from these figures that, at the threshold value $s = s_{min}$, the master equation predicts invariance due to α in the steady state TLS population.

From Eq. (3.50) we can see that for values of s either side of s_{min}, the Collective Coordinate model has qualitatively different behaviour. It is important to understand the two competing processes in incoherent excitation, determined by the fact that $\omega_{32} = \epsilon - \delta\omega$ and $\omega_{14} = \epsilon + \delta\omega$ are changing as a function of phonon-coupling strength, the former being red-shifted and the latter, blue-shifted. On the one hand, there is the sampling of the spectral density $\mathcal{J}(\omega) = (2\pi\epsilon^s)^{-1}\Gamma_0\omega^s$ at these different frequencies, which means $\mathcal{J}(\omega_{14})$ increases and $\mathcal{J}(\omega_{32})$ decreases. This occurs because the displacement causes higher-lying vibrational states to be excited by the optical field. On their own, these processes would lead to an enhancement of excited state population. On the other hand, as $\delta\omega$ increases, the thermal occupation number $n(\omega_{14})$ decreases while $n(\omega_{32})$ increases, which leads to a suppression of Γ_{14} and Γ_{32}, respectively. For $s < s_{min}$, the spectral density is still an increasing function, but this frequency dependence is not enough to outweigh the decrease (increase) in thermal excitation of the absorption (emission) transitions.

Through this analysis, we can now explain the population inversion observed in the previous section as a phenomenon that depends entirely on the cubic form of the electromagnetic spectral density.

3.6 Spectrum of resonance fluorescence

Here we take the same monomer system as in the previous section, but instead of exciting it incoherently with thermal light, we take a low-temperature EM environment and model coherent driving with a continuous-wave (CW) laser. This is a typical experiment that is performed in order to characterise the emission properties of a fluorescent system, such as a molecule or quantum dot.

The emission properties of single molecules has become of great interest over the last few decades, since it has been found that they can behave like nearly-ideal two-level systems [95, 96]. TLS have the property that the light they emit is anti-bunched, which means that they can be used a sources of single photons. Single photon sources are of great importance to the fields of quantum computing, quantum cryptography and quantum communication, where pure, single photon quantum states are manipulated and interfered. Furthermore, these single photons must be indistinguishable from each other, in order for interference effects to be properly observed, e.g. for coincidence counts to be minimised in Hong-Ou-Mandel experiments [97]. This means that highly efficient sources of indistinguishable photons are a requirement for making linear optical quantum computing a reality [98].

There is a growing amount of research into using quantum dots in single-photon source applications [99, 100, 101], since these *artificial atoms* can be made to behave like single two-level systems, which have anti-bunched photon emission statistics. The possibility of

exploiting Purcell enhancement to increase spontaneous emission rates and efficiencies has been a major focus, although recent work on quantum dots has shown fundamental trade-offs in efficiency and indistinguishability due to phonon interactions [102].

Over the last few decades, experimental developments have also allowed single organic molecules to be isolated and trapped in transparent molecular crystals [103]. Similarly to quantum dots, the TLS absorption frequencies changes with the size of the molecule, as this changes the confinement of delocalised electrons. Recently, single Dibenzothiophene (DBT) molecules have been trapped by Van Der Waals forces within a host crystal of anthracene [103], which is completely transparent around the zero-phonon line of DBT near 785nm. The Van der Waals forces are very weak, which means that there is very little phonon-interaction within the DBT molecule due to the host [104], which differentiates them from quantum dots. Bulk phonon modes and discrete vibrational modes present in DBT, which while leading to deleterious effects on indistinguishability are also exploited in order to attain population inversion in the TLS [105].

Although quantum information generally relies on pulsed, monochromatic single photons, broadband and CW sources are still of value in the quantum communications industry [105]. Here we build a simple model of the latter, which is intended to pave the way for future work and also understand the extent to which non-additivity plays a role in these systems.

3.6.1 Photon-statistics, emission spectra and quantum regression theorem

In order to study the spectrum of emitted light under resonance fluorescence, we need to relate system observables to electromagnetic fields. We quote the result from Ref. [22] for the probability of detecting a photon of frequency ν in the interval from $t = 0$ to $t = T$, with an ideal detector,

$$P(\nu) \propto \int_0^T dt \int_0^T dt' e^{-i\nu(t-t')} \left\langle \tilde{\sigma}_+(t)\tilde{\sigma}_-(t') \right\rangle . \tag{3.54}$$

When the system is in the steady-state and the dynamics are described by a Born-Markov master equation, we can express the spectrum of emitted light under coherent driving as

$$S(\nu) = \int_{-\infty}^{\infty} d\tau e^{i\nu\tau} g_1^{ss}(\tau) \tag{3.55}$$

where we have defined $\tau \equiv t' - t$, for $t' \geq t$ and

$$g_1^{ss}(\tau) \propto \left\langle \tilde{\sigma}_+(0)\tilde{\sigma}_-(\tau) \right\rangle_{ss} \equiv \lim_{t\to\infty} \left\langle \tilde{\sigma}_+(t)\tilde{\sigma}_-(t+\tau) \right\rangle . \tag{3.56}$$

Two-level emitters behave like single photon sources because at the moment that they have just emitted, the probability of them re-emitting goes to zero. The probability then increases with time and depends on how fast the TLS is repopulated. This means that the

emission of photons from a single two level system should be anti-bunched, because it is less likely for photons to be emitted at around the same time. As the number of emitters increases, the more likely it is that two of them can emit at the same time. The degree of bunching in photon statistics can be found by measuring the second-order coherence function $g_2(\tau) = G_2(\tau)/\lim_{\tau\to\infty} G_2(\tau)$, where

$$G_2(\tau) = \langle \tilde{\sigma}_+(0)\tilde{\sigma}_+(\tau)\tilde{\sigma}_-(\tau)\tilde{\sigma}_-(0)\rangle_{ss}\,. \tag{3.57}$$

For single-photon sources to operate effectively, the rate with which the system is repopulated by the driving field, known as the Rabi frequency, should be smaller than the spontaneous emission rate. This is to make sure that the TLS will not have been repopulated appreciably within one lifetime of an emission event, as well as preventing the laser from coherently depopulating the TLS.

So far in this thesis, we have explored methods for evolving the reduced density matrix for a system of interest given some bath interactions. From equations (3.54)-(3.57) it is clear that these single time averages alone, will not be sufficient for calculating emission spectra. Instead we need a way of calculating the first-order correlation function $\langle \tilde{\sigma}_+(0)\tilde{\sigma}_-(\tau)\rangle$. Firstly, we define the full density operator of the system and bath as $\chi(t) = \rho(t)\rho_R(t)$, and then use the Heisenberg picture representation of the operators, $\chi(0) = U^{-1}(t)\chi(t)U(t)$ and $\mathcal{O}(t) = U^{-1}(t)\mathcal{O}(0)U(t)$, where $U(t) = e^{-iHt}$:

$$\begin{aligned}\langle \mathcal{O}_1(t)\mathcal{O}_2(t')\rangle &= \mathrm{tr}_s\{\mathrm{tr}_R\{\mathcal{O}_1(t)\mathcal{O}_2(t')\chi(0)\}\}\\ &= \mathrm{tr}_s\{\mathrm{tr}_R\{U^{-1}(t)\mathcal{O}_1(0)U(t)U^{-1}(t')\mathcal{O}_2(0)U(t')U^{-1}(t)\chi(t)U(t)\}\}\\ &= \mathrm{tr}_s\{\mathcal{O}_2(0)\,\mathrm{tr}_R\{U(t'-t)\chi(t)\mathcal{O}_1(0)U^{-1}(t'-t)\}\}\end{aligned} \tag{3.58}$$

where we have used the resolution of the identity $I = U^{-1}(t)U(t)$. If we define $\tau \equiv t' - t$, for $t' \geq t$, then we can identify the object

$$\Lambda_1(t,\tau) \equiv U(\tau)\chi(t)\mathcal{O}_1(0)U^{-1}(\tau) \tag{3.59}$$

which evolves under

$$\frac{d\Lambda_1(t,\tau)}{d\tau} = -i[H, \Lambda_1(t,\tau)], \tag{3.60}$$

with the initial condition $\Lambda_1(t,0) \equiv \chi(t)\mathcal{O}_1(0)$. This gives the second-order correlation function as:

$$\langle \mathcal{O}_1(t)\mathcal{O}_2(t+\tau)\rangle = \mathrm{tr}_s\{\mathcal{O}_2(0)\rho_1(t,\tau)\}, \tag{3.61}$$

where we have also defined $\rho_1(t,\tau) \equiv \mathrm{tr}_R\{\Lambda_1(t,\tau)\}$, $\rho_1(t,0) = \mathrm{tr}_R\{\chi(t)\mathcal{O}_1(0)\}$. To proceed we must assume that the density matrix factorises for all times $\chi(t) = \rho(t) \otimes \rho_R$. This effectively imposes the Born approximation, since we assume that the action of the time-evolution operator does not evolve the bath on timescales relevant to system evolution. This

means that $\rho_1(t,0) = \mathrm{tr}_R\{\rho(t)\mathcal{O}_1 \otimes \rho_R\} = \rho(t)\mathcal{O}_1$. From equations (1.12) and (3.60), we can see that $\chi(t)$ and $\Lambda_1(t,\tau)$ evolve under the same Hamiltonian. This means that after making the Markov approximation a Lindblad master equation can be derived in exactly the same way as before, so we can use master equation definitions (1.41) and (1.42) to approximate the dynamics of $\rho_1(t,\tau)$, giving

$$\langle \mathcal{O}_1(t)\mathcal{O}_2(t+\tau)\rangle = \mathrm{tr}_s\{\mathcal{O}_2(0)e^{\mathcal{L}\tau}[\rho_1(t,0)]\}. \tag{3.62}$$

This means that (3.56) becomes

$$\langle \tilde{\sigma}_+(0)\tilde{\sigma}_-(\tau)\rangle_{ss} = \mathrm{tr}_s\{\sigma_- e^{\mathcal{L}\tau}[\rho_{ss}\sigma_+]\}. \tag{3.63}$$

Similarly (3.57) becomes

$$\begin{aligned}
\langle \tilde{\sigma}_+(0)\tilde{\sigma}_+(\tau)\tilde{\sigma}_-(\tau)\tilde{\sigma}_-(0)\rangle_{ss} &= \mathrm{tr}\{\tilde{\sigma}_-(0)\rho_{ss}\tilde{\sigma}_+(0)\tilde{\sigma}_+(\tau)\tilde{\sigma}_-(\tau)\} &(3.64)\\
&= \mathrm{tr}\big\{U(\tau)\tilde{\sigma}_-(0)\rho_{ss}\tilde{\sigma}_+(0)U^{-1}(\tau)\tilde{\sigma}_+(0)\tilde{\sigma}_-(0)\big\} &(3.65)\\
&\approx \mathrm{tr}\big\{e^{\mathcal{L}t}[\sigma_-\rho_{ss}\sigma_+]\sigma_+\sigma_-\big\}, &(3.66)
\end{aligned}$$

where we have again used the cyclic property of the trace, the resolution of the identity and the Born-Markov approximation on the dynamical evolution.

3.6.2 Monomer-laser Hamiltonian

We will now derive a theory for a coherently-driven emitter with strong vibrational coupling. The treatment includes the transverse (vacuum) field and the laser driving in a non-additive manner. Although the CC approach we employ gives non-Markovian dynamics, the underlying master equations are Markovian, which means that standard quantum regression theorem can be applied.

We start with the Hamiltonian $H = H_M + H_I^{EM} + H_I^{PH} + H_B^{EM} + H_B^{PH}$ where the phonon-renormalised Hamiltonian is $H_M = \epsilon'\sigma^\dagger\sigma$ with molecule-field interaction described by

$$H_I^{EM} = -\vec{d}\cdot[\vec{E}_l(\vec{0},t) + \vec{E}_\perp(\vec{0})], \tag{3.67}$$

with the longitudinal field component $\vec{E}_l(\vec{0},t) = \vec{\mathcal{E}}\cos\omega_L t$. This goes to $H_L = \Omega\sigma_x\cos\omega t$, which we take into the system Hamiltonian, giving $H'_M = \epsilon'\sigma^\dagger\sigma + \Omega\sigma_x\cos\omega t$. The transverse component of the electromagnetic field is given by $-d\cdot\vec{E}_\perp(\vec{0}) = \sum_j \sigma_x(f_j a_j^\dagger + f_j^* a_j)$, which we have seen in the previous sections. Overall, this gives the Hamiltonian

$$H = \epsilon'\sigma^\dagger\sigma + \Omega\sigma_x\cos\omega t + \sum_j \sigma_x(f_j a_j^\dagger + f_j^* a_j) + H_I^{PH} + H_B, \tag{3.68}$$

with

$$H_B = H_B^{EM} + H_B^{PH} = \sum_j \omega_j a_j^\dagger a_j + \sum_k \nu_k b_k^\dagger b_k. \tag{3.69}$$

In order to remove the explicit time-dependence from the system Hamiltonian, we now make a rotating wave approximation by transforming briefly to the interaction picture with $H_I(t) = e^{iH_0 t} H e^{-iH_0 t}$ with $H_0 = \epsilon' \sigma^\dagger \sigma + \sum_j \omega_j a_j^\dagger a_j$, after expanding out the cosine in terms of exponentials it becomes

$$\begin{aligned} \tilde{H}(t) = &\frac{\Omega}{2}(\sigma^\dagger e^{i\epsilon' t} + \sigma e^{-i\epsilon' t})(e^{i\omega_L t} + e^{-i\omega_L t}) \\ &+ \sum_k (\sigma^\dagger e^{i\epsilon' t} + \sigma e^{-i\epsilon' t})(f_j a_j^\dagger e^{-i\omega_j t} + f_j^* a_j e^{i\omega_j t}) + H_I^{PH} + H_B. \end{aligned} \tag{3.70}$$

In the two electromagnetic interaction Hamiltonians, there are terms oscillating with $\pm(\epsilon' \pm \nu)$ where $\nu \in \{\omega_L, \omega_k\}$ the frequencies of the monochromatic laser and the transverse electromagnetic vacuum modes respectively. Around resonance, where the system couples most strongly to the external fields, $\nu \approx \epsilon'$ the processes are either stationary or oscillating with $\approx \pm(2\epsilon')$. These fast interaction terms are likely to affect the bare electronic system on very short time-scales ($\approx 1 - 3$fs) but to average out to zero on the longer timescales that we are interested, so we can approximate the full Hamiltonian by neglecting them, which after transforming back to the Schrödinger picture gives:

$$H(t) \approx \epsilon' \sigma^\dagger \sigma + \frac{\Omega}{2}(\sigma e^{i\omega_L t} + \sigma^\dagger e^{-i\omega_L t}) + \sum_j (f_j \sigma a_j^\dagger + f_j^* \sigma^\dagger a_j) + H_I^{PH} + H_B. \tag{3.71}$$

Next, we transfer the time-dependence from the laser-driving term to the free-field term by moving to a frame rotating at the laser frequency with the unitary transformation $H \to UHU^\dagger - i\dot{U}U^\dagger$, where $U = e^{-i\omega_L \sigma^\dagger \sigma t}$:

$$H_{RW}(t) \approx (\epsilon' - \omega_L)\sigma^\dagger \sigma + \frac{\Omega}{2}(\sigma + \sigma^\dagger) + \sum_j (f_j \sigma a_j^\dagger e^{-i\omega_L t} + f_j^* \sigma^\dagger a_j e^{i\omega_L t}) + H_I^{PH} + H_B. \tag{3.72}$$

3.6.3 Quantum master equations for resonance fluorescence

Next, we perform the collective coordinate mapping on the phonon bath, which takes the salient features of the system-bath interaction and puts them in the system Hamiltonian, this repartitions the closed system as $H_S + H_I^{EM} + H_I^{PH} + H_B^{EM} + H_B^{PH} \to H_S' + H_I^{EM} +$

$H_I^R + H_B^{EM} + H_B^R$:

$$H'_S = H_S + \eta\sigma^\dagger\tilde{\sigma}(b^\dagger + b) + \nu_0 b^\dagger b, \tag{3.73}$$

$$H_S = (\epsilon' - \omega_L)\sigma^\dagger\sigma + \frac{\Omega}{2}(\sigma + \sigma^\dagger) \tag{3.74}$$

$$H_I^R = (b^\dagger + b)\sum_m h_m(\hat{c}_m^\dagger + \hat{c}_m), \tag{3.75}$$

$$H_B^R = \sum_m \tilde{\nu}_m \hat{c}_m^\dagger \hat{c}_m. \tag{3.76}$$

We follow the same procedures for constructing the residual bath and optical field dissipators as in the previous section.

The non-secular master equation is attained by performing the same steps as before, by moving into the interaction picture numerically:

$$\tilde{H}_I^{EM}(t) = \sum_{i,j}\left(\sigma_{(i,j)}\left|\varphi_i\right\rangle\!\left\langle\varphi_j\right| e^{i(\xi_{ij}-\omega_L)t}\sum_k f_k a_k^\dagger e^{i\omega_k t} + \sigma_{(j,i)}^\dagger\left|\varphi_j\right\rangle\!\left\langle\varphi_i\right| e^{-i(\xi_{ij}-\omega_L t)}\sum_k f_k^* a_k e^{-i\omega_k t}\right) \tag{3.77}$$

where $\sigma_{(i,j)} = \langle\varphi_i|\,\sigma\,|\varphi_j\rangle$. This gives the interaction picture operators:

$$\tilde{\sigma}(t) = \sum_{i,j}\sigma_{(i,j)}\left|\varphi_i\right\rangle\!\left\langle\varphi_j\right| e^{i(\xi_{ij}-\omega_L)t} \tag{3.78}$$

$$\tilde{\sigma}^\dagger(t) = \sum_{(i,j)}\sigma_{(j,i)}^\dagger\left|\varphi_j\right\rangle\!\left\langle\varphi_i\right| e^{-i(\xi_{ij}-\omega_L t)}. \tag{3.79}$$

This allows us to define the rate operators, $\hat{\chi}_1 = \sum_{jk}\sigma_{(j,k)}\Gamma_\downarrow(\xi_{ij}-\omega_L)\left|\varphi_j\right\rangle\!\left\langle\varphi_k\right|$ and $\hat{\chi}_2 = \sum_{jk}\sigma_{(j,k)}^*\Gamma_\uparrow(\xi_{ij}-\omega_L)\left|\varphi_k\right\rangle\!\left\langle\varphi_j\right|$. After discarding the Lamb-shift terms, we can find analytic forms for the decay rates:

$$\Gamma_\downarrow(\lambda) = \pi\mathcal{J}(\lambda)(n(\lambda)+1), \tag{3.80}$$

$$\Gamma_\uparrow(\lambda) = \pi\mathcal{J}(\lambda)n(\lambda). \tag{3.81}$$

So we can see that the effect of the rotating wave approximation in the optical dissipator is to the frequency values at which the decay rates are evaluated. This allows us to write the full master equation in the Schrödinger picture

$$\partial_t\rho(t) = \mathcal{L}[\rho(t)] = -i\left[H'_{\mathrm{S}}, \rho(t)\right] + \mathcal{K}_{\mathrm{R}}[\rho(t)] + \mathcal{K}_{\mathrm{EM}}[\rho(t)], \tag{3.82}$$

with the non-additive electromagnetic dissipator in the compact form:

$$\mathcal{K}_{EM}[\rho(t)] = -\left[\hat{\sigma}^\dagger, \hat{\chi}_1\rho(t)\right] - \left[\hat{\sigma}, \hat{\chi}_2\rho(t)\right] + \mathrm{h.\,c.} \tag{3.83}$$

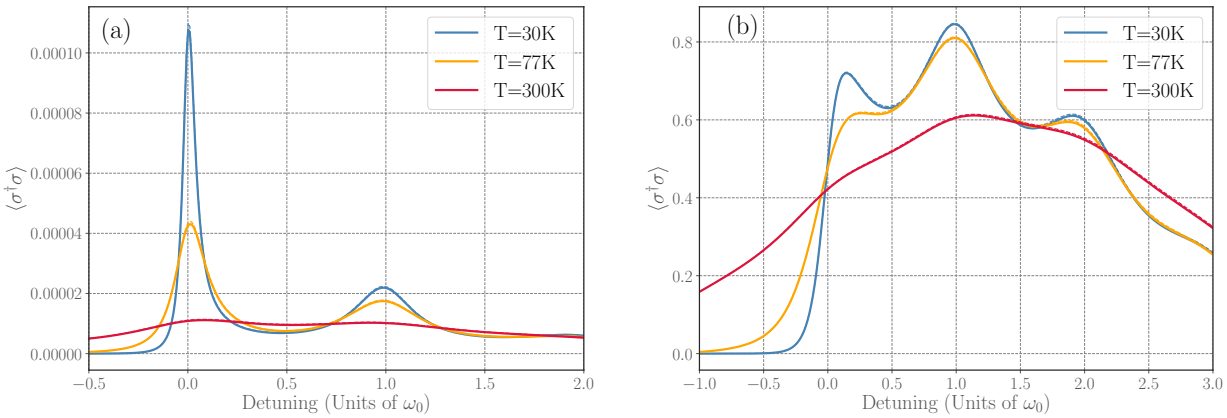

Figure 3.6: Steady-state population as a function of detuning and temperature at: **(a):** weak-driving where $\Omega = \Gamma_{EM}$. **(b):** Strong-driving where $\Omega = 500\Gamma$.

and residual bath dissipator in the exact same form as (5.22) with Drude-Lorentz system-phonon spectral density given by (3.2).

3.6.4 Analysis of resonance fluorescence

Figure (3.6) shows steady-state populations as a function of phonon temperature and detuning for weak-driving (left) and strong-driving (right). The former corresponds to the case where the Rabi frequency is equal to the inverse of the optical lifetime, $\Omega = \Gamma_{EM}$. We can see that in this case, the temperature of the phonons hugely affects the steady-state population, since the vibrational populations equilibrate to higher states in the potential wells, which causes more decay channels to be available. At low-temperature, the electronic population in the excited state is quickly dissipated to the vibrational ground state which emits photons less efficiently than higher vibrational states (due to a reduced FC overlap).

On the right axes in Figure (3.6), the Rabi frequency is much larger, $\Omega = 500\Gamma_{EM}$. In this case, high levels of population inversion are attained when exciting to higher lying vibrational modes, but population always saturates to $\langle\sigma^\dagger\sigma\rangle = 0.5$ when pumping the system on resonance with the zero-phonon line. In the resonant case, population is not trapped in the excited state. The strong-driving case is within the Mollow regime, which means that there are available states to emit through close to resonance with the ZPL. Large population inversion can be achieved through off-resonant driving for Rabi-frequencies much smaller than these.

In Figure (3.7) (a)-(b), we can see dynamics, emission spectra, first and second order coherence functions for the weak-driving case. The emission spectra has been normalised so that the maximum value is always 1, but in reality the peak amplitudes decrease at larger phonon couplings, as seen in figure 3.8 (a), since more power goes into the side-bands and less emits through the zero-phonon line, which is centred close to zero. These vibrational

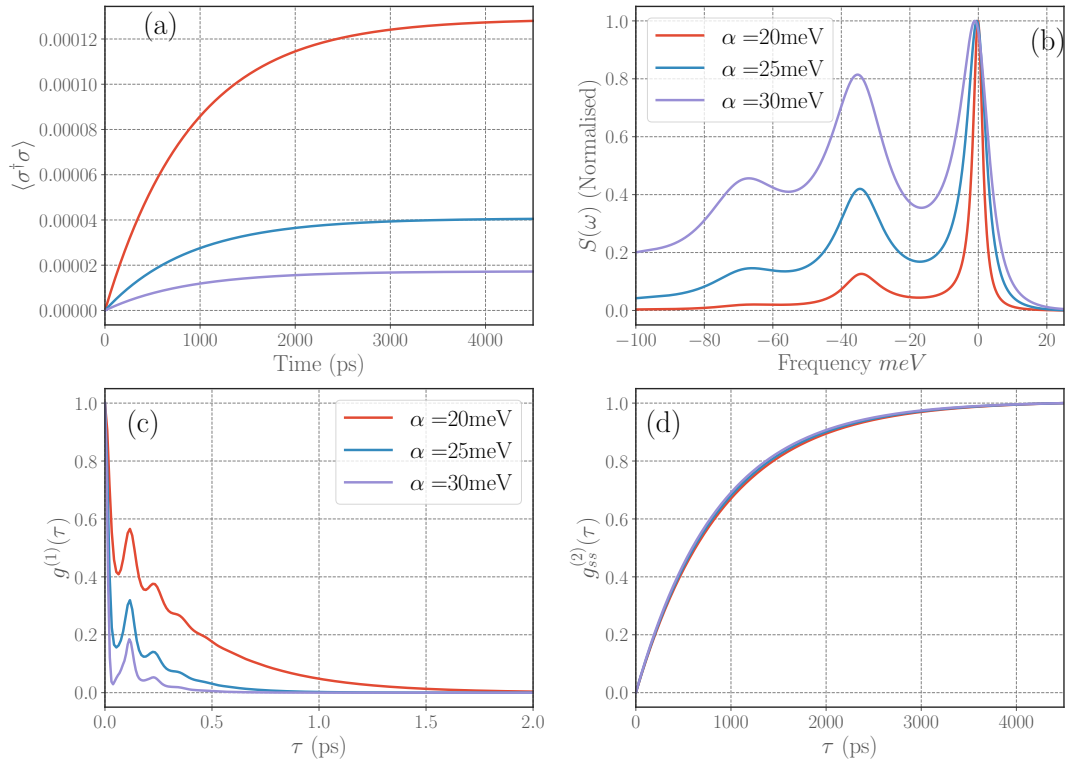

Figure 3.7: **(a)**: Population dynamics, **(b)**: Emission spectra **(c)**: First order optical coherence function $g^{(1)}(\tau)$ **(d)**: Second order coherence function $g^{(2)}(\tau)$ for different phonon couplings at weak-driving: $\Omega = \Gamma_{EM} = 1/4ns^{-1}$. Other parameters: $\Gamma_{ph} = 10\text{meV}$, $T_{ph} = 77K$, $T_{EM} = 0\text{K}$.

side-bands occur due to the phonon spectral density given in (3.2).

3.7 Summary

In summary, we have demonstrated that for models of electronic systems strongly coupled to vibrational environments, including the electromagnetic field in an additive manner can lead to dynamics inconsistent with the FC principle. By developing a dynamical formalism based on collective coordinate mappings, we capture the impact of non-additive effects to recover both transient and stationary non-equilibrium behaviour consistent with FC physics. Furthermore, we find that for common model assumptions on the forms of vibrational and electromagnetic couplings, non-additive phenomena enable steady-state population inversion under incoherent electromagnetic excitation conditions. In relaxing the cubic restriction on the optical spectral density and mapping to a simple four-level laser model, we were also able to analytically show that population inversion due to non-additivity can never occur for ohmic frequency dependency of the electromagnetic field. It would be interesting to

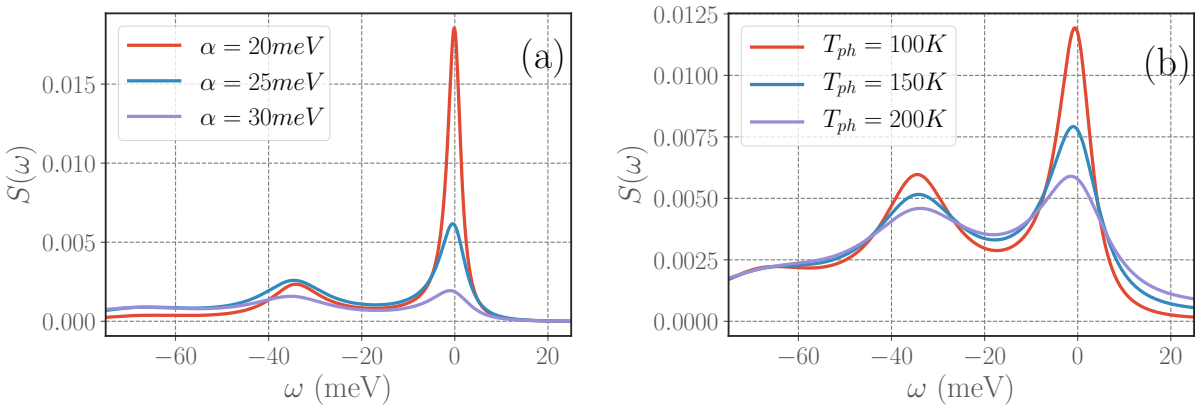

Figure 3.8: **(a)**: Un-normalised version of emission spectra in figure 3.7: $\Omega = \Gamma_{EM} = 1ns^{-1}$, $\Gamma_{ph} = 10$meV, $T_{ph} = 77K$, $T_{EM} = 0$K. We can see that phonon coupling causes a decline in overall emission. **(b)**: Temperature dependence of emission spectra.

explore whether such inversions could be harnessed to enhance work extraction (i.e. current) in models of solar energy conversion devices. Furthermore, we have shown that the CC approach can be used in conjunction with standard quantum regression theorem to calculate optical spectra for emitters with non-Markovian evolution.

Blank page

Chapter 4

Vibronic effects on energy transfer in molecular dimers

Biological systems have been under the lens of quantum physicists ever since the seminal lecture series *What is Life?*, in which Erwin Schrödinger proposed a theory for the chemical basis of genetic information, sparking what would later become the field of molecular biology. Although quantum mechanics underpins the structure of molecules and their interaction with light, non-trivial quantum effects - such as superposition and entanglement - were largely thought to be irrelevant to the biological realm. In the past two decades, quantum effects have been proposed as the explanation for a variety of biological phenomena [44], such as magneto-reception in birds [106], olfaction [107] and energy transfer in photosynthetic systems [44, 46]. The latter has gained most of the attention in the field and forms the background of this chapter. In photosythetic systems, networks of interacting chromophores known as pigment protein complexes (PPCs) can exchange energy via dipole-dipole interactions [48, 52]. The role of PPCs is to transport absorbed excitations from the absorption antennae to the reaction center (RC), where charge-separation occurs, driving the necessary chemical reactions for life to occur. PPCs also act as a valve, moderating the number of excitons which come through the RC [8]. This means that efficiency and tunability are key for the proper function of the system.

Early experiments claimed to observe ultra-fast wave-like transfer of excitons [108, 109, 4], which manifested itself as beating patterns in the 2D optical spectra of a PPC called the Fenna-Matthews-Olsen complex [110] (FMO). These oscillations were seen to persist for several picoseconds, even at physiological temperatures, and were thought to be signals of quantum coherence between electronically excited molecular orbitals. For many years this coherence was thought to be mostly electronic in nature and enabled by relatively strong coupling between the densely-packed chromophores, which can be as close as a few nanometres apart. The protein environments were configured in such a way as to shield the superposition states *just enough* so as to allow for partial wave-like exciton diffusion but also to slightly decohere states in order to trigger efficient energy transfer via non-

adiabatic phonon transitions [11]. This mechanism, known as environment-assisted energy transfer, would allow quantum states which were trapped far from the reaction centre to be destroyed, leading to a quantum speed-up of transfer as compared to purely incoherent or coherent transfer [109, 111, 11]. These theories gained popularity as they hinted at the biological role that coherence could fulfil in enhancing efficiency and the possibility of its emergence from Darwinian evolution.

Theories arose that the spectra could be fully explained by the presence of electron-vibrational interactions. Resonant vibrational modes could transfer energy on ultra-fast timescales and the vibronic coherences would cause off-diagonal peak oscillations in the 2D spectra of FMO [112, 113] and other complexes [114, 115, 116, 7]. Localised vibrations could also cause the formation of polarons around excitations which effectively decrease the interaction between excitations and the transverse phonon environment [9]. Today the dominant explanation for coherence in the spectral signals is through a combination of resonant vibrational modes and intermediate-strength dipole-dipole interactions, although the biological function they serve is still disputed [117].

Of great interest to researchers in this field is how these biological systems can permit such large electron diffusion lengths and fast exciton transfer timescales despite being highly disordered systems [8]. This could be of great benefit in developing organic photovoltaic cells (OPVs), since the efficiencies of these suffer due to short electron diffusion lengths and low charge mobilities [118, 17].

A key theoretical concept in studying these systems is that the molecular electronic degrees of freedom can often be treated as two-level systems, with the highest *occupied* molecular orbital (HOMO) at ambient temperature representing the ground state and the lowest *unoccupied* molecular orbital (LUMO) the excited state. These HOMO and LUMO states are generally the bonding and anti-bonding orbitals of π-conjugated systems, respectively [48, 52].

Another key concept is that, for sufficient interaction-strength between two parallel dipoles, the energy eigenstates can delocalise across the LUMO states of two or more molecules. The alignment of two molecules gives rise to symmetric and anti-symmetric eigenstates in the single-excitation subspace, which are known as *bright* and *dark* states due to the enhancement/suppression of their dipole moments (via constructive/destructive interference). In the ideal case of two identical monomers and in the absence of vibrational mixing, the dark state will have zero optical decay rate and the bright state will have twice that of the underlying monomer. The bright state energy is larger than the dark state energy for *plane-to-plane* parallel dipoles. An analogy can be drawn with H- and J-aggregates of conjugated polymers [119], where inter-chain coupling gives rise to optically active H-aggregate bands which lie higher than the uncoupled monomer energy [120]. For *head-to-tail* arrangements then the opposite structure occurs, giving rise to J-aggregate bands. In the latter, the lowest energy exciton state is optically active, which can lead to super-radiance [120]. This

chapter will focus only on the former dipole arrangement where the bright state lies above the dark state, so excitons vibrationally relax to the optically inactive state. Though we use this analogy, the details of polymeric aggregation is beyond the scope of this work.

Due to their symmetry, transitions between bright and dark states are largely mediated by localised or delocalised vibrational environments which can cause non-adiabatic, irreversible transitions from bright to dark states, given adequate spacing of energy levels ($\psi_+ - \psi_- > k_B T$). This potentially allows *dimer-based* systems to overcome the principle of detailed balance, which restricts classical systems in that "good absorbers must also be good emitters". Instead energy can be absorbed efficiently in the bright state and then *parked* in the dark state, where it will be resilient to spontaneous emission [121, 122]. This has naturally led to the proposal that molecular dimers could be used in photovoltaic devices [18], which could utilise quantum superposition of excited emitter states to overcome classical performance restrictions [121]. These studies have used weak-coupling master equations [121, 122], resonant vibrational modes [69] and recently with strongly-coupled continuous phonon environments [54, 123]. Ultimately, phonons are seen to have a variety of effects on photovoltaic performance, by influencing steady-state populations and mediating non-adiabatic transitions from highly absorbing *bright* states to weakly-emitting *dark* states, a concept that has been termed *dark-state protection* [122].

In this chapter, I investigate the underlying models used in these previous studies by deriving a full non-perturbative model for two coupled emitters in order to elucidate the interplay between vibrational and electromagnetic degrees of freedom. This allows us to further the understanding of using realistic dimer systems as absorbers in proposed photocell applications. I employ the Collective-Coordinate model, which extends the validity of master equations well into the strong-coupling and non-Markovian regimes, for the electron-vibrational interactions. This method not only shows substantial qualitative differences to weak-coupling theory but also offers a concise framework to understand and explain the behaviour. As well as explaining the influence that phonons have on populations in these dimer models, steady-state quantum coherence is observed in the excitonic basis which is not predicted at all by a secular weak-coupling master equation approach and is not replicated accurately by Redfield theory beyond the weak-coupling and broad phonon-spectrum regimes. I show that stronger phonon coupling does not increase the transition rates from bright to dark states, ultimately putting into question the notion that dark-state protection can be sustained in realistic molecular systems. Recently, a similar conclusion was arrived at independently by using a polaron theory treatment [123], although the analysis is complementary to this work as it focuses on changes to absorption coefficients rather than our approach which is based on eigenstructure and thermalisation considerations.

In section 4.1.1 I lay out the model and Hamiltonians for the bare electronic systems, electromagnetic interactions and phonon environments. In section 4.1.2 the Redfield theory is introduced. In section 4.1.3 I derive the CC master equation and non-additive optical

master equations. In the remaining sections I explore the behaviour of the model and gain physical insight in order to understand the predicted steady-state populations and coherences of the dimer system.

4.1 The dimer model

4.1.1 Dipole-dipole interactions and the dimer Hamiltonian

Here we derive a Hamiltonian for dipole-coupled monomers with inter-molecular coupling, each with independent, continuous vibrational environments due to the dynamical conformation changes of the host nuclei. The set of states in the combined space is written as $\{|OO\rangle, |OX\rangle, |XO\rangle, |XX\rangle\}$, where tensor products of the two subsystem states are represented as $|m_1\rangle \otimes |m_2\rangle = |m_1 m_2\rangle$, with $m_i \in \{O, X\}$ corresponding to ground and excited states of each two-level system (TLS). In the subspace of each TLS the raising and lowering operators are $\sigma^\dagger = |X\rangle\langle O|$, $\sigma = |O\rangle\langle X|$, with identity operator $\mathcal{I} = |X\rangle\langle X| + |O\rangle\langle O|$. In order to maintain simplicity in the model, we assume that all the electronic states are singlet in nature and that no inter-system crossing occurs. However, spin-characteristics of excitons are hugely important, with singlet fission an active area within photovoltaic research, due to its potential to greatly enhance quantum yield.

Following [124], we arrive at the full dimer Hamiltonian, which has explicit longitudinal dipole-dipole and dipole-host couplings, in addition to the coupling between each dipole and the transverse (vacuum) electric field modes. The notion of *phonons* arises from the quantisation of host excitations in the coulomb gauge and must therefore be consistent with the transverse field interaction - this gauge consistency is important at strong phonon-coupling and is commonly overlooked. In total, this yields a Hamiltonian of the form $H = H_d + H_I^\perp + H_B^\perp + H_B^{ph} + H_I^{ph}$, where $H_d = H_{M_1} + H_{M_2} + H_I^\parallel$, with the Hamiltonian for monomer j given by H_{M_j} and the dipole-dipole (longitudinal) and dipole-field (transverse) interaction Hamiltonians given by $H_I^\parallel$ and $H_I^\perp$, respectively. Setting the ground state energy of each TLS to zero, we write

$$H_d = \omega_1(\sigma^\dagger\sigma \otimes \mathcal{I}) + \omega_2(\mathcal{I} \otimes \sigma^\dagger\sigma) + V(\sigma^\dagger + \sigma) \otimes (\sigma^\dagger + \sigma) + \omega_{xx}\sigma^\dagger\sigma \otimes \sigma^\dagger\sigma \tag{4.1}$$

$$\begin{aligned} &= \omega_1 |XO\rangle\langle XO| + \omega_2 |OX\rangle\langle OX| + \omega_{XX} |XX\rangle\langle XX| \\ &\quad + V(|XO\rangle\langle OX| + |OX\rangle\langle XO| + |OO\rangle\langle XX| + |XX\rangle\langle OO|) \end{aligned} \tag{4.2}$$

where V is the dipole-dipole coupling strength between the two monomers and $\omega_{XX} = \omega_{xx} + \omega_1 + \omega_2$ is the energy of the doubly occupied state subject to Coulomb repulsion ω_{xx}. The coupling terms $|OO\rangle\langle XX| + |XX\rangle\langle OO|$ are fast-oscillating and are often omitted due to time-scale considerations, which we will analyse later when looking at the transverse field

Hamiltonian. We can relabel the basis states for convenience such that

$$H_d = \omega_1 |1\rangle\langle 1| + \omega_2 |2\rangle\langle 2| + \omega_{XX} |3\rangle\langle 3| + V \left(|1\rangle\langle 2| + |2\rangle\langle 1| + |0\rangle\langle 3| + |3\rangle\langle 0|\right). \tag{4.3}$$

We take $\omega_1 = \omega_2 + \epsilon$, with $\epsilon > 0$. The eigenstates of the single-excitation subspace are:

$$|\nu_\pm\rangle = \frac{1}{\sqrt{2\eta}} \left(\sqrt{\eta \pm \epsilon}\, |1\rangle \pm \sqrt{\eta \mp \epsilon}\, |2\rangle\right). \tag{4.4}$$

with corresponding energies

$$\lambda_\pm = \omega_2 + \frac{1}{2}(\epsilon \pm \eta) \tag{4.5}$$

where $\omega_1 = \omega_2 + \epsilon$ and $\eta = \sqrt{\epsilon^2 + 4V^2}$. The excited monomer states can be expressed in terms of these eigenstates

$$\begin{aligned} |1\rangle &= \frac{1}{\sqrt{2\eta}} \left(\sqrt{\eta + \epsilon}\, |\nu_+\rangle + \sqrt{\eta - \epsilon}\, |\nu_-\rangle\right) \\ |2\rangle &= \frac{1}{\sqrt{2\eta}} \left(\sqrt{\eta - \epsilon}\, |\nu_+\rangle - \sqrt{\eta + \epsilon}\, |\nu_-\rangle\right). \end{aligned} \tag{4.6}$$

Exciton-phonon coupling

We take the form of electron-phonon coupling which is common throughout the literature [48, 52], akin to two coupled monomers as seen in the previous chapter,

$$H_I^{ph} = \frac{1}{2} \sum_i \sum_k \left(p_{i,k}^2 + \omega_{i,k}^2 \left(x_{i,k} - \frac{g_{i,k}}{\omega_{i,k}^2} \sigma_i^\dagger \sigma_i \right)^2 \right), \tag{4.7}$$

where the vibrational environments cannot directly cause electronic transitions on uncoupled monomers and their whole influence on the electronic system is incorporated into coupling strengths $\{g_{i,k}\}$. We have also introduced the notation $\sigma_1 = |0\rangle\langle 1| + |2\rangle\langle 3|$ and $\sigma_2 = |0\rangle\langle 2| + |1\rangle\langle 3|$. Expanding out the mass-weighted position $x_{i,k}$ and momentum $p_{i,k}$ operators of the bath, which fulfill $[x_{i,k}, p_{i,l}] = \delta_{l,k}$, we have:

$$\begin{aligned} H = H_d &- \sum_i \sigma_i^\dagger \sigma_i \sum_k g_{i,k} (b_{i,k}^\dagger + b_{i,k}) \\ &+ \sum_i \sum_k \frac{g_{i,k}^2}{\omega_{i,k}} (\sigma_i^\dagger \sigma_i)^2 + \sum_i \sum_k \omega_{i,k} b_{i,k}^\dagger b_{i,k} \\ &+ H^\perp. \end{aligned} \tag{4.8}$$

We also now define spectral densities for the phonon environments

$$J_{ph}^{(i)}(\omega) = \sum_k \left| g_{i,k}^2 \right| \delta(\omega - \omega_{i,k}), \tag{4.9}$$

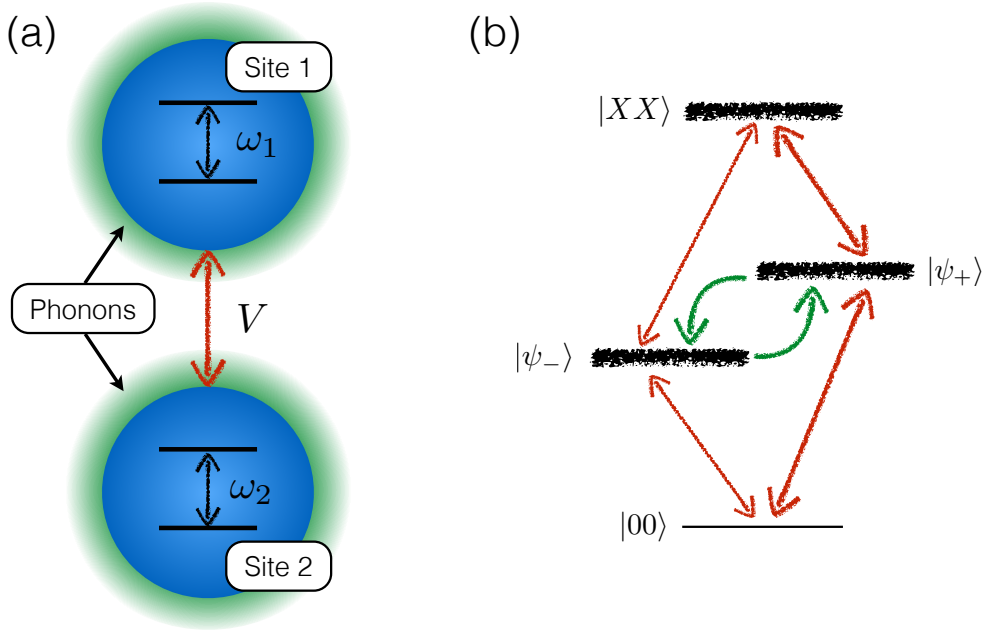

Figure 4.1: **(a)**: diagram of dipole-dipole coupling between sites 1 and 2 of the dimer system. **(b)**: energy eigenbasis of the dimer where green (red) arrows correspond to phonon (photon) mediated population transfer processes.

as seen in previous chapters.

Since the aim of this work is to study the effect that correlations between system and environment have on system observables, we assume that each phonon environment is uncorrelated with the other so as to avoid any effects due to the existence of decoherence-free subspaces. However, the non-Markovian formalism used later allows for inter-bath correlations to build up via their back-action against the electronic subsystem, which can be studied explicitly. The renormalisation terms proportional to $\sum_k \frac{g_{i,k}^2}{\omega_{i,k}}$ are second-order in system-bath coupling strength and a discussion of how they should be treated at the various levels of approximation follows in the next section.

Light-matter coupling

The ambient electromagnetic field Hamiltonian and its interaction with the system dipoles are derived in the long-wavelength limit,

$$H^{\perp} = \sum_k \left(f_{k\lambda}^{(1)}(\sigma_1 + \sigma_1^\dagger) + f_{k\lambda}^{(2)}(\sigma_2 + \sigma_2^\dagger) \right)(d_k + d_k^\dagger) + \sum_k \omega_k d_k^\dagger d_k, \tag{4.10}$$

where d_j are the bath annihilation operators and $f_{k\lambda}^{(i)}$ are the coupling strengths between dipole i and field mode k, which in the Coulomb gauge take the following form [51]:

$$f_{k\lambda}^{(i)} = ie \left(\frac{\omega_i}{2\epsilon_0 L^3} \right)^{\frac{1}{2}} \mathbf{e}_{k\lambda}^{(i)} \cdot \mathbf{d}_i \left(\frac{\omega_i}{\omega_k} \right)^{\frac{1}{2}} \tag{4.11}$$

with the electric field vectors $\vec{e}_{k\lambda}$, polarization λ, dipole orientation vector $\vec{d}_i = |d_i|\hat{d}_i$ and ω_i is the transition frequency. Other constants are the elementary charge e, the quantization volume L and the permittivity of free-space ϵ_0.

The long-wavelength limit means that the distance between each monomer (typically $1-10$nm in light-harvesting complexes [125]) is small compared to the wavelength of the absorbed visible light ($400-900$nm), such that each dipole is influenced by an identical field $\mathbf{e}_{k\lambda} \equiv \mathbf{e}_{k\lambda}^{(1)} \approx \mathbf{e}_{k\lambda}^{(2)}$. We also assume that the electric dipole moments of the two monomers are parallel such that $\frac{\vec{d_1}}{|d_1|} = \frac{\vec{d_2}}{|d_2|}$. This allows the interaction Hamiltonian to be written

$$H_I^{EM} = \sum_j \left(\sigma_x^{(1)} + \mu\sigma_x^{(2)}\right) \otimes f_j^{(1)}(d_j + d_j^\dagger) \tag{4.12}$$

where

$$\mu \equiv \frac{f_j^{(2)}}{f_j^{(1)}} = \frac{\omega_2(\mathbf{e}_j \cdot \mathbf{d}_2)}{\omega_1(\mathbf{e}_j \cdot \mathbf{d}_1)} = \frac{\omega_2|d_2|}{\omega_1|d_1|}, \tag{4.13}$$

and the polarisation vector notation has been omitted for compactness. By this definition, the system-bath interaction strength is fully characterised by the spectral density

$$J_{EM}(\omega) = \sum_j \left|f_j^{(1)}\right|^2 \delta(\omega - \omega_j), \tag{4.14}$$

which, given Eq. (4.11), leads to the expression

$$J_{EM}(\omega) = \frac{e^2\omega_1^2}{2\epsilon_0 L^3} \sum_{k\lambda} \frac{1}{\omega_k} |\mathbf{e}_{k\lambda} \cdot \mathbf{d}_1|^2 \delta(\omega - \omega_k). \tag{4.15}$$

We now choose a coordinate system such that we may write $|\vec{e}_{k\lambda} \cdot \vec{d}_1|^2 = |\vec{d}_1|^2(1 - |\hat{d} \cdot \hat{k}|) = |\vec{d}_1|^2(1 - \cos^2\theta)$ and take the continuum limit using

$$\sum_{k\lambda} \to L^3/(8\pi^3 c^3) \int_0^\infty \mathrm{d}\omega_k\, \omega_k^2 \int_0^\pi \mathrm{d}\theta \sin\theta \int_0^{2\pi} \mathrm{d}\phi \tag{4.16}$$

and find

$$J_{EM}(\omega) = \frac{\pi}{2} \frac{e^2\omega_1^2|\vec{d}_1|^2}{3\epsilon_0\pi^3 c^3}\omega. \tag{4.17}$$

Rather than input specific dipole information into (4.17), we instead consider molecules with zero-temperature excited state lifetimes $\approx 100ps - 1ns$, which gives a value for spontaneous emission rate ($\Gamma_0 \approx 10^9 - 10^{10}s^{-1}$). We can then express the spectral density in terms of this, $J_{EM}(\omega) = \frac{\Gamma_0\omega}{2\pi\omega_1}$.

Now we have set up the Hamiltonian, we will apply the Collective Coordinate mapping to enable modelling of strongly-coupled phonon environments.

4.1.2 Redfield theory for system-phonon interaction

For many years, the dominant method of studying energy transfer in theoretical chemistry and open-quantum systems has been Redfield theory, in which one expands the electron-phonon interaction to second-order in the coupling-strength and derives a (non-secular) master equation in the Born and Markov approximations for the reduced density matrix of the electronic system. Including optical dissipation therefore amounts to deriving a separate (additive) master equation. In order to ensure complete positivity and trace-preservation of the dynamical map, it is also very common to make the secular approximation at the master equation level to get equations of Lindblad form. These simple forms are also appealing since they can quite easily be incorporated into models in a phenomenological way to introduce quantum noise and thermal relaxation.

Given that, in Redfield theory, we expand to second-order in the coupling strength α_i, we will keep the counter terms in the interaction Hamiltonian and expand them to second-order $H_I^{ph} = \sum_\alpha A_\alpha \otimes B_\alpha + \tilde{\lambda}_\alpha A_\alpha^2$, which means that any shifts they induce emerge from commutators in the master equation, which after moving to the continuum limit has the form:

$$\begin{aligned}\frac{\partial \rho_S(t)}{\partial t} = &-i[H_S, \rho_S(t)] - i\tilde{\lambda}_\alpha \left[\tilde{A}_\alpha^2(t), \rho(0)\right] - \tilde{\lambda}_\alpha^2 \int_0^\infty d\tau \left[\tilde{A}_\alpha^2(t), [\tilde{A}_\alpha^2(t-\tau), \tilde{\rho}_S(t)]\right] \\ &- \sum_\alpha \int_0^\infty d\tau \big([A_\alpha, \tilde{A}_\alpha(-\tau)\rho_S(t)]C_\alpha(\tau) + [\rho_S(t)\tilde{A}_\alpha(-\tau), A_\alpha]C_\alpha(-\tau)\big)\end{aligned} \tag{4.18}$$

where $\tilde{\lambda}_\alpha = \int_0^\infty d\omega J_{ph}^{(\alpha)}(\omega)/\omega$, the system operator for sites 1 and 2 are

$$\tilde{A}_1(t) = \frac{(\eta-\epsilon)}{2\eta}|\varphi_-\rangle\langle\varphi_-| + \frac{(\eta+\epsilon)}{2\eta}|\varphi_+\rangle\langle\varphi_+| + \frac{V}{\eta}\Big(|\varphi_+\rangle\langle\varphi_-|\, e^{i\zeta t} + |\varphi_-\rangle\langle\varphi_+|\, e^{-i\zeta t}\Big) \tag{4.19}$$

$$\tilde{A}_2(t) = \frac{(\eta+\epsilon)}{2\eta}|\varphi_-\rangle\langle\varphi_-| + \frac{(\eta-\epsilon)}{2\eta}|\varphi_+\rangle\langle\varphi_+| - \frac{V}{\eta}\Big(|\varphi_+\rangle\langle\varphi_-|\, e^{i\zeta t} + |\varphi_-\rangle\langle\varphi_+|\, e^{-i\zeta t}\Big) \tag{4.20}$$

and correlation functions are

$$C_\alpha(\tau) = \int_0^\infty d\omega J_{ph}^{(\alpha)}(\omega)\coth\left(\frac{\beta_\alpha\omega}{2}\right)\cos\omega\tau - i\int_0^\infty d\omega J_{ph}^{(\alpha)}(\omega)\sin\omega\tau. \tag{4.21}$$

Making use of (4.19)-(4.21) and (4.18) gives the Redfield master equation:

$$\mathcal{L}_\alpha[\rho_S(t)] = -ic_\alpha[\sigma_\alpha^\dagger\sigma_\alpha, \rho_S(t)] - \sum_\alpha \big([\sigma_\alpha^\dagger\sigma_\alpha, Z_\alpha\rho_S(t)] - [\rho_S(t)Z_\alpha^\dagger, \sigma_\alpha^\dagger\sigma_\alpha]\big) \tag{4.22}$$

where

$$Z_\alpha = \int_0^\infty d\tau \tilde{A}_\alpha(-\tau)C_\alpha(\tau). \tag{4.23}$$

This Born and Markov approximations that have been made in reaching (4.22) mean that

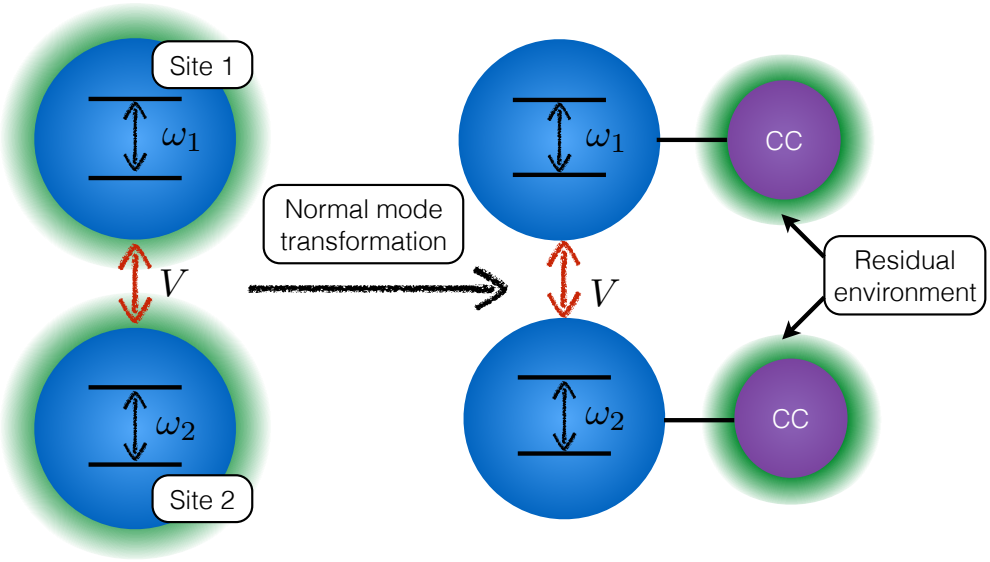

Figure 4.2: Schematic of dimer system before and after the Collective Coordinate mapping. After a normal mode transformation, the sites do not couple directly to the a phonon bath, instead interacting only with the discrete CCs.

it is only valid in the weak-coupling limit, however we will see that it does not give reliable results even within this regime.

4.1.3 CC mapping and quantum master equations

Here we follow the techniques outlined in previous chapters and perform a Collective Coordinate mapping [28, 29, 25] on the electron-phonon interaction Hamiltonian in Equation 4.7. This means that two discrete bosonic modes are incorporated into the system description, which collectively encodes the most salient features of both baths, given by the definition:

$$\lambda_i(a_i^\dagger + a_i) = \sum_k g_{i,k}(b_{i,k}^\dagger + b_{i,k}), \tag{4.24}$$

where λ_i is the coupling of dipole i to the CC of its corresponding bath and a_i are the CC annihilation operators. After the mapping, the system Hamiltonian is expanded as

$$H_S = H_d + \sum_i \delta\omega_i \sigma_i^\dagger \sigma_i - \sum_i \lambda_i \sigma_i^\dagger \sigma_i(\bar{a}_i^\dagger + \bar{a}_i) + \sum_i \Omega_i \bar{a}_i^\dagger \bar{a}_i, \tag{4.25}$$

where we have defined the CC annihilation operators $\bar{a}_1 \equiv I_1 \otimes I_2 \otimes a_1 \otimes I_{CC_2}$ and $\bar{a}_2 \equiv I_1 \otimes I_2 \otimes I_{CC_1} \otimes a_2$ to absorb the total composite Hilbert space. We have also defined the level shifts $\delta\omega_i = \sum_k g_{i,k}^2/\omega_{i,k}$. This leaves the CC oscillator frequencies Ω_i and system-CC coupling strengths λ_i to be defined by the CC mapping and these will depend on the spectral density appropriate for the problem.

Each residual bath is a collection of oscillators, much like in the original frame but with newly defined bosonic operators and dispersion relations

$$H_B^R = \sum_i \sum_k \nu_{i,k} c_{i,k}^\dagger c_{i,k}. \tag{4.26}$$

In the new frame, both of the CCs are coupled bi-linearly to their respective residual baths

$$H_I^R = \sum_i A_i \sum_k f_{i,k}(c_{i,k}^\dagger + c_{i,k}) + \sum_i A_i^2 \sum_k \frac{f_{i,k}^2}{\nu_{i,k}} \tag{4.27}$$

with the system operators being defined as $A_i = \bar{a}_i^\dagger + \bar{a}_i$. We can also define spectral densities for the CC-residual bath interactions $J_R^{(i)}(\omega) = \sum_k f_{i,k}^2 \delta(\omega - \omega_{i,k})$. The second term is an environmentally-induced renormalisation of the bath energies. In this form the total Hamiltonian governing the closed, interacting system and environment dynamics is $H = H_S + H_B^R + H_I^R + H_B^{EM} + H_I^{EM}$.

For the specific case of Lorentzian spectral densities

$$J_{ph}^{(i)}(\omega) = \frac{\alpha_i \Gamma_i \omega_{0,i}^2 \, \omega}{(\omega_{0,i}^2 - \omega^2)^2 + \Gamma_i^2 \omega^2}, \tag{4.28}$$

the mapped parameters in the CC frame are $\lambda_i = \sqrt{\pi \alpha \omega_{0,i}/2}$, $J_R^{(i)}(\omega) = \gamma_i \omega$ with CC-residual bath coupling strength $\gamma_i = \Gamma_i / 2\pi\omega_{0,i}$ and $\Omega_i = \omega_{0,i}$. In the continuum limit $\sum_k \frac{g_k^2}{\omega_k} \to \int_0^\infty J(\omega)/\omega = \pi\alpha_i/2$, so in the mapped frame the energy shift becomes $\delta\omega_i = \lambda_i^2/\Omega_i$. We consider the two residual baths to be kept the same constant temperature $T_R = T_1 = T_2$.

Following the same method as in [25], we derive a master equation under the Born and Markov approximations for the reduced density matrix of the two coupled electronic-vibrational subsystems, such that $\dot{\rho}_s(t) = -i[H_S, \rho_s(t)] + \mathcal{K}_{R_1}[\rho_s(t)] + \mathcal{K}_{R_2}[\rho_s(t)] + \mathcal{K}_{EM}[\rho_s(t)]$, where $\rho(t) = \mathrm{Tr}_R\{\rho_s(t)\}$, this gives

$$\mathcal{K}_{R_j}[\rho_S(t)] = \left[\rho_S(t) Z_j^\dagger, S_j\right] - [S_j, Z_j \rho_S(t)] \tag{4.29}$$

with $S_j = a_j^\dagger + a_j$ and

$$Z_j \approx \sum_{pq} J_R^{(j)}(\xi_{pq}) (\coth\left(\frac{\beta_j \xi_{pq}}{2}\right) + 1) S_{pq}^{(j)} \left|\phi_p\right\rangle\!\left\langle\phi_q\right|. \tag{4.30}$$

Electromagnetic field dissipator

The symmetry of the electronic and phonon Hamiltonians alone means that population is prohibited from leaving and entering the different electronically excited subspaces. The presence of ambient/transverse electromagnetic fields can cause the electronic excitations to spontaneously decay to the ground state as they emit photons. In this study, we are

interested in the effect that high-temperature thermal occupation of electromagnetic fields has on the behaviour of molecular systems, in this case the system can also absorb photons and occupy excited states or decay via stimulated emission.

We will take the thermal occupation of the field to be the blackbody spectrum of the sun, which is approximately 5800K and emits photons with no phase coherence. This incoherent excitation is expected to populate the various energy eigenstates of the dimer system as a classical mixture and to have a much longer time-scale than that of the vibrational coupling.

The Hamiltonian (4.12) is in the form

$$H_I^{EM} = A \otimes B \tag{4.31}$$

with $A = \bar{\sigma}_x^{(1)} + \mu\bar{\sigma}_x^{(2)}$ and $B = \sum_{\mathbf{k}} f_{\mathbf{k}}(b_{\mathbf{k}}^\dagger + b_{j,\mathbf{k}})$. We obtain a quantum master equation in the Schrödinger picture in the manner outlined in previous chapters:

$$\mathcal{K}_{EM}[\rho_S(t)] = -\int_0^\infty d\tau \Big([A, \tilde{A}(-\tau)\rho_S(t)]C(\tau) - [A, \rho_S(t)\tilde{A}(-\tau)]C(-\tau) \Big) \tag{4.32}$$

with autocorrelation function

$$\begin{aligned} C(\tau) &= \sum_k |h_k|^2 \left\langle (b_k^\dagger e^{i\omega_k t} + b_k e^{i\omega_k t})(b_{j,k}^\dagger + b_k) \right\rangle_{\rho_B} \\ &= \sum_k |h_k|^2 ((2\bar{n}_k + 1)\cos\omega_k\tau - i\sin\omega_k\tau) \end{aligned} \tag{4.33}$$

where we have defined the thermal occupation of mode k in bath j by $\bar{n}_k = \left\langle b_k^\dagger b_k \right\rangle = (e^{\beta\omega_k} - 1)^{-1}$, where $\langle\cdot\rangle$ is the expectation value over a thermal state of the electromagnetic field. The autocorrelation function can be written in terms of the spectral density by taking the continuum limit

$$C(\tau) = \int_0^\infty d\omega J(\omega) \left(\coth\left(\frac{\beta\omega}{2}\right)\cos\omega\tau - i\sin\omega\tau \right). \tag{4.34}$$

This permits the ME to be written as

$$\mathcal{K}_{EM}[\rho_S(t)] = [A, \zeta\rho_S(t)] - [\rho_S(t)\zeta, A] \tag{4.35}$$

where

$$\zeta = \int_0^\infty d\tau C(\tau)\tilde{A}(-\tau), \tag{4.36}$$

which can be calculated numerically by expressing the system operator in terms of eigenstates by truncating the Hilbert space of the CC and using

$$\tilde{A}(t) = \sum_{m,n} A_{m,n} e^{i\xi_{mn}t} |\varphi_m\rangle\langle\varphi_n| . \tag{4.37}$$

Bringing this all together yields

$$\zeta = \sum_{m,n} A_{m,n}\Gamma(\xi_{mn})\,|\varphi_m\rangle\langle\varphi_n| \tag{4.38}$$

where the temperature-dependent rates are defined

$$\Gamma(\xi_{mn}) = \int_0^\infty d\tau \int_0^\infty d\omega \big(f_1(\omega)e^{i(\omega-\xi_{mn})\tau} + f_2(\omega)e^{-i(\omega+\xi_{mn})\tau}\big) \tag{4.39}$$

$$\begin{aligned} f_1(\omega) &= \frac{1}{2}J(\omega)(\coth(\beta\omega/2) - 1) \\ f_2(\omega) &= \frac{1}{2}J(\omega)(\coth(\beta\omega/2) + 1). \end{aligned} \tag{4.40}$$

These integrals can be evaluated using the Sokhotski-Plemelj theorem

$$\Gamma(\xi_{mn}) = \begin{cases} \pi f_1(\xi_{mn}) & \text{if } \xi_{mn} > 0, \\ \frac{\pi}{2}\lim\limits_{x\to 0}\big(J(x)\coth\big(\frac{\beta x}{2}\big)\big) & \text{if } \xi_{mn} = 0, \\ \pi f_2(|\xi_{mn}|) & \text{if } \xi_{mn} < 0. \end{cases} \tag{4.41}$$

Additive field approximation

In deriving the optical field dissipator, we moved to the interaction picture $\tilde{H}_I^\perp(t) = U^\dagger(t)H_I^\perp U(t)$ with $U(t) = e^{-iH_S t}e^{-iH_B t}$ using the full augmented system Hamiltonian H_S. Here we will discuss the additive approximation that is often made in calculating the dipole-field dissipator. This amounts to using the bare electronic Hamiltonian when moving into the interaction picture with the unmapped system Hamiltonian $U(t) = e^{-iH_d t}e^{-iH_B t}$. Here H_d should use the bare electronic levels ω_i and not incorporate the phonon-induced level shifts $\Delta\omega_i\sigma^\dagger\sigma_i$.

From Equation 4.8, we can see that the electronic level shifts $\Delta\omega_i$ arise at the Hamiltonian level due to phonon counter terms and are incorporated into the dipole energy scales in the closed evolution and in the derivation of the CC dissipator. In order for the additive approach to be consistent with non-additive in the appropriate regimes, the level shifts should not be included in the Hamiltonian when deriving an optical dissipator. This is so that the bath interactions have no reference to each other and because the energy shifts are cancelled out during diagonalisation, as illustrated in the polaron transformed Hamiltonian 4.47.

The coupling operator $A = \sigma_x^{(1)} + \mu\sigma_x^{(2)}$ for the dimer system is

$$A = |2\rangle\langle XX| + |0\rangle\langle 1| + \mu(|1\rangle\langle XX| + |0\rangle\langle 2|) + h.c \tag{4.42}$$

which in the eigenbasis becomes

$$\begin{aligned} A =& \frac{1}{\sqrt{2\eta}}\big((\sqrt{\eta-\epsilon}+\mu\sqrt{\eta+\epsilon})\,|\nu_+\rangle\langle XX| \\ &-(\sqrt{\eta+\epsilon}-\mu\sqrt{\eta-\epsilon})\,|\nu_-\rangle\langle XX| \\ &+(\sqrt{\eta+\epsilon}+\mu\sqrt{\eta-\epsilon})\,|0\rangle\langle\nu_+| \\ &+(\sqrt{\eta-\epsilon}-\mu\sqrt{\eta+\epsilon})\,|0\rangle\langle\nu_-|\,\big)+h.c. \end{aligned} \tag{4.43}$$

We can transform this operator to the interaction picture with respect to the unperturbed electronic Hamiltonian and decompose it into a sum of eigenoperators such that $A(t) = \sum_\omega A(\omega)e^{-i\omega t} + A^\dagger(\omega)e^{i\omega t}$ given by

$$\begin{aligned} A(\omega_{xx}-\lambda_+) =& \frac{1}{\sqrt{2\eta}}(\sqrt{\eta-\epsilon}+\mu\sqrt{\eta+\epsilon})\,|\nu_+\rangle\langle XX| \\ A(\omega_{xx}-\lambda_-) =& -\frac{1}{\sqrt{2\eta}}(\sqrt{\eta+\epsilon}-\mu\sqrt{\eta-\epsilon})\,|\nu_-\rangle\langle XX| \\ A(\lambda_+) =& \frac{1}{\sqrt{2\eta}}(\sqrt{\eta+\epsilon}+\mu\sqrt{\eta-\epsilon})\,|0\rangle\langle\nu_+| \\ A(\lambda_-) =& \frac{1}{\sqrt{2\eta}}(\sqrt{\eta-\epsilon}-\mu\sqrt{\eta+\epsilon})\,|0\rangle\langle\nu_-|\,. \end{aligned} \tag{4.44}$$

Thus we can calculate $\zeta(t) = \sum_\omega A_\omega\Gamma(-\omega)A(\omega)e^{-i\omega t} + A_\omega^\dagger\Gamma(\omega)A^\dagger(\omega)e^{i\omega t}$, where A_ω corresponds to the matrix element of A corresponding to the bra and ket in the eigenoperator, e.g. $A_{\lambda_+} = \langle 0|\,A\,|\nu_+\rangle$. Note that due to the symmetry of the dipole operator: $A_\omega = A_\omega^\dagger$. Moving back to the interaction picture, we get the non-secular Liouvillian

$$\mathcal{K}_{EM}[\rho_S(t)] = [A, \zeta\rho_S(t)] - \left[\rho_S(t)\zeta^\dagger, A\right] \tag{4.45}$$

where ζ is now additive. This Liouvillian has 128 terms to calculate, many of which will be identically zero due to the overlaps of the eigenoperators. The dipole operator does not couple the populations of $|\nu_+\rangle$ and $|\nu_-\rangle$, but some non-secular terms in the master equation couple populations and coherences of these states together with timescales of $\propto e^{\pm\pi 2\eta t}$ which may be slowly evolving for nearly resonant monomers. One can obtain an equation in Lindblad form by making a further secular approximation in which all terms with time-dependence are discarded, though we only use the non-secular version in this chapter.

4.2 Analysis

Now I will take the above models and analyse their behaviour. Firstly, I determine whether removing the doubly-excited state $|XX\rangle$, which turns the model described by (4.3) into a three-level system (3LS), is a safe approximation to make. I do this by comparing steady-

state observables in the 4LS and 3LS and seeing how their qualitative behaviour changes as a function of phonon bath properties and biexciton Coulomb repulsion ω_{xx}.

Following this, the next few sections are primarily concerned with taking the non-perturbative model we derived above and testing the hypotheses that increasing the phonon coupling causes:

1. faster decay rates of population from bright to dark states

2. larger steady-state population of the dark state,

which are properties that appear in weak-coupling treatments and are posited to increase the output of biologically-inspired photocells [121, 122]. In studying the short-time ($\sim$ ps) population relaxation due to the phonon environments we find that, while larger phonon couplings do cause faster decay rates, they also cause a decrease in dark state population.

In order to gain some insight into the (perhaps surprising) dynamical evolution, I explore the effects of making a single-mode polaron transformation on the two monomer-CC couplings. This transformation elucidates the interplay between the vibronic coupling and the dipole-dipole coupling and ultimately allows us to approximate values for the minimum energies in the bright and dark manifold. To a first approximation, the analytical eigenenergies show that the vibronic coupling actually suppresses the excitonic coupling, which effectively pushes the two manifolds closer together. These energy shifts are seen in the exact diagonalisation of the (CC-dressed) augmented system Hamiltonian (4.46), which agree with the approximate polaronic values relatively well for sufficiently weak excitonic couplings.

I then move onto long-time behaviour of the full CC model under the influence of incoherent optical driving, analogous to solar illumination, where the effects of optical bath dissipation become significant. My results show a significant difference in the qualitative phonon-coupling dependence of the CC and Redfield theories, even in the weak-coupling regime. By deriving an analytical model for the predicted populations of the full model in a restricted regime, I determine that the underlying cause of these qualitative differences is the closing of the energy gap between vibronic manifolds due to phonon renormalisation.

Finally, I move onto studying electronic coherences of the dimer system, distinguishing between site-basis and eigenbasis coherences and highlighting their physical importance.

4.2.1 Single-excitation approximation

One of the most common approximations that is made in studying light-harvesting and energy transfer in molecular systems is to look at only the single excitation subspace. To account for optical dissipation, the state of zero excitations must also be included, so it is a three-level approximation. For dimers, this amounts to removing the doubly-excited state from the Hilbert space, on the basis that it is not appreciably occupied under natural illumination conditions. In Figure 4.3, it can be seen that approximating the electronic levels of the dimer as a three-level system does not change its qualitative behaviour in this

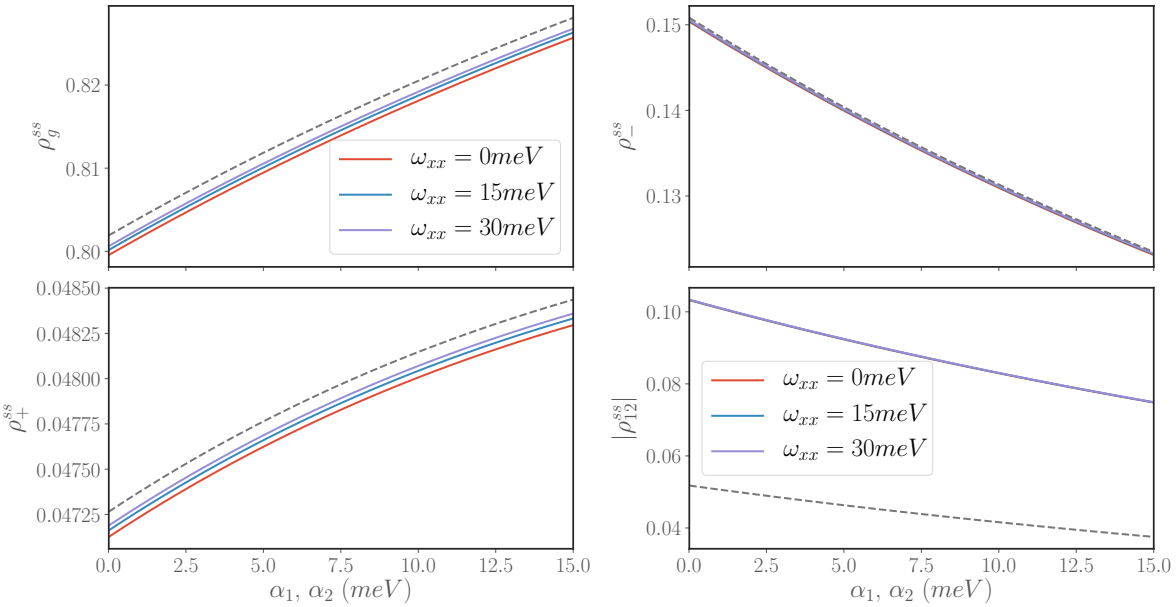

Figure 4.3: Qualitative agreement between the full four-level dimer system (grey dashed) with the three-level approximation for steady-state system observables (solid). System parameters: $\omega_2 = 1.4$eV, $\epsilon = 0$meV, $V = 15$meV. Overdamped phonon baths parameters: $\omega_c = \eta/2$, $\omega_0^{(1)} = \omega_0^{(2)} = 5\eta$, $T_R = 300$K. EM bath parameters: $\Gamma_0 = 1ns^{-1}$, $T_{EM} = 5800$K.

regime where $T_R = 300$K and $\epsilon = 0$. As biexciton repulsion ω_{xx} increases, the three-level approximation becomes more valid, exponentially converging on the four-level theory as $\omega_{xx} \to \infty$. The degree of this agreement is put into perspective in figure 4.4, where the excitonic state populations are plotted on the same axes and the 4LS (solid) and 3LS (dashed) theories are virtually indistinguishable.

Regardless of the parameter regime, the net effect of the three-level approximation is an decrease in total excited state population and smaller inter-site coherence. Given then that it is a safe assumption and that it reduces the complexity and computational requirements of the model considerably, we will continue in the three-level approximation. Therefore the system Hamiltonian becomes

$$H_S = \omega_1' \left|1\right\rangle\!\left\langle 1\right| + \omega_2' \left|2\right\rangle\!\left\langle 2\right| + V(\left|1\right\rangle\!\left\langle 2\right| + \left|2\right\rangle\!\left\langle 1\right|) - \sum_i \lambda_i \left|i\right\rangle\!\left\langle i\right| (\bar{a}_i^\dagger + \bar{a}_i) + \sum_i \Omega_i \bar{a}_i^\dagger \bar{a}_i \qquad (4.46)$$

where $\omega_i' = \omega_i + \delta\omega_i$ for $i = 1, 2$.

4.2.2 Phonon-induced renormalisation of dipole-dipole coupling

After removing the doubly-excited state, we are still left with a model which has several interactions, occurring on a variety of timescales, and we have little intuition about its internal behaviour. We can gain some insight into the augmented system Hamiltonian (4.25) by performing a single-mode polaron transformation on each of the collective coordinates, such

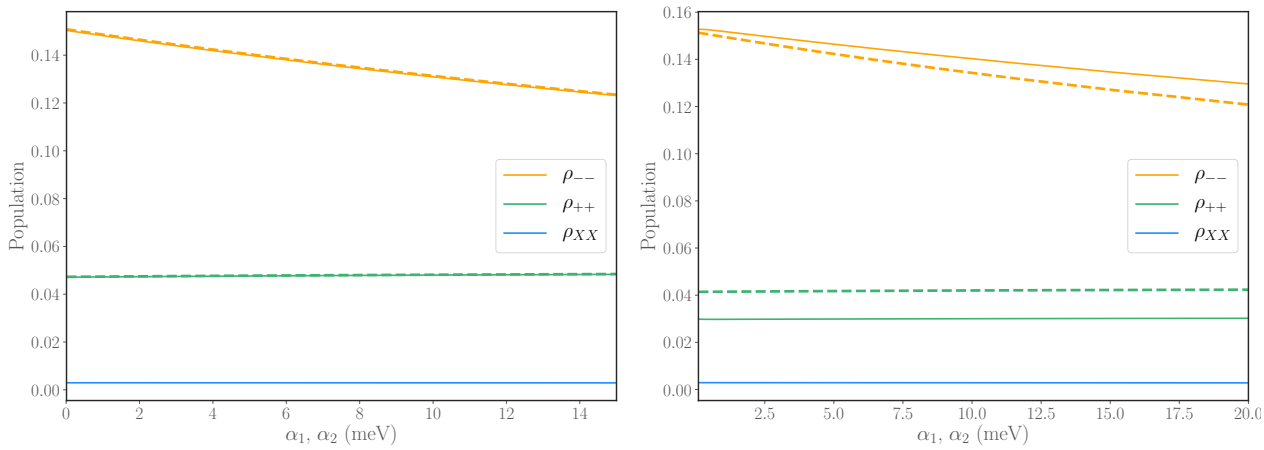

Figure 4.4: Agreement of 4LS (solid) and 3LS (dashed)models (same populations as figure 4.3). Left: $\epsilon = 0$meV and Right: $\epsilon = 15$meV. System parameters: $\omega_2 = 1.4$eV, $V = 15$meV. Overdamped phonon baths parameters: $\omega_c = \eta/2$, $\omega_0^{(1)} = \omega_0^{(2)} = 5\eta$, $T_R = 300$K. EM bath parameters: $\Gamma_0 = 1ns^{-1}$, $T_{EM} = 5800$K.

that $H' = U_1^\dagger U_2^\dagger H U_2 U_1$ where $U_i = \exp\left(\frac{\lambda_i}{\Omega_i}\sigma_i^\dagger\sigma_i(a_i^\dagger - a_i)\right)$. In the three-level approximation this becomes $U_i = |0\rangle\langle 0| + |i\rangle\langle i|\, D_i$ with displacement operators $D_i = \exp\left(\frac{\lambda_i}{\Omega_i}(a^\dagger - a)\right)$. Applying this to the total Hamiltonian mixes the electronic and vibrational subsystems, with the new *system* Hamiltonian part given by

$$H_S' = \omega_1 |1\rangle\langle 1| + \omega_2 |2\rangle\langle 2| + V(|1\rangle\langle 2|\, D_1^\dagger D_2 + |2\rangle\langle 1|\, D_2^\dagger D_1) + \Omega_1 a_1^\dagger a_1 + \Omega_2 a_2^\dagger a_2. \tag{4.47}$$

We can see from (4.47) that the polaron transformation has removes the TLS-CC couplings from the augmented system Hamiltonian by displacing the equilibrium positions of the excited states to the origin, this in turn makes the phonon-influence on excitonic coupling explicit. Here the polaron shift to the monomer energies also exactly cancelled out the counter-term in the original Hamiltonian $\omega_i = \omega_i' - \lambda_i^2/\Omega_i$.

The polaron transformed model is still not exactly solvable, due to the mixing of electron-vibrational subsystems via the non-linear interaction term. In order to investigate how the eigenstates of the coupled system are influenced by the phonon coupling, we can treat this as a perturbation and expand to first order in V, but as a first approximation to the energy of the ground vibrational states in the single-excitation subspace we can (naively) take an ansatz $|\pm, 0, 0\rangle$ and directly calculate the eigenenergy of this state $\varphi_0^\pm = \langle \pm, 0, 0|\, H_S' \,|\pm, 0, 0\rangle$. The justification is that for small enough V, this state should be approximately accurate, since the superposition states have zero displacement. Using this ansatz gives the renormalised excitonic energies:

$$\varphi_0^\pm = \frac{\omega_1 + \omega_2}{2} \pm \frac{\epsilon^2 + 4V^2 B_1 B_2}{2\eta} \tag{4.48}$$

where $B_i = \langle 0|\, D_i \,|0\rangle = \langle 0|f_i\rangle = e^{-f_i^2/2}$, where $f_i = \lambda_i/\Omega_i$ is the equilibrium displacement

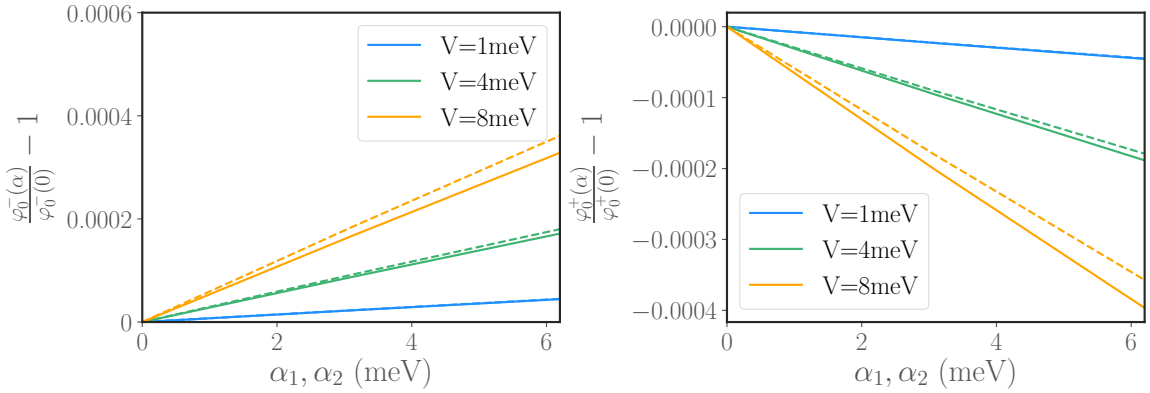

Figure 4.5: Comparison of analytic vibronic energy levels as given by Eq. (4.48) (dashed) and numerically exact (solid) values. The two approaches agree at weak dipole-dipole coupling and/or weak phonon coupling. All energies have been normalised by their bare electronic value.

of the CC in the absence of excitonic coupling. We can see that the B_i factors effectively suppress the excitonic coupling between the two monomers. This suppression increases as a function of phonon-coupling strength, bringing the dark and bright manifolds closer together. If we relabel the last term in (4.48) as $\eta' = \frac{\epsilon^2+4V^2B_1B_2}{\eta}$, we can see that this eigenvalue has the exact same form as the bare electronic version in (4.5), $\varphi_0^{\pm}(\alpha) = \omega_2 + \frac{\epsilon \pm \eta'(\alpha)}{2}$, where we have made the phonon-coupling dependence explicit for convenience.

In Figure 4.5 we compare the analytical eigenvalues $\varphi_0^{\pm}(\alpha)$ to the lowest vibronic eigenstate calculated through exact numerical diagonalisation of (4.46). Note, these eigenvalues are normalised to zero against the $\varphi_0^{\pm}(0)$ values. We can see that the two methods agree for sufficiently small dipole-dipole and/or phonon couplings. This indicates that we can intuitively understand the low-energy eigenstates on the single-excitation manifolds as similar to the phonon-free counterparts $\lambda_{\pm}$ but with suppressed V. As we will see in later sections, the distance between these low-energy eigenstates are important in understanding the qualitative behaviour of the CC model.

4.2.3 Population dynamics

In Figure 4.6 (left) short-time dynamics of bright (dashed lines) and dark state (solid lines) are shown, for the dimer system with overdamped Drude-Lorentz spectral densities (right). The system is initialised in the bright state and we set $T_{EM} = T_{PH} = 300$K. Here we can see that the phonon dissipation causes rapid electronic population redistribution, with decay rates increasing with coupling strength α. Along with an increase in decay rate, there is a decline in dark-state population, which indicates that the suppression of the dipole-dipole coupling and the resultant upward shift of the dark-state energy, as discussed in the previous section, is significant. In the approximate model (4.48), the phonon-renormalisation shifts have exponential dependence on the relative displacement of the manifolds, which in this

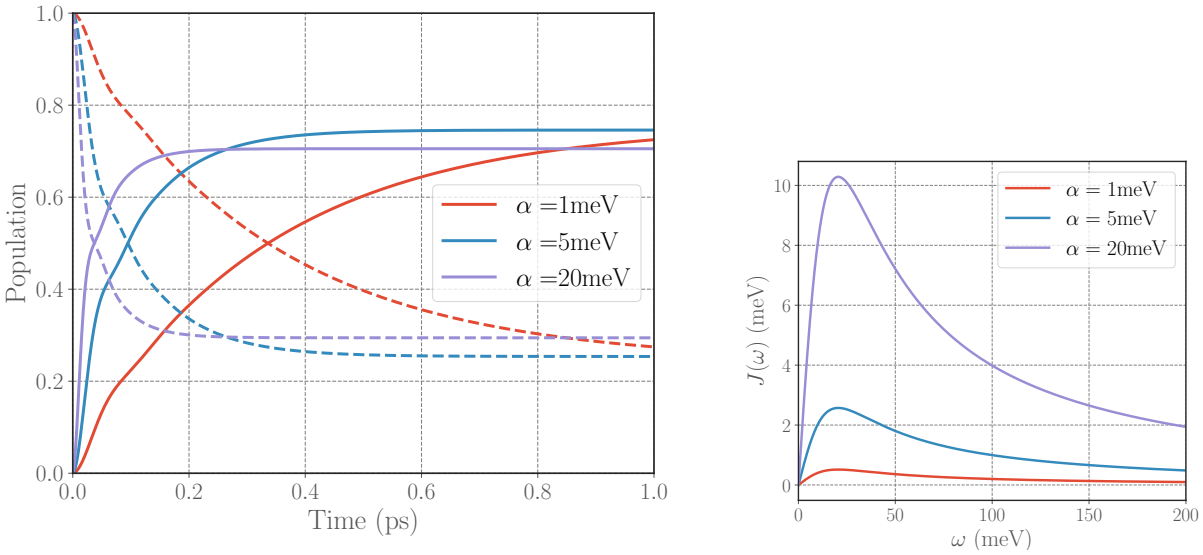

Figure 4.6: Left: Short-time dynamics of bright (dashed lines) and dark (solid lines) state populations at different phonon coupling strengths. Right: Corresponding phonon spectral densities. Parameters: $\epsilon = 0$meV and $V = 15$meV, which give and excitonic energy gap $\eta \sim 33.5$meV. Phonon bath cutoff $\omega_c = \eta/2$, with $\omega_{0_1} = \omega_{0_2} = 5\eta$. We take $T_R = T_{EM} = 300$K, though the optical excitation has no significant effect on this timescale.

case must be more significant than the linear increase in the decay rate due to the phonon spectral density (4.28). Ultimately, this means that even though increasing phonon-coupling causes the underlying phonon dissipation to redistribute electronic populations to the dark-state more quickly, it becomes less energetically favourable for population to remain there. This may be a problem for dark-state protection, since it may lead to increased population to the bright state, which enhances radiative decay of absorbed electronic excitations.

In figure 4.7, we compare the short-time bright-state population dynamics of CC and Redfield theories for zero-bias (left) and $\epsilon = V = 15$meV. Redfield theory tends to over-estimate the bright state decay rates and it predicts that the populations relax to the same quasi-equilibrium distribution in the zero-bias case regardless of phonon-coupling strength. In both the biased and unbiased case, Redfield theory does not account for the oscillations in the dynamics. The fact that they increase in magnitude at larger phonon-couplings indicates that these oscillations are mediated by the non-Markovian phonon environment.

4.2.4 Steady-state populations

So far we have analysed the effect of the 3LS approximation on the long-time behaviour and we have also seen how phonon coupling affects the equilibration of populations on short times. Now we will take a deeper look at the steady state behaviour of the 3LS dimer model and try to understand how it is influenced by the phonon-interactions. We will see that the CC and Redfield approaches predicts markedly different qualitative behaviour and attempts

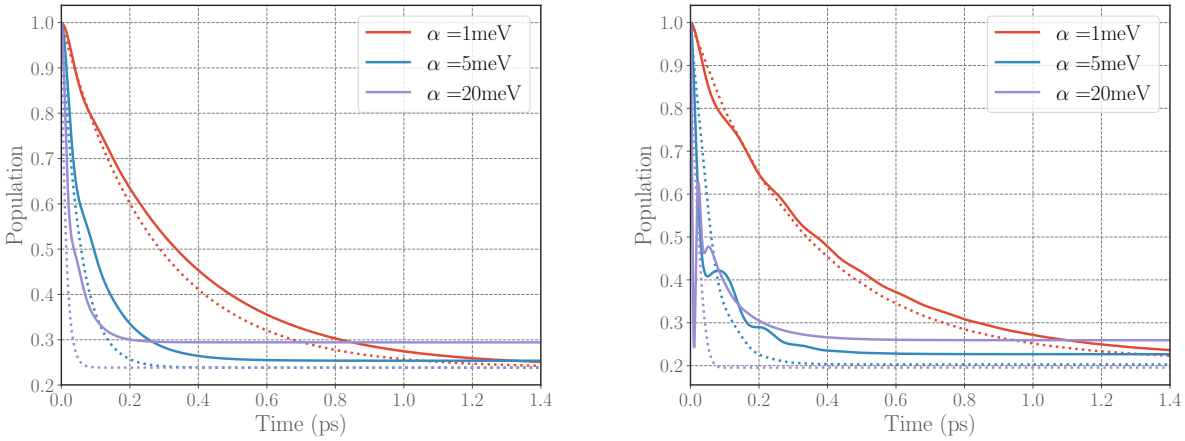

Figure 4.7: Short-time dynamics of dark state population for CC (solid lines) and Redfield (dashed lines) theories. $\epsilon = 0$meV and $V = 15$meV, which give and excitonic energy gap $\eta \sim 33.5$meV. Phonon bath cutoff $\omega_c = \eta/2$, with $\omega_{0_1} = \omega_{0_2} = 5\eta$. We take $T_R = T_{EM} = 300$K, though the optical excitation has no significant effect on this timescale.

will be made to explain these differences with a simple model based on rate equations.

From Figure 4.3, we have already seen that dark state population decreases as a function of coupling strength to broad Drude-Lorentz phonon bath environments. Figure 4.8 shows various steady-state expectation values predicted by the CC and Redfield theories for a similar parameter regime. In the upper-right figure we can see that the weak phonon-coupling approximation leads to a phonon-induced enhancement of dark-state population, in contrast to the CCME, which shows a steady decline in the same quantity. This enhancement of dark state population in the weak-coupling case has been seen in various theoretical studies [121, 69, 122, 126], and is attributed to the enhancement of non-radiative bright to dark transition rates through an increase in phonon coupling. This does not qualitatively agree with the CCME approach, which consistently shows a decrease in dark state population across all feasible parameter regimes.

The ground and bright states seem to be energetically favoured over the dark state, with all three eigenstate populations having a roughly linear dependence on α. We can get an idea of this linear-dependence by restating the analytical eigenenergies (4.48) in terms of α, such that $B_1 = B_2 = e^{-\pi\alpha/4\omega_0}$. For $\frac{\pi\alpha}{2} \ll 2\omega_0$ the change in the energy gap between the dark and bright vibronic manifolds will be roughly linear, which is approximately valid for this Drude-Lorentz spectral density, since $\omega_0 = 10\eta$ and $\alpha < \eta$.

In figure 4.9 we study the zero-bias (homodimer) case, we also find the surprising result that the Redfield theory does not predict any dark-state population enhancement for homodimers, an effect which appears to be robust across the range of parameters we have simulated. The CCME gives quite similar qualitative behaviour to the biased case, except for in the magnitude of eigenstate coherences which shall be discussed later.

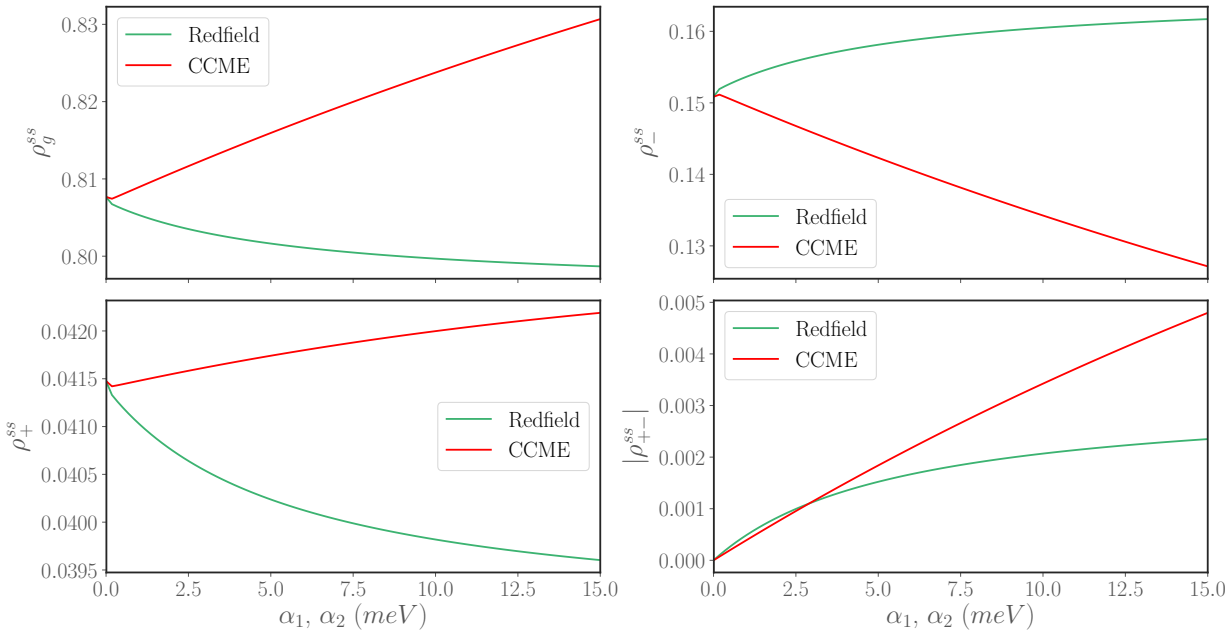

Figure 4.8: Heterodimer comparison between Redfield and Collective Coordinate theories for steady-state populations and eigenstate coherences (abs. value) of the 3LS. The system parameters are $\epsilon = 15$meV and $V = 15$meV, with excitonic energy gap $\eta \sim 33.5$meV. Phonon bath cutoff $\omega_c = \eta/2$, with $\omega_{0_1} = \omega_{0_2} = 5\eta$, $T_R = 300$K and optical bath $T_{EM} = 5800$K.

Analytical model for populations

In order to fully understand the disparities between strong-coupling and Redfield theory, we simplify the population transfer to a simple three level system, such that we have equations of motion for diagonal density matrix elements:

$$\dot{\rho}_+(t) = \Gamma_{g+}\rho_g + \Gamma_{-+}\rho_- - (\Gamma_{+-} + \Gamma_{+g})\rho_+ \tag{4.49}$$

$$\dot{\rho}_-(t) = \Gamma_{g-}\rho_g + \Gamma_{+-}\rho_+ - (\Gamma_{-g} + \Gamma_{-+})\rho_- \tag{4.50}$$

$$\dot{\rho}_g(t) = \Gamma_{-g}\rho_- + \Gamma_{+g}\rho_+ - (\Gamma_{g+} + \Gamma_{g-})\rho_g \tag{4.51}$$

where Γ_{ij} are transitions from $i \to j$ and time arguments on the right-hand side have been made implicit for clarity. Since we are primarily interested in steady-state behaviour, specifically of the relationship between dark and ground state populations, we will set $\rho_i^{ss} \equiv \dot{\rho}_i(\infty) = 0$ and solve for ρ_-^{ss}/ρ_g^{ss}:

$$R_P \equiv \frac{\rho_-^{ss}}{\rho_g^{ss}} = \frac{\Gamma_{g-}}{T_-} + \frac{\Gamma_{+-}\Gamma_{g+}}{T_-(\Gamma_{+-} + \Gamma_{+g})} \tag{4.52}$$

where

$$T_- = \Gamma_{-g} + \Gamma_{-+}\left[1 - \frac{\Gamma_{+-}}{\Gamma_{+-} + \Gamma_{+g}}\right], \tag{4.53}$$

which is a measure of the rate of population decay *out of* the dark state.

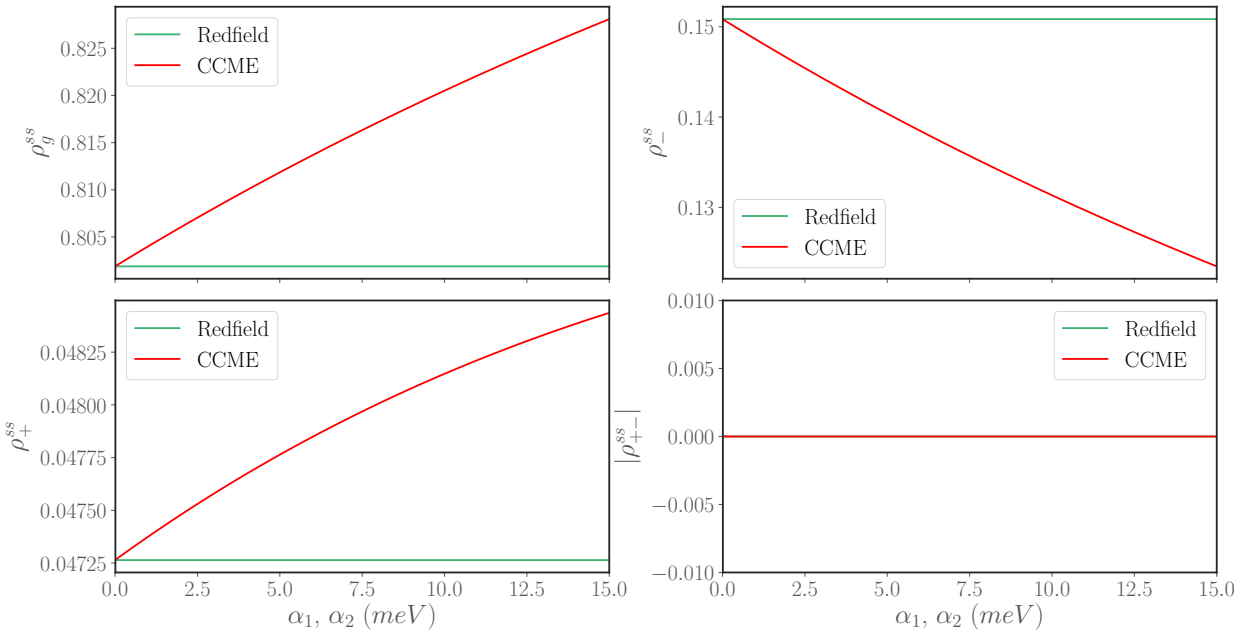

Figure 4.9: Homodimer comparison between Redfield and Collective Coordinate theories for steady-state populations and eigenstate coherences (abs. value) of the 3LS. The system parameters are $\epsilon = 0$meV and $V = 15$meV, with excitonic energy gap $\eta \sim 33.5$meV. Phonon bath cutoff $\omega_c = \eta/2$, with $\omega_{0_1} = \omega_{0_2} = 5\eta$, $T_R = 300$K and optical bath $T_{EM} = 5800$K.

Now we have found a simple analytical expression for the steady-state population, we need to find suitable rates to use. For the transition rates from an initial $i \in \{+, -\}$ manifold and the ground manifold g, as well as the rate from the ground g to some final manifold $f \in \{+, -\}$, we take a Fermi's golden rule-like model from the exact eigenstates of H_S:

$$\Gamma_{ig} = \sum_{nm} p_m \left|\left\langle \varphi_n^{(g)} \right| A_{EM} \left|\varphi_m^{(i)}\right\rangle\right|^2 J_{EM}(\varphi_n^{(g)} - \varphi_m^{(i)}) N(\varphi_n^{(g)} - \varphi_m^{(i)}) \tag{4.54}$$

$$\Gamma_{gf} = \sum_{nm} p_m \left|\left\langle \varphi_n^{(f)} \right| A_{EM} \left|\varphi_m^{(g)}\right\rangle\right|^2 J_{EM}(\varphi_n^{(f)} - \varphi_m^{(g)}) (N(\varphi_n^{(f)} - \varphi_m^{(g)}) + 1) \tag{4.55}$$

where $\left|\varphi_n^{(\nu)}\right\rangle$ corresponds to the nth lowest eigenstate on the manifold $\nu \in \{+, -\}$ with energy φ_n^{ν} and for non-adiabatic phonon-induced transitions we simply take:

$$\Gamma_{-+} = \sum_{j=1,2} \sum_{n} \left|\left\langle \varphi_n^{(+)} \right| A_j \left|\varphi_0^{(-)}\right\rangle\right|^2 J_R^{(j)}(\varphi_n^{(+)} - \varphi_m^{(-)}) N_j(\varphi_n^{(+)} - \varphi_m^{(-)}) \tag{4.56}$$

$$\Gamma_{+-} = \sum_{n} \left|\left\langle \varphi_n^{(-)} \right| A_j \left|\varphi_0^{(+)}\right\rangle\right|^2 J_R^{(j)}(\varphi_n^{(-)} - \varphi_m^{(+)}) (N_j(\varphi_n^{(-)} - \varphi_m^{(+)}) + 1). \tag{4.57}$$

Since for the overdamped Drude-Lorentz spectral densities we use $\Omega_i/k_B T_i \approx 6$, we assume that excitations are localised into the lowest vibronic level on a manifold, before being transferred to the other excitonic state. This is equivalent to taking $p_0 = 1$ in equation (4.54), although we could take a thermal distribution which may improve agreement.

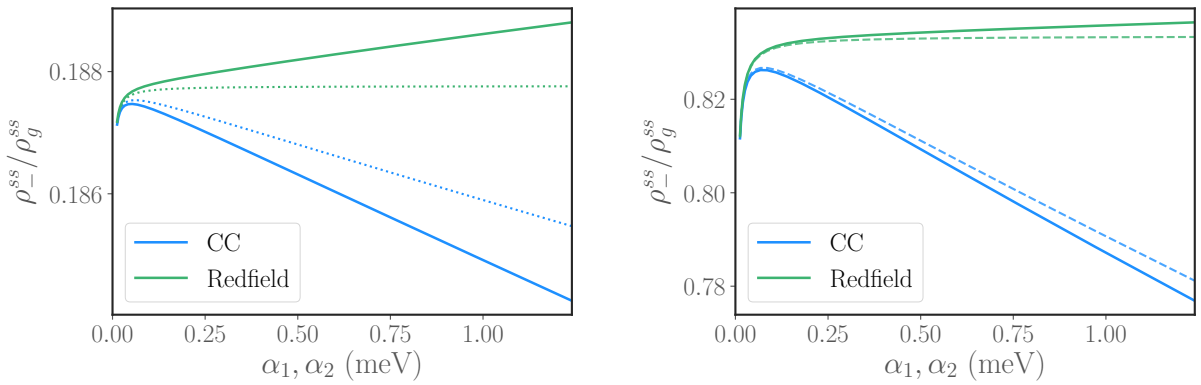

Figure 4.10: Population ratio comparison of master equation treatments (solid) and approximate rate models (dotted). $\epsilon = 15$meV, $V = 15$meV. Left: $T_R = 300$K. Right: $T_R = 101K$. Remaining parameters $\omega_c = \eta/2$, $T_R = 300$K and optical bath $T_{EM} = 5800$K.

We can also approximate Redfield theory rates in a similar manner, using the exact same form as (4.54), but since there are no vibronic manifolds we just use the bare electronic eigenstates $\{|0\rangle, |\nu_-\rangle, |\nu_+\rangle\}$. We now do the same for the phonon rates (4.56) but we also substitute the residual bath for the unmapped spectral density $J_R^{(j)}(\omega) \to J_{ph}^{(j)}(\omega)$.

In Figure 4.10, we plot the population ratio R_P for the full CCME theory (solid) and the rate model (dashed) for $T = 300$K (left) and $T = 101K$ (right). We see that although there is some disagreement at higher-temperature, the rate model works well for $T = 101K$ and shows reasonable qualitative agreement in both regimes. The CC-mapped rate model continues to become more accurate as the temperature decreases below $T = 101K$ but Redfield theory is not suited to low-temperatures and can become unstable and unphysical. From figure 4.10 (right), we can also see that decreasing the temperature has dramatically increased the dark-state population. This occurs because excitations are increasingly localised in the minimum of the dark state, which has a suppressed dipole moment. Being localised in a fewer vibronic states also reduces the number of decay pathways there are to the ground state.

The optical rates as defined in (4.54) are independent of phonon-coupling within this parameter range, so the behaviour of the rate models are dominated by Γ_{+-} and Γ_{-+}. From Fig. 4.11 (left) it seems that the CC and Redfield rates are quite similar with both increasing as a function α. However, in Fig. 4.11 (right) we can see that the ratio $\frac{\Gamma_{+-}}{\Gamma_{-+}}$ of the Redfield rates is actually flat across this entire parameter regime, consistent with detailed balance, whereas the ratio of the CC rates has a negative linear slope. Since $\frac{\Gamma_{+-}}{\Gamma_{-+}}$ is a measure of how much the *downward* decay from bright to dark states dominates over the *upward* re-excitations, it seems likely that this α-dependence determines the qualitative behaviour of each model.

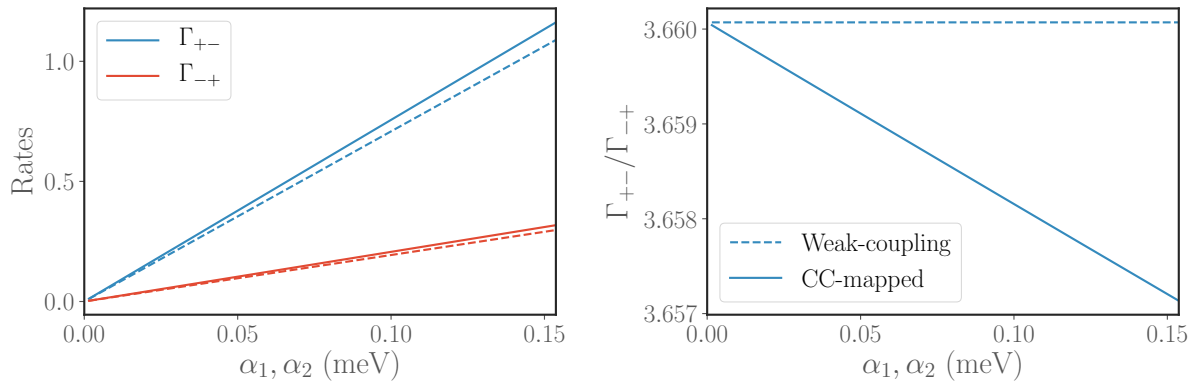

Figure 4.11: Left: Approximate rates corresponding to Figure 4.10 for CC (solid) and Redfield (dashed) theories. Right: Ratio of phonon rates, Γ_{+-}/Γ_{-+}. $\epsilon = 15$meV, $V = 15$meV. Remaining parameters: $\omega_c = \eta/2$, $T_R = 300$K and optical bath $T_{EM} = 5800$K.

Temperature, bias and environmental non-additivity

In Figure 4.12 we investigate the temperature and bias dependence of steady-state observables further, setting $\alpha = 10$meV and $V = 15$meV. Firstly, we can see that low phonon temperatures generally lead to more population in the excited manifolds, as outlined above. For small bias, excitations are more delocalised across the two monomers, which also leads to higher $|\rho_{12}^{ss}|$ and larger dark state populations. As phonon temperatures increase, the coherence that gives rise to the eigenstates is destroyed and population can be more readily excited across the gap between dark and bright manifolds.

In the figures 4.13, we have plotted the eigenstate populations as a function of bias and for increasing phonon-couplings where $T_R = 300$K and $V = 15$meV. The dashed lines indicate that the additive electromagnetic field dissipator has been used in calculating the dynamics. As we can see, the dark state population is actually increasing as a function of bias in this case, since the thermal energy of the phonons is large enough to overcome the unbiased excitonic gap with this dipole-dipole coupling. Increasing the bias then increase the bright state energy which makes it favourable for population to reside in the ground and dark states, with the energy of the latter also decreasing.

Of particular note is the effect that non-additivity has on the populations at stronger system-bath couplings. We can see that the additive approximation still leads to a reduction in dark-state population for increasing phonon-coupling, although slightly less pronounced. The additive theory assumes that the photon emission of the dimer is independent of the phonon coupling, however as we have discussed the CC-dressed eigenstructure of the dimer is still taken account of in the phonon dissipation and the unitary dynamics. Since the coupling to the optical field is much smaller than to the phonon environment, the CC model is dominated by the eigenstate-dressing and population relaxation due to phonons, regardless of whether the additive approximation is made. This also means that non-additivity is a less prominent feature the dimer than in the case of the monomer, since phonon dissipation now

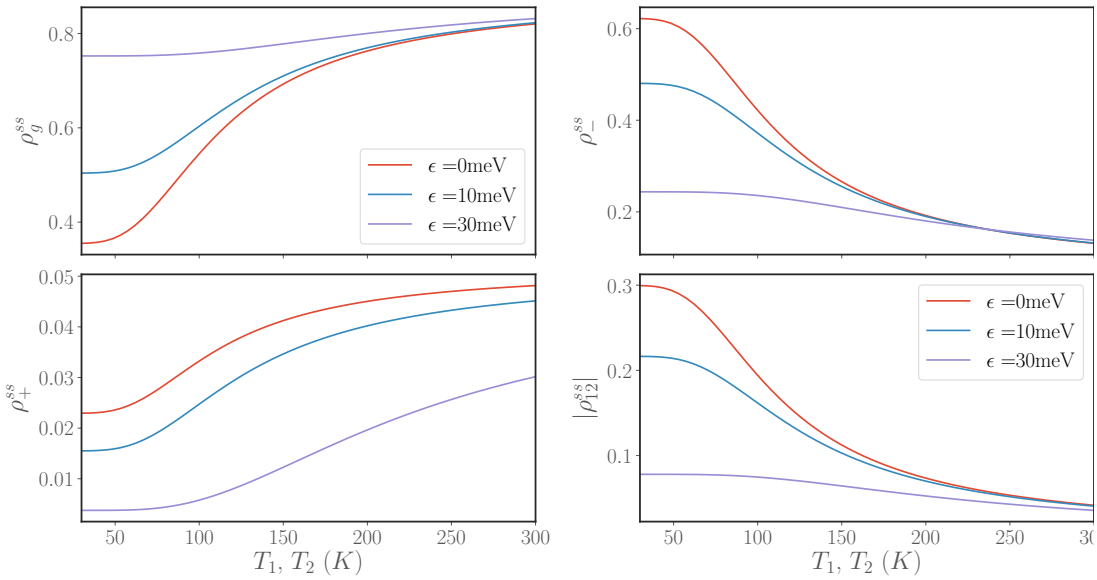

Figure 4.12: Dependence of populations and coherences on bias and phonon temperature. Here $\alpha = 10$meV, $V = 15$meV. Remaining parameters: $\omega_c = \eta/2$, $T_R = 300$K and optical bath $T_{EM} = 5800$K.

has a direct impact on electronic populations.

At larger phonon-couplings, non-additive effects do start to have a significant impact on the steady-state distributions of eigenstate populations, causing the dark-state population to decrease. This is partly due to the linear (Ohmic) spectral density we used for the electromagnetic field interaction, which was shown to lead to reductions in excited state populations for the monomer. This effect was specifically to do with how the displacements affect the optical transition frequencies, which subsequently changes equilibrium thermal populations and system-field interaction strengths. Population that is trapped in the dark state of the dimer will effectively act like a monomer, which means that the same deleterious non-additive effects will occur here.

In addition to the non-additive insights from the monomer, there is vibrational mixing of the electronic dimer eigenstates. This causes states more localised on the dark state manifold to gain some characteristics of the bright state, such as an enhanced dipole moment. This makes the manifold of dark states more emissive than in the bare electronic counterpart, ultimately degrading the ability for population to be trapped there. Similarly, the dipole moment of the bright state decreases, which we can directly in figure 4.13 (right), where populations are actually enhanced by the inclusion of phonons for zero-bias when $\alpha = 30$meV. This is the opposite behaviour of the simple monomer case, indicating that the bright and dark state are not behaving like monomers in this regime due to the electronic delocalisation $V >> \epsilon$. This change to the emission properties of the dimer is only incorporated into a non-additive theory, since the additive approximation ignores the vibronic eigenstructure in the optical dissipator.

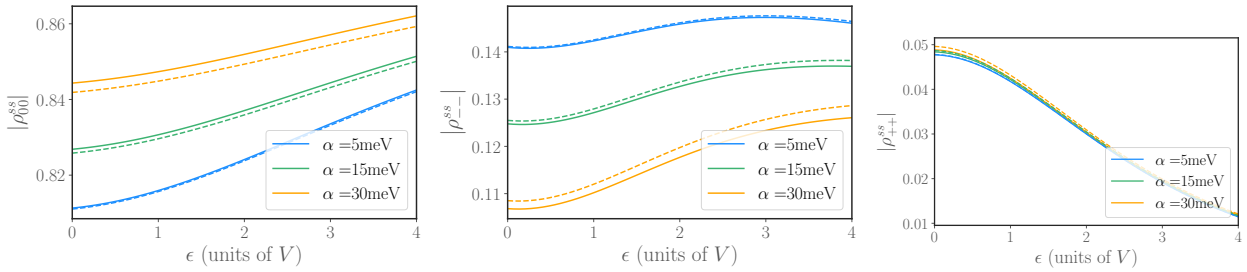

Figure 4.13: Left: Ground state population. Middle: Dark state population. Right: Bright state population, as a function of bias ϵ, for various coupling strengths. Dashed lines indicate the additive electromagnetic theory. Remaining parameters: $V = 15$meV, $\omega_c = \eta/2$, $T_R = 300$K and optical bath $T_{EM} = 5800$K.

4.2.5 A deeper look at coherence

Here we will try to interpret the eigenstate coherences seen in the CC treatment of the dimer. The single excitation subspace of the electronic Hamiltonian is

$$H_d = \omega_1 |1\rangle\langle 1| + \omega_1 |2\rangle\langle 2| + V(|1\rangle\langle 2| + |2\rangle\langle 1|), \tag{4.58}$$

where $\omega_1 \geq \omega_2$. We can define a current operator from state $|2\rangle$ to state $|1\rangle$ as

$$\begin{aligned} j = \dot{N}_1 &= -i[N_1, H] = -i[|1\rangle\langle 1|, H] \\ &= -iV(|1\rangle\langle 2| - |2\rangle\langle 1|) = V\sigma_y \end{aligned} \tag{4.59}$$

where $\sigma_y = i(|2\rangle\langle 1| - |1\rangle\langle 2|)$. The expectation values of this are

$$V \operatorname{Tr}\{\rho\sigma_y\} = iV(\rho_{21} - \rho_{12}) = iV(\rho_{21} - \rho^*_{21}) = -2V \operatorname{Im}(\rho_{21}) \tag{4.60}$$

which means that a positive imaginary part of site basis coherence is equivalent to a particle current from state $|2\rangle$ to state $|1\rangle$. Furthermore, it is straightforward to show that $|\psi_-\rangle\langle\psi_+| - |\psi_+\rangle\langle\psi_-| = -i\sigma_y$, which after taking the expectation value one finds

$$\langle j\rangle = 2V \operatorname{Im}\{\langle|-\rangle\langle+|\rangle\} = 2V \operatorname{Im}\{\langle|2\rangle\langle 1|\rangle\}. \tag{4.61}$$

This states that the imaginary part of the coherence is the same in both the excitonic basis and the site basis and is proportional to the particle current from excited to ground state. Now we can investigate the real part of the exciton coherence:

$$|\psi_-\rangle\langle\psi_+| + |\psi_+\rangle\langle\psi_-| = \frac{2V}{\eta}(|1\rangle\langle 1| - |2\rangle\langle 2|) - \frac{\epsilon}{2\eta}(|2\rangle\langle 1| + |1\rangle\langle 2|). \tag{4.62}$$

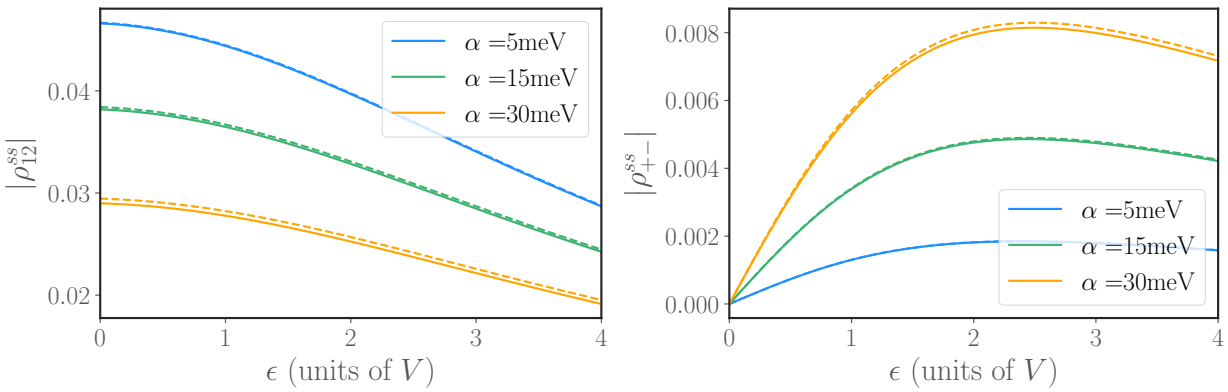

Figure 4.14: Left: Site coherence as a function of bias ϵ, for various coupling strengths. Right: Excitonic coherence as a function of bias ϵ, for various coupling strengths. Remaining parameters: $V = 15\text{meV}$, $\omega_c = \eta/2$, $T_R = 300\text{K}$ and optical bath $T_{EM} = 5800\text{K}$.

$$|\psi_-\rangle\langle\psi_+| + |\psi_+\rangle\langle\psi_-| \to \begin{cases} -\sigma_x, & \text{if} \quad V = 0 \quad \text{or} \quad \epsilon \to +\infty, \\ \sigma_z, & \text{if} \quad \epsilon = 0 \quad \text{or} \quad V \to +\infty, \\ \frac{1}{\sqrt{2}}\sigma_z - \frac{1}{\sqrt{2}}\sigma_x, & \text{when} \quad \epsilon = 2V. \end{cases} \tag{4.63}$$

This means that the real part of the eigenstate coherence - a measure of how delocalised the states are - is a mixture of population imbalance and real coherence in the site basis. When $\epsilon \gg V$, the eigenbasis looks like the site basis. For a homodimer where $\epsilon = 0$, the eigenstate coherence depends entirely on the site population imbalance, which will be zero at equilibrium. We can see in figure 4.14 (right) that eigenstate coherence always vanishes at zero bias. Larger biases tend to increase excitonic coherence, up to the point $\epsilon > 2V$ when the monomer excitations become more localised on each site. At this point the validity of the additive approximation (dashed) also breaks down for the eigenstate coherences, as the dimer system is becoming more like two independent monomers, such that steady-state populations are increasingly determined by the optical decay rates rather than vibrational relaxation. This specific breakdown in additivity is also visible, though not prominent, in the dark state populations in figure 4.13 for $\epsilon > 2V$ and $\alpha = 30\text{meV}$.

4.3 Summary

In this chapter we have seen that non-perturbative phonon interactions lead to a variety of effects within coupled quantum emitters. Firstly, a suppression of inter-molecular couplings and vibrational mixing of the dimer eigenstates, which are accounted for in the system Hamiltonian, cause the gap between bright and dark state manifolds to decrease. Secondly, thermal relaxation due to phonons in the single-excitation subspace happens on timescales orders of magnitude faster than optical excitation and emission. The dissipation into the CC-dressed eigenstates dominates much of the phonon-coupling dependence of the model, leading to a significant diversion from weak coupling (Redfield) predictions. In Redfield

theory, energy and coupling renormalisations are introduced perturbatively through principal value integrals at the level of the dissipator, using a basis that ignores the explicit vibronic component of the system. This ultimately leads to an over-estimation of dark-state populations.

Environmental non-additivity can also be observed in the dimer expectation values depending on the degree of electronic delocalisation and phonon-coupling. Sufficiently strong coupling leads to non-additive suppression of excited state populations, due to the ohmic form of the optical spectral density. This effect tends to be enhanced at large biases, as the two emitters start to behave independently and electronic population is localised on each monomer.

Further work

In light of this work, a few questions remain unresolved. Firstly, the degree to which non-additivity is affected by the coherent inter-molecular coupling could be studied further. One way of approaching this could be to compare the model to the uncoupled monomer case.

Secondly the nature of the eigenstate coherences observed in both the Redfield and CC theories is still unclear. The hypothesis that coherence arises due to the non-secular master equations coupling populations and coherences in the excitonic basis could be investigated further. It may be helpful to cast the electronic part of CC-dressed Hamiltonian into the eigenstate basis $|\nu_{\pm}\rangle$ and investigate coherence in this way.

Another clear drawback of the approach taken in this chapter is the large Hilbert spaces which arise due to the inclusion of two CCs in the augmented system Hamiltonian. Two things are particularly problematic. Firstly, the requirement of building Liouvillians of dimension $(3 * N_1 * N_2)^2$, where N_i is the CC dimension for environment i, means that we are quite restricted in the number of states that we can take in each CC. This ultimately limits the number of applications that this theory can be used for. One potential remedy for this could be in quantum jump approaches to calculating dynamics, however these are generally only easily applicable to the solution of secular master equations.

As well as preventing the use of standard quantum jump methods, the non-secularity of the resultant Liouvillians means that the underlying matrices are poorly conditioned, which means that iterative steady-state solutions are not feasible [127]. Being restricted to direct solvers is another limiting factor in the applicability of CC methods to larger systems. A recent paper has suggested a method of partial secular approximation via a coarse-graining approach [128] to recover the the standard Lindblad form of dissipator. Using this method it might be possible to find secular forms for both the optical and residual bath dissipators, ultimately enabling much more efficient solutions whilst retaining the important dynamical features.

Blank page

Chapter 5

Molecular photocells

5.1 Introduction

Organic photovoltaic cells (PVCs) have the potential to significantly reduce the cost and environmental impact of solar energy, due to cheaper raw materials, manufacturing, transportation and installation processes [129] compared to silicon PVCs. Importantly, the time that it takes for a solar cell to offset the energy used in its own fabrication could be reduced from years to days [130]. These systems are also very lightweight and offer precision tunability of their optical and electronic properties, even enabling transparency in the visible spectrum for potential use as ubiquitous energy conversion layers on surfaces such as windows and screens.

Organic photovoltaics generally use a blend of donor and acceptor molecular materials, where a light-sensitive donor - usually a doped polymer - is interspersed with small molecules which have high electron affinities, such as fullerenes. In other circumstances, small molecules are also used as donor materials, which permits more biologically-inspired design principles based on photosynthetic reaction-centers. As well as increases in performance due to quantum interference, these types of biomimetic photocells could also increase exciton diffusion lengths substantially. Increasing diffusion lengths of energy and charge carriers reduces the surface area requirements of donor-acceptor interfaces, which could lead to reductions in static disorder and non-radiative recombination which could ultimately increase open-circuit voltages [17].

Under illumination, the cell (usually the donor) can absorb photons, which promote the material from its highest occupied molecular orbital (HOMO) at thermal equilibrium, to its lowest unoccupied molecular orbital (LUMO). Molecular materials have very low dielectric constants compared to traditional semiconductors, which means that excited electrons and holes are not screened as effectively. This means that the low-energy excitations are Frenkel excitons rather than free charge-carriers, such that the electron and hole are Coulomb-bound on the same molecule. Organic solar cells need to then dissociate excitons, by donating electrons to a neighbouring acceptor material.

Excitons move randomly in the donor material until they reach an interface with an acceptor, at which point, provided it is thermodynamically preferable, the electrons may move onto the acceptor LUMO. The gap between donor and acceptor LUMOs must be sufficiently greater than the exciton binding energy in order to drive efficient charge-separation and prevent thermal reexcitation back from acceptor to donor [118, 131]. Once the charge carriers have been sufficiently separated, they can tunnel onto opposite electrodes to generate electrochemical work, leaving the system in a positively charged state. After some time another electron will tunnel back onto the HOMO and the cycle starts again. Occupation of both orbitals is also possible, although this is strongly suppressed in many molecular materials due to inefficient screening of charges and low dielectric constants which cause Coulomb repulsion between electrons.

As well as broadening absorption and emission peaks, vibrational interactions also greatly affect energy transport [45] and charge-separation [132]. As briefly discussed in the previous chapter, environment-assisted energy transfer can greatly enhance transport efficiency and is generally pronounced in the intermediate-coupling regime where the phonon-coupling is on the order of excitonic couplings [133, 11, 111]. Additionally, as we have seen in previous chapters, environmental non-additivity can alter decay rates in non-trivial ways, leading to profoundly different qualitative predictions. In this section, we will see an even richer interplay of non-additive effects, due to fermionic environments (leads) as well as bosonic (vibrations). These effects can be seen to increase the steady-state population of excited states, which is seen to enhance the power-output of the photocell.

5.2 Methods

5.2.1 Model

Here I construct a minimal *photocell* model inspired by the various discussions about organic photovoltaics in the previous section as well as by recent studies on bio-inspired quantum photocells [18, 121, 69, 70, 122, 54, 123]. I distinguish between photocell and photovoltaic, in that the latter generates both voltage and current through absorption of photons, whereas the former causes current to flow against an *externally applied* voltage. In practice, the characterisation of photovoltaics is done in precisely this way, by applying an external bias voltage and then studying the current behaviour, so this work is applicable to both cases.

Previous work on photocells use a variety of models and system Hamiltonians, mostly based on molecular dimers, to explore the influence that quantum interference and phonons have on photocurrent. In all but [18], optically dark states are utilised in order to overcome detailed balance and extend exciton lifetimes. Charge-separation and electron-electrode tunnelling is commonly accounted for by positing state-transfer rates described by Lindblad super-operators, though a Redfield theory analysis is also presented in [122] which is shown to agree. However, in all these heat-engine approaches, the authors rely on the phenomeno-

logical definition of a fictitious load or trap which irreversibly draws current from the charge-separated state. In more recent work, intermediate to strong phonon coupling is accounted for using collective-coordinate approaches [54] and polaron theory [123] within the setting of fictitious-load models.

Here I take a HOMO-LUMO system, with a single excitonic state and without excitonic coupling or dark and bright states. Rather than defining an ambiguous charge-separated state, or skipping out the charge separation process altogether, we explicitly define the exciton as being an electron-hole pair localised on the donor molecule, which can be dissociated by electrons tunnelling off and onto two fermionic leads. Upon absorption of a photon an exciton can form, the electron is effectively in a conduction band state and can subsequently tunnel off onto the right lead, subject to some attracting electron-hole binding energy, leaving the system in a positively charged state. In this same scenario, a negatively charged state can also arise from an exciton state if the hole in the valence band is filled by an electron tunnelling on from the left lead before the electron in the conduction band has the chance to tunnel onto the right lead.

Due to the unidirectional flow of current in this model, I am effectively studying a diode. I do this in order to create a simple, minimal model of charge separation and to study the effects of non-additivity in optical, fermionic and vibrational environments. Such a situation is potentially realisable for single molecules with sufficient asymmetry of ground and excited dipole moments [134], or as an effective subspace of a double quantum dot system [135]. This model is also reminiscent of a single-molecule break-junction [136], which may enable some results to be validated in the future through *photoswitch* conductivity experiments [137, 138]. To further aid simplicity, the exciton state is taken to be singlet character, although including spin-effects is an interesting area for future study.

Hamiltonian

We write down a Hamiltonian which describes this system as $H = H_S + H_B + H_I$, where

$$H_S = \epsilon_v d_v^\dagger d_v + \epsilon_c d_c^\dagger d_c - U d_v^\dagger d_v d_c^\dagger d_c, \tag{5.1}$$

which includes the fermionic electron and hole creation and annihilation operators $d_m^\dagger$ and d_m, where $m = c, v$, respectively, each of these have energy ϵ_m and the exciton binding energy U. The total interaction Hamiltonian is given by $H_I = H_I^{vib} + H_I^L + H_I^R + H_I^{EM}$ with the vibrational environments coupling individually to the electrons and holes: $H_I^{vib} = H_{I,h}^{vib} + H_{I,e}^{vib}$ where

$$\begin{aligned} H_{I,m}^{vib} &= -d_m^\dagger d_m \sum_k \left(f_{m,k}^* b_k^\dagger + f_{m,k} b_k - d_m^\dagger d_m \frac{f_{m,k}^2}{\omega_{m,k}} \right), \\ H_B^{vib} &= \sum_k \omega_k b_k^\dagger b_k. \end{aligned} \tag{5.2}$$

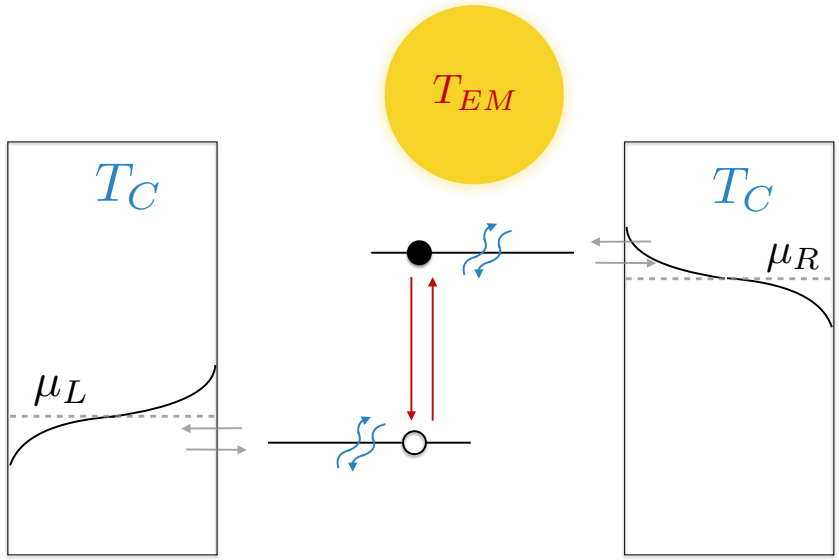

Figure 5.1: Schematic of the fermionic leads model. Grey arrows depict allowed electronic transitions between the molecule and the leads. Red arrows represent photon-mediated processes, blue arrows represent phonon-interactions.

The electromagnetic field Hamiltonians are

$$H_I^{EM} = (d_v^\dagger d_c^\dagger + d_c d_v) \sum_i (g_i a_i^\dagger + g_i a_i) \quad \text{and} \quad H_B^{EM} = \sum_i \omega_i a_i^\dagger a_i, \tag{5.3}$$

where a_i are photon annihilation operators which have frequency ω_i and couple to the system with strength g_i.

As stated above, for simplicity we consider the spectral densities of the left and right leads to be peaked around the valence and conduction energies, respectively, such that the left lead only couples to holes and the right lead only couples to electrons. After making this assumption, the Hamiltonians for the left and right leads can be written as

$$\begin{aligned} H_I^L &= \sum_{k_L} (t_{k_L} d_v c_{k_L} + t_{k_L}^* c_{k_L}^\dagger d_v^\dagger) \\ H_I^R &= \sum_{k_R} (t_{k_R} d_c^\dagger c_{k_R} + t_{k_R}^* c_{k_R}^\dagger d_c) \\ H_B^{L+R} &= \sum_{j=L,R} \sum_{k_j} \epsilon_{k_j} c_{k_j}^\dagger c_{k_j} \end{aligned} \tag{5.4}$$

where c_{k_j} (for $j = L, R$) are fermionic annihilation operators for bath modes with frequency ϵ_{k_j} and system-bath coupling strength t_{k_j}. Note the product of annihilation (creation) oper-

ators in this Hamiltonian, which occur due to holes and electrons having energies of opposite sign and both baths are comprised of electrons. For example, this means that the term $d_v c_{k_L}$ describes a hole being filled in the valence band by removal of an electron from the left lead. The fermionic operators obey the anti-commutation relations:

$$\begin{aligned} \{c_{k_j}, d_i^\dagger\} &= 0, \\ \{c_{k_i}, c_{k_j}^\dagger\} = \{d_i, d_j^\dagger\} &= \delta_{i,j} \\ \{c_{k_i}^\dagger, c_{k_j}^\dagger\} = \{c_{k_i}, c_{k_j}\} &= 0 \\ \{d_i, d_j\} = \{d_i^\dagger, d_j^\dagger\} &= 0. \end{aligned} \tag{5.5}$$

The terminology of *left* and *right* lead comes from the convention of molecular junction diagrams for the electron current to flow from left to right.

Jordan-Wigner Transformation

In the form written above, the molecule-lead interaction Hamiltonians H_I^L and H_I^R do not have tensor product structure so cannot be written in the generic form $H_I = \sum_\alpha A_\alpha \otimes B_\alpha$, where A_α and B_α are operators acting in only the system and bath Hilbert spaces alone. This is due to the fact that fermionic system and bath operators anti-commute with one another. We may however apply the Jordan-Wigner transformation, decomposing the fermionic operators in terms of Pauli operators acting on a set of spins. For illustrative purposes we will state that the bath H_B^μ for $\mu = 1, 2$ has a finite number M_μ fermionic modes and can be written:

$$\begin{aligned} d_v &= (\sigma_- \otimes \sigma_z) \otimes \Big(\bigotimes_{k_L}^{M_L} \mathcal{I}\Big) \otimes \Big(\bigotimes_{k_R}^{M_R} \mathcal{I}\Big) \\ d_c &= (\mathcal{I} \otimes \sigma_-) \otimes \Big(\bigotimes^{M_L} \mathcal{I}\Big) \otimes \Big(\bigotimes^{M_R} \mathcal{I}\Big) \\ c_{k_L} &= (\sigma_z \otimes \sigma_z) \otimes \left[\bigotimes^{k_L - 1} \sigma_z\right] \otimes \sigma_- \otimes \left[\bigotimes^{M_R + (M_L - k_L)} \mathcal{I}\right] \\ c_{k_R} &= (\sigma_z \otimes \sigma_z) \otimes \left[\bigotimes^{M_L} \sigma_z\right] \otimes \left[\bigotimes^{k_R - 1} \sigma_z\right] \otimes \sigma_- \otimes \left[\bigotimes^{M_R - k_R} \mathcal{I}\right]. \end{aligned} \tag{5.6}$$

Substituting the above definitions into the Hamiltonians and using Pauli operator product relations yields with definitions

$$
\begin{aligned}
\tilde{d}_v &= (\sigma_- \otimes \sigma_z) \qquad \tilde{d}_c = (\mathcal{I} \otimes \sigma_-) \\
\tilde{c}_{k_L} &= \left[\bigotimes_{k'<k_L} \sigma_z \right] \otimes \sigma_+ \otimes \left[\bigotimes_{k'}^{M_R+(M_L-k_L)} \mathcal{I} \right] \\
\tilde{c}_{k_R} &= \left[\bigotimes_{k'}^{M_L+k_R-1} \sigma_z \right] \otimes \sigma_+ \otimes \left[\bigotimes_{k'}^{M_R-k_R} \mathcal{I} \right].
\end{aligned}
\tag{5.7}
$$

The above description allows us to find an appropriate basis for the problem by defining $\mathcal{I} \equiv |0\rangle\langle 0| + |1\rangle\langle 1|$, calculating $\mathcal{I} \otimes \mathcal{I} = |00\rangle\langle 00| + |10\rangle\langle 10| + |01\rangle\langle 01| + |11\rangle\langle 11|$, we can relabel the basis:

$$
\begin{aligned}
|\phi\rangle &= |00\rangle \quad \text{excitonic vacuum (filled valence band)} \\
|h\rangle &= |10\rangle \quad \text{extra hole in valence band} \\
|e\rangle &= |01\rangle \quad \text{extra electron in conduction band} \\
|\mathrm{x}\rangle &= |11\rangle \quad \text{exciton state (electron and hole present)}
\end{aligned}
\tag{5.8}
$$

This gives the following operators in the discrete electronic basis:

$$
\begin{aligned}
\tilde{d}_v &= |0\rangle\langle 1| \otimes (|1\rangle\langle 1| - |0\rangle\langle 0|) = |e\rangle\langle \mathrm{x}| - |\phi\rangle\langle h| \\
\tilde{d}_c &= (|1\rangle\langle 1| + |0\rangle\langle 0|) \otimes |0\rangle\langle 1| = |h\rangle\langle \mathrm{x}| + |\phi\rangle\langle e| \\
\tilde{d}_v^\dagger \tilde{d}_v &= |h\rangle\langle h| + |\mathrm{x}\rangle\langle \mathrm{x}| \quad \tilde{d}_c^\dagger \tilde{d}_c = |e\rangle\langle e| + |\mathrm{x}\rangle\langle \mathrm{x}| \\
\tilde{d}_v \tilde{d}_v^\dagger &= |\phi\rangle\langle \phi| + |e\rangle\langle e| \quad \tilde{d}_c \tilde{d}_c^\dagger = |h\rangle\langle h| + |\phi\rangle\langle \phi| \\
\tilde{d}_v \tilde{d}_c &= |\phi\rangle\langle \mathrm{x}| \quad \tilde{d}_c^\dagger \tilde{d}_v^\dagger = |\mathrm{x}\rangle\langle \phi| \\
d_e \tilde{d}_v^\dagger &= |h\rangle\langle e| \quad \tilde{d}_c^\dagger \tilde{d}_v = -|e\rangle\langle h| \\
\tilde{d}_v^\dagger \tilde{d}_v \tilde{d}_c^\dagger \tilde{d}_c &= |\mathrm{x}\rangle\langle \mathrm{x}|
\end{aligned}
\tag{5.9}
$$

from which we rewrite the system Hamiltonian

$$
H_S = \epsilon_v |h\rangle\langle h| + \epsilon_c |e\rangle\langle e| + \epsilon_{\mathrm{x}} |\mathrm{x}\rangle\langle \mathrm{x}|, \tag{5.10}
$$

where $\epsilon_{\mathrm{x}} = \epsilon_h + \epsilon_e - U$. The electron-lead and hole-lead interaction Hamiltonians become

$$
\begin{aligned}
H_I^L =& (|e\rangle\langle \mathrm{x}| - |\phi\rangle\langle h|) \otimes \sum_{k_L} t_{k_L} c_{k_L} \\
&+ (|h\rangle\langle \phi| + |\mathrm{x}\rangle\langle e|) \otimes \sum_{k_L} t_{k_L}^* c_{k_L}^\dagger \\
H_I^R =& (|h\rangle\langle \mathrm{x}| + |\phi\rangle\langle e|) \otimes \sum_{k_R} t_{k_R}^* c_{k_R}^\dagger \\
&+ (|\mathrm{x}\rangle\langle h| - |e\rangle\langle \phi|) \otimes \sum_{k_R} t_{k_R} c_{k_R},
\end{aligned}
\tag{5.11}
$$

which are now in tensor product form. Note that the tensor products have been written explicitly in equation (5.11) but will be omitted in all further Hamiltonians.

Electron-phonon interaction

After the Jordan-Wigner transformation, the phonon-interaction Hamiltonians become

$$\begin{aligned} H_{I,h}^{vib} &= -|h\rangle\langle h| \sum_k \Big(f_{h,k}^* b_k^\dagger + f_{h,k} b_k \Big), \\ H_{I,e}^{vib} &= -|e\rangle\langle e| \sum_k \Big(f_{e,k}^* b_k^\dagger + f_{e,k} b_k \Big), \\ H_{I,\mathrm{x}}^{vib} &= -|\mathrm{x}\rangle\langle \mathrm{x}| \sum_k \Big((f_{h,k}^* + f_{e,k}^*) b_k^\dagger + (f_{h,k} + f_{e,k}) b_k \Big), \end{aligned} \tag{5.12}$$

where the counter-terms become energy shifts on the fermionic states

$$H_S = \tilde{\epsilon}_h |h\rangle\langle h| + \tilde{\epsilon}_e |e\rangle\langle e| + \tilde{\epsilon}_\mathrm{x} |\mathrm{x}\rangle\langle \mathrm{x}|, \tag{5.13}$$

with shifted energies $\tilde{\epsilon}_j = \epsilon_j + \sum_k f_{j,k}^2/\omega_{j,k}$, for $j = e, h$ and $\tilde{\epsilon}_\mathrm{x} = \tilde{\epsilon}_h + \tilde{\epsilon}_e - U$. If we set that $f_k = f_{e,k}$ and assume for simplicity that $f_{h,k} = M f_k$, such that there is a real constant scaling between hole-phonon and electron-phonon interaction strengths (i.e. they have the same mode-dependence), the interaction Hamiltonian becomes

$$H_I^{vib} = -(|e\rangle\langle e| + M |h\rangle\langle h| + (1+M) |\mathrm{x}\rangle\langle \mathrm{x}|) \sum_k \Big(f_k^* b_k^\dagger + f_k b_k \Big). \tag{5.14}$$

We can also define a system-phonon spectral density $J(\nu) = \sum_k |g_k|^2 \delta(\nu - \nu_k)$, which we take to be of Drude-Lorentz form as in previous chapters:

$$J(\omega) = \frac{\alpha \Omega^2 \Gamma \omega}{[(\omega^2 - \Omega^2)^2 + \Gamma^2 \omega^2]}. \tag{5.15}$$

Briefly ignoring the electromagnetic and lead environments we can see that, after accounting for the energy shifts, Hamiltonian (5.14) has the exact same form as the Hamiltonian (2.62). Therefore we can perform the Collective Coordinate mapping[28, 29, 25] in the same way as before:

$$H = H_S' + H_I' + H_B', \tag{5.16}$$

where

$$H_S' = H_S + \big[\Omega a^\dagger a + \lambda s (a^\dagger + a) \big] \tag{5.17}$$

$$\begin{aligned} H_I' &= \sum_k h_k (a^\dagger + a)(b_k^\dagger + b_k) \\ &\quad + \sum_k (b_k^\dagger + b_k)^2 \frac{h_k^2}{\omega_k} \end{aligned} \tag{5.18}$$

with $s = |e\rangle\langle e| + M\,|h\rangle\langle h| + (1+M)\,|\mathrm{x}\rangle\langle \mathrm{x}|$, CC oscillator frequency Ω and system-CC coupling strength λ. The residual bath Hamiltonian is given by

$$H'_B = \sum_k \omega_k b_k^\dagger b_k, \tag{5.19}$$

where we have defined CC-residual bath coupling strengths h_k and mode frequencies ω_k. This gives rise to a new spectral density defined by $J_{CC}(\omega) = \sum_k |h_k|^2 \delta(\omega - \omega_k) = \Gamma\omega/2\pi\Omega$ for the CC-residual bath interaction.

5.2.2 Quantum master Equations

Residual phonon bath

By moving to the interaction picture with respect to $H'_S + H'_B$, in the exact same way as in previous chapters, a time-local master equation can be found for the enlarged-system under the influence of the residual bath $\frac{\partial \rho'_S((t)}{\partial t} \equiv \mathcal{L}[\rho'_S(t)]$ where

$$\mathcal{L}[\rho'_S(t)] = -i[H'_S, \rho'_S(t)] + \mathcal{K}_{CC}[\rho'_S(t)] + \mathcal{K}_R[\rho'_S(t)] + \mathcal{K}_L[\rho'_S(t)] + \mathcal{K}_{EM}[\rho'_S((t)] \tag{5.20}$$

where the residual phonon dissipator has the form

$$\mathcal{L}[\rho'_S] = [S, \rho(t)\zeta] + [\zeta\rho(t)^\dagger, S] \tag{5.21}$$

with $\zeta = a^\dagger + a$ and

$$Z \approx \sum_{pq} J_{CC}(\xi_{pq})(\coth\left(\frac{\beta\xi_{pq}}{2}\right) + 1) S_{pq}\,|\phi_p\rangle\langle\phi_q| \tag{5.22}$$

where $\xi_{pq} = (\varphi_p - \varphi_q)$ given $H'_S\,|\varphi_p\rangle = \varphi_p\,|\varphi_p\rangle$ and $X_{lm} = \langle\varphi_l|\,X\,|\varphi_m\rangle$. The imaginary Lamb-shift terms have been neglected. In the enlarged basis, operators on the system Hilbert space now share the tensor product structure

$$\bar{d}_j \equiv \tilde{d}_j \otimes \mathcal{I}_{CC}. \tag{5.23}$$

Fermionic leads

We now focus on the interaction of the molecule with the fermionic leads, which are described by system operators now embedded in a basis which has been dressed by the Collective Coordinates as described by (5.23). After the Jordan-Wigner transformation, the interaction

Hamiltonian (5.11) has the structure $H_I = \sum_\alpha A_\alpha \otimes B_\alpha$, where

$$\begin{aligned} A_1^R &= |\mathrm{x}\rangle\langle h| - |e\rangle\langle\phi| \quad B_1^R = \sum_{k_R} t_{k_R} c_{k_R} \\ A_2^R &= |h\rangle\langle \mathrm{x}| + |\phi\rangle\langle e| \quad B_2^R = \sum_{k_R} t_{k_R}^* c_{k_R}^\dagger \\ A_1^L &= |e\rangle\langle \mathrm{x}| - |\phi\rangle\langle h| \quad B_1^L = \sum_{k_L} t_{k_L} c_{k_L} \\ A_2^L &= |h\rangle\langle\phi| + |\mathrm{x}\rangle\langle e| \quad B_2^L = \sum_{k_L} t_{k_L}^* c_{k_L}^\dagger \end{aligned} \tag{5.24}$$

so we can see that A_1^L removes a hole from the system (i.e., by removing an electron from the left lead) and A_1^R adds an electron to the system (and takes it from the right lead). Since the two leads are independent, we can find a second order Born-Markov master equation for the interaction between the system and fermionic environments starting from the well-known general form [21]:

$$\begin{aligned} \mathcal{K}[\rho'_S((t)] = -\sum_{j=L,R}\sum_{\alpha,\beta}\int_0^\infty d\tau \Big(& [A_\alpha^j, \tilde{A}_\beta^j(-\tau)\rho'_S(t)] C_{\alpha\beta}^j(\tau) \\ & + [\rho'_S(t)\tilde{A}_\beta^j(-\tau), A_\alpha^j] C_{\beta\alpha}^j(-\tau) \Big), \end{aligned} \tag{5.25}$$

where we have defined $\mathcal{K}[\rho'_S((t)] = \mathcal{K}_L[\rho'_S((t)] + \mathcal{K}_R[\rho'_S((t)]$ for compactness. The system operators A_α^j are now embedded in the enlarged space as in (5.23). The bath correlation functions are defined

$$C_{\alpha\beta}^j(\tau) = \mathrm{tr}_{E_j}(\tilde{B}_\alpha(\tau)\tilde{B}_\beta(0)) \tag{5.26}$$

with the stationary state of both leads given by ρ_E. We now assume that each lead is in a thermal state at all times $\rho_E = \rho_E^L \rho_E^R$, where

$$\rho_E^j = \frac{e^{-\beta_j \sum_{k_j}(\epsilon_{k_j} - \mu_j) b_{k_j}^\dagger b_{k_j}}}{\mathrm{tr}\left(e^{-\beta_j \sum_{k_j}(\epsilon_{k_j} - \mu_j) b_{k_j}^\dagger b_{k_j}} \right)}, \tag{5.27}$$

where β_j and μ_j are the inverse temperature and chemical potential of each lead, respectively. We now calculate the bath correlation functions by noticing that $\left\langle \tilde{c}_{j_\mu}^\dagger \tilde{c}_{k_\mu}^\dagger \right\rangle_E = \left\langle \tilde{c}_{j_\mu} \tilde{c}_{k_\mu} \right\rangle_E = 0$ due to the diagonal form of the thermal state, which leaves

$$\begin{aligned} C_{12}^\nu(\tau) &= \sum_{k_\nu, k'_\nu} t_{k_\nu} t_{k'_\nu}^* e^{-i\epsilon_{k_\nu} t} \left\langle \tilde{c}_{j_\nu} \tilde{c}_{k_\nu}^\dagger \right\rangle_{\rho_E^\nu} \\ C_{21}^\nu(\tau) &= \sum_{k_\nu, k'_\nu} t_{k_\nu}^* t_{k'_\nu} e^{i\epsilon_{k_L} t} \left\langle \tilde{c}_{j_\nu}^\dagger \tilde{c}_{k_\nu} \right\rangle_{\rho_E^\nu} \end{aligned} \tag{5.28}$$

for $\nu = L, R$. We calculate the expectation values by performing the traces over the thermal state, which yields

$$\begin{aligned}\left\langle \tilde{c}^{\dagger}_{k_\mu} \tilde{c}_{k'_\mu} \right\rangle_E &= \delta_{k_\mu k'_\mu} f_j(\epsilon_{k_j}) \\ \left\langle \tilde{c}_{k_\mu} \tilde{c}^{\dagger}_{k'_\mu} \right\rangle_E &= \delta_{k_\mu k'_\mu}(1 - f_j(\epsilon_{k_j})),\end{aligned} \tag{5.29}$$

where $f_j(\epsilon_{k_j}) = (e^{\beta(\epsilon_{k_j} - \mu_j)} + 1)^{-1}$ are the Fermi factors for each lead. We proceed by moving to the continuum limit: $\sum_{k_\nu} \to \int_{-\infty}^{\infty} d\epsilon_\nu$ and by defining the spectral densities:

$$J_\nu(\epsilon_\nu) = \sum_{k_\nu} |t_{k_\nu}|^2 \delta(\epsilon_\nu - \epsilon_{k_\nu}), \tag{5.30}$$

where $\left|t_{k_j}\right|^2$ describes the coupling strength between the system and mode k of the jth lead, which has absorbed the coefficients from the continuum transformation. The two baths are independent and therefore described by different sets of particles, hence the subscript on ϵ_j. This enables us to simplify the correlation functions

$$C^{\nu}_{12}(\tau) = \int_{-\infty}^{\infty} J_\nu(\epsilon_\nu) e^{-i\epsilon_\nu t}(1 - f_\nu(\epsilon_\nu)) \quad \text{and} \quad C^{\nu}_{21}(\tau) = \int_{-\infty}^{\infty} J_\nu(\epsilon_\nu) e^{-i\epsilon_\nu t} f_\nu(\epsilon_\nu). \tag{5.31}$$

In order for the lead dissipators to be consistent with the number-conserving form of the system-lead interaction Hamiltonians (5.11), we make a further secular approximation by discarding terms that have time-dependence in the interaction picture. Note that this is only done for the lead dissipators, and not the residual or electromagnetic baths. Starting from (5.25), we move to the interaction picture with respect to the full augmented system Hamiltonian and decompose operators into sums of operators with a spectrum of eigenenergy differences $\tilde{A}_\alpha(t) = \sum_\omega e^{-i\omega t} A_\alpha(\omega)$,

$$\begin{aligned}D_\nu[\rho'_S(t)] = -\sum_{\alpha\beta}\sum_{\omega\omega'} \int_0^{\infty} \Bigg(d\tau e^{i\omega'\tau} e^{-i(\omega+\omega')t} \Bigg(& C_{\alpha\beta}(\tau)[A_\alpha(\omega), A_\beta(\omega')\rho'_S(t)] \\ & + C_{\beta\alpha}(-\tau)[\rho'_S(t) A_\beta(\omega'), A_\alpha(\omega)] \Bigg) \Bigg) + h.c.\end{aligned} \tag{5.32}$$

for the right lead $\nu = R$, we explicitly define $A_1(t) = \sum_\omega e^{i\omega t} A_1(\omega)$ and $A_2(t) = \sum_\omega e^{-i\omega t} A_2(\omega)$. The reason for this becomes clear if we inspect the additive case, where $A_2(t) = d_c(t) = |h\rangle\langle x| e^{-i(\epsilon_c - U)t} + |\phi\rangle\langle e| e^{-i\epsilon_c t}$, the annihilation operator for electrons has negative time dependence. With this definition:

$$\begin{aligned}D_\nu[\rho'_S(t)] = -\sum_{\alpha\beta}\sum_{\omega\omega'} \int_0^{\infty} \Bigg(d\tau e^{i\omega'\tau} e^{i(\omega-\omega')t} \Bigg(& C_{12}(\tau)[A_1(\omega), A_2(\omega')\rho'_S(t)] \\ & + C_{21}(-\tau)[\rho'_S(t) A_2(\omega'), A_1(\omega)] \Bigg) \Bigg) + h.c.\end{aligned} \tag{5.33}$$

We now discard terms for which $\omega' \neq \omega$ to ensure that the Liouvillians are completely positive trace preserving maps, therefore ensuring physical evolution of the reduced density matrix. The secular approximation results in a form of Liouvillian which is in Lindblad form:

$$\begin{aligned} D_\nu(\rho'_S(t)) = \sum_\omega \Gamma^\nu_{12}(\omega)\Big(2A^\nu_2(\omega)\rho'_S(t)A^\nu_1(\omega) - \{A^\nu_1(\omega)A^\nu_2(\omega), \rho'_S(t)\}\Big) - iS^\nu_{12}(\omega)[A^\nu_1(\omega)A^\nu_2(\omega), \rho'_S(t)] \\ +\Gamma^\nu_{21}(\omega)\Big(2A^\nu_1(\omega)\rho'_S(t)A^\nu_2(\omega) - \{A^\nu_2(\omega)A^\nu_1(\omega), \rho'_S(t)\}\Big) - iS^\nu_{21}(\omega)[A^\nu_2(\omega)A^\nu_1(\omega), \rho'_S(t)] \end{aligned} \tag{5.34}$$

with the decay rates

$$\begin{aligned} \Gamma^R_{12}(\omega) &= \pi J_R(\omega)(1 - f_R(\omega)) \\ \Gamma^R_{21}(\omega) &= \pi J_R(\omega) f_R(\omega) \\ \Gamma^L_{12}(\omega) &= \pi J_L(-\omega)(1 - f_L(-\omega)) \\ \Gamma^L_{21}(\omega) &= \pi J_L(-\omega) f_L(-\omega) \end{aligned} \tag{5.35}$$

and energy level shifts

$$\begin{aligned} S^R_{12}(\omega) &= -iP\left[\int_{-\infty}^{\infty} d\epsilon \frac{J_\nu(\epsilon)(1 - f_\nu(\epsilon))}{\epsilon - \omega}\right] \\ S^R_{21}(\omega) &= -iP\left[\int_{-\infty}^{\infty} d\epsilon \frac{J_\nu(\epsilon) f_\nu(\epsilon)}{\epsilon - \omega}\right] \\ S^L_{21}(\omega) &= -iP\left[\int_{-\infty}^{\infty} d\epsilon \frac{J_\nu(\epsilon) f_\nu(\epsilon)}{\epsilon + \omega}\right] \\ S^L_{12}(\omega) &= -iP\left[\int_{-\infty}^{\infty} d\epsilon \frac{J_\nu(\epsilon)(1 - f_\nu(\epsilon))}{\epsilon + \omega}\right]. \end{aligned} \tag{5.36}$$

From the above expressions, we can see that the energies of the holes are summed together within the rates, which which highlights the fact that they are destroyed by electrons which have energy of the opposite sign. In practice, the operators are decomposed in the augmented system basis with $A_\alpha(\xi_{jk}) = \langle\varphi_k| A_\alpha |\varphi_j\rangle |\varphi_k\rangle\langle\varphi_j|$ and the secular approximation is performed on the spectrum of eigenenergy differences.

Fermionic leads : the additive case

In the weak phonon-coupling regime, the vibrational contribution to the system eigenstructure is negligible, so the decomposition $\{|\varphi_j\rangle\}$ can be well approximated by using the original unmapped basis $\{|\phi\rangle, |h\rangle, |e\rangle, |\mathrm{x}\rangle\}$. In this case, the operators in the interaction picture be-

come:

$$\begin{aligned}
\tilde{A}_1^R(t) &= d_c^\dagger(t) = |\mathrm{x}\rangle\langle h|\, e^{i(\epsilon_c - U)t} + |e\rangle\langle\phi|\, e^{i\epsilon_c t} \\
\tilde{A}_2^R(t) &= d_c(t) = |h\rangle\langle \mathrm{x}|\, e^{-i(\epsilon_c - U)t} + |\phi\rangle\langle e|\, e^{-i\epsilon_c t} \\
\tilde{A}_1^L(t) &= d_v(t) = |e\rangle\langle \mathrm{x}|\, e^{-i(\epsilon_v - U)t} - |\phi\rangle\langle h|\, e^{-i\epsilon_v t} \\
\tilde{A}_2^L(t) &= d_v^\dagger(t) = |\mathrm{x}\rangle\langle e|\, e^{i(\epsilon_v - U)t} - |h\rangle\langle\phi|\, e^{i\epsilon_v t},
\end{aligned} \tag{5.37}$$

which leads to Liouvillians of the form

$$\begin{aligned}
D_L[\rho_S(t)] = &-i[H_{LS}^L, \rho_S(t)] \\
&+ \pi J_L(-\epsilon_v)(1 - f_L(-\epsilon_v))\mathcal{L}_{|h\rangle\langle\phi|}[\rho_S(t)] \\
&+ \pi J_L(-\epsilon_v) f_L(-\epsilon_v)\mathcal{L}_{|\phi\rangle\langle h|}[\rho_S(t)] \\
&+ \pi J_L(-\epsilon_v + U)(1 - f_L(-\epsilon_v + U))\mathcal{L}_{|x\rangle\langle e|}[\rho_S(t)] \\
&+ \pi J_L(-\epsilon_v + U) f_L(-\epsilon_v + U)\mathcal{L}_{|e\rangle\langle x|}[\rho_S(t)]
\end{aligned} \tag{5.38}$$

and

$$\begin{aligned}
D_R[\rho_S(t)] = &-i[H_{LS}^R, \rho_S(t)] \\
&+ \pi J_R(\epsilon_c)(1 - f_R(\epsilon_c))\mathcal{L}_{|\phi\rangle\langle e|}[\rho_S(t)] \\
&+ \pi J_R(\epsilon_c) f_R(\epsilon_c)\mathcal{L}_{|e\rangle\langle\phi|}[\rho_S(t)] \\
&+ \pi J_R(\epsilon_c - U)(1 - f_R(\epsilon_c - U))\mathcal{L}_{|h\rangle\langle x|}[\rho_S(t)] \\
&+ \pi J_R(\epsilon_c - U) f_R(\epsilon_c - U)\mathcal{L}_{|x\rangle\langle h|}[\rho_S(t)].
\end{aligned} \tag{5.39}$$

In the limit $U \to 0$ this gives the total lead dissipator:

$$\begin{aligned}
D_{L+R}[\rho_S(t)] = -i[H_{LS}, \rho_S(t)] &+ \pi J_L(-\epsilon_v)(1 - f_L(-\epsilon_v))\mathcal{L}_{d_v^\dagger}[\rho_S(t)] + \pi J_L(-\epsilon_v) f_L(-\epsilon_v)\mathcal{L}_{d_v}[\rho_S(t)] \\
&+ \pi J_R(\epsilon_c)(1 - f_R(\epsilon_c))\mathcal{L}_{d_c}[\rho_S(t)] + \pi J_R(\epsilon_c) f_R(\epsilon_c)\mathcal{L}_{d_c^\dagger}[\rho_S(t)],
\end{aligned} \tag{5.40}$$

where Lindblad terms are described by $\mathcal{L}_O[\rho] = 2O\rho O^\dagger - \{O^\dagger O, \rho\}$ and the coherent Lamb-shift Hamiltonian is

$$\begin{aligned}
H_{LS} = &\, S_{12}^L(\epsilon_v)(|\phi\rangle\langle\phi| + |e\rangle\langle e|) + S_{21}^L(\epsilon_v)(|h\rangle\langle h| + |x\rangle\langle x|) \\
&+ S_{12}^R(\epsilon_c)(|e\rangle\langle e| + |x\rangle\langle x|) + S_{21}^R(\epsilon_c)(|\phi\rangle\langle\phi| + |h\rangle\langle h|).
\end{aligned} \tag{5.41}$$

A brief inspection of the Fermi factors $f_L(-\epsilon_v) = (e^{-\beta(\epsilon_v + \mu_L)} + 1)^{-1}$ shows that:

$$f_L(-\epsilon_v) \to \begin{cases} 1 & \text{if } \mu_L \gg -\epsilon_v, \\ 1/2 & \text{if } \mu_L = -\epsilon_v, \\ 0 & \text{if } \mu_L \ll -\epsilon_v, \end{cases} \tag{5.42}$$

which means that the creation and annihilation of holes must be carried out by electrons with energy of the opposite sign. As we will see later, this determines the characteristics of the current-voltage behaviour. The conditions for exchange of particles between the right lead and the conduction band are straightforward:

$$f_R(\epsilon_c) \to \begin{cases} 1 & \text{if } \mu_R \gg \epsilon_c, \\ 1/2 & \text{if } \mu_R = \epsilon_c, \\ 0 & \text{if } \mu_R \ll \epsilon_c. \end{cases} \tag{5.43}$$

Solar radiation field

After a Jordan-Wigner transformation, the Hamiltonian describing the interaction between the system and its electromagnetic environment in (5.3) becomes

$$H_I^{EM} = (|\mathrm{x}\rangle\langle\phi| + |\phi\rangle\langle\mathrm{x}|) \sum_k (g_k b_k^\dagger + g_k b_k), \tag{5.44}$$

where it is clear that the electromagnetic field creates and destroys excitons through photon absorption and radiative recombination, respectively. The above Hamiltonian has the structure $H_I = A \otimes B$ where $A = |\mathrm{x}\rangle\langle\phi| + |\phi\rangle\langle\mathrm{x}|$ and $B = \sum_k g_k(b_k^\dagger + b_k)$, which means we can derive an optical dissipator for the system bath interaction via the method outlined in [38]. This gives a Liouvillian of the form

$$\mathcal{K}_{EM}[\rho_S(t)] = [A, Z\rho_S(t)] - \left[\rho_S(t)Z^\dagger, A\right] \tag{5.45}$$

where the rate operator

$$Z = \int_0^\infty d\tau \mathcal{C}(\tau)\tilde{S}(-\tau) \tag{5.46}$$

and correlation function

$$\mathcal{C}(\tau) = \int_0^\infty d\omega J_{EM}(\omega) \left(\coth\left(\frac{\beta\omega}{2}\right) \cos\omega\tau - i \sin\omega\tau \right). \tag{5.47}$$

are defined in terms of $J_{EM}(\omega) = \sum_k |f_k|^2 \delta(\omega - \omega_k)$, the electromagnetic bath spectral density. After decomposing the operator A into eigenstates of the augmented system Hamiltonian H_S' and moving into the interaction picture, as above, we find

$$Z = \sum_{m,n} A_{m,n} \Lambda(\xi_{mn}) \, |\varphi_m\rangle\langle\varphi_n| \tag{5.48}$$

where the complex, temperature-dependent factors are defined

$$\Lambda(\xi_{mn}) = \int_0^\infty d\tau \int_0^\infty d\omega \big(f_1(\omega) e^{i(\omega - \xi_{mn})\tau} + f_2(\omega) e^{-i(\omega + \xi_{mn})\tau} \big) \tag{5.49}$$

where

$$\begin{aligned} f_1(\omega) &= \frac{1}{2}J(\omega)(\coth(\beta\omega/2) - 1) \\ f_2(\omega) &= \frac{1}{2}J(\omega)(\coth(\beta\omega/2) + 1). \end{aligned} \tag{5.50}$$

Note that the real and imaginary parts of $\Lambda(\xi_{mn})$ are effectively transition rates and energy shifts associated with the transition ξ_{mn}. These integrals can be evaluated in the same way as in previous sections

$$\Lambda(\xi_{mn}) = \begin{cases} \pi f_1(\xi_{mn}) + i\mathcal{S}^+(\xi_{mn}) & \text{if } \xi_{mn} > 0, \\ \frac{\pi}{2}\lim\limits_{x\to 0}\left(J_{ph}(x)\coth\left(\frac{\beta x}{2}\right)\right) - i\mathcal{S}(0) & \text{if } \xi_{mn} = 0, \\ \pi f_2(|\xi_{mn}|) + i\mathcal{S}^-(\xi_{mn}) & \text{if } \xi_{mn} < 0. \end{cases} \tag{5.51}$$

given

$$\begin{aligned} \mathcal{S}^+(\xi_{mn}) &= \mathcal{P}\left[\int_0^\infty \left(\frac{f_1(\omega)}{\omega - \xi_{mn}} - \frac{f_2(\omega)}{\omega + \xi_{mn}}\right) d\omega\right] \\ \mathcal{S}(0) &= \mathcal{P}\left[\int_0^\infty \frac{J_{ph}(\omega)}{\omega} d\omega\right] \\ \mathcal{S}^-(\xi_{mn}) &= \mathcal{P}\left[\int_0^\infty \left(\frac{f_1(\omega)}{\omega + |\xi_{mn}|} - \frac{f_2(\omega)}{\omega - |\xi_{mn}|}\right) d\omega\right]. \end{aligned} \tag{5.52}$$

All of the above can now be calculated numerically in a straightforward manner and we can bring together the four Liouvillians to explore photocurrent in this simple model. We use the electromagnetic field spectral density in cubic form [51, 38]

$$J_{EM}(\omega) = \frac{\Gamma_0}{2\pi\epsilon_{\mathrm{x}}^3}\omega^3 \tag{5.53}$$

where the characteristic frequency ϵ_{x} corresponds to the excitonic energy gap. The above spectral density means that the bare electronic transition, in the absence of phonons has the rate $2\pi J(\epsilon_{\mathrm{x}}) = \Gamma_0$, which also becomes the total transition rate for the additive theory.

Solar radiation field: the additive case

The additive dissipator is found by ignoring the vibronic contributions to the system Hamiltonian when moving the relevant system operators $|\phi\rangle\langle \mathrm{x}|$ and $|\mathrm{x}\rangle\langle\phi|$ into the interaction picture, and also making the rotating wave approximation on the interaction Hamiltonian. This results in $|\phi\rangle\langle \mathrm{x}|\,(t) = e^{iH_{\mathrm{S}}t}\,|\phi\rangle\langle \mathrm{x}|\,e^{-iH_{\mathrm{S}}t} = |\phi\rangle\langle \mathrm{x}|\,e^{-i\epsilon_{\mathrm{x}}t}$, where H_{S} is given by (5.10). This

results in the standard Lindblad form of quantum optical Liouvillian:

$$\mathcal{K}_{\mathrm{EM}}[\rho(t)] = \frac{\Gamma_0}{2}(n(\epsilon_{\mathrm{x}})+1)\mathcal{L}_{|\phi\rangle\langle \mathrm{x}|}[\rho(t)] \tag{5.54}$$

$$+ \frac{\Gamma_0}{2} n(\epsilon_{\mathrm{x}})\mathcal{L}_{|\mathrm{x}\rangle\langle\phi|}[\rho(t)]. \tag{5.55}$$

which can form part of the total master equation given in equation (5.45).

5.2.3 Note on parameters

Certain symmetries are imposed and parameters defined, in order to simplify the analysis of the model. The reverse-bias voltage is taken to be the difference between the electrochemical potentials of the two fermionic reservoirs $eV = (\mu_R - \mu_L)$. I consider a central chemical potential μ which the leads are symmetric about $\mu_L = \mu - eV/2$ and $\mu_R = \mu + eV/2$. I also take the leads and phonon bath to be the same temperature $T_C \equiv T_{ph} = T_L = T_R$ to avoid any intrinsic thermoelectric effects between the leads and the phonons.

I define a bandgap ε, a valence band energy ϵ_v and an exciton binding energy U, which fixes the conduction band $\epsilon_c = \epsilon_v + \varepsilon$ and exciton energy $\epsilon_{\mathrm{x}} = 2\epsilon_v + \varepsilon - U$. In all of the following, $\varepsilon = 1.4\mathrm{eV}$ and $\epsilon_v = 300\mathrm{meV}$.

In all but the end of Section 5.3.2 of this chapter, the lead spectral densities are taken to be Lorentzians

$$J_L(\omega) = \frac{1}{2\pi}\frac{\gamma\delta^2}{((\omega+\omega_v)^2+\delta^2)} \quad \text{and} \quad J_R(\omega) = \frac{1}{2\pi}\frac{\gamma\delta^2}{((\omega-\omega_c)^2+\delta^2)}, \tag{5.56}$$

where δ and γ are the widths and heights of the peaks, respectively. Unless otherwise stated $\gamma = \Gamma_0 = 1\mathrm{ns}^{-1}$ for simplicity, which means that the lead and optical decay processes occur on the same time-scale. Unless otherwise state $\delta = 15\mathrm{meV}$, the width of phonon spectral density $\Gamma = 10\mathrm{meV}$ and $T_{EM} = 5800\mathrm{K}$.

5.2.4 Photocell performance metrics

Much of the behaviour of a photovoltaic (or photocell) can be understood through the analysis of current-voltage (I-V) diagrams, whereby an external reverse-bias voltage is applied across the two electrodes and the resultant photocurrent is measured.

The most common figure of merit used in the analysis of photovoltaics is the power conversion efficiency (PCE), which is the amount of power generated from the incident light which hits the cell. The PCE is proportional to open-circuit voltage, V_{OC} and short-circuit current, I_{SC}. Open-circuit voltage of cell is heavily dependent on the difference between donor HOMO and acceptor LUMO. Short-circuit current depends on the most amount of light being absorbed (with the fewest recombination losses), which is increased by reducing the donor band-gap. The great challenge in the last few decades has been to optimise both

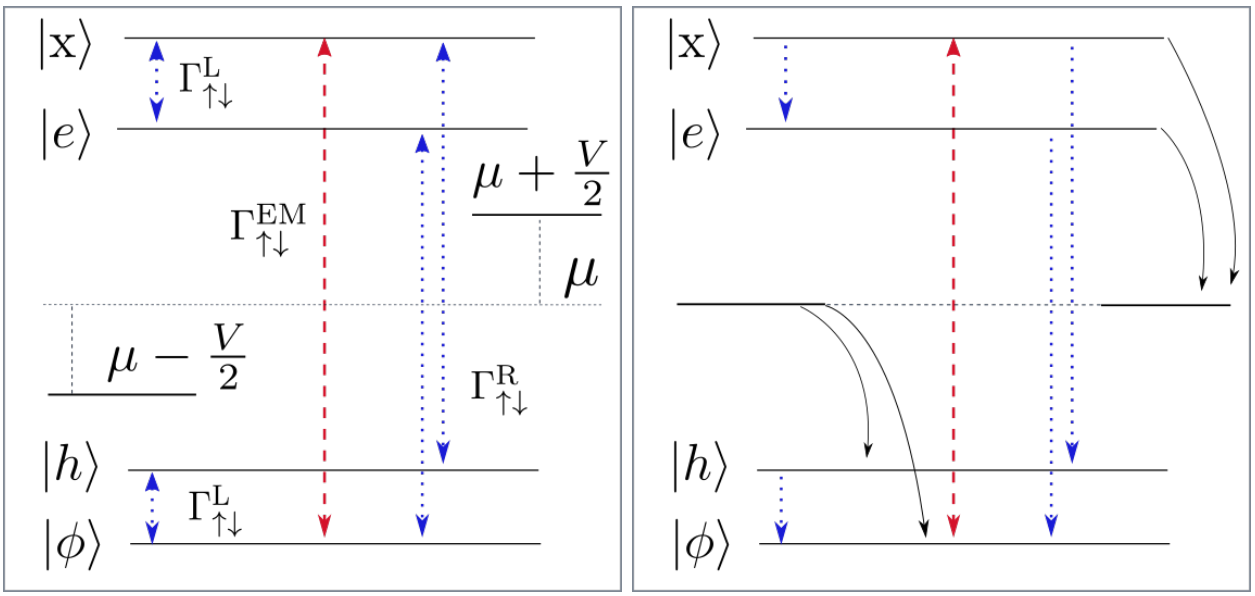

Figure 5.2: Left: schematic of the fermionic leads model in the energy basis. Red and blue arrows correspond to optical and phonon induced processes, respectively. Right: schematic for model under short-circuit conditions, $V = 0$ and $k_B T_C \ll \mu$. Black arrows illustrate which electron transitions are allowed under these conditions, with blue arrows now unidirectional.

of these simultaneously, resulting in PCEs of up to 13% in of single-layer devices [139] and 17.29% tandem devices [140], which use two active layers with complementary absorption profiles (long and short wavelengths) to further increase photocurrent.

For the model derived above, current can be calculated from the steady-state density matrix $\mathcal{L}[\rho_{SS}] = 0$. Although the total time-derivative is zero, the phonons do not directly affect electronic populations so the optical and lead processes should balance out: $\mathcal{K}_{EM}[\rho_{SS}] = -\mathcal{K}_R[\rho_{SS}] > 0$. Since there are no other internal recombination effects, the current can thus be found by simply taking the steady-state density matrix, acting on it with the right-lead dissipator and taking the trace with the conduction band occupation operator:

$$I = -\operatorname{tr}\{\mathcal{K}_R[\rho_{SS}] n_c\}. \tag{5.57}$$

Here, the minus sign fixes the direction of the *dark* current to flow from left to right, i.e. in the absence of incoherent excitation when $T_{EM} = 0$ but when $V > \varepsilon$.

On current-voltage diagrams, there are usually two points where zero power-output occurs, one where no bias is applied ($V = 0$) and the other where V is large enough to completely suppress current ($I = 0$). The actual maximum attainable power $P_{\max}$ occurs somewhere between these limits.

The current that passes through the system at the point where the $V = 0$ is the *short-circuit current*, denoted by I_{SC}. The voltage that is required in order to suppress $I \to 0$ is the *open-circuit voltage*, V_{OC}. Usually $I_{max} = I_{SC}$ and V_{OC} is the maximum possible potential that can be overcome, so these two metrics are intrinsic figures of merit to each photocell.

Another metric, called the filling factor $F_F = P_{\max}/I_{SC}V_{OC}$, is often used to study photo-

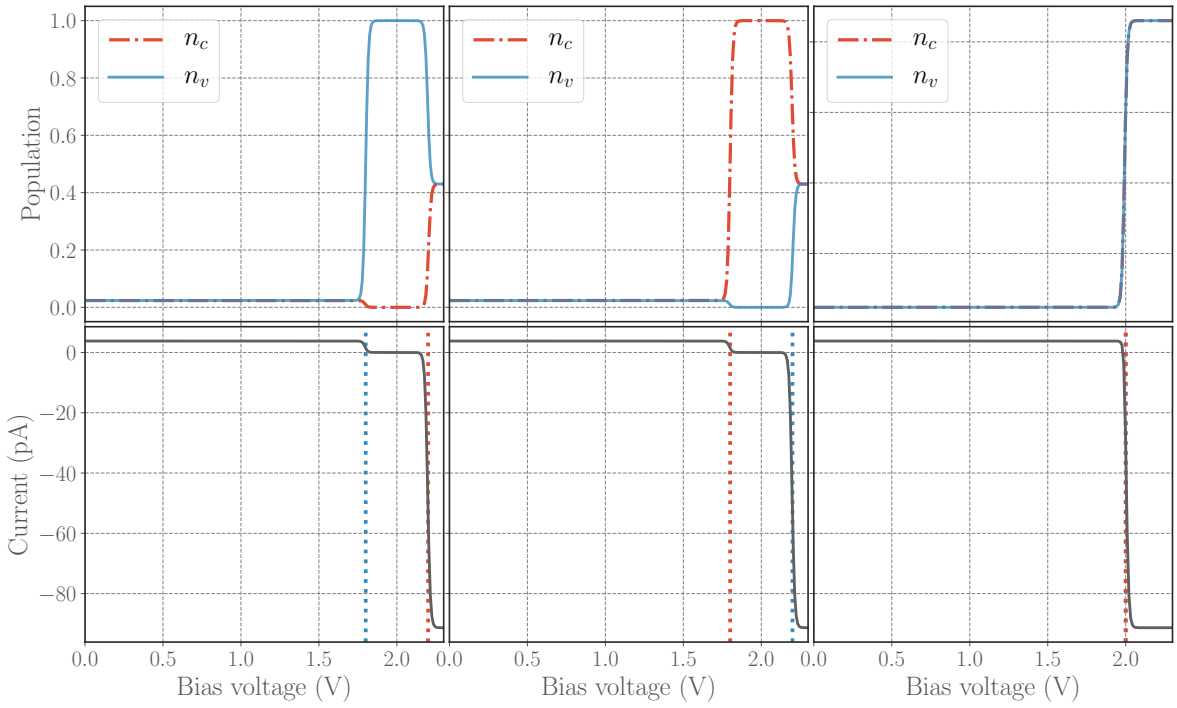

Figure 5.3: Top: Conduction and valence band populations as a function of reverse-bias voltage and in the absence of phonon-coupling and binding energy. Bottom: Corresponding current-voltage diagrams. $\alpha = 0$, $U = 0$. Voltage is defined as $\mu_L = \mu - V/2$, where **(Left)**: $\mu = \varepsilon - 100\text{meV}$. **(Middle)**: $\mu = \varepsilon + 100\text{meV}$. **(Right)**: $\mu = \varepsilon$.

voltaic performance because of its close relation to various internal experimental values [129]. Intuitively, the filling factor compares the actual $P_{\max}$ to the theoretical maximum, where the cell is generating I_{SC} whilst working against V_{OC}. For $F_F = 1$, the I-V curve would need to be a perfect step function around V_{OC}, so F_F can be thought of as the curvature of the I-V diagram.

The final - and most commonly quoted - metric we describe is the power conversion efficiency which was introduced earlier. This compares the power of the sunlight that is incident on the cell with the amount of power generated by the cell, $\eta_{PCE} = P_{out}/P_{inc.}$. Since the electromagnetic field is kept fixed for each set of photocell parameters, $P_{inc.}$ is redundant and P_{out} will be qualitatively the same as η_{PCE}. Due to the nature of our model, the following discussion will be primarily focused on I_{SC}, V_{OC} and $P_{\max}$ as figures of merit.

5.3 Results and discussion

5.3.1 Photocell performance at zero phonon-coupling

Characteristics of zero binding energy

In order to understand the current-voltage behaviour of the above model, it is useful to inspect the behaviour of the lead dissipators in the limit of no phonon-coupling or exciton

binding energy, as in Eq. (5.34). As we have already seen, exchange between the valence band and the left lead is determined by the relationship between μ_L and $-\epsilon_v$ given by Eq. (5.42). The steps on the I-V diagram are determined by which energy levels are included within the bias window, or between the left and right chemical potentials. In the lower plots of fig 5.3, the steps that occur at the dotted red and blue lines on the I-V curves correspond to points where $\mu_R = \epsilon_c$ and $\mu_L = -\epsilon_v$, respectively. We can calculate the location of these steps by defining $\mu_R^{(\mathrm{red})} = \epsilon_c$ which gives a left chemical potential $\mu_L^{(\mathrm{red})} = \mu - (\epsilon_c - \mu) = 2\mu - \epsilon_c$ and a bias $eV_r = 2(\epsilon_c - \mu)$. Similarly for the step at the blue dotted line $\mu_L^{(\mathrm{blue})} = -\epsilon_v$ so $\mu_R^{(\mathrm{blue})} = 2\mu + \epsilon_v$ and $eV_b = 2(\mu + \epsilon_v)$. By equating the expressions for V_r and V_b, we can see that the relative position of the steps is determined by the value of μ, the central value of the bias window, and whether this sits above or below the centre of the bandgap: $\varepsilon/2$. In the fig 5.3 (right), $\mu = \varepsilon/2$ which means that the blue and red dotted lines coincide. Note that, in order to exaggerate the steps in the I-V diagrams, we have taken a relatively low lead reservoir temperature of $T_C = 50\mathrm{K}$.

When $\mu < \varepsilon/2$ as in figure 5.3 (left), increasing the bias from $V = 0$ incorporates the valence band energy (blue dotted) before the conduction band. As V increases $f_L \to 0$ as μ_L decreases beyond $\mu_L < -\epsilon_v$, according to (5.42). This causes a large spike in hole population as electrons can freely jump off from the valence band onto the left lead. Then as V increases further, the window incorporates the conduction band (red dotted), which means that $f_R \to 1$ and electrons can freely tunnel onto the conduction band from the right lead.

For $\mu > \varepsilon/2$ in figure 5.3 (center), the opposite occurs, as shown in the central plot in figure 5.3, since the bias window now incorporates the conduction energy before valence energy and the ordering of the red and blue lines is reversed.

As already discussed, the case where $\mu = \varepsilon/2$ as in the right-hand figure, the conduction and valence steps overlap exactly, so the system goes directly from positive to negative current behaviour around a single point, $\epsilon_{\mathrm{x}} = \epsilon_v + \epsilon_c$. For positive or negative current to exist, both n_c and n_v must simultaneously have non-zero expectation value.

Characteristics of finite binding energy

Now we increase the complexity of the model slightly by considering non-zero exciton binding energy, governed by the additive dissipators (5.38) and (5.39), since the non-additive theory reduces to additive theory in the absence of phonons. Now there are two sets of steps in the I-V diagram, since the dissociation of an exciton into a free charge occurs at a lower energy than that of a free charge on the system hopping onto a lead. Using a similar analysis carried out in the previous section on figure 5.4, we find that the dashed blue and red and vertical lines correspond to the points where the charge-separation processes are suppressed, occurring at $\tilde{\mu}_L^{\mathrm{blue}} = -(\epsilon_v - U)$ and $\tilde{\mu}_R^{\mathrm{red}} > \epsilon_c - U$, where the tildes distinguish them from the binding energy-free processes. These chemical potentials give the bias voltages

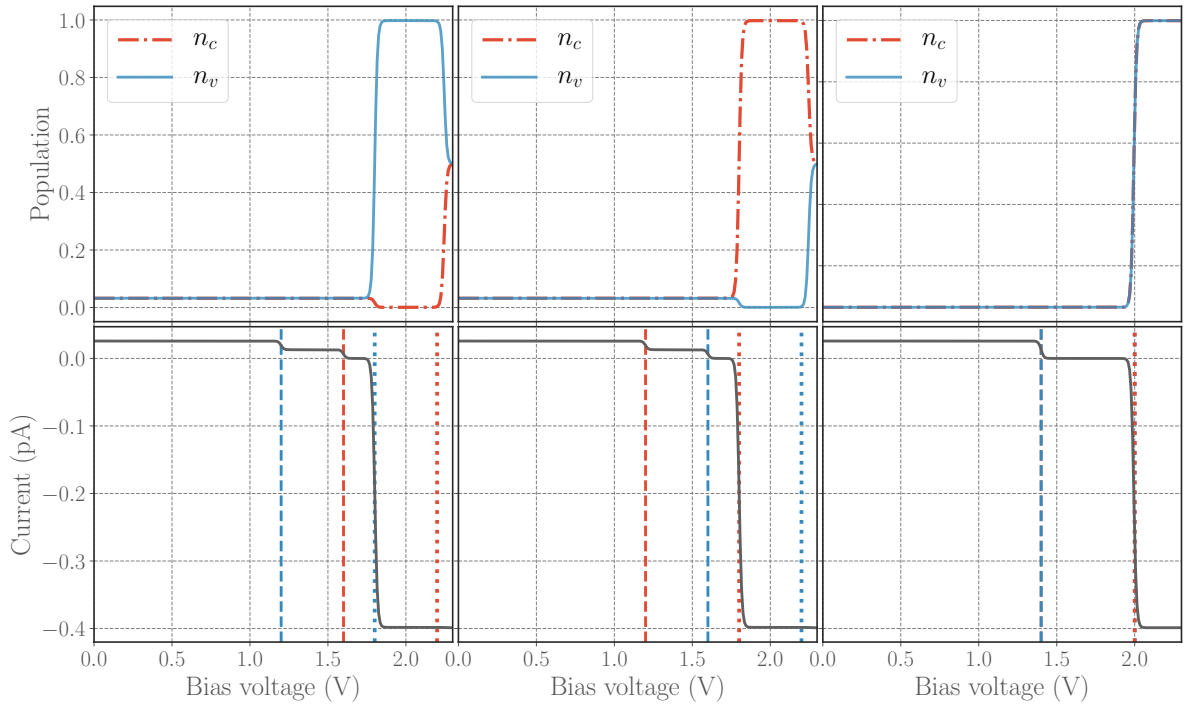

Figure 5.4: Top: Conduction and valence band populations as a function of reverse-bias voltage and in the absence of phonon-coupling for different values of μ. Bottom: Corresponding current-voltage diagrams. $\alpha = 0$, $U = \epsilon_v = 300$meV. Voltage is defined by $\mu_L = \mu - \mathrm{eV}/2$, where **(Left):** $\mu = \varepsilon - 100$meV. **(Middle):** $\mu = \varepsilon + 100$meV. **(Right):** $\mu = \varepsilon$.

of $\tilde{V}_b = 2(\mu+\epsilon_v-U)/e$ and $\tilde{V}_r = 2(\epsilon_c-U-\mu)/e$ for the blue and red dashed lines respectively.

We can also see that the scale of the y-axis has changed considerably, with two orders of magnitude less current being generated for $U = \epsilon_v = 300$meV. This is due to the fact that the exciton-dissociation processes are now off-resonant with the Lorentzian lead spectral densities, since these have been set to be centred exactly at the band energies.

Figure 5.5 includes the I-V (left) and P-V (right) curves for the case where $T_C = 300$K and $\alpha = 0$, this time the axes are zoomed in to the area where positive current occurs, since in practice this is the most important regime of operation. For higher temperature leads, the steps in current occur more smoothly and we can see that their close proximity causes the current to approach zero at an angle. I_{SC} and V_{OC} are strong indicators of $P_{\max}$ and in figure 5.5 (right) we can see that for a given U, $P_{\max}$ is maximised where $\mu = \varepsilon/2$ and $V_{OC} = \epsilon_{\mathrm{x}}$. If V_{OC}, U and μ stay fixed, then P_{max} is directly proportional to I_{SC}, so there is no need to calculate the entire I-V curve. We will use this property in the next section.

5.3.2 Finite phonon-coupling and environmental non-additivity

From Eq. (5.10) - (5.12), we can see that the system and the phonon-interaction Hamiltonians commute, which means that the phonon-mediated processes will never directly affect populations. The non-perturbative treatment of the phonons gives rise to an enlarged basis, where the eigenstates will be vibronic in nature, with a mixture of both electronic and vi-

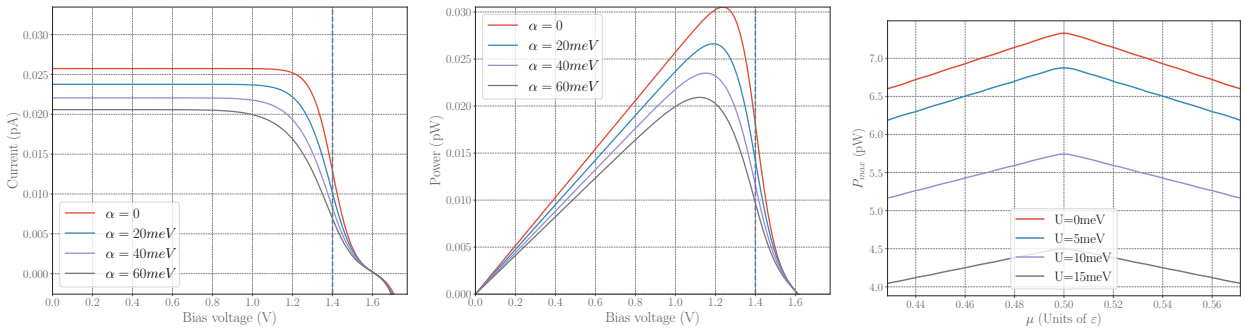

Figure 5.5: **(Left):** I-V curves for different values of phonon-coupling where $U = 300$meV, $\Omega = 50$meV. **(Middle):** P-V curves for same parameters. Together, these plots show that maximum power is dominated by I_{SC} since V_{OC} is largely unaffected by phonon-coupling. From the peak of the right-hand curves we can see that phonon-coupling does slightly reduce the voltage at which maximum power is attained. **(Right):** Maximum power as a function of μ and U for $\alpha = 0$, we can see that P_{max} is maximised when $\mu = \varepsilon/2$.

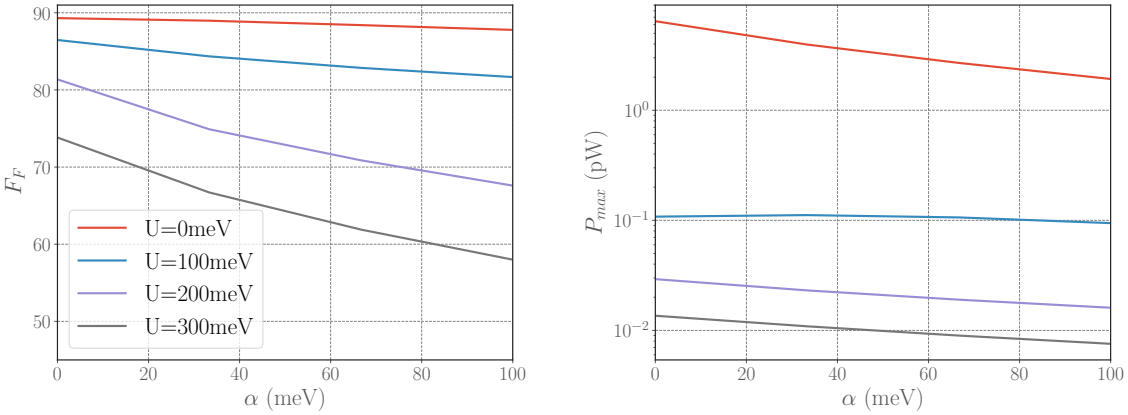

Figure 5.6: **(Left):** Filling factor F_F and **(Right):** P_{max} as a function of phonon-coupling strength, for $\Omega = 50$meV, $\Gamma = 15$meV in the peaked spectral density regime for the leads.

brational characteristics. We have seen how utilising this basis in deriving master equations for additional weakly-interacting bath processes, such as the system-lead and system-photon interactions, gives rise to non-additive dissipators. In fact, as we will see in more detail, non-additivity is the only way that phonons will affect current and photocell performance in this model. From Eq. (5.54), (5.38) and (5.39) we can also see that in an additive treatment, the Liouvillians for the lead and electromagnetic field interactions do not depend on any phonon influence at all. This means that the baths do not *see* the vibronic states, only the bare electronic eigenstates of Eq. (5.10). For truly perturbative phonon-coupling, an additive treatment may provide adequate predictions, however any dependence on phonon-coupling is lost within such a theory.

In this section, we will analyse how environmental non-additivity due to the phonon-coupling affects the performance of the photocell. In doing so, we identify two important parameter regimes which completely determine the qualitative behaviour of the model, namely where the spectral density of the fermionic leads is either relatively flat around the system energy scales or more sharply peaked. These are referred to as the *flat* and *peaked* spectrum regimes, since they define the width of the energetic window within which states can interact with the fermionic bath. Note that we consider a sharp cutoff of the spectral densities to ensure that the left and right leads only ever couple, respectively, to holes and electrons.

Regime of peaked spectral density for fermionic leads

In order to gain some intuition about environmental non-additivity, we inspect some example I-V curves for finite phonon-couplings in figure 5.5 (left). For these parameters, we see that an increase in phonon-coupling leads to a decrease in I_{SC}, but no change to $V_{OC} \approx 1.6V$ since all four curves converge to zero current at the same voltage. Although V_{OC} is largely unaffected by phonon coupling, the current does begin to decline for lower V. This change in curvature ultimately decreases the voltage at which maximum power is attained - visible as a gradual peak-shift in the P-V diagram, as well as having some effect on P_{max}. As can be seen in the power-voltage diagram in figure 5.5 (middle), the decrease in I_{SC} and this change in curvature leads to a reduction in the maximum power output of the photocell.

The filling factor F_F, takes into account both the maximum power and the short-circuit current and thus shows how exactly how the power output of the cell is affected by the change in curvature of the I-V curve due to phonon interactions. In figure 5.6 (left) we can see that F_F decreases as a function of both binding energy and phonon-coupling strength. Figure 5.6 (right) also shows the extent to which P_{max} is affected by both phonon-coupling and binding energy.

Despite the behaviour of the filling factor, I_{SC} remains a very accurate indicator of $P_{\max}$, even in the presence of phonons, which permits it to be used as the primary figure of merit in much of the following discussion. Limiting the discussion to I_{SC} also simplifies the analysis of the model, since the chemical potentials of the leads are sufficiently far away from the

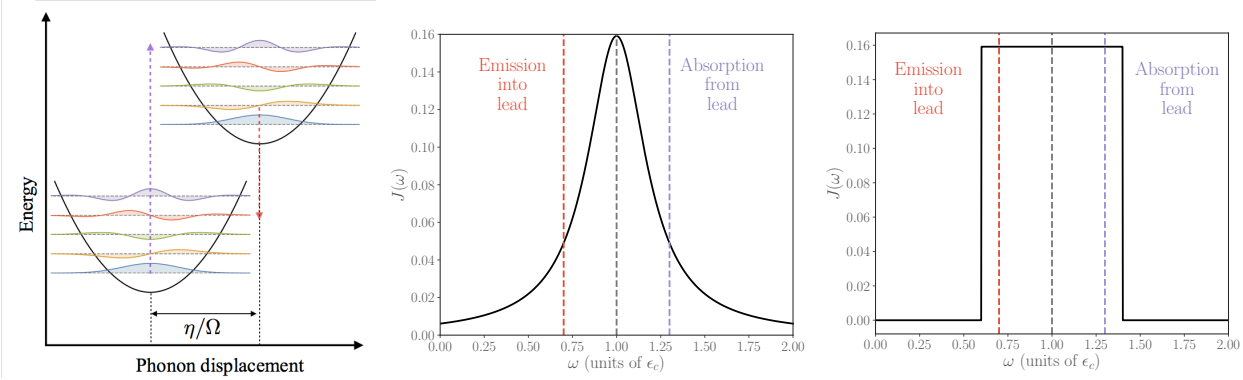

Figure 5.7: **(Left):** Schematic of the electronic manifold displacements induced by coupling to vibrational environments. Upward transitions are blue-shifted and downward transitions are red-shifted, which causes the average frequencies sampled by the optical and lead spectral densities to be augmented, these are indicated by purple and red dashed lines, respectively. **(Middle):** Depiction of non-additive effects for Lorentzian leads. The coupling between the conduction band and the right lead decreases due to curvature of spectral density. Red-shifted (blue-shifted) emission (absorption) frequency, leading to a diminished transition rate. **(Right):** Depiction of non-additive effects for locally-flat leads. The phonon-induced shifts to transition energies are less significant.

band edges so as to suppress any back-flow of current, as depicted in figure 5.2 (right). In other words, the tunnelling of electrons from the filled valence state to the left lead (creating a hole) are suppressed , i.e. $f_L \to 1$, as is the tunnelling of electrons from the right lead onto the conduction band state, $f_R \to 0$. Also, only the $V = 0$ case needs to be calculated, rather than the entire I-V curve, which has enormous computational benefits.

From figure 5.5 (left) we can see that, for this set of parameters, increasing phonon-coupling leads to a decline in short-circuit current. This can be understood by using a similar analysis as in the case of optical non-additivity. Where $U = 0$, in the absence of phonon-coupling and under short-circuit conditions, the four dominant processes are proportional to $\mathcal{L}_{|h\rangle\langle \mathrm{x}|}$ and $\mathcal{L}_{|\phi\rangle\langle e|}$, due to the right lead and $\mathcal{L}_{|\phi\rangle\langle h|}$, $\mathcal{L}_{|e\rangle\langle \mathrm{x}|}$ due to the left. Under these conditions, the processes are all on resonance with their respective lead. Finite phonon-coupling leads to relative displacements between the various electronic manifolds, associated with a change in equilibrium position of the nuclear coordinates. As we have seen in the case of optical processes in Chapter 3, these displacements cause a decrease (increase) in the average emission (absorption) wavelength, as depicted in figure 5.7 (left), but in this case instead of photons being emitted to the EM field it is electrons tunnelling into the leads. This shift to the transition frequency pushes the processes out of resonance with the leads as depicted in figure 5.7 (middle).

From the analysis of figures 5.5-5.6 above, it would appear that phonon-coupling only has a deleterious effect and inevitably diminishes current and power, however there are certain regimes where this is not the case. In the left and middle figures of 5.8, we calculate the percentage change of I_{SC} over a change in phonon-coupling strength $\Delta\alpha$ from $\alpha = 0$ to $\alpha = \Delta\alpha$, for $\Omega = 120$meV and $\Omega = 50$meV, respectively. This allows us to see how

current is affected by the inclusion of phonons and to identify any vibrationally-induced current enhancements. By scanning across a range of binding energies, we can see that the dependence of current-increase on binding energy is non-monotonic, with peaks where I_{SC} is enhanced. These peaks correspond to resonances between the binding energy U and the vibrational harmonics.

In order to fully understand the peaks in figure 5.8 (a) and (b) where $T_C = 300\text{K}$, we compare to the low-temperature case in figure (b), where normalised I_{SC} is given as a function of increasing α for different binding energies at $T_C = 50\text{K}$. In this figure we can see that I_{SC} always decreases as a function of α, even when binding energy and mode frequency are on resonance $U = \Omega = 50\text{meV}$. This is because the first vibrationally-excited state is never populated at $T_C = 50\text{K}$, so the non-additive renormalisation of fermion emission frequencies pushes the transitions away from the maximum of the Lorentzian, exactly as the central diagram in figure 5.7 shows.

Now we return to the $T_C = 300\text{K}$ case, where $\Omega = U$ as shown in figure 5.9, where left and middle plots show $\Omega = 50\text{meV}$ and $\Omega = 120\text{meV}$, respectively. As discussed, under these conditions increasing the phonon-coupling gives an increase in the current (blue solid lines). After a point, increasing phonon-coupling any further causes the average transition frequency to get pushed too far out of the optimal window, which causes current to decrease. This means that there is an intermediate coupling regime which maximises the non-additive current enhancement. The red dashed lines use a non-additive theory for the fermionic leads, but additive in the thermal electromagnetic field, this is included to gain insight into the underlying behaviour of the full model.

For lower vibrational frequencies, the non-additivity is dominated by the lead dissipators, since the large mode occupations cause large current enhancements to occur. For larger mode frequencies, a similar effect happens, however now the average vibrational mode occupations are lower, which diminishes the non-additive component in the lead dissipators. The electromagnetic dissipation is less influenced by the mode occupation, being largely dictated by the effective decay rates and thermal occupations of optically-active vibronic transitions, which means that optical non-additivity is more prominent in this regime. This is seen as a discrepancy between the fully non-additive (solid blue) and additive EM (dashed red) curves in the left and central plots in figure 5.9.

Due to the dependence on mode occupation at T_C, the efficacy of non-additive enhancement of current decreases as the mode frequency increases, causing it to be suppressed beyond $U > 130\text{meV}$. This means that for organic materials, where binding energies are normally $\geq 300\text{meV}$, a resonant mode may have too low an occupation for non-additive current enhancement to take place.

When the lead spectral density is flat around the range of important electronic transitions, as in figure 5.7 (right), then the non-additive renormalisation of fermionic transition frequencies does not have a significant effect on current and power. In this regime, the

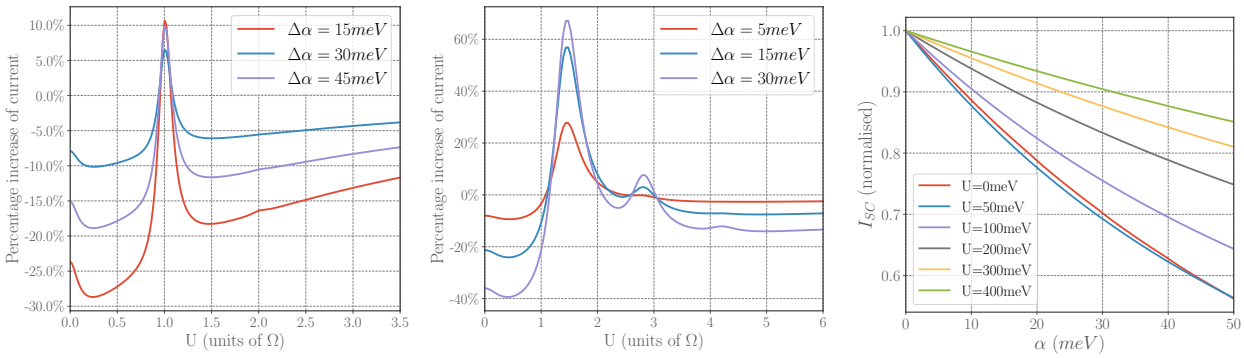

Figure 5.8: Percentage increase in I_{SC} due to a change in phonon-coupling strength from $\alpha = 0$ to $\alpha = \Delta\alpha$ as a function of binding energy, U. The peaks correspond to current enhancements due to resonances between the binding energy and the vibrational mode with **Left:** $\Omega = 120$meV. **Middle:** $\Omega = 50$meV. **Right:** Normalised short-circuit current as a function of phonon-coupling strength at low temperature, $T_C = 50$K, $\Omega = 50$meV. It can be seen that at low temperatures, current is never enhanced by phonons. For all plots we take Lorentzian lead SDs with width $\delta = 15$meV, also a phonon SD width of $\Gamma = 10$meV and $T_{EM} = 5800$K.

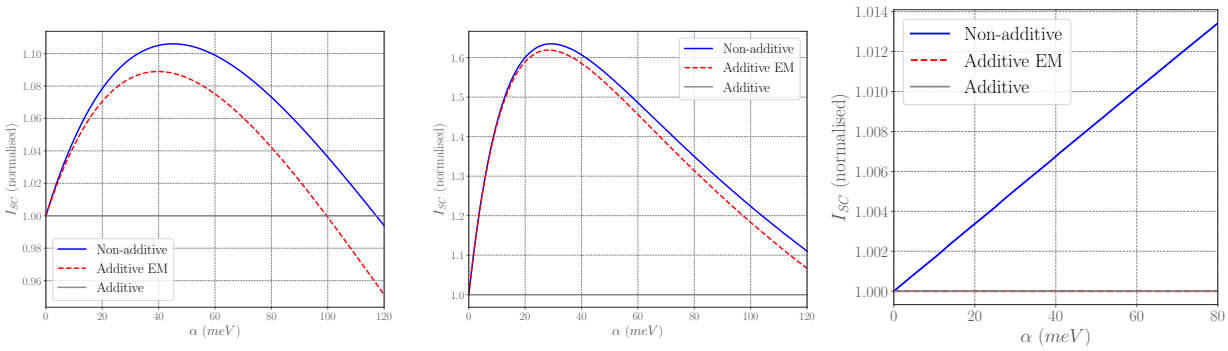

Figure 5.9: Comparison of short-circuit current for non-additive, fully additive and the optically additive theories. Binding energy is resonant with first vibrational level, $U = \Omega$. Narrow-lead regime gives rise to non-additivity which can enhance current by bringing exciton-dissociation processes onto resonance with the lead via the first vibrational state. **(Left):** $\Omega = 120$meV. **(Middle):** $\Omega = 50$meV. **(Right):** Wide-lead regime with $\Omega = 50$meV. Optical non-additivity dominates and an enhancement of current is observed due to the super-ohmic spectral density for the electromagnetic field.

phonon-coupling dependence of current is instead dominated by the non-additivity in the optical dissipator (as described in Chapter 3). The choice of super-ohmic spectral density gives rise to a positive increase in current with increasing α, as shown in figure 5.9 (right).

5.4 Conclusions

I have introduced a minimal model for a photocell device which explicitly takes into account the electrons and holes as separate charges. In performing the collective coordinate mapping, I have accounted for non-perturbative phonon interactions, which manifest themselves primarily as non-additive bath effects in the lead and electromagnetic dissipators. I have identified regimes where this non-additivity increases and decreases performance of the photocell and explained the physical basis for this.

One particularly interesting case where non-additive phonon effects enhance photocurrent is when the peak of the vibrational spectral density coincides with the exciton binding energy. Given sufficient vibrational mode occupation, this can increase the coupling between the leads and the excitonic levels, ultimately improving the performance of the photocell. For locally flat lead spectral densities, the phonon-induced processes are dominated by the optical non-additivity effects observed in the monomer model of Chapter 3.

Further work

The prevailing method for studying quantum photocells in the literature is through the use of fictitious-load models [18, 121, 122, 123], which attempt to account for the voltage generation of photovoltaics through equilibrium thermodynamic arguments. Rigorously linking the work in this chapter to the fictitious-load models is of great interest in future work.

Another area for future work would be to relax the restrictive form of system-leads coupling, which means that the valence and conduction band only couple to the left and right lead, respectively. This type of coupling currently prevents the model from being used in conjunction with larger molecular systems, such as the dimer model seen in the previous chapter. In this case the Jordan-Wigner transformation could become considerably more involved. Additionally, the way we have defined current in equation (5.57) may no longer hold, since phonons would now directly affect populations and so the same symmetry arguments would not hold.

It could also be possible to use the same model treated in this chapter to investigate light emitting diodes and other photonic systems. This could be done by setting $T_{EM} = 0$ and investigating the emission properties of the system under different potential biases, using the theory from Chapter 3.

Blank page

Chapter 6

Concluding remarks

In this thesis I have developed a methodology for modelling strongly-coupled open-quantum systems that interact with multiple baths at different temperatures. A common theme in this work has been that non-perturbative phonon coupling can cause a break-down of traditional quantum optics approaches and that enforcing additivity between environments should be exercised with caution. This has specifically been applied to models of interest within the contexts of natural and artificial light-harvesting, however the same phenomena are likely to arise in many damped-driven quantum systems with strongly-coupled low-frequency baths.

In Chapter 3, it was shown that the collective coordinate approach gives rise to non-additive effects in the optical decay rates of a quantum emitter. Under incoherent thermal driving, the frequency dependence of the light-matter coupling and thermal occupations can lead to population inversion for super-ohmic optical spectral densities. I investigated the conditions for this behaviour in detail with an effective analytical model, identifying a restriction on the form of the optical spectral density for non-additive population enhancement to occur.

In Chapter 4, I studied a model dimer and demonstrated how strongly-coupled phonons leads to renormalisation of the dipole-dipole coupling. This is a non-perturbative effect which is accounted for in the additive theory as well, but is completely missed in a weak-coupling approach. Non-additive optical effects were also seen to be significant at strong phonon coupling, ultimately diminishing the excited state population, due to the linear optical spectral density used. The inclusion of phonons is seen to always be deleterious to the excitation of the dimer, which may cast doubt onto the practical importance of dark-state protection in proposed molecular photocells.

In Chapter 5, I derived a model of a toy molecular photocell. In this setting, it was shown how phonon-coupling might affect photocurrent, directly through environmental non-additivity. This ultimately depends on the form of lead-molecule coupling and on the curvature of the lead and optical spectral densities. Regimes were identified where phonon effects could increase the power output of the photocell, by overcoming the Coulombic binding energy to allow dissociation of excitons into free charges.

Blank page

Appendices

.1 Contour integration in the Fourier-space CC operator

This can be done by using the residue theorem - integrating anti-clockwise around a semicircle on the upper-half of the complex plane, the straight section of which is along the real line. First, we locate the poles of the integrand. The denominator has zeros at $\nu = \pm z$ and $\nu = 0$, but since we are concerned with only the upper-half plane only the positive z (depending on how we define it) will be contained inside the semicircle. The singularity at $\nu = 0$ must be *removable* since it lies *on* the boundary of the contour (causing residue theorem to breakdown otherwise) which imposes a restriction on the form of $J_{SB}(\nu)$ that it must be at least proportional to ν. Other restrictions on J_{SB} are that it is a real-valued function with an arbitrary number of poles and (for applications later on) that it is an odd function. We decompose the SD into the form

$$J_{SB}(\nu) = \frac{\nu f(\nu)}{\prod_l^N (\nu - \alpha_l)(\nu - \alpha_l^*)}, \tag{1}$$

where any poles are explicitly shown as conjugate pairs of arbitrary complex numbers, so that the function is real-valued. The function $f(\nu)$ is some analytic function and the ν in the numerator is necessary to remove the singularity at $\nu = 0$ in the denominator. We also know that the function $f\nu$ must be real valued, since the spectral density must also be real valued. Inspecting the integral in equation 2.17 we have

$$I(z) = \int_0^\infty d\nu \frac{\nu f(\nu)}{\left(\prod_l^N (\nu - \alpha_l)(\nu - \alpha_l^*)\right)} \cdot \frac{1}{\nu(\nu - z)(\nu + z)}, \tag{2}$$

where the singularity at $\nu = 0$ has now been removed. We now make some simplifying assumptions. Firstly, we assume that $\{\alpha_l\}$ are purely imaginary such that $\alpha = ia_l$ where $a_l > 0$, this is justified since we do not expect a physical spectral density to diverge at specific points on the real line. Secondly, we set $N = 2$, in order to simplify calculations. The integral now becomes

$$\begin{aligned} I(z) &= \int_0^\infty \frac{f(\nu)}{(\nu - ia_1)(\nu + ia_1)(\nu - ia_2)(\nu + ia_2)} \cdot \frac{1}{(\nu - z)(\nu + z)} \\ &= \int_0^\infty \frac{f(\nu)}{(\nu^2 + a_1^2)(\nu^2 + a_2^2)(\nu - z)(\nu + z)}, \end{aligned} \tag{3}$$

for which we calculate the residues in the upper-half plane $\nu \in \{z, ia_1, ia2\}$,

$$Res(z) = \lim_{\nu \to z} \frac{f(\nu)}{(\nu - ia_1)(\nu + ia_1)(\nu - ia_2)(\nu + ia_2)(\nu + z)} = \frac{f(z)}{2z(z^2 + a_1^2)(z^2 + a_2^2)} \tag{4}$$

$$Res(ia_1) = \lim_{\nu \to ia_1} \frac{f(\nu)}{(\nu + ia_1)(\nu - ia_2)(\nu + ia_2)(\nu - z)(\nu + z)} = \frac{if(ia_1)}{2a_1(a_2^2 - a_1^2)(z^2 + a_1^2)} \tag{5}$$

$$Res(ia_2) = \lim_{\nu \to ia_2} \frac{f(\nu)}{(\nu - ia_1)(\nu + ia_1)(\nu + ia_2)(\nu - z)(\nu + z)} = \frac{if(ia_2)}{2a_2(a_1^2 - a_2^2)(z^2 + a_2^2)}. \tag{6}$$

From the residue theorem, we know that the integral around the whole contour is equal to the sum of the residues. This integral consists of a straight section along the real line and an arc section, we introducing a change of variables $\nu = \rho e^{i\theta}$,

$$\oint_{Contour} f(\nu)d\nu = \oint_{Real} f(\nu)d\nu + \oint_{Arc} f(\nu)d\nu \tag{7}$$

$$= \int_{-\rho}^{\rho} \frac{J_{SB}(\nu)}{\nu(\nu^2 - z^2)} d\nu + \int_0^{\pi} \frac{\rho i e^{i\theta} J_{SB}(\rho e^{i\theta})}{\rho e^{i\theta}(\rho^2 e^{2i\theta} - z^2)} d\theta \equiv I_1 + I_2, \tag{8}$$

where the integral over the straight section has been extended over the whole real line by the assumption $J_{SB}(-\nu) = -J_{SB}(\nu)$. For simplicity, we will now consider only situations where the arc contribution of the integral goes to zero value. Since the value of the entire integral only depends on the residues contained in the contour not on the radius of the arc, it should be the same when taking the limit $\rho \to \infty$. We will now see what restrictions on the spectral density $J_{SB}(\nu)$ need to be made in order for $I_2 \to 0$ as $\rho \to \infty$. A simple way of doing this is to show that the modulus of the integrand in

$$I_2 = \int_0^{\pi} i \frac{J_{SB}(\rho e^{i\theta})}{\rho^2 e^{2i\theta} - z^2} d\theta, \tag{9}$$

is less than or equal to zero; since a modulus can not be negative the equality follows. Taking the modulus of the whole integral and using the triangle inequality $|a + b| \leq |a| + |b|$ leads us to

$$\left| \int_0^{\pi} i \frac{J_{SB}(\rho e^{i\theta})}{\rho^2 e^{2i\theta} - z^2} d\theta \right| \leq \int_0^{\pi} \left| i \frac{J_{SB}(\rho e^{i\theta})}{\rho^2 e^{2i\theta} - z^2} d\theta \right| = \int_0^{\pi} \frac{\left| J_{SB}(\rho e^{i\theta}) \right|}{|\rho^2 e^{2i\theta} - z^2|} d\theta \leq \int_0^{\pi} \frac{\left| J_{SB}(\rho e^{i\theta}) \right|}{\rho^2 - |z^2|} d\theta. \tag{10}$$

Where the denominator in the final step is reached by using the reverse triangle inequality $|a - b| \geq |a| - |b|$. Now we suppose that J_{SB} is always bounded by some polynomial: $\exists \rho, k$ s.t. $|J_{SB}(\rho e^{i\theta})| \leq k\rho^s$, where ρ needs to be large enough to contain the poles in the upper-half plane. This yields

$$I_2 \leq \int_0^{\pi} \frac{k\rho^s}{\rho^2 - |z^2|} d\theta = \frac{\pi k \rho^s}{\rho^2 - |z^2|}, \tag{11}$$

which tends to zero as $\rho \to \infty$ if $s < 2$, as long as $|z^2|$ is finite. Here we have assumed only two poles, but we will show that the number of poles does not explicitly change the result

we are interested in.

We have now enforced some restrictions on the spectral density, that it has two poles and increases slower than ν^2 as $\nu \to \infty$,

$$\tilde{K}(z) = -z^2\Bigg(1 + 2\pi i\Bigg(\frac{f(z)}{(z^2+a_1^2)(z^2+a_2^2)(2z)} + \frac{if(ia_1)}{(a_1^2-a_2^2)(a_2^2+z^2)(2a_1)} + \frac{if(ia_2)}{(a_1^2-a_2^2)(a_1^2+z^2)(2a_2)}\Bigg)\Bigg). \tag{12}$$

Comparing $Res(\nu = z)$ to the original spectral density in 1, it can be seen that performing the integral has resulted in the function $J_{SB}(\nu)$ being evaluated at z and divided by $2z^2$. We can then recast 12 as

$$\tilde{K}(z) = -z^2\left(1 + i\pi\left(\frac{J_{SB}(z)}{z^2}\right) - \frac{\pi f(ia_1)}{(a_1^2-a_2^2)(a_2^2+z^2)(a_1)} - \frac{\pi f(ia_2)}{(a_1^2-a_2^2)(a_1^2+z^2)(a_2)}\right). \tag{13}$$

Blank page

Bibliography

[1] A. Nazir and D. P. McCutcheon, "Modelling exciton-phonon interactions in optically driven quantum dots," *J. Phys.: Condens. Matter*, vol. 28, p. 103002, 2016.

[2] A. Carmele and S. Reitzenstein, "Non-markovian features in semiconductor quantum optics: Quantifying the role of phonons in experiment and theory," *Nanophotonics*, pp. 655–683, 04 2019.

[3] P. Kok and B. W. Lovett, *Introduction to Optical Quantum Information Processing*. Cambridge University Press, 2010.

[4] G. Engel, J. Stenger, H. M. Vaswani, M. Cho, R. E. Blankenship, and G. R. Fleming, "Evidence for wavelike energy transfer through quantum coherence in photosynthetic systems," *Nature*, vol. 446, no. 7137, pp. 782–786, 2007.

[5] G. Panitchayangkoon, D. Voronine, D. Abramavicius, J. Caram, N. Lewis, S. Mukamel, and G. S Engel, "Direct evidence of quantum transport in photosynthetic light-harvesting complexes," *Proceedings of the National Academy of Sciences of the United States of America*, vol. 108, pp. 20908–12, 12 2011.

[6] E. Collini, C. Y. Wong, K. E. Wilk, P. M. G. Curmi, P. Brumer, and G. D. Scholes, "Coherently wired light-harvesting in photosynthetic marine algae at ambient temperature," *Nature*, vol. 463, no. 7281, pp. 644–647, 2010.

[7] Y. Sato and B. Doolittle, "Influence of intra-pigment vibrations on dynamics of photosynthetic exciton," *Journal of Chemical Physics*, vol. 141, no. 18, p. 185102, 2014.

[8] S. J. Jang and B. Mennucci, "Delocalized excitons in natural light-harvesting complexes," *Reviews of Modern Physics*, vol. 90, no. 3, p. 35003, 2018.

[9] Z. Zhang and J. Wang, "Origin of long-lived quantum coherence and excitation dynamics in pigment-protein complexes," *Scientific Reports*, vol. 6, p. 37629, 2016.

[10] M. Maiuri, E. E. Ostroumov, R. G. Saer, R. E. Blankenship, and G. D. Scholes, "Coherent wavepackets in the Fenna Matthews Olson complex are robust to excitonic-structure perturbations caused by mutagenesis," *Nature Chemistry*, vol. 10, no. 2, pp. 177–183, 2018.

[11] F. Caruso, A. W. Chin, A. Datta, S. F. Huelga, and M. B. Plenio, "Highly efficient energy excitation transfer in light-harvesting complexes: The fundamental role of noise-assisted transport," *Journal of Chemical Physics*, vol. 131, no. 10, p. 105106, 2009.

[12] E. K. Irish, R. Gómez-Bombarelli, and B. W. Lovett, "Vibration-assisted resonance in photosynthetic excitation-energy transfer," *Phys. Rev. A*, vol. 90, p. 012510, Jul 2014.

[13] A. Kolli, E. J. O'Reilly, G. D. Scholes, and A. Olaya-Castro, "The fundamental role of quantized vibrations in coherent light harvesting by cryptophyte algae," *Journal of Chemical Physics*, vol. 137, no. 17, 2012.

[14] Y. Fujihashi, G. R. Fleming, and A. Ishizaki, "Influences of quantum mechanically mixed electronic and vibrational pigment states in 2D electronic spectra of photosynthetic systems: Strong electronic coupling cases," *arXiv e-prints*, June 2015.

[15] M. B. Plenio, J. Almeida, and S. F. Huelga, "Origin of long-lived oscillations in 2D-spectra of a quantum vibronic model: Electronic versus vibrational coherence," *The Journal of chemical physics*, vol. 139, p. 235102, Dec. 2013.

[16] J. Iles-Smith, A. G. Dijkstra, N. Lambert, and A. Nazir, "Energy transfer in structured and unstructured environments: Master equations beyond the Born-Markov approximations," *Journal of Chemical Physics*, vol. 144, no. 4, p. 44110, 2016.

[17] J. L. Brédas, E. H. Sargent, and G. D. Scholes, "Photovoltaic concepts inspired by coherence effects in photosynthetic systems," *Nature Materials*, vol. 16, no. 1, pp. 35–44, 2016.

[18] K. E. Dorfman, D. V. Voronine, S. Mukamel, and M. O. Scully, "Photosynthetic reaction center as a quantum heat engine," *Proceedings of the National Academy of Sciences*, vol. 110, no. 8, pp. 2746–2751, 2013.

[19] D. Gelbwaser-Klimovsky and A. Aspuru-Guzik, "On thermodynamic inconsistencies in several photosynthetic and solar cell models and how to fix them," *Chemical Science*, vol. 8, no. 2, pp. 1008–1014, 2017.

[20] R. Barnett, S. Barnett, P. Radmore, and D. Radmore, *Methods in Theoretical Quantum Optics*. Oxford Series in Optical & Imaging Sciences, Clarendon Press, 1997.

[21] H.-P. Breuer and F. Petruccione, *The Theory of Open Quantum Systems*. Oxford University Press, 2002.

[22] H. Carmichael and S.-V. (Berlin)., *Statistical Methods in Quantum Optics 1: Master Equations and Fokker-Planck Equations*. Physics and astronomy online library, Springer, 1998.

[23] P. Strasberg, G. Schaller, N. Lambert, and T. Brandes, "Nonequilibrium thermodynamics in the strong coupling and non-Markovian regime based on a reaction coordinate mapping," *New Journal of Physics*, vol. 18, no. 7, p. 073007, 2016.

[24] G. W. Ford, J. T. Lewis, and R. F. Oconnell, "Quantum Langevin equation," *Physical Review A*, vol. 37, no. 11, pp. 4419–4428, 1988.

[25] J. Iles-Smith, N. Lambert, and A. Nazir, "Environmental dynamics, correlations, and the emergence of noncanonical equilibrium states in open quantum systems," *Physical Review A - Atomic, Molecular, and Optical Physics*, vol. 90, no. 3, pp. 1–9, 2014.

[26] R. Silbey and R. A. Harris, "Variational calculation of the dynamics of a two level system interacting with a bath," *The Journal of Chemical Physics*, vol. 80, no. 6, pp. 2615–2617, 1984.

[27] D. P. S. McCutcheon and A. Nazir, "Quantum dot rabi rotations beyond the weak exciton–phonon coupling regime," *New Journal of Physics*, vol. 12, p. 113042, Nov 2010.

[28] A. Garg, J. N. Onuchic, and V. Ambegaokar, "Effect of friction on electron transfer in biomolecules," *The Journal of Chemical Physics*, vol. 83, no. 9, pp. 4491–4503, 1985.

[29] K. H. Hughes, C. D. Christ, and I. Burghardt, "Effective-mode representation of non-markovian dynamics: A hierarchical approximation of the spectral density. i. application to single surface dynamics," *The Journal of Chemical Physics*, vol. 131, no. 2, p. 024109, 2009.

[30] A. Strathearn, P. Kirton, D. Kilda, J. Keeling, and B. Lovett, "Efficient non-Markovian quantum dynamics using time-evolving matrix product operators," *Nature Comms.*, vol. 9, p. 3322, 2018.

[31] N. Makri and D. E. Makarov, "Tensor propagator for iterative quantum time evolution of reduced density matrices. I. Theory," *The Journal of chemical physics*, vol. 102, pp. 4600–4610, Mar 1995.

[32] N. Makri and D. E. Makarov, "Tensor propagator for iterative quantum time evolution of reduced density matrices. II. Numerical methodology," *The Journal of chemical physics*, vol. 102, pp. 4611–4618, Mar 1995.

[33] F. A. Y. N. Schröder, D. H. P. Turban, A. J. Musser, N. D. M. Hine, and A. W. Chin, "Tensor network simulation of multi-environmental open quantum dynamics via machine learning and entanglement renormalisation," *Nature Communications*, vol. 10, no. 1, p. 1062, 2019.

[34] H. Wang and H.-D. Meyer, "On regularizing the ml-mctdh equations of motion," *The Journal of Chemical Physics*, vol. 149, no. 4, p. 044119, 2018.

[35] T. Yoshitaka and K. Ryogo, "Time Evolution of a Quantum System in Contact with a Nearly Gaussian-Markoffian Noise Bath," *J. Phys. Soc. Jpn.*, vol. 58, no. 1, pp. 101–114, 1989.

[36] J. Jin, X. Zheng, and Y. Yan, "Exact dynamics of dissipative electronic systems and quantum transport: Hierarchical equations of motion approach," *The Journal of Chemical Physics*, vol. 128, no. 23, p. 234703, 2008.

[37]

[38] H. Maguire, J. Iles-Smith, and A. Nazir, "Environmental nonadditivity and franck-condon physics in nonequilibrium quantum systems," *Phys. Rev. Lett.*, vol. 123, p. 093601, Aug 2019.

[39] F. Haake, *Statistical Treatment of Open Systems by Generalized Master Equations*, pp. 98–168. Berlin, Heidelberg: Springer Berlin Heidelberg, 1973.

[40] H. Liu, L. Zhu, S. Bai, and Q. Shi, "Reduced quantum dynamics with arbitrary bath spectral densities: Hierarchical equations of motion based on several different bath decomposition schemes," *The Journal of Chemical Physics*, vol. 140, no. 13, p. 134106, 2014.

[41] R. Martinazzo, B. Vacchini, K. H. Hughes, and I. Burghardt, "Communication: Universal Markovian reduction of Brownian particle dynamics," *Journal of Chemical Physics*, vol. 134, no. 1, p. 011101, 2011.

[42] G. Mahan, *Many-Particle Physics*. Physics of Solids and Liquids, Springer US, 2000.

[43] S. S. Mukamel, *Principles of nonlinear optical spectroscopy*. Oxford series in optical and imaging sciences ; 6, New York ;: Oxford University Press, c1995.

[44] N. Lambert, Y.-N. Chen, Y.-C. Cheng, C.-M. Li, G.-Y. Chen, and F. Nori, "Quantum biology," *Nature Physics*, vol. 9, p. 10, Dec 2012.

[45] S. F. Huelga and M. B. Plenio, "Vibrations, quanta and biology," *Contemporary Physics*, vol. 54, no. 4, pp. 181–207, 2013.

[46] E. Romero, R. Augulis, V. I. Novoderezhkin, M. Ferretti, J. Thieme, D. Zigmantas, and R. Van Grondelle, "Quantum coherence in photosynthesis for efficient solar-energy conversion," *Nature Physics*, vol. 10, no. 9, 2014.

[47] M. Thoss, H. Wang, and W. H. Miller, "Self-consistent hybrid approach for complex systems: Application to the spin-boson model with Debye spectral density," *Journal of Chemical Physics*, vol. 115, no. 7, pp. 2991–3005, 2001.

[48] V. May and O. Kühn, *Charge and Energy Transfer Dynamics in Molecular Systems*. Wiley, Feb 2004.

[49] C. Gerry and P. Knight, *Introductory Quantum Optics*. Cambridge University Press, 2004.

[50] J.-B. Trebbia, H. Ruf, P. Tamarat, and B. Lounis, "Efficient generation of near infra-red single photons from the zero-phonon line of a single molecule," *Opt. Express*, vol. 17, pp. 23986–23991, Dec 2009.

[51] A. Stokes, A. Kurcz, T. P. Spiller, and A. Beige, "Extending the validity range of quantum optical master equations," *Physical Review A - Atomic, Molecular, and Optical Physics*, vol. 85, no. 5, pp. 1–14, 2012.

[52] A. Nitzan, *Chemical Dynamics in Condensed Phases*. Oxford University Press, 2006.

[53] S. Jang and Y.-C. Cheng, "Resonance energy flow dynamics of coherently delocalized excitons in biological and macromolecular systems: Recent theoretical advances and open issues," *WIREs Comput. Mol. Sci.*, vol. 3, no. 1, pp. 84–104, 2012.

[54] M. Wertnik, A. Chin, F. Nori, and N. Lambert, "Optimizing co-operative multi-environment dynamics in a dark-state-enhanced photosynthetic heat engine," *Journal of Chemical Physics*, vol. 149, no. 8, p. 84112, 2018.

[55] I. Akihito and T. Yoshitaka, "Quantum Dynamics of System Strongly Coupled to Low-Temperature Colored Noise Bath: Reduced Hierarchy Equations Approach," *J. Phys. Soc. Jpn.*, vol. 74, no. 12, pp. 3131–3134, 2005.

[56] A. Ishizaki and G. R. Fleming, "Unified treatment of quantum coherent and incoherent hopping dynamics in electronic energy transfer: Reduced hierarchy equation approach," *Journal of Chemical Physics*, vol. 130, no. 23, p. 234111, 2009.

[57] N. Makri and D. E. Makarov, "Tensor propagator for iterative quantum time evolution of reduced density matrices. I. Theory," *Journal of Chemical Physics*, vol. 102, no. 11, pp. 4600–4610, 1995.

[58] N. Makri and D. E. Makarov, "Tensor propagator for iterative quantum time evolution of reduced density matrices. II. Numerical methodology," *Journal of Chemical Physics*, vol. 102, no. 11, pp. 4611–4618, 1995.

[59] P. Nalbach, D. Braun, and M. Thorwart, "Exciton transfer dynamics and quantumness of energy transfer in the Fenna-Matthews-Olson complex," *Phys. Rev. E*, vol. 84, p. 41926, Oct 2011.

[60] R. Rosenbach, J. Cerrillo, S. F. Huelga, J. Cao, and M. B. Plenio, "Efficient simulation of non-Markovian system-environment interaction," *New J. Phys.*, vol. 18, no. 2, p. 23035, 2016.

[61] F. A. Y. N. Schröder and A. W. Chin, "Simulating open quantum dynamics with time-dependent variational matrix product states: Towards microscopic correlation of environment dynamics and reduced system evolution," *Phys. Rev. B*, vol. 93, p. 75105, 2016.

[62] C. Kreisbeck, T. Kramer, M. Rodrguez, and B. Hein, "High-Performance Solution of Hierarchical Equations of Motion for Studying Energy Transfer in Light-Harvesting Complexes," *Journal of Chemical Theory and Computation*, vol. 7, no. 7, pp. 2166–2174, 2011.

[63] A. G. Dijkstra and Y. Tanimura, "The role of the environment time scale in light-harvesting efficiency and coherent oscillations," *New J. Phys.*, vol. 14, no. 7, p. 73027, 2012.

[64] F. Fassioli, A. Olaya-Castro, and G. D. Scholes, "Coherent Energy Transfer under Incoherent Light Conditions," *J. Phys. Chem. Lett.*, vol. 3, no. 21, pp. 3136–3142, 2012.

[65] P. Kaer, T. R. Nielsen, P. Lodahl, A.-P. Jauho, and J. Mørk, "Microscopic theory of phonon-induced effects on semiconductor quantum dot decay dynamics in cavity QED," *Phys. Rev. B*, vol. 86, p. 85302, Aug 2012.

[66] A. Ulhaq, S. Weiler, C. Roy, S. M. Ulrich, M. Jetter, S. Hughes, and P. Michler, "Detuning-dependent Mollow triplet of a coherently-driven single quantum dot," *Opt. Express*, vol. 21, no. 4, p. 4382, 2013.

[67] D. P. S. McCutcheon and A. Nazir, "Model of the Optical Emission of a Driven Semiconductor Quantum Dot: Phonon-Enhanced Coherent Scattering and Off-Resonant Sideband Narrowing," *Phys. Rev. Lett.*, vol. 110, p. 217401, May 2013.

[68] R. Betzholz, J. M. Torres, and M. Bienert, "Quantum optical master equation for solid-state quantum emitters," *Phys. Rev. A*, vol. 90, p. 63818, Dec 2014.

[69] N. Killoran, S. F. Huelga, and M. B. Plenio, "Enhancing light-harvesting power with coherent vibrational interactions: A quantum heat engine picture," *Journal of Chemical Physics*, vol. 143, no. 15, p. 155102, 2015.

[70] H.-B. Chen, P.-Y. Chiu, and Y.-N. Chen, "Vibration-induced coherence enhancement of the performance of a biological quantum heat engine," *Phys. Rev. E*, vol. 94, p. 52101, Nov 2016.

[71] A. M. Barth, A. Vagov, and V. M. Axt, "Path-integral description of combined Hamiltonian and non-Hamiltonian dynamics in quantum dissipative systems," *Phys. Rev. B*, vol. 94, p. 125439, Sep 2016.

[72] M. Qin, H. Z. Shen, X. L. Zhao, and X. X. Yi, "Effects of system-bath coupling on a photosynthetic heat engine: A polaron master-equation approach," *Phys. Rev. A*, vol. 96, p. 12125, Jul 2017.

[73] R. Stones, H. Hossein-Nejad, R. van Grondelle, and A. Olaya-Castro, "On the performance of a photosystem II reaction centre-based photocell," *Chem. Sci.*, vol. 8, no. 10, pp. 6871–6880, 2017.

[74] I. B. Juhász and Á. I. Csurgay, "Impact of undamped and damped intramolecular vibrations on the efficiency of photosynthetic exciton energy transfer," *AIP Advances*, vol. 8, no. 4, p. 45318, 2018.

[75] H. C. H. Chan, O. E. Gamel, G. R. Fleming, and K. B. Whaley, "Single-photon absorption by single photosynthetic light-harvesting complexes," *J. Phys. B: At. Mol. Opt. Phys*, vol. 51, no. 5, p. 54002, 2018.

[76] O. J. Gómez-Sánchez and H. Y. Ramírez, "Solid-state emitter embedded in a microcavity under intense excitation: A variational master-equation approach," *Physical Review A*, vol. 98, no. 5, pp. 1–9, 2018.

[77] L. Dong, C. Zhu, and H. Pu, "Photon-induced spin-orbit coupling in ultracold atoms inside optical cavity," *Atoms*, vol. 3, p. 182, 04 2015.

[78] M. Scala, B. Militello, A. Messina, J. Piilo, and S. Maniscalco, "Microscopic derivation of the Jaynes-Cummings model with cavity losses," *Phys. Rev. A*, vol. 75, p. 13811, Jan 2007.

[79] M. Scala, B. Militello, A. Messina, S. Maniscalco, J. Piilo, and K.-A. Suominen, "Cavity losses for the dissipative JaynesCummings Hamiltonian beyond rotating wave approximation," *Journal of Physics A: Mathematical and Theoretical*, vol. 40, no. 48, p. 14527, 2007.

[80] G. G. Giusteri, F. Recrosi, G. Schaller, and G. L. Celardo, "Interplay of different environments in open quantum systems: Breakdown of the additive approximation," *Physical Review E*, vol. 96, no. 1, pp. 1–10, 2017.

[81] J. Kołodyński, J. B. Brask, M. Perarnau-Llobet, and B. Bylicka, "Adding dynamical generators in quantum master equations," *Phys. Rev. A*, vol. 97, p. 062124, Jun 2018.

[82] M. T. Mitchison and M. B. Plenio, "Non-additive dissipation in open quantum networks out of equilibrium," *New J. Phys.*, vol. 20, no. 3, p. 33005, 2018.

[83] P. P. Hofer, M. Perarnau-Llobet, L. D. M. Miranda, G. Haack, R. Silva, J. B. Brask, and N. Brunner, "Markovian master equations for quantum thermal machines: local versus global approach," *New J. Phys.*, vol. 19, no. 12, p. 123037, 2017.

[84] J. O. Gonzlez, L. A. Correa, G. Nocerino, J. P. Palao, D. Alonso, and G. Adesso, "Testing the Validity of the Local and Global GKLS Master Equations on an Exactly Solvable Model," *Open Syst. Inf. Dyn.*, vol. 24, no. 04, p. 1740010, 2017.

[85] J. Olšina, A. G. Dijkstra, C. Wang, and J. Cao, "Can Natural Sunlight Induce Coherent Exciton Dynamics?," *arXiv:1408.5385*.

[86] J. del Pino, F. A. Y. N. Schröder, A. W. Chin, J. Feist, and F. J. Garcia-Vidal, "Tensor network simulation of non-Markovian dynamics in organic polaritons," *arXiv:1804.04511*.

[87] H. J. Carmichael, *Statistical Methods in Quantum Optics 2:˜Non-Classical Fields*. Springer, 2009.

[88] A. G. Dijkstra and Y. Tanimura, "Linear and third- and fifth-order nonlinear spectroscopies of a charge transfer system coupled to an underdamped vibration," *Journal of Chemical Physics*, vol. 142, no. 21, p. 212423, 2015.

[89] R. Loudon, *The Quantum Theory of Light*. Oxford University Press, 2000.

[90] G. S. Agarwal, *Quantum Optics*. Cambridge University Press, 2013.

[91] R. C. Schofield, K. D. Major, S. Grandi, S. Boissier, E. A. Hinds, and A. S. Clark, "Efficient excitation of dye molecules for single photon generation," *Journal of Physics Communications*, vol. 2, p. 115027, Nov 2018.

[92] R. L. De Sousa, J. L. Alves, and H. W. Alves, "Vibrational properties of PPP and PPV," *Materials Science and Engineering C*, vol. 24, no. 5, pp. 601–605, 2004.

[93] J. Du, T. Teramoto, K. Nakata, E. Tokunaga, and T. Kobayashi, "Real-time vibrational dynamics in chlorophyll a studied with a few-cycle pulse laser.," *Biophysical journal*, vol. 101, no. 4, pp. 995–1003, 2011.

[94] E. Romero, R. Augulis, V. I. Novoderezhkin, M. Ferretti, J. Thieme, D. Zigmantas, and R. van Grondelle *Nature Phys.*, vol. 10, p. 676, 2014.

[95] T. Basché, W. E. Moerner, M. Orrit, and H. Talon, "Photon antibunching in the fluorescence of a single dye molecule trapped in a solid," *Phys. Rev. Lett.*, vol. 69, pp. 1516–1519, Sep 1992.

[96] F. Treussart, A. Clouqueur, C. Grossman, and J.-F. Roch, "Photon antibunching in the fluorescence of a single dye molecule embedded in a thin polymer film," *Opt. Lett.*, vol. 26, pp. 1504–1506, Oct 2001.

[97] C. K. Hong, Z. Y. Ou, and L. Mandel, "Measurement of subpicosecond time intervals between two photons by interference," *Phys. Rev. Lett.*, vol. 59, pp. 2044–2046, Nov 1987.

[98] M. Varnava, D. E. Browne, and T. Rudolph, "How good must single photon sources and detectors be for efficient linear optical quantum computation?," *Phys. Rev. Lett.*, vol. 100, p. 060502, Feb 2008.

[99] N. Somaschi, V. Giesz, L. De Santis, J. C. Loredo, M. P. Almeida, G. Hornecker, S. L. Portalupi, T. Grange, C. Antón, J. Demory, C. Gómez, I. Sagnes, N. D. Lanzillotti-Kimura, A. Lemaítre, A. Auffeves, A. G. White, L. Lanco, and P. Senellart, "Near-optimal single-photon sources in the solid state," *Nature Photonics*, vol. 10, pp. 340 EP –, 03 2016.

[100] P. Senellart, G. Solomon, and A. White, "High-performance semiconductor quantum-dot single-photon sources," *Nature Nanotechnology*, vol. 12, p. 1026, 11 2017.

[101] L. Hanschke, K. A. Fischer, S. Appel, D. Lukin, J. Wierzbowski, S. Sun, R. Trivedi, J. Vučković, J. J. Finley, and K. Müller, "Quantum dot single-photon sources with ultra-low multi-photon probability," *npj Quantum Information*, vol. 4, no. 1, p. 43, 2018.

[102] J. Iles-Smith, D. P. McCutcheon, A. Nazir, and J. Mørk, "Phonon scattering inhibits simultaneous near-unity efficiency and indistinguishability in semiconductor single-photon sources," *Nature Photonics*, vol. 11, no. 8, pp. 521–526, 2017.

[103] C. Polisseni, K. D. Major, S. Boissier, S. Grandi, A. S. Clark, and E. A. Hinds, "Stable, single-photon emitter in a thin organic crystal for application to quantum-photonic devices," *Optics Express*, vol. 24, no. 5, p. 5615, 2016.

[104] S. Grandi, K. D. Major, C. Polisseni, S. Boissier, A. S. Clark, and E. A. Hinds, "Quantum dynamics of a driven two-level molecule with variable dephasing," *Physical Review A*, vol. 94, no. 6, 2016.

[105] R. C. Schofield, K. D. Major, S. Grandi, S. Boissier, E. A. Hinds, and A. S. Clark, "Efficient excitation of dye molecules for single photon generation," *Journal of Physics Communications*, vol. 2, no. 11, p. 115027, 2018.

[106] T. Ritz, S. Adem, and K. Schulten, "A model for photoreceptor-based magnetoreception in birds," *Biophysical Journal*, vol. 78, no. 2, pp. 707 – 718, 2000.

[107] R. D. Hoehn, D. E. Nichols, H. Neven, and S. Kais, "Status of the vibrational theory of olfaction," *Frontiers in Physics*, vol. 6, p. 25, 2018.

[108] T. Brixner, J. Stenger, H. M. Vaswani, M. Cho, R. E. Blankenship, and G. R. Fleming, "Two-dimensional spectroscopy of electronic couplings in photosynthesis.," *Nature*, vol. 434, no. 7033, pp. 625–628, 2005.

[109] J. Adolphs and T. Renger, "How Proteins Trigger Excitation Energy Transfer in the FMO Complex of Green Sulfur Bacteria," *Biophysical Journal*, vol. 91, no. 8, pp. 2778–2797, 2006.

[110] R. E. Fenna and B. W. Matthews, "Chlorophyll arrangement in a bacteriochlorophyll protein from chlorobium limicola," *Nature*, vol. 258, no. 5536, pp. 573–577, 1975.

[111] M. Mohseni, P. Rebentrost, S. Lloyd, and A. Aspuru-Guzik, "Environment-assisted quantum walks in photosynthetic energy transfer," *Journal of Chemical Physics*, vol. 129, no. 17, 2008.

[112] A. W. Chin, J. Prior, R. Rosenbach, F. Caycedo-Soler, S. F. Huelga, and M. B. Plenio, "The role of non-equilibrium vibrational structures in electronic coherence and recoherence in pigmentprotein complexes," *Nature Physics*, vol. 9, no. 2, pp. 113–118, 2013.

[113] V. Butkus, D. Zigmantas, D. Abramavicius, and L. Valkunas, "Distinctive character of electronic and vibrational coherences in disordered molecular aggregates," *Chemical Physics Letters*, vol. 587, pp. 93–98, 2013.

[114] J. M. Womick and A. M. Moran, "Vibronic enhancement of exciton sizes and energy transport in photosynthetic complexes," *Journal of Physical Chemistry B*, vol. 115, no. 6, pp. 1347–1356, 2011.

[115] F. Novelli, A. Nazir, G. H. Richards, A. Roozbeh, K. E. Wilk, P. M. Curmi, and J. A. Davis, "Vibronic Resonances Facilitate Excited-State Coherence in Light-Harvesting Proteins at Room Temperature," *Journal of Physical Chemistry Letters*, vol. 6, no. 22, pp. 4573–4580, 2015.

[116] J. Hauer, H. von Berlepsch, D. Zigmantas, F. Caycedo-Soler, M. B. Plenio, J. Lim, C. N. Lincoln, D. Paleček, S. F. Huelga, and J. Prior, "Vibronic origin of long-lived coherence in an artificial molecular light harvester," *Nature Communications*, vol. 6, no. 1, pp. 4–10, 2015.

[117] M. Thorwart, H.-G. Duan, R. J. Cogdell, K. Ashraf, A. L. Stevens, R. J. D. Miller, and V. I. Prokhorenko, "Nature does not rely on long-lived electronic quantum coherence for photosynthetic energy transfer," *Proceedings of the National Academy of Sciences*, vol. 114, no. 32, pp. 8493–8498, 2017.

[118] T. M. Clarke and J. R. Durrant, "Charge Photogeneration in Organic Solar Cells," *Chemical Reviews*, vol. 110, no. 11, pp. 6736–6767, 2010.

[119] N. J. Hestand and F. C. Spano, "Expanded Theory of H- and J-Molecular Aggregates: The Effects of Vibronic Coupling and Intermolecular Charge Transfer," *Chemical Reviews*, vol. 118, pp. 7069–7163, Aug 2018.

[120] F. C. Spano and C. Silva, "H- and j-aggregate behavior in polymeric semiconductors," *Annual Review of Physical Chemistry*, vol. 65, no. 1, pp. 477–500, 2014. PMID: 24423378.

[121] C. Creatore, M. A. Parker, S. Emmott, and A. W. Chin, "Efficient biologically inspired photocell enhanced by delocalized quantum states," *Phys. Rev. Lett.*, vol. 111, p. 253601, Dec 2013.

[122] A. Fruchtman, R. Gomez-Bombarelli, B. W. Lovett, and E. M. Gauger, "Photocell optimization using dark state protection," *Physical Review Letters*, vol. 117, no. 20, pp. 1–6, 2016.

[123] D. M. Rouse, E. M. Gauger, and B. W. Lovett, "Optimal power generation using dark states in dimers strongly coupled to their environment," *New Journal of Physics*, vol. 21, p. 063025, Jun 2019.

[124] A. Stokes and A. Nazir, "A master equation for strongly interacting dipoles," *New J. Phys.*, vol. 20, no. 4, p. 43022, 2018.

[125] A. Camara-Artigas, R. E. Blankenship, and J. P. Allen, "The structure of the fmo protein from chlorobium tepidum at 2.2 å resolution," *Photosynthesis Research*, vol. 75, pp. 49–55, Jan 2003.

[126] Y. Zhang, S. Oh, F. H. Alharbi, G. S. Engel, and S. Kais, "Delocalized quantum states enhance photocell efficiency," *Physical Chemistry Chemical Physics*, vol. 17, no. 8, pp. 5743–5750, 2015.

[127] D. M. Young in *Iterative Solution of Large Linear Systems* (D. M. Young, ed.), Academic Press, 1971.

[128] D. Farina and V. Giovannetti, "Open-quantum-system dynamics: Recovering positivity of the redfield equation via the partial secular approximation," *Phys. Rev. A*, vol. 100, p. 012107, Jul 2019.

[129] K. A. Mazzio and C. K. Luscombe, "Erratum: The future of organic photovoltaics," *Chemical Society Reviews*, vol. 44, no. 15, p. 5744, 2015.

[130] N. Espinosa, M. Hsel, D. Angmo, and F. Krebs, "Solar cells with one-day energy payback for the factories of the future," *Energy & Environmental Science*, vol. 5, pp. 5117–5132, 01 2012.

[131] M. Einax, M. Dierl, and A. Nitzan, "Heterojunction organic photovoltaic cells as molecular heat engines: A simple model for the performance analysis," *Journal of Physical Chemistry C*, vol. 115, no. 43, pp. 21396–21401, 2011.

[132] S. M. Falke, C. A. Rozzi, D. Brida, M. Maiuri, M. Amato, E. Sommer, A. De Sio, A. Rubio, G. Cerullo, E. Molinari, and C. Lienau, "Coherent ultrafast charge transfer in an organic photovoltaic blend," *Science*, vol. 344, pp. 1001 LP – 1005, May 2014.

[133] M. B. Plenio and S. F. Huelga, "Dephasing-assisted transport: quantum networks and biomolecules," *New Journal of Physics*, vol. 10, p. 113019, Nov 2008.

[134] M. Galperin and A. Nitzan, "Current-induced light emission and light-induced current in molecular-tunneling junctions," *Physical Review Letters*, vol. 95, no. 20, pp. 1–4, 2005.

[135] B. Rutten, M. Esposito, and B. Cleuren, "Reaching optimal efficiencies using nanosized photoelectric devices," *Physical Review B - Condensed Matter and Materials Physics*, vol. 80, no. 23, pp. 1–5, 2009.

[136] C. Huang, M. Jevric, A. Borges, S. T. Olsen, J. M. Hamill, J.-T. Zheng, Y. Yang, A. Rudnev, M. Baghernejad, P. Broekmann, A. U. Petersen, T. Wandlowski, K. V. Mikkelsen, G. C. Solomon, M. Brøndsted Nielsen, and W. Hong, "Single-molecule detection of dihydroazulene photo-thermal reaction using break junction technique," *Nature Communications*, vol. 8, no. 1, p. 15436, 2017.

[137] M. Irie, T. Fukaminato, T. Sasaki, N. Tamai, and T. Kawai, "A digital fluorescent molecular photoswitch," *Nature*, vol. 420, no. 6917, pp. 759–760, 2002.

[138] C. Jia, A. Migliore, N. Xin, S. Huang, J. Wang, Q. Yang, S. Wang, H. Chen, D. Wang, B. Feng, Z. Liu, G. Zhang, D.-H. Qu, H. Tian, M. A. Ratner, H. Q. Xu, A. Nitzan, and X. Guo, "Covalently bonded single-molecule junctions with stable and reversible photoswitched conductivity," *Science*, vol. 352, no. 6292, pp. 1443–1445, 2016.

[139] B. Yang, J. Hou, S. Li, Y. Zhang, H. Yao, W. Zhao, and S. Zhang, "Molecular Optimization Enables over 13% Efficiency in Organic Solar Cells," *Journal of the American Chemical Society*, vol. 139, no. 21, pp. 7148–7151, 2017.

[140] C. Li, Y. Zhang, L. Ding, R. Xia, Y. Cao, Y. Chen, L. Meng, Z. Xiao, Y. Wang, X. Wan, X. Ke, X. Zhang, and H.-L. Yip, "Organic and solution-processed tandem solar cells with 17.3% efficiency," *Science*, vol. 361, no. 6407, pp. 1094–1098, 2018.